THEORETICAL STUDIES OF VIBRONIC DYNAMICS OF FLUORINATED ORGANIC HYDROCARBONS

A Thesis

Submitted for the Degree of

DOCTOR OF PHILOSOPHY

By

TANMOY MONDAL

SCHOOL OF CHEMISTRY

PROF. C. R. RAO ROAD

UNIVERSITY OF HYDERABAD

HYDERABAD 500 046

INDIA

November 2010

STATEMENT

I hereby declare that the matter embodied in this thesis is the result of investigations carried out by me in the School of Chemistry, University of Hyderabad, Hyderabad, under the supervision of **Prof. Susanta Mahapatra**.

In keeping with the general practice of reporting scientific observations, due acknowledgment has been made wherever the work described is based on the findings of other investigators.

November 2010 (**Tanmoy Mondal**)

Hyderabad - 46

CERTIFICATE

Certified that the work contained in this thesis entitled "Theoretical studies of vibronic dynamics of fluorinated organic hydrocarbons " has been carried out by Mr. **Tanmoy Mondal** under my supervision and the same has not been submitted elsewhere for a degree.

November 2010
Hyderabad - 46

(**Prof. Susanta Mahapatra**)
Thesis Supervisor

Dean
School of Chemistry
Prof. C. R. Rao Road
University of Hyderabad
Hyderabad 500 046
INDIA

ACKNOWLEDGMENTS

My stay at School of Chemistry, University of Hyderabad has been a very fruitful, rewarding and enjoyable experience which I will cherish forever. This experience was made possible by the presence of a great set of people around me, who never let me feel that I was living so far away from my family.

First and foremost, I would like to express my deep sense of gratitude to **Prof. Susanta Mahapatra** for his excellent guidence and constant encouragement throughout my research work, and introducing me to this wonderful realm of conical intersections. The experience that I gained in the last five years through his suggestions, comments and even critiques will help me in all my future endeavors. His scientific knowledge and human skills are something which I will cherish foreever.

My sincere respect to Prof. M. Durga Prasad for his co-guidence for some other research project. It has been my great privilege to work with him. I extend my sincere thanks to the former and present Deans, School of Chemistry, for providing all necessary facilities to carry out my research work. I also thank all the faculty members for their assistance during my graduate years. I would like to extend my thanks to ACRHEM, University of Hyderabad and Council of Scientific and Industrial Research (CSIR), New Delhi for financial support and Centre for Modelling Simulation and Design (CMSD) for computational facilities.

I express my heartful thanks to my lab mates Dr. R. Padmanaban, Dr. Subhas Ghoshal, Dr. T. S. Venkatesan, Dr. Jayachander Rao, Siva, Susanta, Rajgopal Rao, Rajagopala Reddy, Tanmoy Roy, Nagaprasad, Biswarup and Aleem for many fruitful discussions, help and their warm company on various occasions. Their association will remain forever in my memory.

I am highly thankful to Dr. Pranab Sarkar and Dr. Bidhan Chandra Bag of Visva-Bharati University for their prompt help, care and valuable suggestions.

I wish to thank Mrs. Gitashree Mahapatra (madam), cute Anusha and charm-

ing Anish for their delightful company in various occasions.

I would like to thank my friends Subhasis Sarkar, Bankim, Subhasis kundu, Sudipta, Bulbul, Avisek, Adris and many more for their support and friendship.

I would also like to thank to all my seniors with whom I have enjoyed some wonderful memories in my Ph.D. life. The seniors who still matter are Abhik-da, Moloy-da, Ani-da, Bhaswati-di, Saikat-da, Manab-da, Archan-da, Dinu-da, Pradip-da, Ghona, Prashant-da, Prasun-da, Rahul-da, Binoy-da, Sunirban-da, Sandy-da, Utpal-da, Masum-da, Shatabdi-di, Anindita-di, Sriparna-di. I am really fortunate to have great friends like Sandip, Tapta, Arindam, Vasudhara, subrata, Pati and Rumpa. I am glad to have my juniors like Tulika, Rishi, susruta, palash, dinesh, Sanghamitra, Sudhansu, Meheboob, Anup, Nayan, Pramiti, Supratim, Satyajit, Raja, Sutanuka, Poulami, Krishnendu, Suman, Chandrani, monima and many more. I am thankful to Saritha, Kumar, Ravi, Arun and many others

Throughout my life I have been lucky enough to be surrounded by lot of wonderful friends. Therefore, it is indeed a difficult task to mention them all here. But I acknowledge **each and every one** of them from the bottom of my heart for helping me to get through the difficult times, all the support, entertainment and the caring they have provided.

Lastly, and most importantly, I thank my parents and extended family members for their love, care and unconditional support without which life would have appeared pale. But for some people mere thanks is not enough. Therefore, I dedicate this thesis to the most important people to me: My parents.

November 2010 (**Tanmoy Mondal**)

Hyderabad - 46

List of Abbreviations

$\mathbf{1}_n$	n-dimensional unit matrix
ADT	Adiabatic-to-diabatic transformation
aug-cc-pVnZ	augmented correlation consistent polarized valence n - ζ
BO	Born-Oppenheimer
CIs	Conical intersection(s)
DOF	Degrees of freedom
ECP	Effective core potential
EOM-CCSD	Equation-of-motion coupled-cluster singles and doubles
FC	Franck-Condon
FWHM	Full-width at half-maximum
IREPs	Irreducible representation(s)
JT	Jahn-Teller
LIF	Laser-induced fluorescence
LVC	Linear vibronic coupling
MATI	Mass analyzed threshold ionization
MCTDH	Multiconfiguration time-dependent Hartree
MP2	Second order Møller-Plesset perturbation theory
OVGF	Outer valence Green's function
PEFCO	Photoelectron-fluorescence coincidences
PES(s)	Potential energy surface(s)
PJT	pseudo-Jahn-Teller
QVC	Quadratic vibronic coupling
REMPI	Resonance enhanced multiphoton ionization
RT	Renner-Teller
SPFs	Single particle functions
VC	Vibronic coupling
WP	Wave packet

Contents

Chapter 1

Introduction

1.1 A brief overview of the Jahn-Teller effect and vibronic coupling

The Born-Oppenheimer (BO) adiabatic approximation [1–3], which represents one of the cornerstones of molecular physics and chemistry, supports the calculation of molecular dynamical processes to be divided into two steps. The first step involves into the solution of electronic problem keeping the atomic nuclei clamped in space whereas the nuclear dynamics on a given predetermined electronic potential energy surface (PES) is treated in the second step. This approximation is based on the fact that the spacing of electronic eigenvalues is generally large compared to typical spacings of the energy levels associated with nuclear motion. Clearly, the approximation breaks down when electronic states are close in energy (approach to within a quantum of energy of nuclear vibration) and the residual coupling via the nuclear kinetic energy operator causes transitions between the adiabatic electronic states. Therefore, the nuclear motion is no longer confined to a single 'adiabatic' electronic PES. In this situation there will be a strong coupling between the nuclear and electronic motions which is termed as vibronic coupling (VC). A pictorial outcome of these phenomena in polyatomic molecules

is the occurrence of *conical intersection* (CI) [4–14]. An overview of CIs and their ramification in chemical dynamics has been presented in the next section.

The most striking deviations from the adiabatic approximation arises due to the presence of orbitally degenerate electronic states. From a historic perspective, the concept of instability and spontaneous distortion of the nuclear configuration of a non-linear molecule in an orbitally degenerate electronic state was first proposed by Jahn and Teller in 1937 [15, 16]. This type of VC is known as Jahn-Teller (JT) effect [16–23] which is one of the most fascinating phenomena in chemical physics. Later through the seminal work of Longuet-Higgins *et al.* [24, 25] it was recognized that the degeneracy of electronic wavefunction requires a coupled-surface treatment of the nuclear motion; the spectral intensity distribution for the so-called $(E\times e)$-JT effect (JT effect in a doubly degenerate (E) electronic state caused by the degenerate (e) vibrational modes) was computed accordingly (for an explicit demonstration of the nonadiabatic coupling effects see, for example [26]) and opens the doorway for further research to elucidate its nature and importance in a wide variety of systems including, transition metal complexes [27], solid-state physics and chemistry [28–30], organic hydrocarbons, radicals and ions [4,17,21,31–34], and fullerenes [35]. A typical phenomena associated with the $(E \times e)$-JT CI is the formation of "Mexican hat" type of topography within a linear coupling limit. Where the lower PES containing three equivalent minima and three equivalent saddle points connecting pairs of minima and the upper one resembles a conical shape with its vertex touching the lower one at the point of 3-fold-symmetry [36]. In multimode situation, because of these CIs the vibrational levels of the upper surface are completely mixed with the quasi-continuum vibrational levels of the lower surface [4] which leads a highly diffuse spectral envelope. In a time-dependent picture this generally yields a femtosecond non-radiative decay of the upper electronic state [4, 37–41].

In 1957, Öpik and Pryce first noted that effects similar to the JT effect may be inherent in systems with near (quasi-degenerate or pseudo-degenerate) electronic

states [42]. This is known as pseudo-Jahn-Teller (PJT) effect in the literature [4,14,22,43–45]. In the following year in 1958, Longuet-Higgins along with Öpik, Pryce and Sack worked on the dynamic aspects of the JT effect, that is the interaction between motions of the nuclei and the electrons [24]. In general, the degeneracy of an electronic state can be removed both by degenerate and non-degenerate nuclear motion. While the former one occurs rather widely in physics and chemistry [17, 21, 24] the latter one is also encountered in the molecules possessing two or four fold axis of symmetry, for example, C_4, C_{4v}, C_{4h}, D_4, D_{2d}, D_{4h}, S_4, and D_{4d} point groups [4,17,21,28,37,46,47]. This is known as $(E \times b)$-JT effect since here the degeneracy is lifted by vibrational modes of b symmetries. In this case vibrational modes of e symmetries participate in PJT activity. The JT effect as well as the PJT effect have been studied extensively over the past few decades (see, for example, the Refs. [4, 14, 17–23, 33] and the references therein). Although most of the applications of the JT effect are related to the field of spectroscopy, excited state dynamics and structural phase transformations, it has also played a key role in one of the most important (Nobel Prize in 1987) discoveries of modern physics: high temperature superconductivity [48].

A situation analogous to the JT effect in nonlinear polyatomic molecules also occurs in linear molecules in their degenerate or pseudo-degenerate states within quadratic VC scheme and is termed as Renner-Teller (RT) effect, following the original paper of Renner in 1934 [49]. In that paper he describes the vibronic interactions in degenerate Π electronic states of linear triatomic molecules. In the course of time, the RT effect has been extended to consider tetra-atomic linear molecules [50], treatment of Δ states [51], inclusion of magnetic-coupling effects [52], inclusion of anharmonic coupling and Fermi Resonances [53], inclusion of molecular rotation [54], etc. For a detailed survey of the RT effects, see the review by Rosmus and Chambaud [55].

1.2 Classification of CIs and their importance in chemical dynamics

While crossing of electronic states of the same symmetry is prohibited by von Neumann and Wigner's non-crossing rule [56] in diatomic molecules, the same constraint does not apply to the polyatomic molecules due to the presence of three or more nuclear degrees of freedom. In this situation electronic states do cross, and they form a CI which is a (3N-6-2)-dimensional seam (or hyperline) of the electronic energy for an N-atomic molecular system. Historically, the crossing of electronic PESs was discovered in the early 1930s [5, 16, 49]. In the course of time, an intense theoretical research activity started in this area and predicts a wide range of physical phenomena that emerge from PES crossings. The field has undergone a monumental growth thereafter following the outstanding contributions of several research groups [4, 7, 17–19, 21, 28, 57–59]. The CIs of electronic PESs are classified into few groups as follows: (i) by electronic state symmetry: the noncrossing rule, (ii) by topography and (iii) by dimension of the branching space.

Symmetry-required (enforced) CIs do occur when two electronic states form the components of a degenerate irreducible representation (IREP). An example of this class of CI is the JT intersection by two lowest excited states of Na_3 which corresponds to the components of an E IREP of C_{3v} point group. Conical intersections which are not required by symmetry are accidental intersection. Accidental intersection corresponds to two states of distinct spatial symmetry is known as *accidental symmetry-allowed (different symmetry)* CI. The two lowest excited singlet electronic states (A'') of H-S-H, provides an example of this type of CI. For C_{2v} geometries these states are of $^1A_2$ and $^1B_1$ symmetry, so that symmetry allowed accidental CI occurs [60–63]. Likewise when PESs of two states of same symmetry cross, the intersection is termed as *accidental same symmetry* CI. An intersection of electronically excited 2^1A and 3^1A states of

CH_3-S-H provides an example of this type of CI [60, 63, 64].

Based on the shape and orientation of the PESs, CIs are further classified as *peaked* and *sloped* CI [65–67]. *Peaked* CIs appear when both the PESs are elliptical cones pointing towards each other with a common tip. In this case, the crossing point is the minimum of the upper PES and the topology at this point looks like a double cone. At *slopped* CIs, both the PESs have downhill slope and touch each other at the crossing point in branching space. Here, the crossing point is always at higher energies compare to the minimum of the upper PES and the crossing appear as a seam of intersections. While a large variety of photochemical reactions via excited-state reaction pathways are controlled by *peaked* CIs, the *sloped* CIs are key factor for the unsuccessful chemical reactions and arrange decay channels for the ultrafast nonradiative deactivation of excited states [66, 67].

Seams of the CI can also be catagorised based on the dimension of the branching space, η, for intersection of two PESs with $\eta = 2$, 3 or 5 [68]. Among them $\eta = 2$ is the most common case of a two state CI for even electronic molecular system in a non-relativistic situation.

Not surprisingly, CIs of electronic PESs have now emerged to be the paradigm of triggering strong nonadiabatic effects leading to blurring of vibrational level structure of molecular electronic states, various ultrafast molecular processes [14] and also serve as the "bottleneck " in photophysical and photochemical transitions [9–11]. They are also referred to as *photochemical funnels* in the literature [69]. The book edited by Domcke, Yarkony and Köppel represents an excellent collection of articles in this emerging area of chemical dynamics [14]. Nowadays, CIs can be considered as generalizations of the JT intersections in lower symmetric cases or in other way JT degeneracies are recognized as special cases of CIs [4, 6, 7, 10, 14, 70, 71], because the linear coupling terms predicted by JT theorem leads to a conical shape of the JT split PESs near the point of degeneracy [17,21,23]. Novel signature of VC and the associated JT and PJT effects are

the appearance of nominally forbidden electronic bands, odd quantum excitation of nontotally symmetric modes, unusual and complex vibronic fine structures of electronic spectra, loss of mirror symmetry of absorption and emission bands and observed quenching of fluorescence emission [4, 14, 72]. As the optical absorption and photoelectron spectroscopy probes the excited state within Franck-Condon (FC) region, these features becomes dominant when the CIs occur near or within the FC zone.

1.3 Current state of research and outline of the thesis

Aromatic fluorinated compounds are prototype organic species of fundamental importance for which electronic structure, spectroscopy and dynamics have received great attention in literature both theoretically and experimentally [73–91]. The perfluoro effect - fluorination causes a stabilization of the σ-type molecular orbitals (MO) [92, 93]. As a result the energetic minimum of the seam of various CIs and the equilibrium minimum of a state varies with fluorine substitution, causing a difference in its emissive properties for both cation and neutral fluorinated hydrocarbons. It is already established from experimental studies [94, 95] that 1,3,5-trifluorobenzene radical cation ($TFBz^+$) shows considerable emmision in contrast to the parent benzene radical cation (Bz^+) and as the number of fluorine substituent increases the absorption spectra of the neutral fluorinated benzenes becomes increasingly congested and the well resolved vibrational spectra of it's parent compound is almost completely lost [85]. This highly diffuse and complex pattern of molecular electronic spectra indeed bears the signature of complex entanglement of electronic and nuclear motion and indicates the paramount importance of the nonadiabatic effects on the spectral envelope and energy relaxation process [4]. Although a contemporary knowledge of electronic structure

and spectroscopy of these molecules have been collected in several experimental and theoretical studies [73–91], at the same time some important aspects of the excited states are poorly understood and a rich theoretical interpretation of the observed spectral envelope is yet to be explored. Even less is known of the nuclear dynamics following electronic excitation, the possible energy redistribution and relaxation mechanism.

Therefore in the present thesis, a rigorous quantum-mechanical formalism is devised for studying the dynamics of polyatomic fluorinated systems (both cation and neutral) on n electronically adiabatic state, interacting due to the presence of nonadiabatic couplings. This formalism is then applied to investigate the complex vibronic spectra and nonradiative decay dynamics of highly symmetric multimode JT and related systems as well as the structure and dynamics at conically intersecting PESs in lower symmetry polyatomic molecules with the help of *ab initio* electronic structure calculations and quantum dynamical simulations. More specifically, the electronic states displaying the JT and PJT interactions are probed through photoelectron spectroscopic experiment where as conically intersecting electronic states of lower symmetric molecules are probed through optical absorption spectroscopic experiment. The dynamical observables are predicted both by time-independent matrix diagonalization and time-dependent wave packet (WP) propagation approach. While the time-independent matrix diagonalization method is used to unravel the nonadiabatic effects on the complex and irregular vibronic spectra, the nonradiative decay of excited electronic states and the broadening of the vibronic bands are investigated within a time-dependent framework by propagating WPs.

Chapter 2 presents the theoretical and computational methodologies to investigate the static and dynamic aspects of multimode VC effects. The fundamental concept of adiabatic approximation and the necessity of a diabatic electronic representation to examine both the JT and PJT interactions and vibronic interactions in multimode molecular systems have been outlined. Construction of

model diabatic vibronic Hamiltonian using the elementary symmetry selection rules and electronic structure calculations to extract parameters of Hamiltonian follow. The time-independent and time-dependent approaches for solving the quantum eigenvalue equation to calculate vibronic spectra are also illustrated.

A detailed theoretical account of the multimode JT and PJT interactions in the five lowest electronic states of CF_3CN^+ have been presented in Chapter 3 to elucidate highly complex vibronic structure of the first two photoelectron bands of CF_3CN. Extensive *ab initio* electronic structure calculations are performed to develop a model vibronic Hamiltonian and first-principles calculations are carried out both via time-independent and time-dependent quantal methods to simulate the nonadiabatic nuclear motion on the coupled manifold of these electronic states.

Chapter 4 provides the static and dynamic aspects of multimode JT and PJT interactions in the four lowest electronic states of $TFBz^+$. Detail topography of the adiabatic PES and various low-energy CIs among them are estimated through model vibronic Hamiltonian. Nonadiabatic effects due to these intersections on the vibronic dynamics are examined by WP propagation method. Reduced dimensional calculations are also performed to unravel the better resolved vibrational level structures of the mass analyzed threshold ionization (MATI) spectroscopy. The impact of the increasing fluorination on the structure and dynamics of the excited states is discussed in relation to the parent benzene radical cation and its mono- and di-fluoro derivatives.

Chapter 5 deals with the photophysics of the first few low-lying singlet electronic states of four fluorinated benzene, namely monofluorobenzene (MFBz), ortho-difluorobenzene (*o*-DFBz), meta- difluorobenzene (*m*-DFBz) and pentafluorobenzene (PFBz). The complex and broad absorption spectra and the nonradiative internal conversion rate of the excited states are calculated by developing model vibronic Hamiltonian and solving the eigenvalue equation. Theoretical results are compared with the available experimental results. Justification is also

provided for the low quantum yield and biexponential fluorescence emission with increasing number of fluorine substitution.

Final conclusions and prospects of the current thesis are presented in Chapter 6.

Chapter 2

Theoretical Methodology

2.1 Basic concepts of nonadiabatic dynamics

2.1.1 Nonadiabatic coupling and adiabatic electronic representation

The typical molecular Hamiltonian is

$$H = T_e + T_N + U(\mathbf{r}, \mathbf{R}) \tag{2.1}$$

where T_e and T_N are the electronic and nuclear kinetic energy operators, respectively, and $U(\mathbf{r}, \mathbf{R})$ is the total potential energy of the molecule. The vector $\mathbf{r}$ denotes the set of electronic coordinates and the vector $\mathbf{R}$ stands for the nuclear coordinates describing the displacements from a reference configuration. By setting the kinetic energy of the nuclei equal to zero, i.e., $T_N = 0$, one defines the familiar electronic Hamiltonian:

$$H_e = T_e + U(\mathbf{r}, \mathbf{R}). \tag{2.2}$$

Obviously, H_e is an operator in the electronic space which depends parametrically on $\mathbf{R}$. Its eigenfunctions $\mathbf{\Phi_n(r,\ R)}$ and eigenvalues $\mathbf{V_n(R)}$ fulfill

$$H_e\mathbf{\Phi_n}(\mathbf{r},\mathbf{R}) \ = \mathbf{V_n}(\mathbf{R})\mathbf{\Phi_n}(\mathbf{r},\mathbf{R}). \tag{2.3}$$

They are known as the BO adiabatic electronic states and adiabatic PESs [96], respectively. The full molecular wavefunction $\mathbf{\Psi}(\mathbf{r},\mathbf{R})$ can now be expanded in terms of the above adiabatic electronic states as

$$\mathbf{\Psi}(\mathbf{r},\mathbf{R}) \ = \ \sum_n \chi_\mathbf{n}(\mathbf{R})\mathbf{\Phi_n}(\mathbf{r},\mathbf{R}). \tag{2.4}$$

This expansion is known as the BO expansion [3]. Formally, Eq.(2.4) is exact, since the set $\{\mathbf{\Phi_n}(\mathbf{r},\mathbf{R})\}$ is complete. It is only when the expansion is truncated that approximation is introduced. The BO expansion certainly provides a perfectly valid ansatz if $\mathbf{\Phi_n}(\mathbf{r},\mathbf{R})$ describes a bound state solution of the full Schrödinger equation

$$(H-E)\mathbf{\Psi}(\mathbf{r},\mathbf{R}) \ = \ 0. \tag{2.5}$$

From the Schrödinger Eq.(2.5) one can readily obtain [96] the coupled equations for the expansion coefficients $\chi_\mathbf{n}(\mathbf{R})$ in the ansatz (2.4). Inserting Eq. (2.4) into (2.5), multiplying from the left by $\mathbf{\Phi^*_m}(\mathbf{r},\mathbf{R})$ and integrating over the electronic coordinates leads to

$$\left[T_N + \mathbf{V_n}(\mathbf{R}) - E\right]\chi_\mathbf{n}(\mathbf{R}) \ = \ \sum_m \mathbf{\hat{\Lambda}_{nm}}\chi_\mathbf{m}(\mathbf{R}). \tag{2.6}$$

The operators $\mathbf{\Lambda_{nm}}$ are known as the nonadiabatic operators describe the dynamical interaction between the electronic and nuclear motion. They are given

by [3]

$$\hat{\mathbf{\Lambda}}_{\mathbf{nm}} = -\int \mathbf{dr}\mathbf{\Phi}^{\star}_{\mathbf{n}}(\mathbf{r},\mathbf{R})[\mathbf{T_N},\mathbf{\Phi_m}(\mathbf{r},\mathbf{R})]. \tag{2.7}$$

and are obviously operators in **R**-space. Decomposition of the nonadiabatic operators in terms of the first- and second-order derivative couplings, in Cartesian coordinates reads [4, 97, 98]

$$\hat{\mathbf{\Lambda}}_{\mathbf{nm}} = -\sum_k \frac{\hbar^2}{M_k}\mathbf{F_{nm}}\frac{\partial}{\partial R_k} - \sum_k \frac{\hbar^2}{2M_k}\mathbf{G_{nm}}, \tag{2.8}$$

where M_k are nuclear masses and

$$\mathbf{F^{(k)}_{nm}} = \langle \mathbf{\Phi_n}(\mathbf{r})| \bigtriangledown_k |\mathbf{\Phi_m}(\mathbf{r})\rangle, \tag{2.9}$$

$$\mathbf{G^{(k)}_{nm}} = \langle \mathbf{\Phi_n}(\mathbf{r})| \bigtriangledown_k^2 |\mathbf{\Phi_m}(\mathbf{r})\rangle, \tag{2.10}$$

in which $\bigtriangledown_k \equiv \partial/\partial R_k$.

Returning to the fundamental set of equations given in Eq. (2.6) one can rewrite this set of coupled equations as a matrix Schrödinger equation

$$\left(\underbrace{T_N\mathbf{1} + \mathbf{V}(\mathbf{R}) - \hat{\mathbf{\Lambda}}}_{\mathcal{H}} - E\mathbf{1}\right)\chi = 0. \tag{2.11}$$

The matrix Hamiltonian $\mathcal{H}$ describes the nuclear motion in the manifold of electronic states. χ is the column vector with elements χ_n; **1** is the unit matrix, and $\mathbf{V}(\mathbf{R}) = \{\mathbf{V_n}(\mathbf{R})\delta_{nm}\}$ is the diagonal matrix of electronic energies. The quantity $\hat{\mathbf{\Lambda}}$ represents the nonadiabatic coupling effects in the adiabatic electronic representation.

From the aforementioned description it can be seen that in an adiabatic electronic representation, nuclear kinetic energy operator is non-diagonal and the po-

tential energy operator is diagonal. The elements of $\mathbf{\Lambda_{nm}}$ define the off-diagonal elements of the nuclear kinetic energy operator (cf., Eq. 2.6) and therefore states are coupled through the nuclear kinetic energy operator. When $\mathbf{\Lambda_{nm}}$ is set to zero altogether, one arrives at the well-known BO or adiabatic approximation [1, 59] and the coupled dynamical equation of motion (Eq. 2.6) reduces to the one describing the motion of the nuclei on the uncoupled adiabatic PESs

$$\{T_N(\mathbf{R}) + \mathbf{V_n}(\mathbf{R}) - E\}\chi_{\mathbf{n}}(\mathbf{R}) \;=\; 0 \tag{2.12}$$

Although the adiabatic approximation is often a very useful approach, it may fail in cases where the PESs of different electronic states are energetically close. In these cases the elements of the nonadiabatic coupling matrix $\mathbf{\Lambda_{nm}}$ can become extremely large, and huge ratio of nuclei to electronic masses is overcome by the large derivative coupling $\mathbf{F_{nm}}$ and the BO approximation remains no longer valid. The derivative coupling matrix elements diverge at the intersection of the PESs according to Hellmann-Feynmann type of relation [4, 99]

$$\mathbf{F^{(k)}_{nm}} \;=\; \frac{\langle \mathbf{\Phi_n}(\mathbf{r})| \bigtriangledown_k \mathcal{H}_{el}(\mathbf{r},\mathbf{R})|\mathbf{\Phi_m}(\mathbf{r})\rangle}{\mathbf{V_n}(\mathbf{R}) - \mathbf{V_m}(\mathbf{R})}, \tag{2.13}$$

where $\mathcal{H}_{el}$ defines the electronic Hamiltonian for fixed nuclear coordinates. When the two surfaces are degenerate, $V_n(\mathbf{R}) = V_m(\mathbf{R})$ the $\mathbf{F_{nm}}$ exhibit singular behavior [4]. As a result, both the electronic wavefunction and energy become discontinuous at the seam of CIs which makes the adiabatic electronic representation unsuitable for dynamical studies. To circumvent this problem the concept of diabatic electronic states is introduced [100].

2.1.2 Diabatic electronic representation

In a diabatic electronic representation the diverging kinetic energy couplings of the adiabatic representation are transformed into smooth potential energy cou-

plings through a suitable unitary transformation. In this representation the nuclear kinetic energy operator is diagonal and the coupling between the electronic states is introduced through the off-diagonal elements of potential energy operator of the molecular Hamiltonian. In a diabatic electronic representation the coupled equations of motion (cf, Eq. 2.6) takes the form [59, 72]

$$\{T_N(\mathbf{R}) + \mathbf{U_{nn}}(\mathbf{R}) - E\}\chi_{\mathbf{n}}(\mathbf{R}) \;=\; \sum_{m\neq n} \mathbf{U_{nm}}(\mathbf{R})\chi_{\mathbf{m}}(\mathbf{R}), \tag{2.14}$$

where $\mathbf{U_{nn}}(\mathbf{R})$ are the diabatic PESs and $\mathbf{U_{nm}}(\mathbf{R})$ are their coupling elements. The latter are given by

$$\mathbf{U_{nm}}(\mathbf{R}) \;=\; \int d\mathbf{r}\phi_n^\star(\mathbf{r},\mathbf{R})[T_e + \mathbf{V}(\mathbf{r},\mathbf{R})]\phi_m(\mathbf{r},\mathbf{R}), \tag{2.15}$$

where ϕ represents the diabatic electronic wavefunction.

The diabatic electronic states $\phi(\mathbf{r},\mathbf{R})$ are defined via a unitary transformation of the adiabatic electronic states $\mathbf{\Phi}(\mathbf{r},\mathbf{R})$ through

$$\phi(\mathbf{r},\mathbf{R}) \;=\; \mathbf{S}\mathbf{\Phi}(\mathbf{r},\mathbf{R}), \tag{2.16}$$

where $\mathbf{S}$ is orthogonal transformation matrix

$$\mathbf{S}(\mathbf{Q}) \;=\; \begin{pmatrix} \cos\theta(\mathbf{Q}) & \sin\theta(\mathbf{Q}) \\ -\sin\theta(\mathbf{Q}) & \cos\theta(\mathbf{Q}) \end{pmatrix}. \tag{2.17}$$

The matrix $\mathbf{S(Q)}$ is called the adiabatic-to-diabatic transformation (ADT) matrix and $\theta(\mathbf{Q})$ defines the transformation angle. The required condition for such transformation is the first-order derivative coupling of Eq. (2.13) vanishes in this diabatic representation for all nuclear coordinates [101, 102]

$$\int d\mathbf{r}\phi_{\mathbf{n}}^*(\mathbf{r},\mathbf{R})\frac{\partial}{\partial\mathbf{R_k}}\phi_{\mathbf{m}}(\mathbf{r},\mathbf{R}) \;=\; 0. \tag{2.18}$$

This requirement yields the following differential equations for the transformation matrix [103–105]

$$\frac{\partial \mathbf{S}}{\partial \mathbf{R_k}} + \mathbf{F^{(k)}S} = 0, \tag{2.19}$$

where the elements of the first-order derivative coupling matrix $F^{(k)}$ are given by Eq. (2.13). A unique solution of the above equation exist only when [103–105]

$$\frac{\partial \mathbf{A^{(k)}_{nm}}}{\partial \mathbf{R_l}} - \frac{\partial \mathbf{A^{(l)}_{nm}}}{\partial \mathbf{R_k}} = [\mathbf{A^{(k)}_{nm}}, \mathbf{A^{(l)}_{nm}}]. \tag{2.20}$$

The concept of diabatic electronic basis was introduced quite early in the literature in the context of describing the electron-nuclear coupling in atomic collision processes [100] as well as in molecular spectroscopy [25, 70]. However, construction of the latter for polyatomic molecular systems is a tedious and difficult since it is a problem depending on multi-coordinates rather than a single nuclear coordinate. Therefore, various approximate mathematical schemes have been proposed in the literature [101–103, 106–112] to accomplish this task.

2.1.3 Normal Coordinates

Following the traditional approach [19–21, 25], we introduce normal coordinates [113] to describe small vibrations around the equilibrium geometry of the electronic ground state. We assume here that we are dealing with a closed-shell molecular system. The normal coordinates are defined by

$$\mathbf{q} = \mathbf{L}^{-1}\delta\mathbf{R} \tag{2.21}$$

where $\delta\mathbf{R}$ is the $3N-6$ ($3N-5$ for linear molecules) dimensional vector of internal displacement coordinates (changes of bond lengths and bond angles) for an N atomic molecule, and $\mathbf{L}$ is the L-matrix of the well-known Wilson FG-matrix

method [113]. It is convenient to introduce dimensionless normal displacement coordinates via

$$Q_i = (\omega_i/\hbar)^{1/2} q_i \tag{2.22}$$

where ω_i is the harmonic vibrational frequency of the ith normal mode. In the harmonic approximation, the kinetic-energy and potential-energy operators of the electronic ground state take the simple form (let us consider that $\hbar = 1$)

$$T_N = -\frac{1}{2}\sum_i \omega_i \frac{\partial^2}{\partial Q_i^2} \tag{2.23}$$

$$V_0 = \frac{1}{2}\sum_i \omega_i Q_i^2 \tag{2.24}$$

In the following sections, we proceed by expanding the diabatic excited-state potential-energy functions and coupling elements in terms of normal mode displacement coordinate Q_i.

2.1.4 Linear Vibronic Coupling Scheme

Let us assume that a diabatic basis has been obtained for a given set of vibronically interacting electronic states. In this basis the matrix Hamiltonian is given by [4]

$$\mathcal{H} = T_N \mathbf{1} + \mathbf{W}(\mathbf{Q}). \tag{2.25}$$

The matrix elements of the potential matrix $\mathbf{W}(\mathbf{Q})$ read

$$W_{nm}(\mathbf{Q}) = \int d\mathbf{r} \phi_n^\star(\mathbf{r}, \mathbf{Q}) H_e \phi_m(\mathbf{r}, \mathbf{Q}). \tag{2.26}$$

The $\phi_n(\mathbf{r},\mathbf{Q})$ are the diabatic wavefunctions for an electronic state of index n. For a polyatomic molecule, the accurate solution of the matrix Hamiltonian (Eq. 2.25)

is very tedious and often impracticable. Therefore, an approximate form of the matrix Hamiltonian is often considered for which the Schrödinger equation can be accurately solved. The simplest, yet elegant approximation is to expand the potential-energy matrix $\mathbf{W}(\mathbf{Q})$ about a reference nuclear configuration $\mathbf{Q}_0$ and retaining the terms linear in $\mathbf{Q}$ for the off-diagonal terms. This method is known as the linear vibronic coupling (LVC) scheme [4,97]. The linear approximation is often sufficient since the elements of the $\mathbf{W}(\mathbf{Q})$ matrix are, by definition, slowly varying functions of $\mathbf{Q}$. Without any loss of generality it is assumed that the diabatic and adiabatic states are identical at the reference geometry $\mathbf{Q}_0$.

For the interacting electronic states n and m, the elements of the matrix Hamiltonian in the linear approximation are

$$\mathcal{H}_{nn} = T_N + V_0(\mathbf{Q}) + E_n + \sum_s \kappa_s^{(n)} Q_s \tag{2.27}$$

$$\mathcal{H}_{nm} = \sum_s \lambda_s^{(n,m)} Q_s. \tag{2.28}$$

The energies E_n which appear in the diagonal of $\mathcal{H}$ are constants given by $W_{nn}(\mathbf{Q_0})$. The quantities $\kappa_s^{(n)}$ and $\lambda_s^{(n,m)}$ are known as *intrastate* and *interstate* electron-vibrational coupling constants, respectively, given by [4]

$$\kappa_s^{(n)} = \left(\frac{\partial V_n(\mathbf{Q})}{\partial Q_s}\right)_{\mathbf{Q_0}}, \tag{2.29}$$

$$\lambda_s^{(n,m)} = \left(\frac{\partial V_{nm}(\mathbf{Q})}{\partial Q_s}\right)_{\mathbf{Q_0}}. \tag{2.30}$$

The non-vanishing interstate coupling constants $\lambda_s^{(n,m)}$ are those for which the product of the irreducible representations of electronic states ϕ_n and ϕ_m, and of the nuclear coordinate Q_s contains the totally symmetric representation Γ_A,

i.e. [4],

$$\Gamma_n \times \Gamma_{Q_s} \times \Gamma_m \supset \Gamma_A. \tag{2.31}$$

The analogous condition for the intrastate coupling constants $\kappa_s^{(n)}$ is

$$\Gamma_n \times \Gamma_{Q_s} \times \Gamma_n \supset \Gamma_A. \tag{2.32}$$

Certainly all totally symmetric modes can couple to the electronic motion which emphasize the important role of these modes in the VC problem. From the above symmetry selection rules (Eqs. 2.31 and 2.32), we can say that, only the totally symmetric modes give rise to nonzero intrastate coupling constants and only nontotally symmetric modes to nonzero interstate coupling constants.

2.1.5 Vibronic coupling involving degenerate modes and degenerate states

The degenerate electronic states are outstanding examples of the failure of the adiabatic approximation. In the case of linear molecules the VC problem is known as the RT effect [49]; otherwise, it is known as the JT effect [16]. Starting with the JT effect, which is the part of essential ingredient of this thesis, nearly all (nonlinear) molecules with degenerate electronic states possess several degenerate modes which can vibronically couple the components of these states. It is thus clear that we have to solve the multimode JT problem in order to arrive at an understanding of the interactions that occur in actual molecules.

2.1.5.1 The Jahn-Teller Effect

The derivation of JT Hamiltonians follows general principles of vibronic coupling theory, several of which have, in fact, first been formulated within JT theory [17, 25]. The component of degenerate electronic states at the high-symmetry

reference configuration are used as an electronic basis *also for displaced,* lower-symmetry nuclear configurations. The JT Hamiltonian is then represented as a matrix with respect to this basis, and the matrix elements are usually expanded in a Taylor series for small displacements Q_i $(i = 1, \cdots, n)$ from the reference configuration: [4, 17, 21]

$$\mathcal{H}_{\alpha\alpha'}{}^{JT} = H_0\delta_{\alpha\alpha'} + \sum_i \frac{\partial V_{\alpha\alpha'}}{\partial Q_i} Q_i + \sum_{i,j} \frac{\partial^2 V_{\alpha\alpha'}}{\partial Q_i \partial Q_j} Q_i Q_j + \mathcal{O}\left(Q^3\right). \tag{2.33}$$

Here $V_{\alpha\alpha'}$ $(\alpha, \alpha' = 1, \cdots, m)$ denote the matrix elements of the potential energy operator in the electronic basis chosen, and the derivatives are to be taken at the symmetric conformation $Q_i = Q_j = 0$ $(i, j = 1, \cdots, n)$. The term H_0 includes the zero-order element of the expansion, *i.e.,* the degenerate electronic energy eigenvalue $V(0)$ at the high-symmetry nuclear configuration, the nuclear kinetic energy, and also the "JT-unperturbed" vibrational potential energy. The latter is usually specified in the harmonic approximation, comprising all relevant vibrational degrees of freedom and serves to define the displacement normal coordinates Q_i $(i = 1, \cdots, n)$ of the expansion in Eq. (2.33). Generally, it can be chosen to represent vibrational motion on the arithmetic mean of the JT split potential energy surfaces. Alternatively, it is often equated with the vibrational Hamiltonian of the initial, nondegenerate electronic state, if such an electronic transition is under investigation.

Comparison between the above written JT Hamiltonian (2.33) and other vibronic coupling Hamiltonians discussed in the literature immediately reflects that the underlying concepts between them are virtually identical. The only essential difference is that for JT cases, the relative sizes and signs of the derivatives of $V_{\alpha\alpha'}$ within a degenerate electronic manifold are constrained by symmetry. Also, the degeneracy itself, being a conical intersection for finite first derivatives $\partial V_{\alpha\alpha'}/\partial Q_i$, occurs for $Q_i = Q_j = 0$, *i.e.* it is not accidental, but again fixed by symmetry. Finally, the symmetries of the JT-active normal modes, within LVC

scheme, are determined by the requirement that their irreducible representations Γ_{vib} are contained in the decomposition of the symmetrized direct product of the irreducible representation Γ_{el} of the electronic state according to [15, 17, 21]

$$(\Gamma_{el})^2 \supset \Gamma_{vib} \tag{2.34}$$

In the following, these general statements will be exemplified for prototype cases of CF_3CN^+ and $TFBz^+$ involving twofold degenerate electronic states on Chapter 3 and Chapter 4. The extensions to include additional (nondegenerate) states will also be discussed there.

2.1.5.2 The single-mode $E \otimes e$ Jahn-Teller effect

The simplest case which shows the JT effect is a system with a doubly degenerate electronic state and a threefold principal rotation axis. In this system there are always doubly degenerate vibrational modes that are (linearly) JT-active, that is, the derivatives $\partial V_{\alpha\alpha'}/\partial Q_i$ do not vanish for their (cartesian) displacement components Q_x and Q_y. Now considering the elementary symmetry selection rule mentioned above (2.34), the corresponding 2×2 JT matrix Hamiltonian up to second order is found to be [17, 23, 24]

$$\mathbf{H}^{E\otimes e} = H_0\mathbf{1} + k\begin{pmatrix} Q_x & Q_y \\ Q_y & -Q_x \end{pmatrix} + \frac{g}{2}\begin{pmatrix} Q_x^2 - Q_y^2 & 2Q_xQ_y \\ 2Q_xQ_y & Q_y^2 - Q_x^2 \end{pmatrix}. \tag{2.35}$$

$$H_0 = \frac{\omega}{2}\left(-\frac{\partial^2}{\partial Q_x^2} - \frac{\partial^2}{\partial Q_y^2} + Q_x^2 + Q_y^2\right). \tag{2.36}$$

H_0 is seen to represent the Hamiltonian of the isotropic two-dimensional harmonic oscillator (with frequency ω), and the electronic energy at the origin $Q_x = Q_y = 0$ has been chosen to be zero. $\mathbf{1}$ denotes the 2×2 unit matrix. The parameters k ($k > 0$) and g are called the first-order (or linear) and second-order (or quadratic) coupling constants, respectively.

To start with, let us first consider the second-order coupling constant g to zero. This then reduces the Eq. (2.35) to the well-known Hamiltonian of the linear $E \otimes e$ JT effect which has been amply studied in the literature (see, for example, Refs. [4,17,21] and references therein). Diagonalization of the potential energy part leads to the famous "Mexican hat" potential energy surfaces

$$V_{\pm} = \frac{\omega}{2}\rho^2 \pm k\rho, \tag{2.37}$$

$$\rho^2 = Q_x^2 + Q_y^2. \tag{2.38}$$

These rotationally symmetric surfaces are characterized by the JT stabilization energy

$$E_{JT} = \frac{k^2}{2\omega}, \tag{2.39}$$

occurring at the optimum distortion

$$\rho_0 = k/\omega. \tag{2.40}$$

The so-called pseudorotational angle ϕ is defined as

$$\phi = \arctan\left(Q_y/Q_x\right). \tag{2.41}$$

The corresponding eigenvector matrix reads

$$\mathbf{S} = \begin{pmatrix} \cos\left(\phi/2\right) & -\sin\left(\phi/2\right) \\ \sin\left(\phi/2\right) & \cos\left(\phi/2\right) \end{pmatrix}, \tag{2.42}$$

where the two columns represent the expansion coefficients of the adiabatic wavefunctions in the diabatic electronic basis. Transforming the complete Hamiltonian

(2.35) to the adiabatic basis leads to

$$\mathbf{H}_{ad}^{E\otimes e} = \mathbf{S}^{\dagger}\mathbf{H}^{E\otimes e}\mathbf{S} = H_0\mathbf{1} + \begin{pmatrix} V_+ & 0 \\ 0 & V_- \end{pmatrix} + \mathbf{\Lambda}, \tag{2.43}$$

with the nonadiabatic coupling operator

$$\mathbf{\Lambda} = \frac{\omega}{2\rho^2}\begin{pmatrix} \frac{1}{4} & i\frac{\partial}{\partial\phi} \\ i\frac{\partial}{\partial\phi} & \frac{1}{4} \end{pmatrix}, \tag{2.44}$$

which is seen to diverge at the origin $\rho = 0$, where the two adiabatic potential energy surfaces exhibit the JT intersection.

2.1.6 Influence of additional modes

The above comprehensive presentation of the single-mode $E \otimes e$ JT effect serves as the basis for the discussion of related and more general systems. These will be discussed more briefly, focussing on their similarities and differences with respect to the prototype case. We start with the inclusion of additional vibrational modes.

2.1.6.1 Additional e vibrational modes

Additional e modes are included in the Hamiltonian (2.35) by replacing the corresponding single-mode terms by summations over all relevant vibrations, *e.g.*

$$kQ_x \rightarrow \sum_i k_i Q_x^i, \quad kQ_y \rightarrow \sum_i k_i Q_y^i, \tag{2.45}$$

in a self-explanatory notation (and an analogous extension in the zero-order Hamiltonian H_0). Since virtually all molecules exhibiting the $E \otimes e$ JT effect possess several e modes (except for equilateral X_3 systems) this generalization is of immediate relevance. Although the total JT stabilization energy E_{JT} is

additive, *i.e.*

$$E_{JT} = \sum_i \frac{k_i^2}{2\omega_i} \equiv \sum_i E_{JT}^{(i)}, \tag{2.46}$$

the Hamiltonians $\mathbf{H}_i^{E\otimes e}$ for the various modes do not commute ($i \neq j$):

$$\left[\mathbf{H}_i^{E\otimes e}, \mathbf{H}_j^{E\otimes e}\right] \neq 0. \tag{2.47}$$

Thus, the eigenvalue problem of the individual Hamiltonians cannot be solved separately. Rather, the multi-mode vibronic secular matrix has to be diagonalized as a whole [4].

The nonseparability of the JT active modes makes it necessary to sum over all contributions $\mathcal{H}_j$ of the individual modes

$$\mathcal{H} \;=\; \sum_j^M \mathcal{H}_j, \tag{2.48}$$

and treat the total matrix Hamiltonian $\mathcal{H}$ as a whole rather than the individual terms separately. As a consequence, the vibronic symmetries are reduced considerably. The individual vibronic angular momenta

$$\mathbf{J}_j \;=\; \frac{1}{i}\frac{\partial}{\partial\phi_j}\mathbf{1_2} + \frac{1}{2}\begin{pmatrix} 1 & 0 \\ 0 & -1 \end{pmatrix} \tag{2.49}$$

are no longer constants of the motion. It is only the total vibronic angular momentum

$$\mathbf{J} \;=\; \sum_j^M \frac{1}{i}\frac{\partial}{\partial\phi_j}\mathbf{1_2} + \frac{1}{2}\begin{pmatrix} 1 & 0 \\ 0 & -1 \end{pmatrix} \tag{2.50}$$

that commutes with $\mathcal{H}$ [4]. In the adiabatic PESs this manifests itself in a dependence of $\mathcal{V}_\pm$ on the azimuthal angles ϕ_j of the individual modes. The potentials are invariant only under a common change of the angles of all vibrational modes

otherwise of a very complicated shape. In addition, the locus of intersection is no longer a single point in coordinate space, but rather a subspace of dimension $2M$ - 2. It must be evident from these remarks that the multimode JT problem leads to much more complicated nuclear dynamics than the single-mode problem. We note that it is important to take these multimode effects into consideration in order to arrive at a realistic treatment of actual molecules [4].

2.1.6.2 Inclusion of totally symmetric vibrational modes

From Eq. (2.27) it is clear that displacements along totally symmetric vibrations can *tune* the energy gap ($|E_2 - E_1|$) between two electronic states and generally lead to intersections of the potential-energy functions, which are allowed by symmetry. These vibrational modes have therefore been termed *tuning modes* [4]. On the other hand, the nontotally symmetric modes satisfying Eq. (2.31) describe the coupling between two electronic states. Therefore, they are termed as *coupling modes* [4]. Within the LVC approach, the tuning modes contribute only to the diagonal elements of the electronic Hamiltonian matrix, see Eq. (2.27). Therefore, the inclusion of these modes to the VC models described earlier becomes straightforward.

In the $(E \times e)$-JT case the N_t tuning modes are represented by

$$H^t_{JT} = \sum_{i=1}^{N_t} \left[\left(\frac{\partial^2}{\partial Q_i^2} + Q_i^2 \right) \mathbf{1_2} + \begin{pmatrix} \kappa_i^E & 0 \\ 0 & \kappa_i^E \end{pmatrix} Q_i \right], \tag{2.51}$$

where the normal coordinates Q_i, $i = 1 \cdots N_t$, are the totally symmetric modes and the κ_i^E are the gradients of the adiabatic potential-energy functions of the E state with respect to the i^{th} tuning mode.

From Eqs. (2.35) and (2.51), we have

$$\left[\mathbf{H}^{E\otimes e}, H^t_{JT}\right] = 0. \tag{2.52}$$

For this reason a_1 modes are usually omitted from JT treatments and included in the computation of optical spectra.

2.1.7 The pseudo-Jahn-Teller effect involving degenerate electronic states

So far the discussion has been restricted to an isolated doubly degenerate (E) electronic state which is not always be suitable for a real molecular system. This is particularly very true when there are other electronic states energetically very close to this doubly degenerate electronic state, where couplings to other electronic states may play a crucial role. As a simple generalization we will therefore consider now the interaction of an E electronic state with a nondegenerate state, characterized by the symmetry label A. The intra-state (JT) interaction within the E state will initially be suppressed for clarity.

2.1.7.1 The single-mode $(E + A) \otimes e$ pseudo-Jahn-Teller effect

Considering the same general principles and symmetry selection rule for the construction of the vibronic Hamiltonian as indicated above and discussed in section 2.1.5.1, the Hamiltonian for the linear $(E + A) \otimes e$ pseudo-Jahn-Teller effect is found to be [4, 43]

$$\mathcal{H} = H_0\mathbf{1} + \begin{pmatrix} E_E & 0 & \lambda Q_x \\ 0 & E_E & \lambda Q_y \\ \lambda Q_x & \lambda Q_y & E_A \end{pmatrix}. \tag{2.53}$$

Here E_E and E_A denote the E and A state energies for the undistorted nuclear configuration ($Q_x = Q_y = 0$) and $\mathbf{1}$ represents the 3×3 unit matrix.

We note that the Hamiltonian (2.53) shares many features with the general vibronic coupling problem for two nondegenerate electronic states, discussed amply in the literature. We also note that the notion "pseudo-Jahn-Teller" (PJT)

interaction has been used for systems where one of the interacting states as well as the coupling mode are degenerate and unlike general vibronic coupling systems, the totally symmetric modes are nonseparable from the PJT problem and play an important role already in first order. Although they are neglected in Eq. (2.53) for simplicity but are included in the examples discussed in this thesis whenever applicable.

The adiabatic eigenvectors corresponding to Eq. (2.53) involve either the asymmetric (potential surface V_0) or symmetric (potential surfaces V_+ and V_-) linear combinations of the E component basis states. The eigenvalues are

$$\begin{aligned} V_0 &= \frac{\omega}{2}\left(Q_x^2+Q_y^2\right)+E_E \\ V_\pm &= \frac{\omega}{2}\left(Q_x^2+Q_y^2\right)+\frac{E_E+E_A}{2} \\ &\pm \sqrt{\left(\frac{E_E-E_A}{2}\right)^2+\lambda^2\left(Q_x^2+Q_y^2\right)}. \end{aligned} \tag{2.54}$$

It depends on the sign of $E_E - E_A$ whether V_+ or V_- correlates with the E state for $Q_x = Q_y = 0$ and becomes degenerate there with the "unperturbed" surface V_0.

2.1.7.2 The single-mode $(E \otimes e + A) \otimes e$ pseudo-Jahn-Teller effect

Let us now address the more general case of systems with simultaneous JT and PJT vibronic interactions. Depending on the particular symmetries prevailing, the same vibrational mode may be JT and PJT active in first order. This is, quite likely the case, for example, in trigonal point groups with a single doubly degenerate irreducible representation (it follows necessarily, if there exists a single mode of this symmetry only). Then the relevant Hamiltonian is obtained by adding Eqs. (2.35, 2.36, 2.53) for the same mode [4, 43, 114]:

$$\mathcal{H}^{PJT} = H_0\mathbf{1} + k\begin{pmatrix} Q_x & Q_y & 0 \\ Q_y & -Q_x & 0 \\ 0 & 0 & 0 \end{pmatrix} + \frac{g}{2}\begin{pmatrix} Q_x^2 - Q_y^2 & 2Q_xQ_y & 0 \\ 2Q_xQ_y & Q_y^2 - Q_x^2 & 0 \\ 0 & 0 & 0 \end{pmatrix} + \begin{pmatrix} E_E & 0 & \lambda Q_x \\ 0 & E_E & \lambda Q_y \\ \lambda Q_x & \lambda Q_y & E_A \end{pmatrix}. \quad (2.55)$$

As in the preceding subsection, the second-order PJT couplings have been suppressed. (While their form is straightforward to work out, they may often be less important, if the E-A energy gap is not too small). The meaning of the zero-order Hamiltonian H_0 and of the coupling constants is also the same as above. Although the totally symmetric modes has an important influence on the system dynamics, they are not included in the Hamiltonian (2.55) for simplicity. However, they may be not only Condon-active through finite first-order coupling constants, but also modulate the $E - A$ energy gap through *different* first-order constants in the two electronic states. This is the same behavior as in vibronic coupling systems with nondegenerate states [4] and as in the $(E + A) \otimes e$ PJT coupling systems discussed above. It may lead to additional conical intersections with two or three (for PJT systems) intersecting potential energy surfaces.

2.2 Calculation of the excitation spectrum

Assume that a molecule initially in the state Ψ_0 is excited by some operator $\hat{T}$ into a manifold of vibronically coupled electronic state. According to Fermi's Golden rule, the excitation spectrum is described by the function

$$P(E) = \sum_v \left|\langle\Psi_v|\hat{T}|\Psi_0\rangle\right|^2 \delta(E - E_v + E_0), \quad (2.56)$$

where $|\Psi_0\rangle$ is the reference state of the molecule with energy E_0. $|\Psi_v\rangle$ is the final vibronic state in the coupled electronic manifold and E_v is the vibronic energy. Considering the reference state is energetically well separated and decoupled from the excited electronic manifold, the initial and final states are given by

$$|\Psi_0\rangle = |\Phi^0\rangle|\chi_0^0\rangle, \tag{2.57}$$

$$|\Psi_v\rangle = |\Phi^1\rangle|\chi_v^1\rangle + |\Phi^2\rangle|\chi_v^2\rangle, \tag{2.58}$$

where $|\Psi\rangle$ and $|\chi\rangle$ represent the diabatic electronic and vibrational part of the wavefunction, respectively. The superscripts 0, 1, and 2 refer to the ground and the two interacting diabatic electronic states, respectively. With the use of Eqs. (2.57-2.58), the excitation function of Eq. 2.56 can be rewritten as [4]

$$P(E) = \sum_v \left|\tau^1\langle\chi_v^1|\chi_0^0\rangle + \tau^2\langle\chi_v^2|\chi_0^0\rangle\right|^2 \delta(E - E_v + E_0), \tag{2.59}$$

where

$$\tau^m = \langle\Phi^m|\hat{T}|\Phi^0\rangle, \tag{2.60}$$

represent the matrix elements of the transition dipole operator of the final electronic state m. Upon rewriting Eq. (2.59), the matrix elements of the transition dipole operator are treated to be independent of nuclear coordinates. These elements are not calculated and are treated as constants, in accordance with the applicability of the generalized Condon approximation in a diabatic electronic basis [115].

2.2.1 Time-Independent quantum mechanical approach

In a time-independent quantum mechanical approach the excitation spectrum is calculated by solving the eigenvalue equation

$$\mathcal{H}|\Psi_v\rangle = E_v|\Psi_v\rangle \tag{2.61}$$

numerically, by representing the vibronic Hamiltonian $\mathcal{H}$ in a complete direct product basis of one dimensional harmonic oscillator eigenfunctions of $\mathcal{H}_0$. In this basis, $|\chi_v^m\rangle$ takes the following form [4]:

$$|\chi_v^m\rangle = \sum_{n_1,n_2,\ldots,n_k} a^m_{v,n_1,n_2,\ldots,n_k}|n_1\rangle|n_2\rangle\ldots|n_k\rangle. \tag{2.62}$$

Here m is the electronic state index, n_l is the quantum number associated with the l^{th} vibrational mode, and k is the total number of such modes. The summation runs over all possible combinations of quantum numbers associated with each mode. For each vibrational mode, the oscillator basis is suitably truncated in the numerical calculations. The maximum level of excitation for each mode is approximately estimated from the corresponding Poisson parameter $[\frac{1}{2}\,(\frac{\kappa or \lambda}{\omega})^2]$. The Hamiltonian matrix written in such a direct product basis is usually highly sparse, and is tridiagonalized using the Lanczos algorithm prior to diagonalization [116]. The diagonal elements of the resulting eigenvalue matrix give the eigenenergies of the vibronic energy levels and the relative intensities of the vibronic lines are obtained from the squared first components of the Lanczos eigenvectors [72, 116].

Finally, the spectral envelope is calculated by convoluting the line spectrum with a suitable Lorentzian line-shape function of appropriate width of the following:

$$\mathcal{L}(E) = \frac{1}{\pi}\frac{\Gamma/2}{E^2 + (\Gamma/2)^2}. \tag{2.63}$$

The quantity Γ represents the full width at the half maximum (FWHM) of the Lorentzian.

2.2.2 Time-Dependent Wave Packet Approach

In a time-dependent approach the Fourier transform representation of the Dirac delta function is used in the Golden formula (Eqs. 2.56, 2.59) to calculate the spectral intensity. In this representation the delta function is expressed as

$$\delta(x) = \frac{1}{2\pi}\int_{-\infty}^{+\infty} e^{ixt/\hbar}\delta t. \tag{2.64}$$

Using this the spectral intensity (Eq. (2.56)) transforms into the following useful form, readily utilized in a time-dependent picture

$$P(E) \approx 2Re\int_0^{\infty} e^{iEt/\hbar}\langle\Psi_f(0)|\boldsymbol{\tau}^{\dagger}e^{-i\mathcal{H}t/\hbar}\boldsymbol{\tau}|\Psi_f(0)\rangle dt, \tag{2.65}$$

$$\approx 2Re\int_0^{\infty} e^{iEt/\hbar}\, C_f(t)\, dt, \tag{2.66}$$

where the elements of the transition dipole matrix $\boldsymbol{\tau}^{\dagger}$ is given by, $\boldsymbol{\tau}^f = \langle\Phi^f|\hat{T}|\Phi^i\rangle$.

The above integral represents the Fourier transform of the time-autocorrelation function [4, 117]

$$C(t) = \langle\Psi_f(0)|e^{-i\mathcal{H}t/\hbar}|\Psi_f(0)\rangle = \langle\Psi_f(0)|\Psi_f(0)\rangle, \tag{2.67}$$

of the WP, initially prepared on the f^{th} electronic state and, $\Psi_f(t) = e^{-i\mathcal{H}t/\hbar}\,\Psi_f(0)$.

In the time-dependent calculations, the time autocorrelation function is damped with a suitable time-dependent function before Fourier transformation. The usual choice has been a function of type

$$f(t) \;\; = \;\; exp[-t/\tau_r] \;\; , \tag{2.68}$$

where τ_r represents the relaxation time. Multiplying $C(t)$ with $f(t)$ and then Fourier transforming it is equivalent to convoluting the spectrum with a Lorentzian line shape function (cf., Eq. 2.63) of FWHM, $\Gamma = 2/\tau_r$.

In case of multimode nonadiabatic dynamical studies this traditional approach to solve the Schrödinger equation becomes computationally impracticable with increase in the electronic and nuclear degrees of freedom. Therefore, for large molecules and with complex vibronic coupling mechanism this method often becomes impracticable. The WP propagation approach within the multiconfiguration time-dependent Hartree (MCTDH) scheme provides an alternative efficient tool to circumvent this problem [118–123]. The key ingredient of this scheme is to use a multiconfigurational ansatz [121, 123] for the wavefunction, with each configuration being expressed as a Hartree product of time-dependent basis functions, known as Single Particle Functions (SPFs). For the nonadiabatic problem examined here, a *multiset* formulation is much more appropriate and the corresponding wavefunction can be expanded as:

$$\begin{aligned}
\Psi(Q_1, Q_2, ..., Q_f, t) &= \Psi(q_1, q_2, ..., q_p, t) \\
&= \sum_{\alpha=1}^{\sigma} \sum_{j_1=1}^{n_1^{(\alpha)}} ... \sum_{j_p=1}^{n_p^{(\alpha)}} A^{(\alpha)}_{j_1...j_p}(t) \\
&\quad \times \prod_{k=1}^{p} \phi^{(\alpha,k)}_{j_k}(q_k, t)|\alpha\rangle \qquad (2.69) \\
&= \sum_{\alpha} \sum_{J} A^{(\alpha)}_J \Phi^{(\alpha)}_J |\alpha\rangle, \qquad (2.70)
\end{aligned}$$

where, f and p represent the number of vibrational degrees of freedom, and MCTDH *particles* (also called *combined* modes), respectively. $A^{(\alpha)}_{j_1...j_p}$ denote the MCTDH expansion coefficients and the $\phi^{(\alpha,k)}_{j_k}$ are the one-dimensional expansion functions, known as SPFs. The labels $\{\alpha\}$ are indices denoting the discrete set of electronic states considered in the calculation. Thus, the WP, $\Psi^{(\alpha)}$ ($= \sum_J A^{(\alpha)}_J \Phi^{(\alpha)}_J$) associated with each electronic state is described using a different

set of SPFs, $\{\phi_{j_k}^{(\alpha,k)}\}$. Here the multiindex, $J = j_1 \ ... \ j_p$ depends implicitly on the state α as the maximum number of SPFs may differ for different states. The summation $\sum_J$ is a shorthand notation for summation over all possible index combinations for the relevant electronic state. The variables for the p sets of SPFs are defined in terms of one or multidimensional coordinates of a particle.

The equations of motion for the expansion coefficients, $A_J^{(\alpha)}$ and SPFs, $\phi_{j_k}^{(\alpha,k)}$ have been derived using the Dirac-Frankel variational principle [124, 125]. The resulting equations of motion are coupled differential equations for the coefficients and the SPFs. For k degrees of freedom there are n_k SPFs, and these SPFs are represented by N_k primitive basis functions or grid points. The efficiency of the MCTDH algorithm grows with increasing N_k/n_k [123]. The use of the variational principle ensures that the SPFs evolve so as to optimally describe the true WP; i.e., the time-dependent basis moves with the WP. This provides the efficiency of the method by keeping the basis optimally small.

We mention that the accuracy of a MCTDH calculation depends on both the size of the primitive and the SPF bases. The populations of the primitive basis functions, *e.g.* the grid points is used to check that enough primitive basis functions have been used for the calculation. This can be done either by calculating the maximum population, or by evaluating the change of population with time of the points at the ends of the grid.

The quality of SPF basis is reflected in the population of natural orbitals. If a calculation contains natural orbital with a low population, these are not significant for the representation of the wavefunction, and the calculation is of a reasonable quality. Unfortunately, different properties have different convergence criteria. Therefore, it is not possible to give absolute figures for when the natural orbitals are insignificant. As a general rule of thumb, when the population of highest (least populated) natural orbital is below 1% (*i.e.* a population below 0.01), the calculation will be reasonable, although convergence may be a way off. Experience has shown that it is important that the SPF bases for all modes are

balanced *i.e.* the lowest natural orbital populations are similar for all. There is little point spending effort on converging the SPF basis for one mode when the dynamics can be seriously affected by the poor representation of another mode.

Next the efficiency of a calculation can be improved by knowing how much time is spent in the various sections of the calculation. For instance, if in a constant mean-field (CMF) run the Bulirsch-Stoer (BS)-integrator (used to propagate SPFs) takes less than one or two percent of the total effort, one should combine more SPFs. If on the other hand, the BS-integrator takes more than 80 % of totall effort, one should remove some of the combinations. Again if the propagation of one certain mode takes much longer time than the propagation of the other modes although the combined grid sizes are comparable, then one should check whether the DVR representation is appropriate

Here we provide a brief overview on the memory requirement for the MCTDH method. The memory required by standard method is proportional to N^f, where N is the total number of grid points or primitive basis functions and f is the total number of degrees of freedom. In contrast, memory needed by the MCTDH method scales as

$$memory \quad \sim \quad fnN + n^f \tag{2.71}$$

where, n represent the SPFs. The memory requirements can however reduced if SPFs are used that describe a set of degrees of freedom, termed as *multimode* SPFs. By combining d degrees of freedom together to form a set of $p{=}f/d$ particles, the memory requirement changes to

$$memory \quad \sim \quad f\tilde{n}N^d + \tilde{n}^f \tag{2.72}$$

where $\tilde{n}$ is the number of multimode functions needed for the new particles. If only single-mode functions are used i.e. $d{=}1$, the memory requirement, Eq. 2.72,

is dominated by n^f. By combining degrees of freedom together this number can be reduced, but at the expense of longer product grids required to describe the multimode SPFs.

Chapter 3

Complex dynamics at conical intersections : vibronic spectra and ultrafast decay of electronically excited trifluoroacetonitrile radical cation

3.1 Introduction

A detailed theoretical account on the multimode JT and PJT interactions in the five lowest electronic states of $CF_3CN^+$is presented in this chapter. The ground state equilibrium geometry of the trifluoroacetonitrile (CF_3CN) molecule belongs to the C_{3v} symmetry point group. Ionization of an electron from each of its five highest occupied $6e$, $10a_1$, $1a_2$, $9a_1$ and $5e$ molecular orbitals (MOs) yields CF_3CN^+ in its ground $\widetilde{X}^2E$ and first four excited $\widetilde{A}^2A_1$, $\widetilde{B}^2A_2$, $\widetilde{C}^2A_1$ and $\widetilde{D}^2E$ electronic states, respectively. The 12 vibrational degrees of freedom of CF_3CN are grouped into $4a_1 \oplus 4e$ irreducible representations of the C_{3v} symmetry

point group. The symmetrized direct product of two E representations in the C_{3v} point group yields

$$(E)^2 = a_1 + e \tag{3.1}$$

Similarly, the direct products of $E \otimes A_1$ and $E \otimes A_2$ in the C_{3v} symmetry point group result,

$$\begin{aligned} E \otimes A_1 &= e \\ E \otimes A_2 &= e \end{aligned} \tag{3.2}$$

These symmetry rules suggest that the degenerate $\widetilde{X}^2E$ and $\widetilde{D}^2E$ electronic states of CF_3CN would undergo JT splitting in first-order when distorted along the degenerate vibrational modes of e symmetry (note that the symmetry of the electronic and nuclear degrees of freedom are designated by the upper and lower case symbols, respectively). From Eq. (3.2) it can be seen that the same JT active degenerate vibrational modes also cause PJT type [4, 43–45] of coupling between different electronic states. The totally symmetric a_1 vibrational modes, on the other hand, cannot lift the electronic degeneracy and are Condon active [4]. The impact of these four JT and PJT active degenerate and four Condon active totally symmetric vibrational modes in the vibronic dynamics of CF_3CN^+ in its five low-lying electronic states is examined below.

The photoelectron spectrum of CF_3CN has been recorded by various experimental groups using He I, He II, and synchrotron radiation [126,127] as ionization sources. These experiments revealed different energy resolution and intensity of peaks in the vibronic bands. The first two photoelectron bands in the ∼13.3 - ∼17.7 eV energy range revealed highly overlapping and diffuse vibronic structures, resulting from ionization of electron from the $6e$, $10a_1$, $1a_2$, $9a_1$ and $5e$ MOs of CF_3CN, respectively. They are attributed to the vibronic structures of

the energetically close lying five lowest electronic states of CF_3CN^+ [126, 127].

In this chapter, we attempt to develop a theoretical model in order to examine the nuclear motion underlying the vibronic structures of the mentioned photoelectron bands. It is clear from the discussion above that various electronic coupling mechanisms need to be incorporated in the model to reach to a satisfying interpretation of the highly overlapping and complex structures of the latter. Our theoretical model consists of five low-lying (seven altogether when JT splitting is taken into consideration) electronic states of CF_3CN^+ plus its twelve vibrational degrees of freedom. The JT coupling within the $\widetilde{X}$ and $\widetilde{D}$ electronic states and their PJT coupling with the $\widetilde{A}$, $\widetilde{B}$ and $\widetilde{C}$ electronic states are taken into consideration. The PJT coupling between the JT split $\widetilde{X}$ and $\widetilde{D}$ electronic states are not considered mainly because they are vertically ∼3.32 eV apart and expected to not have any profound effect on the nuclear dynamics. While the JT coupling due to e vibrational modes is treated upto fourth-order and the Condon activity due to a_1 vibrational modes is treated upto second-order, the PJT coupling due to e vibrational modes is treated with a linear coupling scheme.

3.2 Equilibrium structure and normal vibrational modes of the electronic ground state of CF_3CN

The electronic structure calculations of CF_3CN are carried out at the Møller-Plesset perturbation (MP2) level of theory and employing both cc-pVDZ as well as 6-311++g** basis sets using Gaussian-03 program package [128]. The optimized equilibrium geometry of its electronic ground state ($\widetilde{X}^1A_1$) belongs to the C_{3v} symmetry point group. The optimized geometry parameters are : r_{CF}=1.33 Å, r_{CC}=1.48 Å, r_{CN}=1.17 Å, ∠ F-C-F=108.54^o and ∠ C-C-F=109.33^o, in good agreement with their experimental values [129]: 1.33 Å, 1.49 Å, 1.15 Å, 109.23^o and 109.74^o in that order, respectively. Examination of occupied canonical MOs

reveals a configuration, $\cdots(3e)^4(4e)^4(5e)^4(9a_1)^2(1a_2)^2(10a_1)^2(6e)^4$, for the electronic ground state of CF_3CN. The sequence of MOs above are in agreement with the results of Shimizu et al. [129] and differs with the results of Åsbrink et al. [130] and understandably the difference arises from the the level of quantum chemistry calculations that could be performed at that time.

Ionization of electrons from the degenerate highest occupied molecular orbital (HOMO) (6e), HOMO-1 ($10a_1$), HOMO-2 ($1a_2$), HOMO-3 ($9a_1$) and HOMO-4 (5e) results CF_3CN^+ in its $\widetilde{X}^2E$, $\widetilde{A}^2A_1$, $\widetilde{B}^2A_2$, $\widetilde{C}^2A_1$ and $\widetilde{D}^2E$ electronic states, respectively. These MOs are schematically shown in Fig. 3.1. According to Shimizu et al. [129] the characteristics of these MOs are as follows : HOMO is C-N π bonding, HOMO-1 is mainly the nitrogen lone pair, HOMO-2 is non-bonding and purely F 2p lone-pair, HOMO-3 is delocalized over the entire molecule and is bonding in nature. HOMO-4 is mostly F 2p lone-pair but also reveals C-F bonding. The diagrams shown in Fig. 3.1, describe the nature of these MOs illustrated above. These MOs are energetically close lying. The $\widetilde{A}$, $\widetilde{B}$, $\widetilde{C}$ and $\widetilde{D}$ electronic states are vertically ∼0.50 eV, ∼2.67 eV, ∼2.84 eV and ∼3.32 eV above the $\widetilde{X}$ state of CF_3CN^+ . The harmonic frequencies (ω_i, i=1-12) of the vibrational modes of the electronic ground state of CF_3CN are calculated by diagonalizing the MP2 force field, and are given in Table 3.1 along with their fundamental values available from the experiment [131]. Along with the frequencies the mass weighted normal coordinates are obtained, which are transformed into their dimensionless form by multiplying with $\sqrt{\omega_j}$ (in atomic units used here) [113]. These coordinates represent the normal displacement coordinates (from their equilibrium value at **Q=0**), referred here as Q_i for the i^{th} vibrational mode. Analysis shows that the twelve vibrational modes of CF_3CN decompose into $4a_1 \oplus 4e$ irreducible representations of the C_{3v} symmetry point group. These vibrational modes are schematically shown in Fig. 3.2, and their predominant nature are given in Table 3.1.

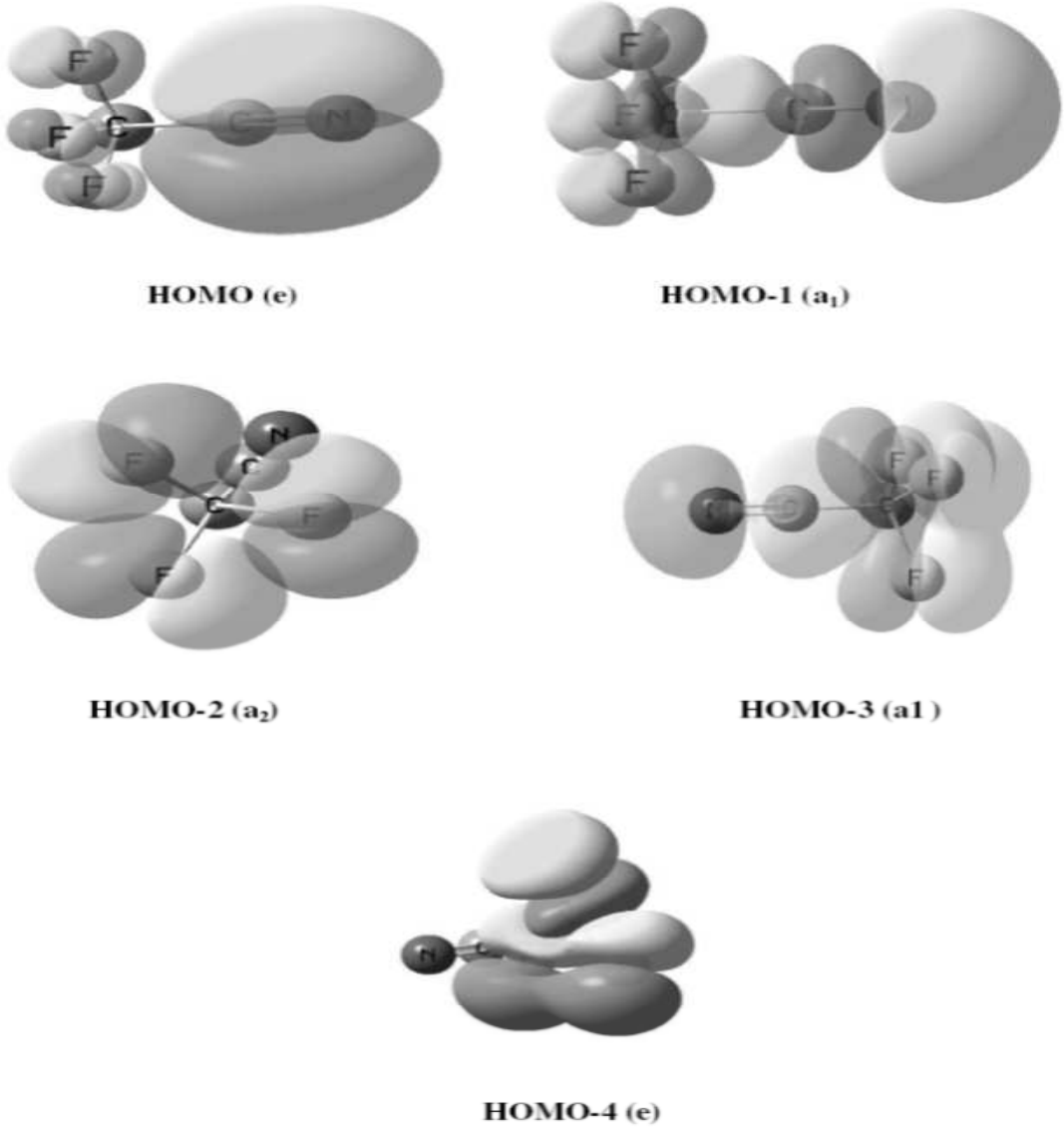

Figure 3.1: Schematic representation of the five valence type molecular orbitals of the electronic ground state of CF_3CN.

Table 3.1: Symmetry, frequency and description of the normal vibrational modes of the electronic ground state of trifluoroacetonitrile. The experimental results are reproduced from Ref. [131]. Note that, theoretical frequencies are harmonic, whereas, experimental ones are fundamental.

		Vibrational Frequency (ω_i)/eV		Predominant	
Symmetry	Mode	MP2/6-311++G**	Experiment	nature	Coordinate
a_1	ν_1	0.2716	0.2821	C-N Stretching	Q_1
	ν_2	0.1559	0.1521	C-C Stretching	Q_2
	ν_3	0.1010	0.0994	CF_3 Bending	Q_3
	ν_4	0.0656	0.0647	Umbrella Bending	Q_4
e	ν_5	0.1508	0.1505	C-F Stretching	Q_{5x}, Q_{5y}
	ν_6	0.0779	0.0766	C-C-F Scissoring	Q_{6x}, Q_{6y}
	ν_7	0.0583	0.0574	F-C-C Twisting	Q_{7x}, Q_{7y}
	ν_8	0.0234	0.0243	C-C-N Bending+F-C-F twisting	Q_{8x}, Q_{8y}

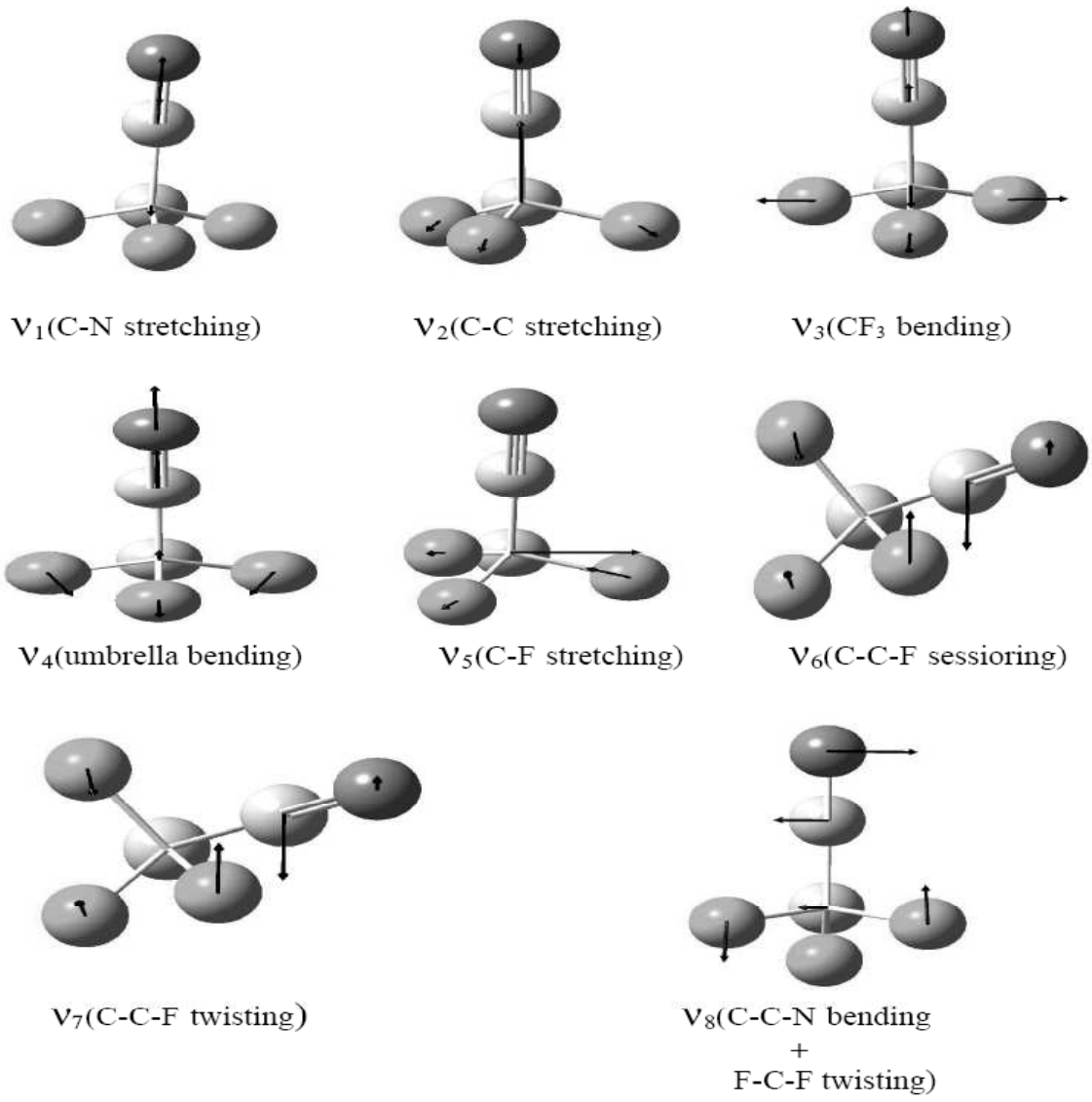

Figure 3.2: Schematic representation of the normal vibrational modes of the electronic ground state of CF_3CN.

3.3 The vibronic coupling model

Electronic structure and nuclear dynamics of CF_3CN^+ in its coupled $\widetilde{X}$ -$\widetilde{A}$ -$\widetilde{B}$ -$\widetilde{C}$ -$\widetilde{D}$ electronic states are examined in this chapter. As mentioned above these electronic states are energetically close and are readily accessible upon photoionization of CF_3CN and give rise to highly overlapping vibronic bands. An analysis of the structure of the latter requires the potential energies of these electronic states and their interaction potentials along various nuclear coordinates. The two degenerate ($\widetilde{X}$ and $\widetilde{D}$) electronic states of CF_3CN^+ undergo a JT splitting upon displacement along the degenerate vibrational modes. The latter modes can also cause PJT type of coupling between the two degenerate (which is not considered here) and also between the degenerate and nondegenerate electronic states. The four totally symmetric vibrational modes are Condon active within each electronic state [4]. In order to describe these couplings in the vibronic Hamiltonian we use a diabatic electronic basis [100, 115], in which they are represented in the electronic part and are smoothly varying functions of nuclear coordinates. The Hamiltonian is written in terms of the dimensionless normal coordinates of the vibrational modes of CF_3CN as discussed above and defined in Table 3.1, in conjunction with the stated symmetry selection rules [Eqs. (3.1-3.2)]. Therefore, the Hamiltonian for the coupled manifold of seven electronic states of CF_3CN^+ can be written as

$$\mathcal{H} = \mathcal{H}_0\mathbf{1_7} + \begin{pmatrix} \mathcal{W}_1^X & \mathcal{W}_{12}^X & \mathcal{W}_1^{X-A} & \mathcal{W}_1^{X-B} & \mathcal{W}_1^{X-C} & 0 & 0 \\ & \mathcal{W}_2^X & \mathcal{W}_2^{X-A} & \mathcal{W}_2^{X-B} & \mathcal{W}_2^{X-C} & 0 & 0 \\ & & \mathcal{W}^A & 0 & 0 & \mathcal{W}_1^{A-D} & \mathcal{W}_2^{A-D} \\ & & & \mathcal{W}^B & 0 & \mathcal{W}_1^{B-D} & \mathcal{W}_2^{B-D} \\ & h.c. & & & \mathcal{W}^C & \mathcal{W}_1^{C-D} & \mathcal{W}_2^{C-D} \\ & & & & & \mathcal{W}_1^D & \mathcal{W}_{12}^D \\ & & & & & & \mathcal{W}_2^D \end{pmatrix} \quad (3.3)$$

Here, $\mathcal{H}_0 = \mathcal{T}_N + \mathcal{V}_0$, represents the Hamiltonian of the unperturbed electronic ground state of CF_3CN. Nuclear motions in the latter are treated as harmonic with

$$\mathcal{T}_N = -\frac{1}{2}\sum_{i=1}^{4}\omega_i\frac{\partial^2}{\partial Q_i^2} - \frac{1}{2}\sum_{i=5}^{8}\omega_i\left(\frac{\partial^2}{\partial Q_{ix}^2} + \frac{\partial^2}{\partial Q_{iy}^2}\right), \tag{3.4}$$

and

$$\mathcal{V}_0 = \frac{1}{2}\sum_{i=1}^{4}\omega_i Q_i^2 + \frac{1}{2}\sum_{i=5}^{8}\omega_i\left(Q_{ix}^2 + Q_{iy}^2\right). \tag{3.5}$$

The matrix Hamiltonian with elements $\mathcal{W}$ in Eq. (3.3) describes the change in the electronic energy upon ionization from this unperturbed electronic ground state and define the details of diabatic electronic potential energy surfaces of CF_3CN^+ [4]. These elements are expanded in a Taylor series around the C_{3v} equilibrium geometry of CF_3CN along each normal mode displacement coordinates. Excluding various intermode coupling terms, the following expansions are retained for these elements :

$$\begin{aligned}\mathcal{W}_{1,2}^{X(D)} = {} & E_0^{X(D)} + \sum_{i=1}^{4}\kappa_i^{X(D)}Q_i \pm \sum_{i=5}^{8}\lambda_i^{X(D)}Q_{ix} + \frac{1}{2}\sum_{i=1}^{4}\gamma_i^{X(D)}Q_i^2 + \\ & \frac{1}{2}\sum_{i=5}^{8}[\gamma_i^{X(D)}(Q_{ix}^2 + Q_{iy}^2) \pm \eta_i^{X(D)}(Q_{ix}^2 - Q_{iy}^2)] + \\ & \frac{1}{6}\sum_{i=5}^{8}[\delta_i^{X(D)}(-6Q_{ix}Q_{iy}^2 + 2Q_{ix}^3) \pm \mu_i^{X(D)}(Q_{ix}^3 + Q_{ix}Q_{iy}^2)] + \\ & \frac{1}{24}\sum_{i=5}^{8}[\zeta_i^{X(D)}(Q_{ix}^2 + Q_{iy}^2)^2 \pm \alpha_i^{X(D)}(Q_{ix}^4 - 6Q_{ix}^2Q_{iy}^2 + Q_{iy}^4) \pm \\ & \beta_i^{X(D)}(Q_{ix}^4 - Q_{iy}^4)]\end{aligned} \tag{3.6a}$$

$$\mathcal{W}_{12}^{X(D)} = \sum_{i=5}^{8}\lambda_i^{X(D)}Q_{iy} - \sum_{i=5}^{8}\eta_i^{X(D)}Q_{ix}Q_{iy} + \frac{1}{6}\sum_{i=5}^{8}\mu_i^{X(D)}(Q_{ix}^2Q_{iy} + Q_{iy}^3) + \frac{1}{24}\sum_{i=5}^{8}[4\alpha_i^{X(D)}Q_{ix}Q_{iy}(Q_{ix}^2 - Q_{iy}^2) - 2\beta_i^{X(D)}Q_{ix}Q_{iy}(Q_{ix}^2 + Q_{iy}^2)] \quad (3.6b)$$

$$\mathcal{W}_1^{X(D)-k} = \sum_{i=5}^{8}\lambda_i^{X(D)-k}Q_{ix} \quad (3.6c)$$

$$\mathcal{W}_2^{X(D)-k} = -\sum_{i=5}^{8}\lambda_i^{X(D)-k}Q_{iy} \quad (3.6d)$$

$$\mathcal{W}^k = E_0^k + \sum_{i=1}^{4}\kappa_i^kQ_i + \frac{1}{2}\sum_{i=1}^{4}\gamma_i^kQ_i^2 + \frac{1}{2}\sum_{i=5}^{8}\gamma_i^k(Q_{ix}^2 + Q_{iy}^2) + \frac{1}{24}\sum_{i=5}^{8}\zeta_i^k(Q_{ix}^4 + Q_{iy}^4)\ ; \quad k \in \widetilde{A}, \widetilde{B}\ and\ \widetilde{C}. \quad (3.6e)$$

The quantity E_0^j represents the vertical ionization potential of the j^{th} electronic state. The linear intrastate and JT coupling parameters of the j^{th} electronic state are denoted by κ_i^j and λ_i^j for the symmetric and degenerate vibrational modes, respectively. The linear PJT coupling parameters for the latter modes between the electronic states j and k are represented by λ_i^{j-k}. The diagonal second-order coupling parameters for the vibrational modes are given by γ_i^j, and η_i^j represents the quadratic JT coupling parameters for the degenerate vibrational modes. The diagonal cubic and quartic [132] coupling parameters for these vibrational modes are given by δ_i^j and ζ_i^j, respectively, whereas the corresponding off-diagonal coupling parameters are given by μ_i^j, α_i^j and β_i^j. To calculate these coupling parameters, we perform direct calculations of vertical ionization energies

(VIEs) of CF_3CN by the outer valence Green's function method [133] employing the same basis sets as noted above. The VIEs are calculated for $Q_i = \pm 0.10$, ± 0.25 (0.25) ± 1.50, along the i^{th} vibrational mode keeping others at their equilibrium value. These VIEs are equated with the adiabatic potential energies of CF_3CN^+ relative to the electronic ground state of CF_3CN. Subsequently, these energies are fitted to the adiabatic form of the diabatic electronic Hamiltonian of Eq. (3.3), using least-squares algorithm and thereby the coupling parameters are obtained. Since the latter represent the derivatives of various order in the Taylor series expansion of the elements of the electronic Hamiltonian of [Eq. (3.6a-3.6e)], they are also estimated by numerical finite difference schemes. The parameters that represent the best agreement between the model and the *ab initio* adiabatic potentials are given in Tables 3.2, 3.3 and 3.4.

Table 3.2: Parameters of the vibronic Hamiltonian for the degenerate ground $\widetilde{X}^2E$ electronic state of CF_3CN^+, derived from the *ab initio* electronic structure results (see text for details). The vertical ionization energy of this electronic state (E_0^X) is also given in the table. All quantities are in eV.

Mode	κ_i or λ_i	γ_i	η_i	ζ_i	ϕ_i	μ_i	α_i	β_i
ν_1	0.2779	0.0325	–	–	–	–	–	–
ν_2	0.2890	-0.0165	–	–	–	–	–	–
ν_3	-0.0669	0.0005	–	–	–	–	–	–
ν_4	-0.0040	-0.0027	–	–	–	–	–	–
ν_5	0.0109	-0.0100	-0.0032	-0.0080	-0.0060	-0.0008	-0.0003	-0.0002
ν_6	0.0082	-0.0070	0.0037	-0.0040	-0.0025	0.0009	0.0005	0.0002
ν_7	0.0093	-0.0085	-0.0013	-0.0063	-0.0040	0.0009	0.0004	0.0002
ν_8	0.0092	-0.0082	-0.0004	-0.0065	-0.0061	-0.0003	-0.0002	-0.0002
E_0^X	14.031							

Table 3.3: Parameters of the vibronic Hamiltonian for the three lowest nondegenerate $\widetilde{A}^2A_1$, $\widetilde{B}^2A_2$ and $\widetilde{C}^2A_1$ electronic states of CF_3CN^+, derived from the *ab initio* electronic structure results (see text for details). The vertical ionization energies of these three electronic states (E_0^A, E_0^B, E_0^C) are also given in the table. All quantities are in eV.

Mode	κ_i $\widetilde{A}$ /$\widetilde{B}$ /$\widetilde{C}$	γ_i $\widetilde{A}$ /$\widetilde{B}$ /$\widetilde{C}$	ϕ_i $\widetilde{A}$ /$\widetilde{B}$ /$\widetilde{C}$
ν_1	-0.0927/0.0515/-0.0915	-0.0081/-0.0033/-0.0163	
ν_2	0.2612/-0.1642/0.1685	-0.0271/-0.0110/-0.0229	
ν_3	-0.0326/0.0593/-0.0639	-0.0003/-0.0107/ 0.0065	
ν_4	0.0270/-0.0744/0.0907	-0.0006/ 0.0029/-0.0039	
ν_5	–	-0.0075/-0.0916/-0.0514	-0.0020/-0.0002/-0.0007
ν_6	–	-0.0037/-0.0182/-0.0184	-0.0025/-0.0030/-0.0050
ν_7	–	0.0022/-0.0280/-0.0077	0.0009/-0.0035/-0.0029
ν_8	–	0.0066/-0.0048/-0.0080	0.0019/-0.0015/-0.0035
E_0^A	14.529		
E_0^B	16.701		
E_0^C	16.872		

Table 3.4: Same as in Table 3.2 for the degenerate $\widetilde{D}^2E$ electronic state of CF_3CN^+.

Mode	κ_i or λ_i	γ_i	η_i	ζ_i	ϕ_i	μ_i	α_i	β_i
ν_1	0.0556	0.0033	–	–	–	–	–	–
ν_2	-0.2526	0.0037	–	–	–	–	–	–
ν_3	0.0231	-0.0098	–	–	–	–	–	–
ν_4	-0.0945	-0.0075	–	–	–	–	–	–
ν_5	0.1910	-0.0348	-0.0742	-0.0008	-0.0008	-0.0006	-0.0005	-0.0003
ν_6	0.0428	0.0023	-0.0044	0.0009	0.0005	-0.0009	-0.0005	-0.0003
ν_7	0.0614	-0.0026	-0.0020	-0.0006	-0.0004	-0.0007	-0.0004	-0.0002
ν_8	0.0014	-0.0010	0.0008	0.0007	0.0005	0.0005	0.0004	0.0001
E_0^D	17.350							

3.4 Adiabatic potential energy surfaces

The adiabatic PESs of the lowest five electronic states are obtained by diagonalizing the diabatic electronic Hamiltonian matrix given in Eqs. (3.3-3.6e) using the parameters of Tables 3.2, 3.3 and 3.4. One dimensional cuts of these multidimensional PESs along the dimensionless normal coordinate of each vibrational mode are shown in Figs. (3.3-3.4). In each plot, the points represent the adiabatic potential energies computed *ab initio* , and the curves superimposed on them represent those obtained by the present vibronic model of Section 3.3. In Figs. 3.3(a-d) the potential energies of $\widetilde{X}$, $\widetilde{A}$, $\widetilde{B}$, $\widetilde{C}$ and $\widetilde{D}$ electronic states (indicated in the panel) are plotted along the symmetric vibrational modes ν_1-ν_4, respectively. It can be seen that the model reproduces *ab initio* data extremely well. The degeneracy of the $\widetilde{X}$ and $\widetilde{D}$ states remains unperturbed on distortion along these symmetric vibrational modes. While the crossing of the $\widetilde{X}$ state with the others seems not very important (except with the $\widetilde{A}$ state; panel a), the crossings of the $\widetilde{D}$ state with $\widetilde{B}$ and $\widetilde{C}$ electronic states appear to have crucial role in shaping up the details structure of the second vibronic band. The participating electronic states in the latter are energetically close and the curve crossings seen in the diagram would lead to multiple low-lying energetically accessible conical intersections among them. The locus of degeneracy of the two components of the $\widetilde{X}$ and also $\widetilde{D}$ electronic states define the seam of the JT conical intersections within these states, occurring at the C_{3v} symmetry configuration of CF_3CN^+. In a second-order coupling approach the energetic minimum of these seams are given by

$$\mathcal{V}^{(c)}_{min,X(D)} = E_0^{X(D)} - \frac{1}{2}\sum_{i=1}^{4}\frac{(\kappa_i^{X(D)})^2}{(\omega_i + \gamma_i^{X(D)})}, \tag{3.7}$$

with the parameters of Table 3.2-3.4, these minima occur at, $\mathcal{V}^{(c)}_{min,X} \sim 13.58$ eV and $\mathcal{V}^{(c)}_{min,D} \sim 17.06$ eV.

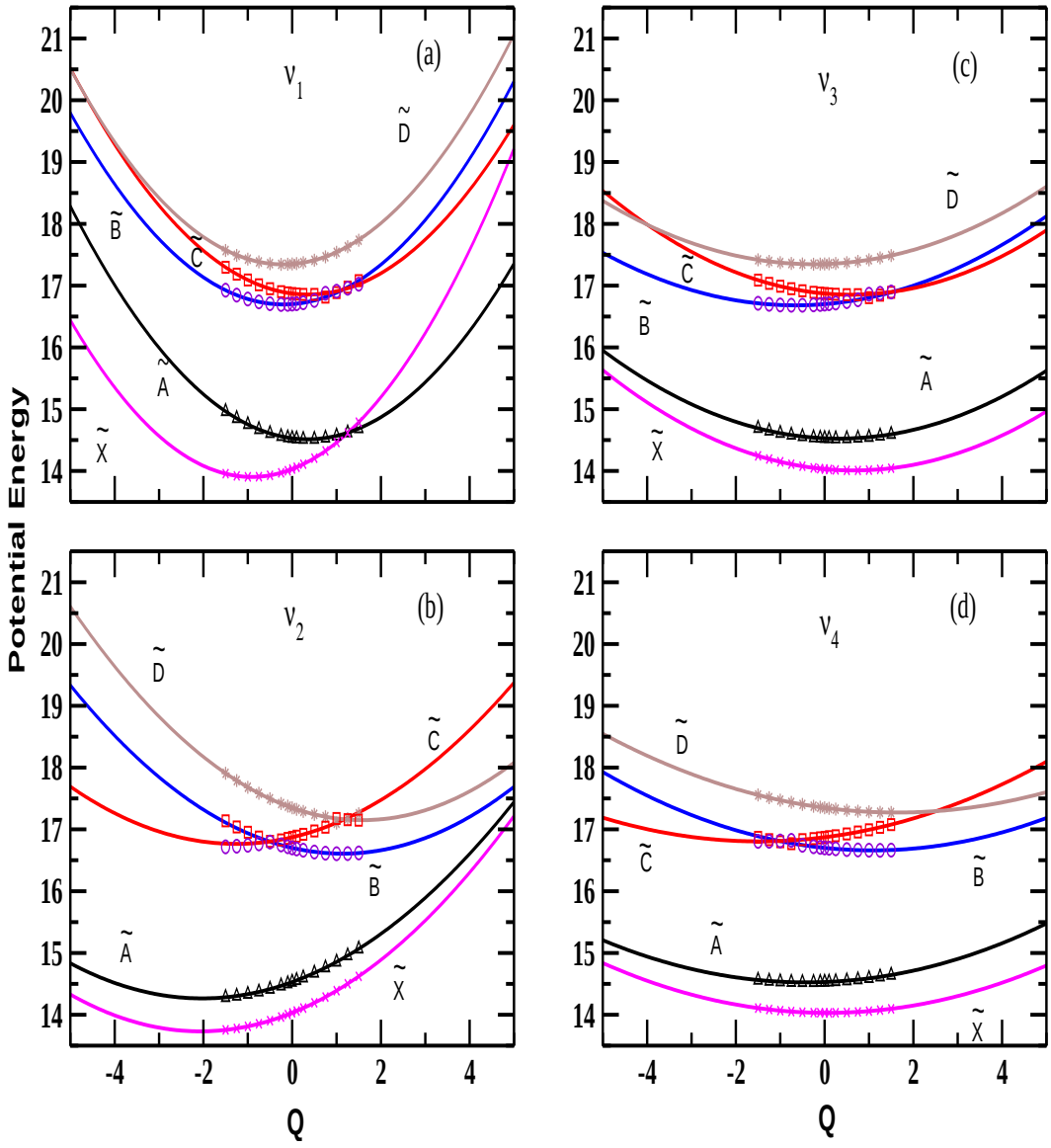

Figure 3.3: Adiabatic potential energies of the lowest five electronic states of CF_3CN^+ along the dimensionless normal co-ordinates of its four totally symmetric vibrational modes ν_1-ν_4. The potential energies obtained from the present vibronic model are shown by solid lines and the computed *ab initio* data are superimposed on them are shown by the points.

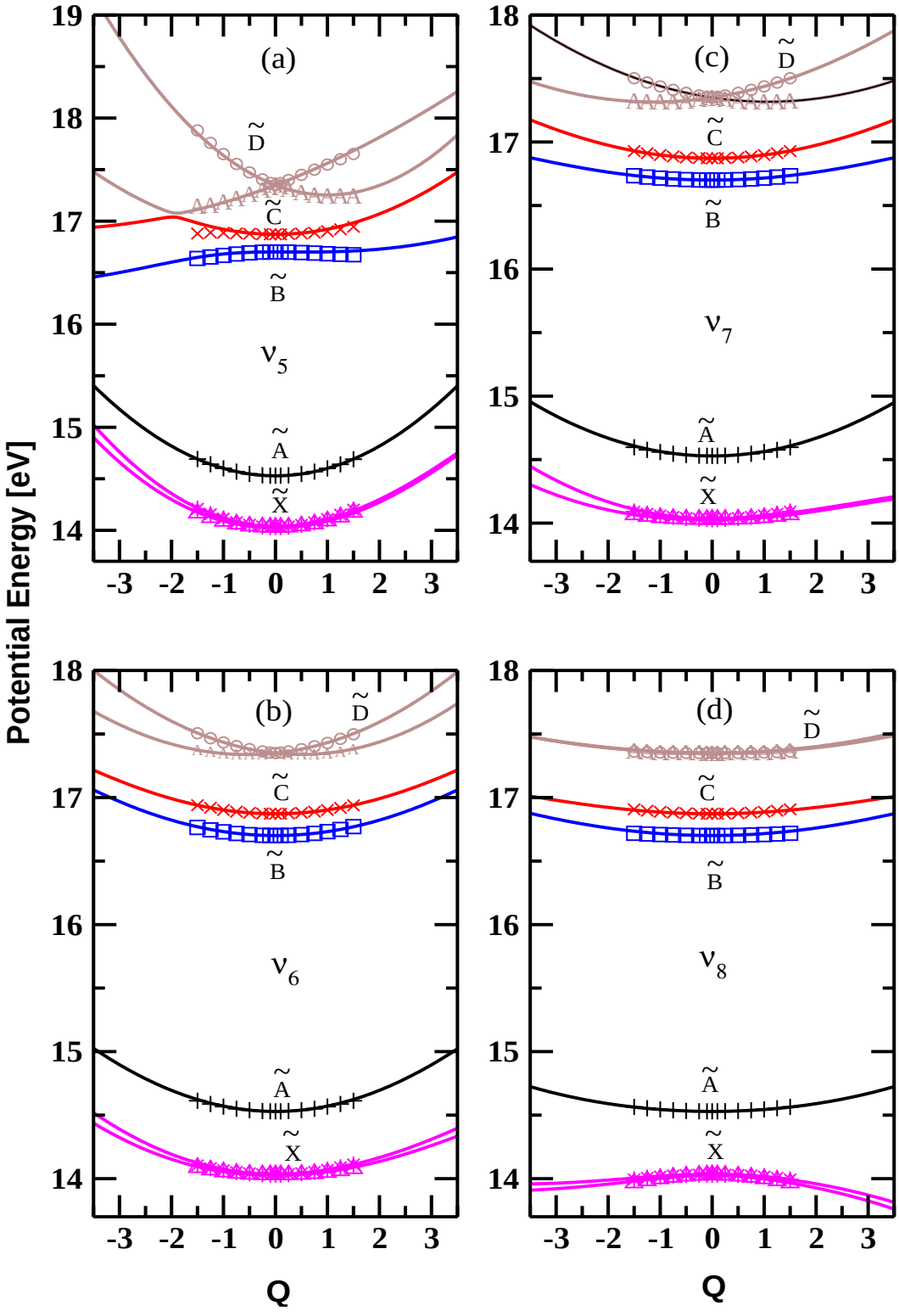

Figure 3.4: Same as in Fig. 3.3, along the dimensionless normal coordinates of the x component of the degenerate vibrational modes ν_5-ν_8.

The electronic degeneracy of the $\widetilde{X}$ and $\widetilde{D}$ states splits on distortion along the degenerate vibrational modes $\nu_5 - \nu_8$ and this splitting leads to a total of seven states altogether in the $\widetilde{X}$ -$\widetilde{A}$ -$\widetilde{B}$ -$\widetilde{C}$ -$\widetilde{D}$ electronic manifold. The potential energies of the $\widetilde{X}$, $\widetilde{A}$, $\widetilde{B}$, $\widetilde{C}$ and $\widetilde{D}$ electronic states of CF_3CN^+ are shown in Figs. 3.4(a-d) along the x component of the degenerate vibrational modes $\nu_5 - \nu_8$, respectively. The symmetry rule forbids the first-order coupling due to these vibrational modes in the nondegenerate $\widetilde{A}$, $\widetilde{B}$ and $\widetilde{C}$ electronic states. However, these modes are JT active in first-order in the $\widetilde{X}$ and $\widetilde{D}$ states. It can be seen from Fig. 3.4 that, the JT splitting is very small in the $\widetilde{X}$ state along all the degenerate vibrational modes, in contrast significant splitting can be observed along ν_5, ν_6 and ν_7 vibrational modes in the $\widetilde{D}$ state. As before, the points on the diagram are the computed adiabatic energies and the curves superimposed on them represent fit to the present theoretical model. Moreover, the quartic terms of the Taylor expansion (Eqs. 3.6a-3.6e) seem to have significant role in representing the potential energies of the $\widetilde{X}$ state, particularly along the vibrational mode ν_8. The seam of JT conical intersections in the $\widetilde{X}$ and $\widetilde{D}$ electronic states occurs in the coordinate space of a_1 vibrational modes. The energetic minimum of these seams becomes critical point on the surface upon JT distortion. New minimum on the lower adiabatic sheets of the JT split $\widetilde{X}$ and $\widetilde{D}$ states occurs at ∼13.57 eV and ∼ 16.58 eV, respectively, and give rise to JT stabilization energies of $\sim 4.6 \times 10^{-3}$ eV and ∼ 0.48 eV for the $\widetilde{X}$ and $\widetilde{D}$ states, respectively.

Table 3.5: Pseudo-Jahn-Teller coupling parameters (in eV) of the vibronic Hamiltonian of equation (3.3).

Mode	$\lambda_i^{X,A}$	$\lambda_i^{X,B}$	$\lambda_i^{X,C}$	$\lambda_i^{A,D}$	$\lambda_i^{B,D}$	$\lambda_i^{C,D}$
ν_5	0.0203	0.0050	0.0020	0.0100	0.1570	0.0798
ν_6	0.0500	0.0400	0.0400	0.0636	0.0572	0.0496
ν_7	0.0500	0.0040	0.0800	0.0090	0.0639	0.0239
ν_8	0.1250	0.2500	0.2800	0.0070	0.0030	0.0070

Approximate estimates of the energetic minimum of various PJT crossing

seams are as follows. The minimum of the seam of $\widetilde{X}$ -$\widetilde{A}$ conical intersections occurs $\sim$ 0.43 eV above the minimum of the JT conical intersections in the $\widetilde{X}$ state. The minimum of the $\widetilde{X}$ -$\widetilde{B}$ and $\widetilde{X}$ -$\widetilde{C}$ conical intersections occurs $\sim$ 2.02 eV and $\sim$ 1.81 eV above the latter. The minimum of the $\widetilde{D}$ -$\widetilde{A}$, $\widetilde{D}$ -$\widetilde{B}$ and $\widetilde{D}$ -$\widetilde{C}$ conical intersections, on the other hand, occurs at $\sim$ 0.5 eV, $\sim$ 0.27 eV below and $\sim$ 0.04 eV above the minimum of the JT conical intersections in the $\widetilde{D}$ state, respectively. All these critical points of the PESs occur well within the energy range of the first two photoelectron bands studied here.

3.5 Vibronic energy levels

Vibronic energy levels of the $\widetilde{X}^2E$, $\widetilde{A}^2A_1$, $\widetilde{B}^2A_2$, $\widetilde{C}^2A_1$ and $\widetilde{D}^2E$ electronic states of CF_3CN^+ are shown and discussed in this section. These are calculated by the quantum mechanical methods described above using the parameters of Tables 3.2-3.4. To start with, let us first examine the energy levels of each of these electronic states excluding the PJT coupling with their neighbors and using a second-order model Hamiltonian. The final theoretical results of this chapter are, however, obtained by including all couplings [as described in the Hamiltonian of Eq.(3.3)] and propagating WPs using the MCTDH algorithm [118–123]. In the following, we start with various reduced dimensional models and systematically approach to carry out the final simulation of nuclear dynamics using the seven electronic states and twelve vibrational modes.

In the uncoupled states situation and in absence of any intermode coupling terms, the Hamiltonian for the $\widetilde{X}$ and $\widetilde{D}$ states are separable in terms of the a_1 and e vibrational modes. One can therefore calculate partial spectra separately for the a_1 and e vibrational modes and convolute them to generate the complete spectrum, for these degenerate electronic states. Such a separation reduces the dimension of the secular matrix and facilitates the numerical computation. The vibronic energy level spectrum of the $\widetilde{X}$ electronic manifold is shown in Fig. 3.5.

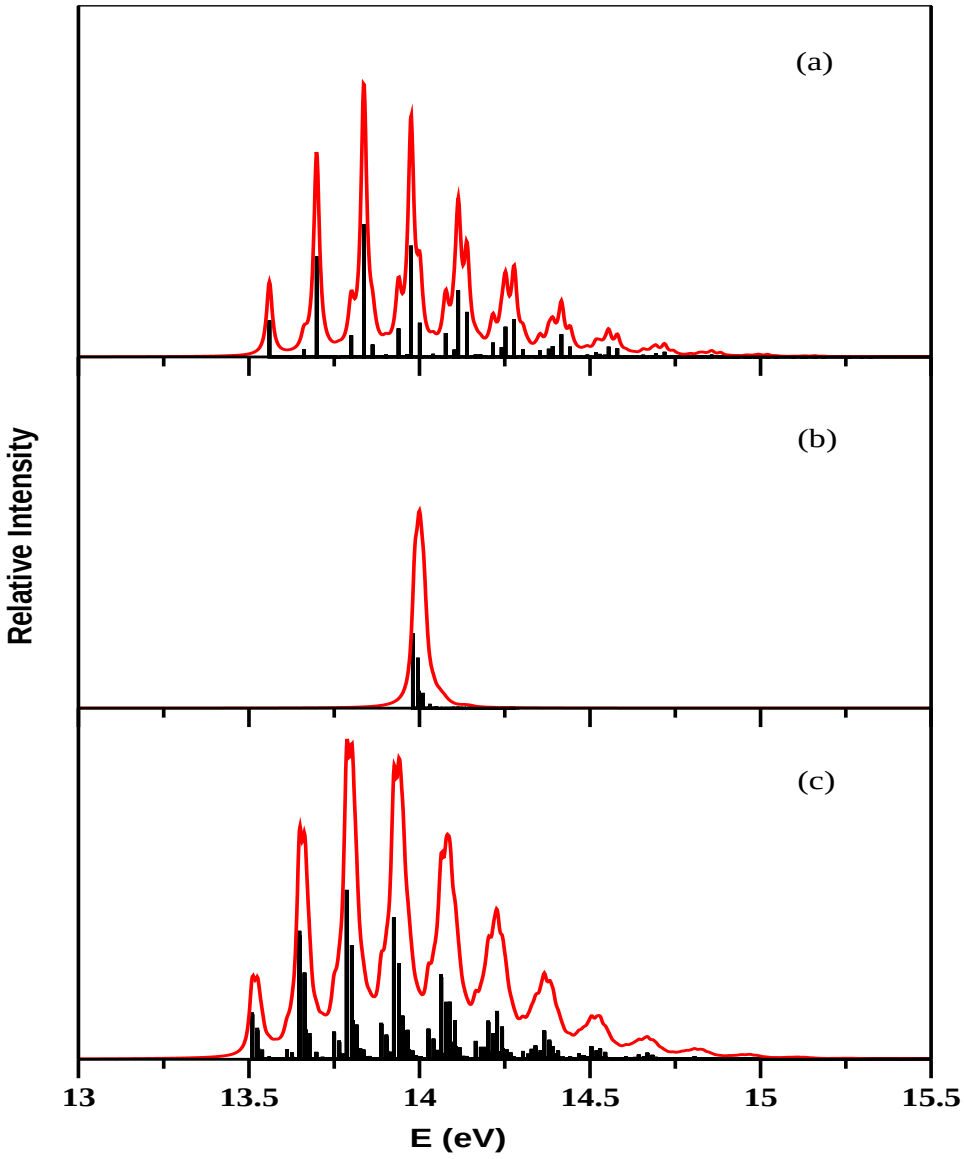

Figure 3.5: Vibronic energy levels of the $\widetilde{X}^2E$ electronic manifold of CF_3CN^+: (a) partial spectrum computed with the four totally symmetric a_1 vibrational modes ν_1-ν_4, (b) partial spectrum computed with the four JT active degenerate e vibrational modes ν_5-ν_8, and (c) the composite theoretical spectrum obtained by convoluting the above partial spectra. The relative intensity (in arbitrary units) is plotted as a function of the energy of the final vibronic state. The zero of energy correspond to the equilibrium minimum of the electronic ground state of CF_3CN. The theoretical stick spectrum in each panel is convoluted with a Lorentzian function of 20 meV FWHM to generate the spectral envelope. The stick spectrum of panel c is multiplied by a factor of 3 for a better clarity.

The two partial spectra of the a_1 and e vibrational modes are shown in panels a and b, respectively. The results of convolution of the two partial spectra are shown in the panel c. The vibronic energy eigenvalues are obtained by diagonalizing the Hamiltonian matrix using the Lanczos algorithm and are shown as the stick lines in the figure. The envelopes are obtained by convoluting these stick lines with a Lorentzian function with a full width at the half maximum (FWHM) of 20 meV. Further details of the calculations are given in Table 3.6. The partial

Table 3.6: The number of harmonic oscillator (HO) basis functions along each vibrational mode and the dimension of the secular matrix used to calculate the converged theoretical stick spectrum shown in various figures noted below.

No. of HO basis functions								Dimension of the secular matrix	Figure(s)
ν_1	ν_2	ν_3	ν_4	ν_5	ν_6	ν_7	ν_8		
12	39	6	2	-	-	-	-	11232	3.5(a)
-	-	-	-	2	2	4	30	460800	3.5(b)
2	38	2	30	-	-	-	-	9120	3.6(a)
-	-	-	-	17	5	11	2	6993800	3.6(b)
6	54	5	8	-	-	-	-	25920	3.7(a)
2	12	10	28	-	-	-	-	13440	3.7(b)
3	16	14	60	-	-	-	-	80640	3.7(c)

spectrum of the e vibrational modes (panel b) is essentially structureless because of their very weak JT coupling in the $\widetilde{X}$ state (cf., Table 3.2 and Fig. 3.4). The a_1 vibrational modes (panel a), ν_1, ν_2 and ν_3 form progressions and peaks are ∼0.302 eV, ∼0.138 eV and ∼ 0.101 eV spaced in energy corresponding to the frequencies of these vibrational modes (cf., Table 3.1), respectively. The vibrational mode ν_2 forms the dominant progression in the band. Fundamental transition due to ν_7 and ν_8 vibrational modes are observed in the partial spectrum for the degenerate vibrational modes (panel b). Lines are ∼0.049 eV and ∼0.015 eV spaced in energy and correspond to the frequency of the ν_7 and ν_8 vibrational modes, respectively. Similar spectra for the JT split $\widetilde{D}^2E$ electronic manifold of CF_3CN^+ are shown in Figs. 3.6 (a-c). In contrast to the $\widetilde{X}$ state spectrum

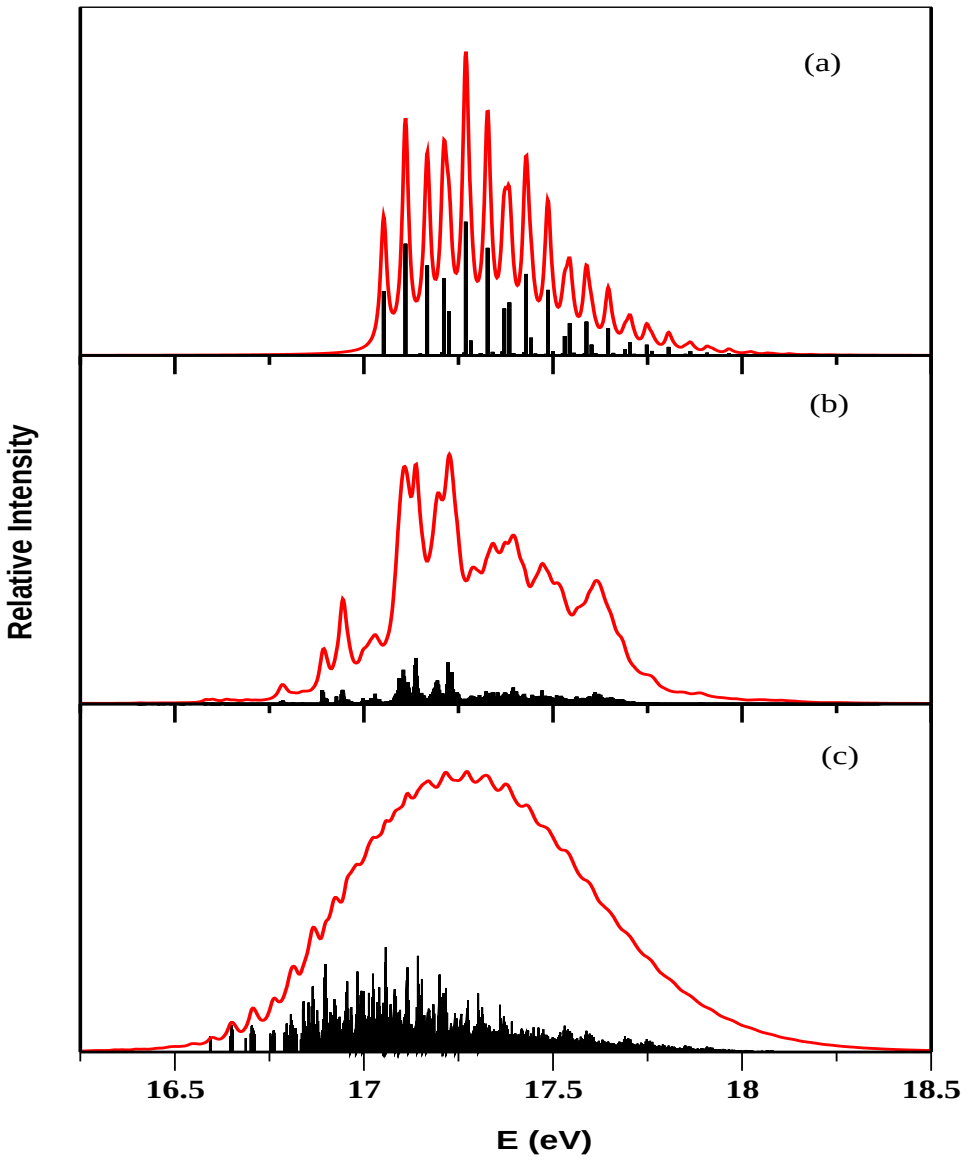

Figure 3.6: Same as Fig. 3.5, for the $\widetilde{D}^2E$ electronic manifold of CF_3CN^+.

(cf, Fig. 3.5(a)), the symmetric mode spectrum of this state (panel a) reveals dominant excitations of the ν_2 and ν_4 vibrational modes. The dominant lines are ∼0.058 eV and ∼0.154 eV spaced relative to the band origin and correspond to the frequency of the ν_4 and ν_2 vibrational modes in the $\widetilde{D}$ electronic state, respectively. The excitation of the ν_1 and ν_3 vibrational modes in this case are found to be much weaker compared to that in the $\widetilde{X}$ state. The spectrum for the JT active vibrational modes (panel b) clearly reveals that the JT effect is much stronger in this electronic manifold. Excitations due to the degenerate ν_5, ν_6 and ν_7 vibrational modes can be found in this case. The irregular spacings of lines in the spectrum result from the multimode JT interactions. The composite vibronic spectrum shown in panel c turned out to be very diffuse, due to much increase in the spectral line density arising from relatively stronger JT coupling strength of the degenerate vibrational modes in the $\widetilde{D}$ state.

The three nondegenerate electronic states ($\widetilde{A}$, $\widetilde{B}$ and $\widetilde{C}$) of CF_3CN^+ lie (vertically) in between the two degenerate electronic states ($\widetilde{X}$ and $\widetilde{D}$). The vibronic band structures of the latter electronic states shown above in Figs. (3.5-3.6) differ significantly from the experimental results (presented later in Fig. 3.8). Therefore, it seems necessary to consider their possible PJT interactions with these three nondegenerate electronic states to account for the detail fine structure of the first two photoelectron bands of CF_3CN. The vibronic energy level spectrum of these nondegenerate electronic states without including the coupling with their neighbors are shown in Figs. 3.7(a-c). The vibronic structure of the uncoupled $\widetilde{A}^2A_1$ electronic state (panel a) reveal dominant excitation of the ν_2 vibrational mode upto its seventh overtone. The other three symmetric vibrational modes are very weakly excited in this band. The vibronic structure of the $\widetilde{B}^2A_2$ (panel b) and $\widetilde{C}^2A_1$ (panel c) electronic states, on the other hand, reveals dominant excitations of ν_2 and ν_4 vibrational modes.

So far we did not consider the PJT coupling of various electronic states in the numerical calculations. On inclusion of this coupling, the separation of the

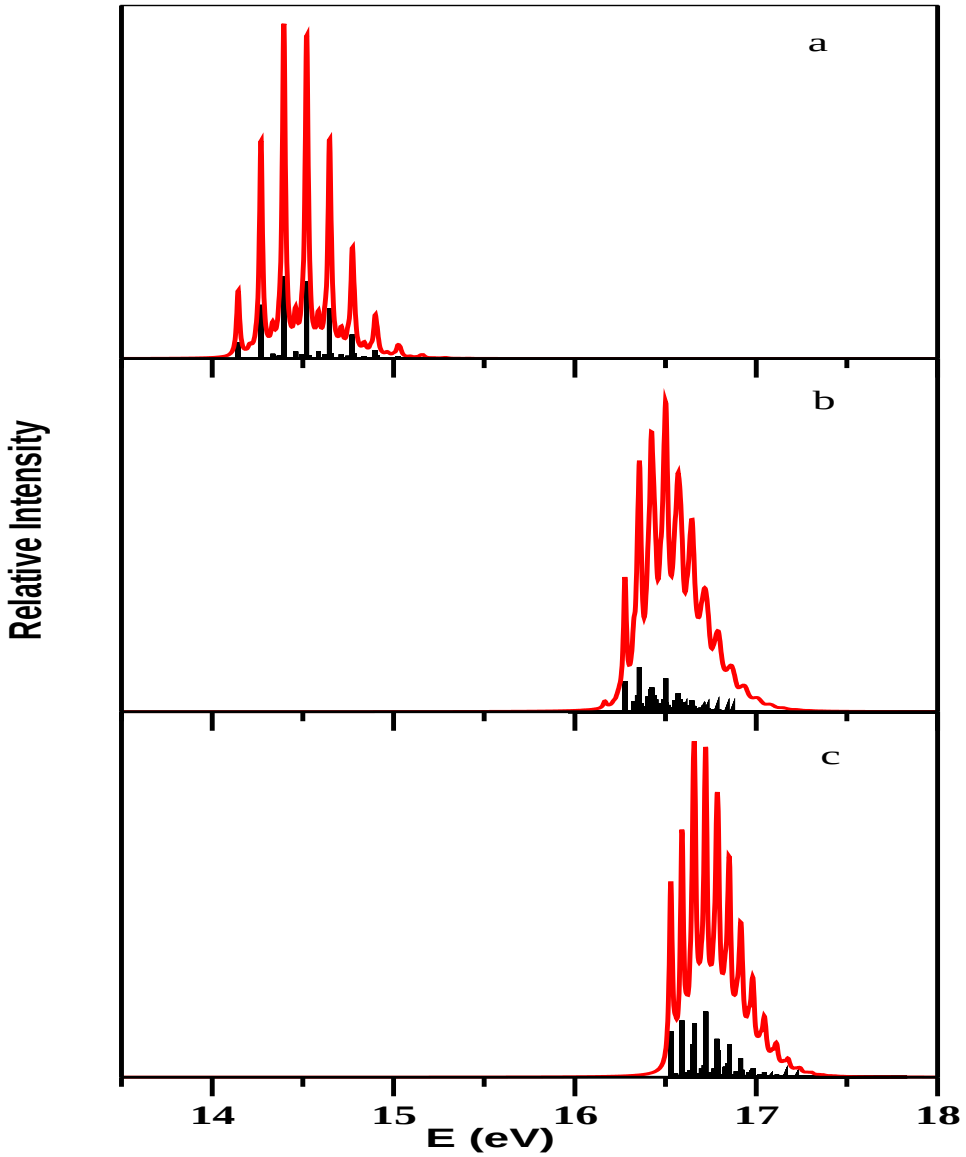

Figure 3.7: Same as Fig. 3.5, for the nondegenerate $\widetilde{A}^2A_1$ (panel a), $\widetilde{B}^2A_2$ (panel b) and $\widetilde{C}^2A_1$ (panel c) electronic states of CF_3CN^+.

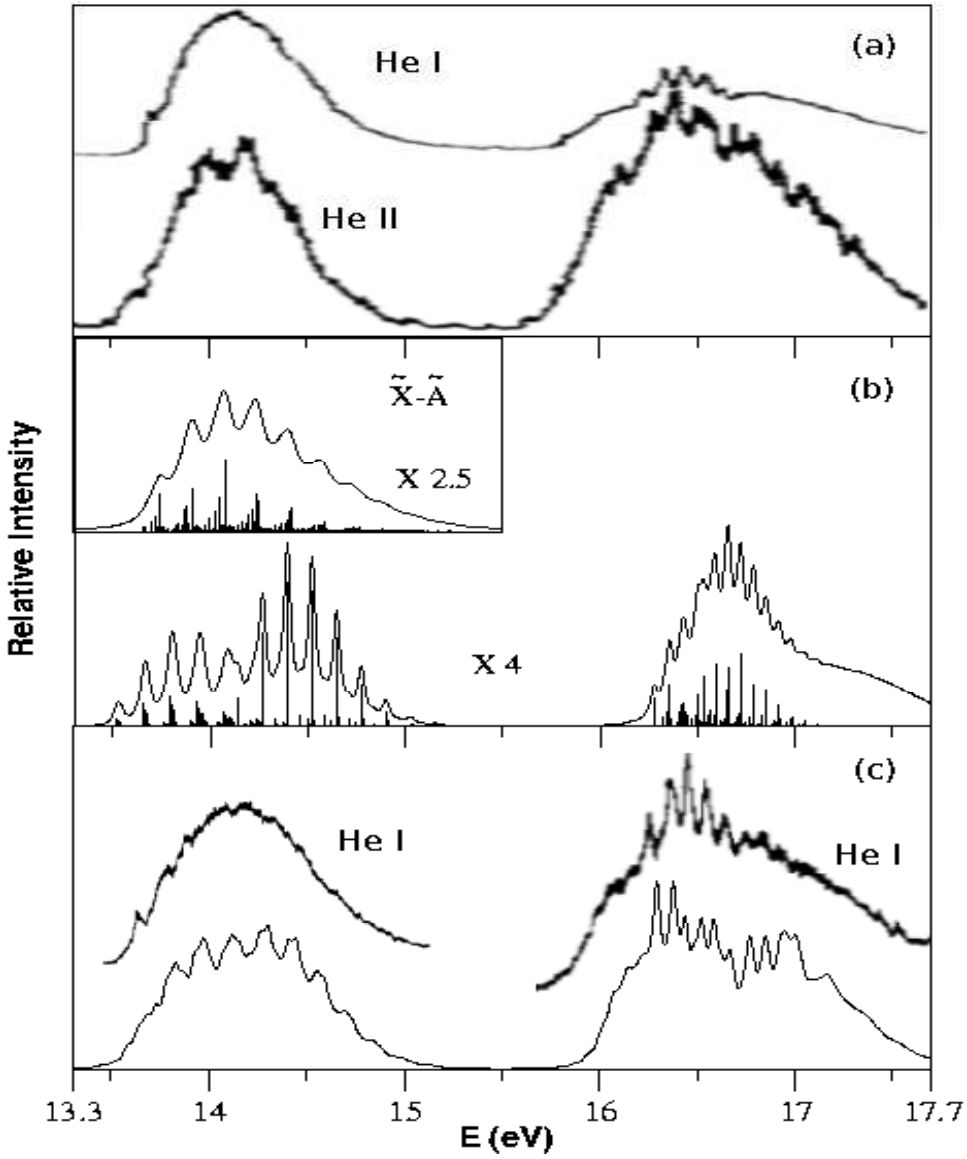

Figure 3.8: Comparison of the present theoretical and experimental photoelectron bands of CF_3CN: (a) He-I and He-II experimental spectrum [126], (b) composite theoretical spectrum employing a full second-order Hamiltonian and without considering the PJT coupling. The stick vibronic spectrum is multiplied by a factor 4 for clear representation, (c) the final theoretical results obtained by including all couplings described in the Hamiltonian of Eqs.(3.3-3.6e). The theoretical spectral envelopes in panel b and c correspond to a Lorentzian line shape function with 40 meV FWHM. The vibronic stick eigenvalue spectrum obtained by diagonalizing the $\widetilde{X}^2E$ -$\widetilde{A}^2A_1$ block of the Hamiltonian is shown in the inset of panel b (see text for details). The spectral envelop in it correspond to a Lorentzian function with 40 meV FWHM. The stick vibronic spectrum is multiplied by a factor of 2.5. The magnified version of the experimental He I band are also included on top of the theoretical results of panel c for a better clarity.

Hamiltonian in terms of the symmetric and degenerate vibrational modes for the degenerate electronic states as explored above is no longer possible. It is therefore necessary to follow the nuclear dynamics simultaneously on seven coupled electronic states (four from the two JT split $\widetilde{X}$ and $\widetilde{D}$ states plus three nondegenerate $\widetilde{A}$, $\widetilde{B}$ and $\widetilde{C}$ electronic states) including all relevant vibrational degrees of freedom. Computationally, it turns out to be a daunting task to simulate the nuclear dynamics quantum mechanically by the matrix diagonalization approach employed above. We therefore resort to the promising MCTDH algorithm [118–123], and propagate WPs on seven coupled electronic states including all twelve vibrational degrees of freedom in order to arrive at our goal. The twelve vibrational degrees of freedom are grouped into four three dimensional particles. The combination scheme of the vibrational modes is given in Table 3.7, along with the sizes of the primitive and SPF bases.

Table 3.7: The normal mode combinations, sizes of the primitive and the single particle basis used in the WP propagation employing the MCTDH algorithm on the ($\widetilde{X}^2E$ -$\widetilde{A}^2A_1$ -$\widetilde{B}^2A_2$ -$\widetilde{C}^2A_1$ -$\widetilde{D}^2E$) coupled electronic manifold using the complete vibronic Hamiltonian of Eqs. (3.3-3.6e). The CPU time and the required memory of each run is also given.

Normal modes[a]	Primitive basis[b]	SPF basis[c]	CPU time	Required RAM [Mbyte]	Figure
		[E^x_X, E^y_X, $A_1{}^A$ A_2, $A_1{}^C$, E^x_D, E^y_D]			
(ν_{6x}, ν_3, ν_{5x})	(7, 6, 6)	[9, 9, 12, 14, 14, 23, 23]	E^x_X: 14h 01min 31.2s	435.4	Fig. 3.8
(ν_4, ν_{5y}, ν_{8y})	(4, 6, 8)	[5, 5, 9, 9, 11, 9, 9]	E^y_X: 14h 01min 31.7s	”	
(ν_2, ν_1, ν_{7x})	(17, 10, 7)	[23, 23, 9, 9, 11, 21, 21]	A_1: 12h 23min 19.9s	”	
(ν_{8x}, ν_{7y}, ν_{6y})	(8, 7, 7)	[14, 14, 14, 9, 9, 12, 12]	A_2: 10h 11min 43.0s	”	
			A_1: 9h 19min 26.6s	”	
			E^x_D: 8h 7min 4.4s	”	
			E^y_D: 8h 7min 26.2s	”	

The calculations were converged with respect to the spectrum. [a]Vibrational modes bracketed together were treated as a single particle, e.g., particle 1 is a 3-dimensional particle that combines ν_{6x}, ν_3, and ν_{5x} vibrational modes. [b] The primitive basis is the number of harmonic oscillator DVR functions, in the dimensionless coordinate system required to represent the system dynamics along the relevant mode. The full primitive basis consists of a total of 2.26 $\times 10^{10}$ functions. [c] The SPF basis is the number of single-particle functions used, one set for the each component of the seven electronic states. Here they are same in numbers in order to give equal weight for the x and y components of the degenerate $\widetilde{X}^2E$ and $\widetilde{D}^2E$ electronic state. Total number of configurations are 172368.

The parameters documented there are optimally chosen to ensure the numerical convergence of the vibronic bands shown below. The WP in each calculation is propagated for 200 *fs* which effectively yields results for 400 *fs* propagation [134]. Fig. 3.8 displays in comparison, the experimental and present theoretical photoelectron bands of CF_3CN in the energy range ∼13-18 eV, resulting from ionization from the five valence type MOs of CF_3CN (cf., Fig. 3.1). The theoretical results are shown in panel b and c along with the experimental He I and He II results in panel a [126]. The theoretical results of panel b are obtained by superimposing the spectra shown in Figs. (3.5-3.7) without considering the PJT interactions among the states. The results shown in panel c, are obtained by including all coupling terms as given in the Hamiltonian of Eqs. (3.3-3.6e) and propagating WPs employing the MCTDH scheme [118–123]. Details of the MCTDH calculations are given in Table 3.7. Seven WP propagations in the coupled $\widetilde{X}$ -$\widetilde{A}$ -$\widetilde{B}$ -$\widetilde{C}$ -$\widetilde{D}$ electronic manifold are carried out by initially preparing the WP separately on each of the component state of this manifold. Finally, results from these seven calculations are combined with appropriate statistical weights (2:1 statistical ratio for lines of E and A vibronic symmetries). The resulting time autocorrelation function is damped with an exponential function, $e^{-t/\tau}$, with τ=33 *fs* (which corresponds to a 40 meV FWHM Lorentzian function) before Fourier transformation to generate the spectral envelopes of panel c. The stick spectrum of panel b is also convoluted with a 40 meV FWHM Lorentzian function to obtained the corresponding spectral envelope. A comparison of the theoretical results of panel b and c with the experimental one in panel a, immediately reveals strong impact of PJT interactions in the fine structure of the vibronic bands. For clarity the experimental He I bands in magnified form are included on top of the theoretical bands of panel c. The JT couplings within the $\widetilde{X}$ state and its PJT coupling with the $\widetilde{A}$ state primarily contribute to the vibronic structure of the first band. The JT coupling within the $\widetilde{D}$ state plus the $\widetilde{B}$ -$\widetilde{C}$ -$\widetilde{D}$ PJT couplings, on the other hand, yield the irregular and highly overlapping structure of the second band. The the-

oretical results of panel c are in good accord with the experimental, particularly with the He II, data.

The foregoing discussions reveal that, in practice the seven coupled electronic states Hamiltonian assumes a block diagonal structure hence the final results can be obtained by solving the eigenvalue equations separately for each block. These blocks consist of $\widetilde{X}$ -$\widetilde{A}$ and $\widetilde{B}$ -$\widetilde{C}$ -$\widetilde{D}$ coupled electronic states. We attempted to diagonalize each of these two blocks of the Hamiltonian matrix separately. While a nearly converged stick eigenvalue spectrum could be obtained for the $\widetilde{X}$ -$\widetilde{A}$ block, we miserably failed (due to large computer hardware requirements) to get a presentable structure of the vibronic eigenvalue spectrum for the $\widetilde{B}$ -$\widetilde{C}$ -$\widetilde{D}$ block. The nearly converged vibronic level spectrum of the $\widetilde{X}$ -$\widetilde{A}$ coupled electronic states is included as an inset in panel b of Fig. 3.8. The precise location of the adiabatic ionization positions of the seven states of CF_3CN^+ are not reported in the experimental investigations [126]. However, the onset of the experimental band is found at $\sim$ 13.6 eV, we adjusted our theoretical result of the band origin to the latter value. It was necessary to decrease the vertical ionization energy of the $\widetilde{A}$ state by $\sim$ 0.2 eV (from its *ab initio* value reported in Table 3.3) to obtained the experimentally observed maximum of the $\widetilde{X}$ -$\widetilde{A}$ band at $\sim$ 14.3 eV. We note that apart from this, no other adjustments of parameters (reported in various tables in this chapter) are made. Precise quantitative informations on the vibronic energy levels could not be extracted from the poorly resolved experimental spectra [126, 127], however, our estimates show that the dominant progressions in the $\widetilde{X}$ -$\widetilde{A}$ band caused by the vibrational mode ν_2: the peaks are $\sim$ 0.144 eV apart compared to the experimental (rough) estimate of $\sim$ 0.136 eV. Similarly, the dominant progression in the $\widetilde{B}$ -$\widetilde{C}$ -$\widetilde{D}$ electronic states caused by the vibrational mode ν_2, and the peaks are $\sim$ 0.154 eV apart compared to the estimated experimental value of $\sim$ 0.140 eV.

To this end it is worthwhile to discuss the above results in relation to those found for CH_3CN^+ [135]. Substitution of F atom results into appearance of

many energetically close lying electronic states arising from ionization from MOs of CF_3CN with predominant F lone pair orbital character. The nature of HOMO and HOMO-1 of both CH_3CN [135] and CF_3CN is similar, describing predominantly C-N π bonding and N lone pair orbitals, respectively. However, HOMO-2, HOMO-3 and HOMO-4 (cf., Fig. 3.1) of CF_3CN reveal major contributions from the lone pair orbitals of F atom and are closely spaced in energy. This results into highly overlapping nature of the second photoelectron band of CF_3CN.

As discussed above the first band in the photoelectron spectrum of CF_3CN (cf., Fig. 3.8) describes the vibronic structure of the $\widetilde{X}$ -$\widetilde{A}$ coupled electronic states of CF_3CN^+ . Low energy conical intersections between the $\widetilde{X}$ -$\widetilde{A}$ states are obtained along the symmetric vibrational mode of C-N stretching type. While such conical intersections are located very near to the equilibrium geometries of these states for CF_3CN^+ (cf., panel a of Fig. 3.3), they are located far away from the equilibrium geometries of these states for CH_3CN^+ [135]. The JT interactions are weak in the $\widetilde{X}$ state, in both CH_3CN^+ and CF_3CN^+. However, the $\widetilde{X}$ -$\widetilde{A}$ PJT coupling is far stronger in CF_3CN^+ , particularly along ν_8, compared to that in CH_3CN^+ [135]. The harmonic frequency of this mode also reduces by a factor of 2 in CF_3CN^+ . In summary, the far stronger PJT coupling leads to the highly diffuse vibronic structure of the first band of CF_3CN^+ when compared to the same of CH_3CN^+ [135].

Although He I and He II experimental results for the first band of CF_3CN^+ (cf., panel a of Fig. 3.8) reveal no differences in the spectral intensities, the latter for the second band reveal dramatic differences. This bears the signature of ionization from MOs localized mainly on the CF_3 group and this band appears well within the "finger print" region (15.0-17.5 eV) of CF_3 ionization [136, 137]. The JT interactions in the $\widetilde{D}$ electronic state have been shown to be much stronger than in the $\widetilde{X}$ state. In addition, the PJT couplings between $\widetilde{A}$ -$\widetilde{D}$ (through ν_6), $\widetilde{B}$ -$\widetilde{D}$ (through ν_5, ν_6 and ν_7) and $\widetilde{C}$ -$\widetilde{D}$ (through ν_5, ν_6 and ν_7) electronic states contribute substantially to the observed highly diffuse structure of this vibronic

band.

3.6 Nonadiabatic transitions : time dependent dynamics

In order to examine nonadiabatic transitions in the $\widetilde{X}$ -$\widetilde{A}$ -$\widetilde{B}$ -$\widetilde{C}$ -$\widetilde{D}$ coupled electronic manifold and nonadiabatic decay of electronically excited CF_3CN^+, we recorded the time-dependence of the diabatic electronic populations for an initial transition to each of the above electronic states separately. The results are shown in Figs. 3.9(a-e). In panel a, the population dynamics is shown for an initial transition of the WP to one of the two JT split components of the $\widetilde{X}$ state. The decay and growth of population of these components and the growth of the $\widetilde{A}$ state population can be seen from the diagram. The population of the $\widetilde{B}$ -$\widetilde{C}$ -$\widetilde{D}$ electronic states show only minor variations in this case. It is therefore clear that the electronic nonadiabatic dynamics in this situation is predominantly governed by the JT coupling within the $\widetilde{X}$ state and its PJT coupling with the $\widetilde{A}$ state. The PJT conical intersections with the other electronic states occur at higher energies and remain inaccessible to the WP in this case. The initial decay of the population of the $\widetilde{X}$ state relates to a decay rate of ~ 52 *fs*. It can be seen from panel a that the WP mostly undergoes nonadiabatic transitions back and forth between the two JT split components of the $\widetilde{X}$ state. This is because the minimum of the $\widetilde{X}$ -$\widetilde{A}$ conical intersections occur ~ 0.43 eV above the minimum of the JT conical intersections within the $\widetilde{X}$ state.

The population dynamics changes dramatically when the WP is initially prepared on the $\widetilde{A}$ state, as shown in panel b. The $\widetilde{X}$ -$\widetilde{A}$ PJT conical intersections are readily accessible to the WP packet in this case and therefore the population of the $\widetilde{A}$ state decays at a much faster rate of ~ 22 *fs*. It can be seen that the decay of the $\widetilde{A}$ state population mainly ("only") contributes to the growth of the

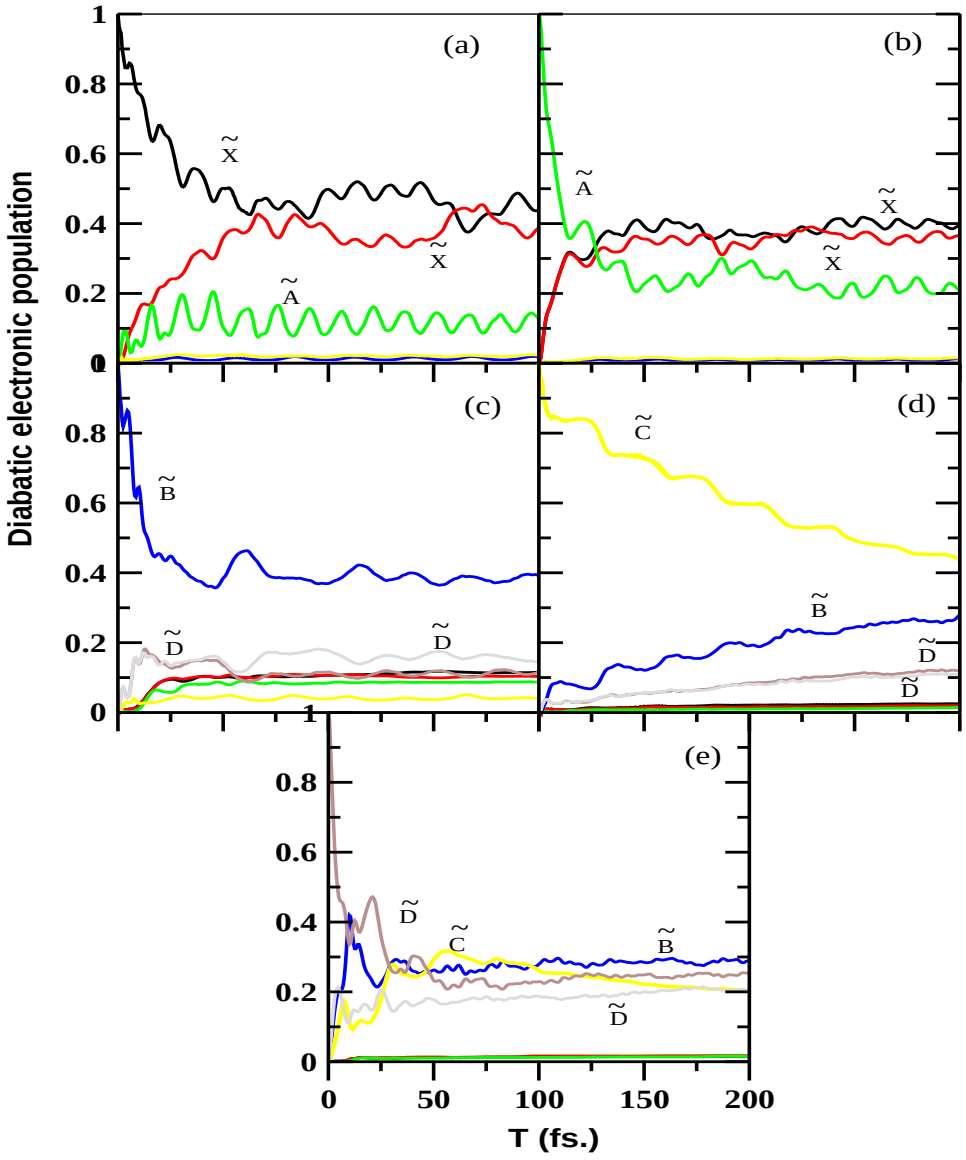

Figure 3.9: Time-dependence of diabatic electronic populations in the $\widetilde{X}$ -$\widetilde{A}$ -$\widetilde{B}$ -$\widetilde{C}$ -$\widetilde{D}$ coupled states nuclear dynamics of CF_3CN^+. The results obtained by initially locating the WP on one component of the JT split $\widetilde{X}$ state, $\widetilde{A}$ state, $\widetilde{B}$ state, $\widetilde{C}$ state and one component of the JT split $\widetilde{D}$ state are shown in panels a-e, respectively.

population of the two components of the $\widetilde{X}$ state. This reflects that the coupling of the $\widetilde{A}$ state with $\widetilde{B}$, $\widetilde{C}$ and $\widetilde{D}$ electronic states is not very significant (cf., Table 3.5).

The nonadiabatic transition dynamics of the WP initially prepared on the $\widetilde{B}$ and $\widetilde{C}$ states are shown in panel c and d, respectively. In these cases the transitions take place primarily within the $\widetilde{B}$ -$\widetilde{C}$ -$\widetilde{D}$ electronic states only. The states within the $\widetilde{X}$ -$\widetilde{A}$ electronic manifold mostly remain unpopulated during the dynamics. The decay rates of the $\widetilde{B}$ and $\widetilde{C}$ electronic states are estimated to be $\sim$ 32 *fs* and $\sim$ 125 *fs*, respectively, and are slower compared to that of the $\widetilde{A}$ state.

Finally, the electronic population dynamics for an initial transition of the WP to one component of the JT split $\widetilde{D}$ state is shown in panel e. It can be seen that the $\widetilde{D}$ state decays at a much faster rate $\sim$ 21 *fs* compared to the $\widetilde{X}$ state. This is due to the relatively stronger JT coupling within the $\widetilde{D}$ state and also due to the energetically close locations of the JT and $\widetilde{B}$ -$\widetilde{D}$ and $\widetilde{C}$ -$\widetilde{D}$ PJT conical intersections. Only minor population transfer takes place to the $\widetilde{X}$ -$\widetilde{A}$ coupled electronic manifold in this case also.

3.7 Summary and outlook

A detailed theoretical account of the multimode JT and PJT interactions in the five lowest electronic states of CF_3CN^+ have been presented here to elucidate highly complex vibronic structure of the first two photoelectron bands of CF_3CN. Extensive *ab initio* electronic structure calculations are performed to develop a vibronic coupling model [Eqs. (3.3-3.6e)] and first principles calculations are carried out both via time-independent and time-dependent quantal methods to simulate the nonadiabatic nuclear motion on the coupled manifold of these electronic states. The theoretical results are found to be in good accord with the available experimental results. The vibronic Hamiltonian is constructed in a di-

abatic electronic basis, including the JT coupling within the degenerate $\widetilde{X}$ and $\widetilde{D}$ electronic states and the PJT couplings of these JT split states with the non-degenerate $\widetilde{A}$, $\widetilde{B}$ and $\widetilde{C}$ electronic states of CF_3CN^+. The coupling parameters of the vibronic Hamiltonian are determined by calculating the adiabatic potential energy surfaces of the $\widetilde{X}^2E$, $\widetilde{A}^2A_1$, $\widetilde{B}^2A_2$, $\widetilde{C}^2A_1$ and $\widetilde{D}^2E$ electronic states along each of the twelve vibrational modes.

The vibronic energy level structure of these electronic states of CF_3CN^+ are systematically examined at various level of theoretical approximations calculated by the time-independent matrix diagonalization approach. The final theoretical simulations using the full Hamiltonian of Eqs. (3.3-3.6e) can only be carried out by propagating WPs employing the MCTDH algorithm [118–123]. A careful examination of various theoretical results enabled us to arrive at the following conclusions. The symmetric vibrational modes ν_1 and ν_2 are crucial and are strongly excited. While the former leads to low-energy crossings of the $\widetilde{X}$ -$\widetilde{A}$ electronic states, the latter and ν_4 are both important for the low-energy crossings of $\widetilde{B}$ -$\widetilde{C}$ -$\widetilde{D}$ electronic states. The JT effects in the $\widetilde{X}$ electronic states is far weaker compared to that in the $\widetilde{D}$ state. The JT stabilization energy of $\sim 4.6 \times 10^{-3}$ eV and$\sim$ 0.48 eV are estimated, respectively, for these electronic states. The JT and PJT interactions of the $\widetilde{X}$ -$\widetilde{A}$ electronic states mostly contributes to the overall vibronic structure of the first photoelectron band. The PJT coupling due to ν_8 vibrational mode is found to be strongest and the vibrational modes ν_2, ν_7 and ν_8 are found to make the progressions in this band. Energetically close lying $\widetilde{B}$ -$\widetilde{C}$ -$\widetilde{D}$ electronic states are found to be responsible for the highly overlapping structure of the second photoelectron band. The relatively stronger JT coupling within the $\widetilde{D}$ electronic state and appreciable PJT coupling due to ν_5 and ν_6 vibrational modes among these electronic states contributes to the diffuse vibronic structure of this band. The vibrational modes ν_2, ν_4, ν_5 and ν_7 form the major progressions in this band.

Chapter 4

The Jahn-Teller and pseudo-Jahn-Teller effects in the low-lying electronic states of 1,3,5-trifluorobenzene radical cation

4.1 Introduction

In this chapter we examine the multimode JT and PJT interactions in the ground $\widetilde{X}^2E''$ and low-lying excited $\widetilde{A}^2A_2''$, $\widetilde{B}^2E'$ and $\widetilde{C}^2A_2'$ electronic states of large 1,3,5-trifluorobenzene radical cation ($TFBz^+$). This study helps us to understand the complexiety involved in the theoretical treatment of a system of growing size. The radical cations of benzene and its derivatives have been extensively studied by electron spectroscopy to understand the complex vibronic structure and dynamics of their low-lying electronic states [138–142]. In particular, the fluorobenzene radical cations have received considerable attention to unravel the ef-

fect of fluorine substitution on the emissive properties of their excited electronic states [94, 95, 140, 143–146]. Laser-induced fluorescence (LIF) technique was extensively used for this purpose [146]. In recent years, a variety of experimental techniques are developed to record the vibronic structure of these systems with increasing energy resolution [147–149]. The symmetric benzene (Bz^+), $TFBz^+$ and hexafluorobenzene ($HFBz^+$) radical cations have attracted special attention to study the vibronic coupling mechanisms arising from the JT instability in their degenerate electronic states [140–143]. In this chapter we consider the $TFBz^+$ as a prototypical system which in contrast to the parent Bz^+ shows considerable emission [94, 95]. The underlying mechanistic details of this observation are examined here by an *ab initio* quantum dynamical approach.

The neutral 1,3,5-trifluorobenzene (TFBz) molecule possesses D_{3h} equilibrium configuration in its electronic ground state ($^1A_1'$). Ionization of an electron from its four highest occupied e'', a_2'', e' and a_2' valence molecular orbitals (MOs) yields $TFBz^+$ in its electronic ground $\widetilde{X}^2E''$ and excited $\widetilde{A}^2A_2''$, $\widetilde{B}^2E'$ and $\widetilde{C}^2A_2'$ states, respectively. The excited $\widetilde{A}$, $\widetilde{B}$ and $\widetilde{C}$ electronic states of $TFBz^+$ are energetically close-lying and occur vertically ∼2.95 eV, ∼4.22 eV and ∼4.30 eV above its $\widetilde{X}$ state, respectively. Therefore, the vibronic interactions among these excited electronic states of $TFBz^+$ expected to have profound impact on its nuclear dynamics. This crucial issue is addressed and examined in this chapter.

The 30 vibrational degrees of freedom of TFBz decompose into the following irreducible representations (IREPs) of the D_{3h} symmetry point group:

$$\Gamma = 4a_1'(\nu_1-\nu_4)+3a_2'(\nu_5-\nu_7)+7e'(\nu_8-\nu_{14})+3a_2''(\nu_{15}-\nu_{17})+3e''(\nu_{18}-\nu_{20}). \quad (4.1)$$

Applying the elementary symmetry selection rule, $\Gamma_n \otimes \Gamma_Q \otimes \Gamma_m \supset A_1$, (with, Γ representing the IREPs; n, m denoting the electronic state index and Q defining the coordinate of the relevant vibrational mode) one finds that the $\widetilde{X}^2E''$ and $\widetilde{B}^2E'$ electronic states would undergo JT splitting in first-order when distorted

along the degenerate vibrational modes of e' symmetry. On the other hand, the degenerate e'' vibrational modes can cause first-order PJT type of coupling between the $\widetilde{A}^2A_2''$ and the $\widetilde{B}^2E'$ electronic states and the degenerate e' vibrational modes can lead to a coupling between the $\widetilde{X}^2E''$ -$\widetilde{A}^2A_2''$ and $\widetilde{B}^2E'$ -$\widetilde{C}^2A_2'$ electronic states. In addition to this, the four totally symmetric (a_1') vibrational modes are Condon active within each electronic state [4].

The photoelectron spectrum of $TFBz^+$ has been recorded by several experimental groups using He II and a mixture of He I and He II [79,150,151] radiations as ionization sources. Among the first three bands in the ∼9-15 eV energy range, the third one revealed highly diffuse and overlapping vibronic structure [151]. These three ionic bands result from the $2e''$, $2a_2''$, $9e'$ and $2a_2'$ valence MOs of the neutral TFBz , respectively. One photon mass analyzed threshold ionization (MATI) spectrum has been recorded by Kwon [152] *et al.* using vacuum ultraviolet radiation. This MATI spectrum revealed a rich vibrational structure of the electronic ground state of $TFBz^+$. Maier *et al.* [153] have estimated the fluorescence life time of ∼57-59 ns for an excitation to the $\widetilde{A}^2A_2''$ state region state of $TFBz^+$ using a photoelectron-fluorescence photon coincidences (PEFCO) technique. Whereas, Dujardin *et al.* [94] have found the same as 54.9 ns using the threshold-PEFCO technique. Cage *et al.* [154] have measured a value ∼57±2 ns for this quantity using an open cylindrical Penning trap.

In this chapter, we aim to develop a theoretical model to examine the vibronic structure and dynamical properties of the mentioned electronic states of $TFBz^+$. It is already obvious from the foregoing discussions that the electronic nonadiabatic coupling may have pivotal role in the dynamics of these electronic states. Therefore, four low-lying (six altogether when JT splitting is taken into consideration) electronic states of $TFBz^+$ are considered including all relevant vibrational degrees of freedom in this study. A diabatic electronic basis is employed and the elements of the electronic Hamiltonian matrix are expanded in a Taylor series. The JT coupling within the $\widetilde{X}$ and $\widetilde{B}$ electronic states and their PJT coupling

with the $\widetilde{A}$ and $\widetilde{C}$ electronic states are taken into consideration.

Extensive *ab initio* electronic structure calculations are carried out to derive the relevant coupling parameters of the vibronic Hamiltonian discussed in Section 4.3 below. A time-independent matrix diagonalization approach to treat the nuclear dynamics on six interacting electronic states including twenty three relevant vibrational degrees of freedom is computationally not viable. This task is therefore accomplished with a time-dependent WP propagation approach employing the multiconfiguration time-dependent Hartree (MCTDH) scheme [118–123]. While the final results of this chapter are obtained by this method, comparison calculations are carried out in reduced dimensions by the time-independent matrix diagonalization approach [4]. The results from the latter calculations enable us to precisely locate and assign various vibrational excitations and to compare with the better resolved experimental data.

4.2 Equilibrium structure and normal modes of vibration of TFBz in its electronic ground state

The geometry optimization and calculation of harmonic vibrational frequencies of TFBz at the equilibrium geometry of its electronic ground state ($^1A_1'$) are carried out at the second-order Møller-Plesset perturbation (MP2) level of theory employing the correlation-consistent polarized valence triple-ζ (cc-pVTZ) basis set of Dunning [155]. Electronic structure calculations are performed using the Gaussian-03 suites of program [128]. The optimized geometry parameters of the electronic ground state of TFBz are given in Table 4.1 along with the available experimental results of Ref. [156]. It can be seen from Table 4.1, that the theoretical results are in good accord with the experiment [156].

The harmonic vibrational frequencies (ω_i) of TFBz are calculated at the same

level of theory by diagonalizing the *ab initio* force constant matrix. These vibrational frequencies are recorded in Table 4.2 along with their available experimental values [157]. The symmetry and the dominant nature of the vibrations are also given in this Table. The mass-weighted normal coordinates of the vibrational modes are calculated from the eigenvectors of the force constant matrix. These are then multiplied with $\sqrt{\omega_i}$ (in a_0) to obtain the dimensionless normal coordinates (Q_i).

Table 4.1: The equilibrium geometry of the electronic ground state of TFBz along with the available experimental data. Theoretical calculations are carried out at the MP2 level of theory employing the cc-pVTZ basis set.

	C-C (Å)	C-F (Å)	∠ C-C(F)-C (deg)	∠ C(F)-C-C(F) (deg)	∠ F-C-C (deg)
MP2/cc-pVTZ	1.386	1.340	122.97	117.03	118.51
Experiment [156]	1.381	1.356	123.81	116.30	118.10

Table 4.2: Description of the vibrational modes of the electronic ground state of TFBz . The theoretical frequencies are harmonic, where as, the experimental ones are fundamental.

Symmetry	Mode	Vibrational Frequency (ω_i)/eV		Predominant nature	Coordinate
		MP2/cc-PVTZ	Experiment [157]		
a_1'	ν_1	0.4053	0.3814	C-H symmetric stretching	Q_1
	ν_2	0.1742	0.1690	C-F symmetric stretching	Q_2
	ν_3	0.1274	0.1255	Trigonal distortion	Q_3
	ν_4	0.0724	0.0719	Ring breathing mode	Q_4
a_2'	ν_5	0.1819	0.1604	C-C stretching	Q_5
	ν_6	0.1507	0.1444	C-H in-plane bending	Q_6
	ν_7	0.0689	0.0699	C-F in-plane bending	Q_7
e'	ν_8	0.4055	0.3863	C-H asymmetric stretching	Q_{8x},Q_{8y}
	ν_9	0.2078	0.2011	C-C stretching	Q_{9x},Q_{9y}
	ν_{10}	0.1871	0.1829	C-C symmetric stretching	Q_{10x},Q_{10y}
	ν_{11}	0.1428	0.1400	C-H in-plane bending	Q_{11x},Q_{11y}
	ν_{12}	0.1261	0.1235	C-C-C scissoring	Q_{12x},Q_{12y}
	ν_{13}	0.0623	0.0625	C-C-C in-plane bending	Q_{13x},Q_{13y}
	ν_{14}	0.0405	0.0407	C-F scissoring	Q_{14x},Q_{14y}
a_2''	ν_{15}	0.1042	0.1050	C-C Twisting	Q_{15}
	ν_{16}	0.0834	0.0822	C-C out of plane Bending	Q_{16}
	ν_{17}	0.0263	0.0257	C-F out of plane Bending	Q_{17}
e''	ν_{18}	0.1056	0.0982	C-C Twisting	Q_{18x},Q_{18y}
	ν_{19}	0.0759	0.0741	C-C out of plane Bending	Q_{19x},Q_{19y}
	ν_{20}	0.0313	0.0305	C-F out of plane Bending	Q_{20x},Q_{20y}

4.3 The Vibronic Hamiltonian and dynamical observables

In this section we construct a suitable Hamiltonian to simulate the nuclear dynamics underlying the complex vibronic structures of the $\widetilde{X}$ -$\widetilde{A}$ -$\widetilde{B}$ -$\widetilde{C}$ electronic states of $TFBz^+$. As noted in the introduction, we employ a diabatic electronic basis and Taylor series expansion of the electronic matrix elements for the purpose. The JT coupling due to the e' vibrational modes and the Condon activity of the a_1' vibrational modes are treated up to second-order and the PJT coupling due to e' and e'' vibrational modes is treated until the linear term. The PJT coupling of the $\widetilde{X}$ state with the $\widetilde{B}$ and $\widetilde{C}$ states is excluded on energetic ground (see below). The diabatic vibronic Hamiltonian in terms of the dimensionless normal coordinates of the vibrational modes is given by

$$\mathcal{H} = \mathcal{H}_0\mathbf{1_6} + \begin{pmatrix} \mathcal{W}_1^X & \mathcal{W}_{12}^X & \mathcal{W}_1^{X-A} & 0 & 0 & 0 \\ & \mathcal{W}_2^X & \mathcal{W}_2^{X-A} & 0 & 0 & 0 \\ & & \mathcal{W}^A & \mathcal{W}_1^{A-B} & \mathcal{W}_2^{A-B} & 0 \\ & & & \mathcal{W}_1^B & \mathcal{W}_{12}^B & \mathcal{W}_1^{B-C} \\ & & h.c. & & \mathcal{W}_2^B & \mathcal{W}_2^{B-C} \\ & & & & & \mathcal{W}^C \end{pmatrix}. \quad (4.2)$$

Here, $\mathcal{H}_0 = \mathcal{T}_N + \mathcal{V}_0$, represents the unperturbed Hamiltonian (treated as harmonic) of the electronic ground state of the neutral TFBz with

$$\mathcal{T}_N = -\frac{1}{2}\sum_{i \in a_1',\, a_2',\, a_2''} \omega_i \frac{\partial^2}{\partial Q_i^2} - \frac{1}{2}\sum_{i \in e',\, e''} \omega_i \left(\frac{\partial^2}{\partial Q_{ix}^2} + \frac{\partial^2}{\partial Q_{iy}^2}\right), \quad (4.3)$$

and

$$\mathcal{V}_0 = \frac{1}{2}\sum_{i\,\in\,a_1',\,a_2',\,a_2''}\omega_i Q_i^2 + \frac{1}{2}\sum_{i\,\in\,e',\,e''}\omega_i\left(Q_{ix}^2+Q_{iy}^2\right). \tag{4.4}$$

The change of electronic energy upon ionization is expressed by the electronic Hamiltonian matrix with elements $\mathcal{W}$ in Eq. (4.2). The diagonal elements of this matrix represent the diabatic potential energies of the electronic states and the off-diagonal elements describe the coupling between them. These elements are expanded in a Taylor series around the reference equilibrium configuration (at $\mathbf{Q}=\mathbf{0}$) as follows

$$\begin{aligned}\mathcal{W}_{1,2}^{X(B)} = {} & E_0^{X(B)} + \sum_{i\,\in\,a_1'}\kappa_i^{X(B)}Q_i \pm \sum_{i\,\in\,e'}\lambda_i^{X(B)}Q_{ix} + \frac{1}{2}\sum_{i\,\in\,a_1',\,a_2',\,a_2''}\gamma_i^{X(B)}Q_i^2 + \\ & \frac{1}{2}\sum_{i\,\in\,e'}[\gamma_i^{X(B)}(Q_{ix}^2+Q_{iy}^2) \pm \eta_i^{X(B)}(Q_{ix}^2-Q_{iy}^2)] + \\ & \frac{1}{2}\sum_{i\,\in\,e''}[\gamma_i^{X(B)}(Q_{ix}^2+Q_{iy}^2)],\end{aligned} \tag{4.5a}$$

$$\begin{aligned}\mathcal{W}^{A(C)} = {} & E_0^{A(C)} + \sum_{i\,\in\,a_1'}\kappa_i^{A(C)}Q_i + \frac{1}{2}\sum_{i\,\in\,a_1',\,a_2',\,a_2''}\gamma_i^{A(C)}Q_i^2 + \\ & \frac{1}{2}\sum_{i\,\in\,e',\,e''}[\gamma_i^{A(C)}(Q_{ix}^2+Q_{iy}^2)],\end{aligned} \tag{4.5b}$$

$$\mathcal{W}_{12}^{X(B)} = \sum_{i\,\in\,e'}\lambda_i^{X(B)}Q_{iy} - \sum_{i\,\in\,e'}\eta_i^{X(B)}Q_{ix}Q_{iy}, \tag{4.5c}$$

$$\mathcal{W}_1^{j-k} = \sum_i \lambda_i^{j-k}Q_{ix}, \tag{4.5d}$$

$$\mathcal{W}_2^{j-k} = -\sum_i \lambda_i^{j-k} Q_{iy}, \tag{4.5e}$$

where, $(j-k) \in (X-A)$, $(A-B)$, $(B-C)$ with, $i \in e'$, e'', e', respectively. Calculations reveal that the intermode bilinear coupling parameters for the active vibrational modes are generally small in magnitude ($\sim 10^{-3}$ or less) therefore, they are excluded from this study. The quantity E_0^j is the vertical ionization energy of the j^{th} electronic state. The first-order intrastate and JT coupling parameters are denoted by κ_i^j and λ_i^j for the symmetric (a_1') and degenerate (e') vibrational modes, respectively. The first-order PJT coupling parameter for the i^{th} degenerate vibrational mode between the electronic states j and k is given by λ_i^{j-k}. The diagonal second-order and the quadratic JT coupling parameters of the i^{th} vibrational mode are denoted by γ_i^j and η_i^j, respectively. To estimate these coupling parameters, the adiabatic electronic PESs of the $\widetilde{X}^2E''$, $\widetilde{A}^2A_2''$, $\widetilde{B}^2E'$ and $\widetilde{C}^2A_2'$ electronic states of $TFBz^+$ are calculated along the dimensionless normal coordinates of its thirty vibrational modes. The vertical ionization energies of these electronic states are calculated for $Q_i = \pm 0.10$, ± 0.25 (0.25), ± 2.00, along the i^{th} vibrational mode (keeping others at their equilibrium value) by the outer valence Green's function (OVGF) method [133] using the same basis set as noted in Sec. 4.2. The ionization energies thus obtained are equated with the adiabatic potential energies (relative to the energy of the electronic ground state of neutral TFBz) of the electronic states of $TFBz^+$. These energies are then fitted to the adiabatic form of the diabatic electronic Hamiltonian of Eq. (4.2) by a least squares procedure to derive the coupling parameters. These parameters for various vibrational modes are given in Tables 4.3 and 4.4. A careful inspection of the data given in these tables reveals that only three totally symmetric a_1' ($\nu_2 - \nu_4$), one nondegenerate a_2' (ν_5), six degenerate e' ($\nu_9 - \nu_{14}$), one nondegenerate a_2'' (ν_{16}) and three degenerate e'' ($\nu_{18} - \nu_{20}$) modes are relevant for the nuclear dynamics

in the coupled $\widetilde{X}$ -$\widetilde{A}$ -$\widetilde{B}$ -$\widetilde{C}$ electronic manifold of $TFBz^+$.

4.4 Adiabatic Potential Energy Surfaces and conical intersections

In this section, we discuss a few relevant static aspects of the adiabatic PESs obtained by performing *ab initio* calculations as discussed above. The model adiabatic PESs are obtained by diagonalizing the diabatic electronic Hamiltonian matrix of Eq. (4.2) and using the parameters documented in Tables 4.3 and 4.4. Locations of various energetic minima and saddle points on these PESs are important to understand the nuclear dynamics on them. In Figs. 4.1(a-c) one dimensional cuts of the multidimensional PESs of $TFBz^+$ along the dimensionless normal coordinate of the tuning vibrational modes $\nu_2 - \nu_4$ (a_1') are shown. The high frequency C-H stretching mode, ν_1, has extremely small coupling strength $[\frac{1}{2}(\kappa/\omega)^2 = 0.0001$ ($\widetilde{X}$ -state), 0.0003 ($\widetilde{A}$ -state), 0.0555 ($\widetilde{B}$ -state) and 0.0001 ($\widetilde{C}$ -state)], and the PESs along this mode are not shown in the diagram. The potential energy values obtained from the present quadratic vibronic coupling (QVC) model are shown by the solid lines and the computed *ab initio* energies are shown by the asterisks in Fig. 4.1. It can be seen that the computed *ab initio* data are well reproduced by the model potential energy functions. The three totally symmetric modes ν_2-ν_4 cannot lift the degeneracy of the $\widetilde{X}$ and $\widetilde{B}$ electronic states. The $\widetilde{X}$ state is energetically well separated from the rest and it does not reveal any significant coupling with the $\widetilde{A}$, $\widetilde{B}$ and $\widetilde{C}$ states in the energy range considered here. The $\widetilde{A}$, $\widetilde{B}$ and $\widetilde{C}$ electronic states on the other hand, are energetically close (cf., Table 4.3) and the crossings among them as seen in Fig. 4.1 would result conical intersections in multidimensions. The impact of such intersections on the vibronic dynamics is examined below.

The adiabatic potential energy cuts of the $\widetilde{X}$, $\widetilde{A}$, $\widetilde{B}$ and $\widetilde{C}$ electronic states of

Table 4.3: *Ab initio* calculated linear and quadratic coupling constants for the $\widetilde{X}^2E''$, $\widetilde{A}^2A_2''$, $\widetilde{B}^2E'$ and $\widetilde{C}^2A_2'$ electronic states of 1,3,5-triflurobenzene radical cation. The vertical ionization energies of these four electronic states are also given in the table. All data are given in eV unit.

Mode (Symmetry)	κ_i or λ_i $\widetilde{X}$	γ_i $\widetilde{X}$	κ_i $\widetilde{A}$	γ_i $\widetilde{A}$	κ_i or λ_i $\widetilde{B}$	γ_i $\widetilde{B}$	κ_i $\widetilde{C}$	γ_i $\widetilde{C}$
$\nu_1(a_1')$	0.0058	0.0021	-0.0093	0.0018	0.1351	-0.0250	-0.0055	0.0022
$\nu_2(a_1')$	-0.2064	-0.0048	- 0.2472	-0.0068	-0.2333	-0.0254	-0.1396	-0.0276
$\nu_3(a_1')$	0.0544	-0.0010	0.1276	0.0022	-0.0886	-0.0394	0.1153	-0.0088
$\nu_4(a_1')$	0.0242	-0.0020	-0.0145	-0.0022	-0.0444	-0.0056	0.0590	-0.0064
$\nu_5(a_2')$	–	0.0568	–	0.0482	–	-0.0544	–	0.0014
$\nu_6(a_2')$	–	0.0074	–	0.0056	–	-0.0458	–	-0.0092
$\nu_7(a_2')$	–	0.0012	–	-0.0020	–	-0.0074	–	-0.0082
$\nu_8(e')$	0.0010	0.0019	–	-0.0014	0.1009	-0.0228	–	0.0096
$\nu_9(e')$	0.1769	0.0038	–	-0.0032	0.2420	-0.0540	–	0.0261
$\nu_{10}(e')$	0.0524	-0.0097	–	-0.0208	0.0961	-0.0500	–	0.0700
$\nu_{11}(e')$	0.0204	-0.0044	–	-0.0026	0.0283	-0.0090	–	0.0090
$\nu_{12}(e')$	0.0387	-0.0011	–	0.0022	0.0997	-0.0146	–	-0.0022
$\nu_{13}(e')$	0.0793	-0.0037	–	-0.0016	0.0776	-0.0072	–	-0.0088
$\nu_{14}(e')$	0.0107	0.0056	–	0.0046	0.0315	-0.0074	–	0.0234
$\nu_{15}(a_2'')$	–	0.0006	–	-0.0054	–	-0.0484	–	-0.0038
$\nu_{16}(a_2'')$	–	-0.0216	–	-0.0124	–	-0.0006	–	-0.0222
$\nu_{17}(a_2'')$	–	0.0106	–	0.0110	–	0.0074	–	0.0142
$\nu_{18}(e'')$	–	0.0038	–	-0.0576	–	-0.0248	–	0.0010
$\nu_{19}(e'')$	–	-0.0058	–	-0.0218	–	-0.0040	–	-0.0078
$\nu_{20}(e'')$	–	-0.0102	–	-0.0152	–	0.0012	–	-0.0056
IP		9.704		12.655		13.929		13.960
Adjusted IP		9.704		12.455		14.060		13.683

Table 4.4: The JT and PJT coupling parameters (in eV) of the vibronic Hamiltonian of Eq. (4.2-4.5e) for the four lowest $\widetilde{X}^2E''$, $\widetilde{A}^2A_2''$, $\widetilde{B}^2E'$ and $\widetilde{C}^2A_2'$ electronic states of $TFBz^+$, estimated from the *ab initio* electronic structure results (see text for details).

Mode	η_i $\widetilde{X}$	η_i $\widetilde{B}$	λ_i' $\widetilde{X}$ -$\widetilde{A}$	λ_i' $\widetilde{A}$ -$\widetilde{B}$	λ_i' $\widetilde{B}$ -$\widetilde{C}$
ν_8	0.0000	-0.0028	0.0617	–	0.0346
ν_9	-0.0056	-0.0380	0.0603	–	0.0590
ν_{10}	-0.0074	0.0534	0.1619	–	0.2400
ν_{11}	0.0010	-0.0120	0.0628	–	0.0750
ν_{12}	0.0000	0.0000	0.0729	–	0.0275
ν_{13}	-0.0004	0.0022	0.0643	–	0.0274
ν_{14}	0.0010	0.0088	0.0818	–	0.0350
ν_{18}	–	–		0.0969	–
ν_{19}	–	–	–	0.0667	–
ν_{20}	–	–	–	0.0638	–

$TFBz^+$ along the degenerate e' vibrational modes are shown in Fig. 4.2. As discussed above, these modes split the JT degeneracy of the $\widetilde{X}$ and $\widetilde{B}$ states and as a result, a total of six electronic states are obtained in the $\widetilde{X}$ -$\widetilde{A}$ -$\widetilde{B}$ -$\widetilde{C}$ electronic manifold. For the nondegenerate $\widetilde{A}$ and $\widetilde{C}$ electronic states the lowest order coupling is described by the second-order terms (cf., Eq. (4.5b)) along these modes. It can be seen from Fig. 4.2 that the JT splitting in the $\widetilde{B}$ state is generally larger compared to that in the $\widetilde{X}$ state. As before, the asterisks on the diagrams represent the computed *ab initio* energies, and the curves superimposed on them represent the model adiabatic potential energy functions of the Hamiltonian of Eq. (4.2). It is well known that the JT distortion causes a symmetry breaking and as a result the new minima on the lower adiabatic sheets of the JT split $\widetilde{X}$ and $\widetilde{B}$ states occur at ∼9.42 eV and ∼13.26 eV, respectively. The minimum of the seam of the JT conical intersections occur at $\mathcal{V}^{(c)}_{min,X} \sim 9.56$ eV and $\mathcal{V}^{(c)}_{min,B} \sim$ 13.66 eV, in the $\widetilde{X}$ and $\widetilde{B}$ electronic state, respectively. The JT stabilization energies amount to ∼ 0.142 eV (∼1145 cm^{-1}) and ∼0.346 eV (∼2791 cm^{-1}) for

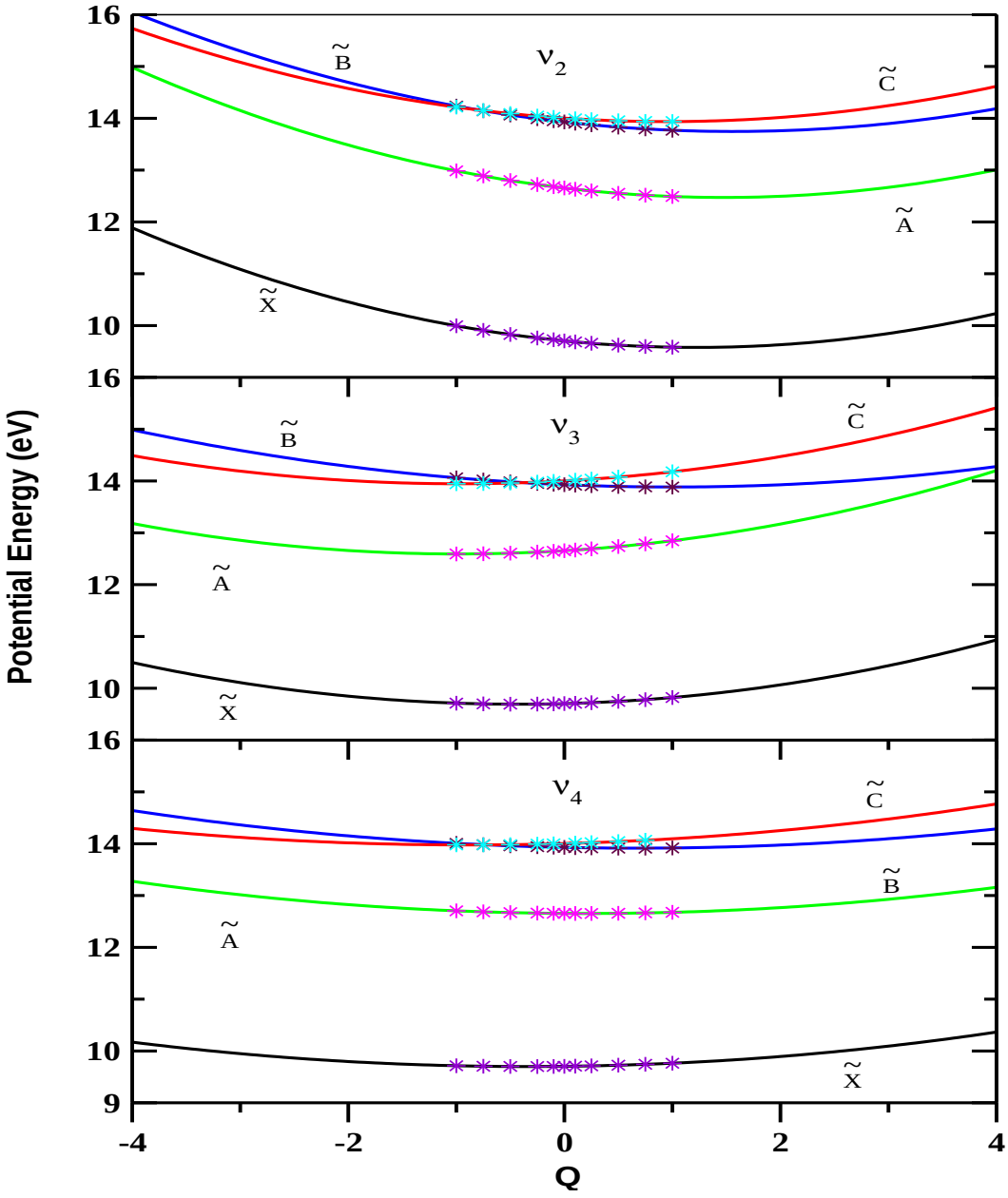

Figure 4.1: Adiabatic potential energies of the lowest four electronic states of $TFBz^+$ along the dimensionless normal coordinates of its three totally symmetric vibrational modes ν_2-ν_4. The potential energies obtained from the present vibronic model are shown by the solid lines and the computed *ab initio* data are shown by the asterisks.

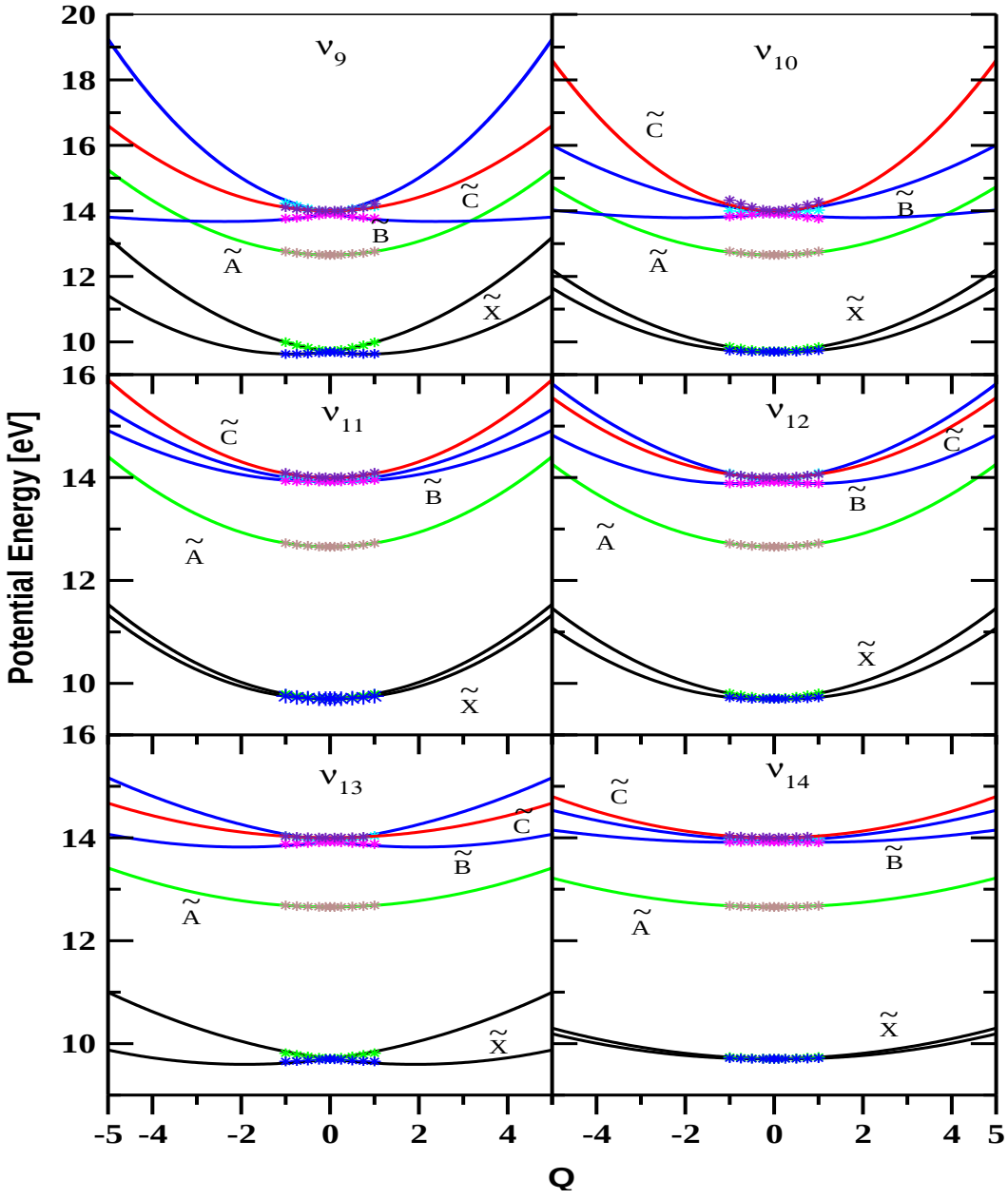

Figure 4.2: Same as in Fig. 4.1, along the dimensionless normal coordinates of the x component of the degenerate vibrational modes ν_9-ν_{14}.

the $\widetilde{X}$ and $\widetilde{B}$ states, respectively. It is worthwhile to mention that the JT stabilization energy estimated above for the $\widetilde{X}$ state is in close agreement with the estimate of ∼1022 cm^{-1} from the experimental data [152]. An examination of various PJT crossings in the space of a_1' and e′ vibrational modes with a linear coupling scheme reveals the following. The minimum of the seam of $\widetilde{A}$ -$\widetilde{B}$ and $\widetilde{B}$ -$\widetilde{C}$ PJT conical intersections occurs at ∼13.56 eV and ∼13.78 eV, respectively. The energetic minimum of the $\widetilde{X}$ -$\widetilde{A}$ conical intersections occurs at ∼21.23 eV, which is ∼11.66 eV above the minimum of the $\widetilde{A}$ state and beyond the energy range of the vibronic bands investigated here. On the other hand, the minimum of $\widetilde{A}$ -$\widetilde{B}$ and $\widetilde{B}$ -$\widetilde{C}$ intersections occur ∼1.43 eV and ∼0.076 eV above the minimum of the $\widetilde{B}$ and $\widetilde{C}$ electronic states, respectively. The nuclear dynamics in the latter electronic states is therefore expected to be perturbed by these intersections.

4.5 Vibronic energy levels

4.5.1 The photoelectron spectrum

The vibronic energy levels of the $\widetilde{X}$ -$\widetilde{A}$ -$\widetilde{B}$ -$\widetilde{C}$ electronic states of $TFBz^+$, calculated with the aid of the diabatic Hamiltonian [cf., Eqs. (4.2-4.5e)] constructed in Sec. 4.3 are reported below. The theoretical results are compared with the low resolution spectral data recorded in photoelectron spectroscopy experiments [79, 151]. In a later section, the resolved vibrational structures of the electronic ground state of $TFBz^+$ recorded in a MATI spectroscopy experiment by Kwon *et al.* [152] are also examined in detail. To proced systematically, we construct various reduced dimensional models and examine the vibrational energy levels of each of these electronic states by excluding the PJT coupling with their neighbors. These results help us to understand the role of various vibrational modes and electronic states in the complex vibronic structures of $TFBz^+$. The final simulation of the nuclear dynamics is carried out by including all rel-

evant couplings of the Hamiltonian and propagating WPs using the MCTDH algorithm [118–123]. The Hamiltonian for the degenerate ($\widetilde{X}$ and $\widetilde{B}$) electronic states is separable in terms of the a_1' and e' vibrational modes in absence of the PJT and bilinear coupling terms. Therefore, in the reduced dimensional investigations partial spectra for the a_1' and e' vibrational modes are calculated separately and finally convoluted to generate the composite band. The vibrational structures of the $\widetilde{X}$ electronic manifold of $TFBz^+$ are shown in Fig. 4.3. The two partial spectra of the a_1' and e' vibrational modes and the composite spectrum are shown in panels a, b and c, respectively. Three a_1' vibrational modes ($\nu_2 - \nu_4$) and three e' vibrational modes (ν_9, ν_{12} and ν_{13}) are included in the calculations. The vibronic energy eigenvalues are obtained by diagonalizing the Hamiltonian matrix using the Lanczos algorithm [116]. These are shown as stick lines in the figure. The stick spectrum is further convoluted with a Lorentzian function of 20 meV full width at the half maximum (FWHM) to generate the spectral envelope. The dominant progression in the band of panel a is caused by the ν_2 vibrational mode. Both the fundamental and overtones of this mode are excited. Peak spacing of ∼0.169 eV corresponding to the frequency of this mode can be estimated from the band. Apart from this, the vibrational mode ν_3 and combination level $\nu_2 + \nu_3$ are also excited in the band. Corresponding peak spacing of ∼0.126 eV and ∼0.295 eV, respectively, can be estimated from the spectrum. Fundamental transition due to ν_9 and ν_{13} vibrational modes are observed in the partial spectrum for the degenerate e' vibrational modes shown in panel b. Lines are ∼0.220 eV and ∼0.067 eV spaced in energy and correspond to the frequency of the ν_9 and ν_{13} vibrational modes, respectively.

Similar spectra for the JT split $\widetilde{B}$ electronic manifold of $TFBz^+$ are shown in Figs. 4.4(a-c). Here also the symmetric vibrational modes, ν_2, ν_3, and their combinations form the dominant progressions in the symmetric mode spectrum of panel a. The intense lines are ∼0.147 eV and ∼0.079 eV spaced relative to the band origin and correspond to the frequency of the ν_2 and ν_3 vibrational modes,

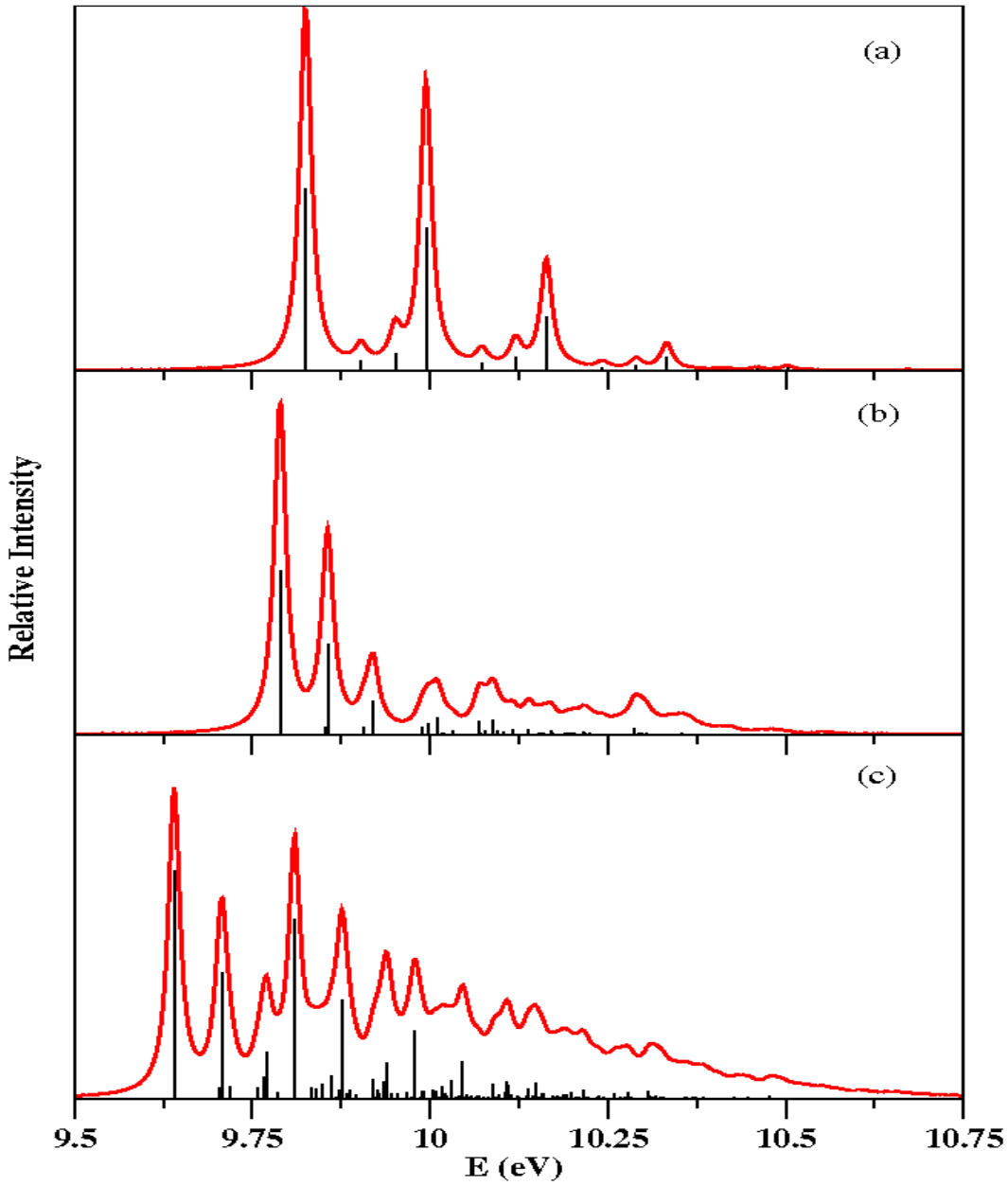

Figure 4.3: Vibrational energy levels of the $\widetilde{X}^2E''$ electronic manifold of $TFBz^+$: (a) partial spectrum computed with the three totally symmetric a_1' vibrational modes ν_2-ν_4, (b) partial spectrum computed with the three JT active degenerate e' vibrational modes ν_9, ν_{12} and ν_{13}, and (c) the composite theoretical spectrum obtained by convoluting the above two partial spectra. The relative intensity (in arbitrary units) is plotted as a function of the energy of the final vibronic state. The zero of energy correspond to the equilibrium minimum of the electronic ground state of TFBz . The theoretical stick spectrum in each panel is convoluted with a Lorentzian function of 20 meV FWHM to generate the spectral envelope. The stick spectrum of panel c is multiplied by a factor of 3 for a better clarity.

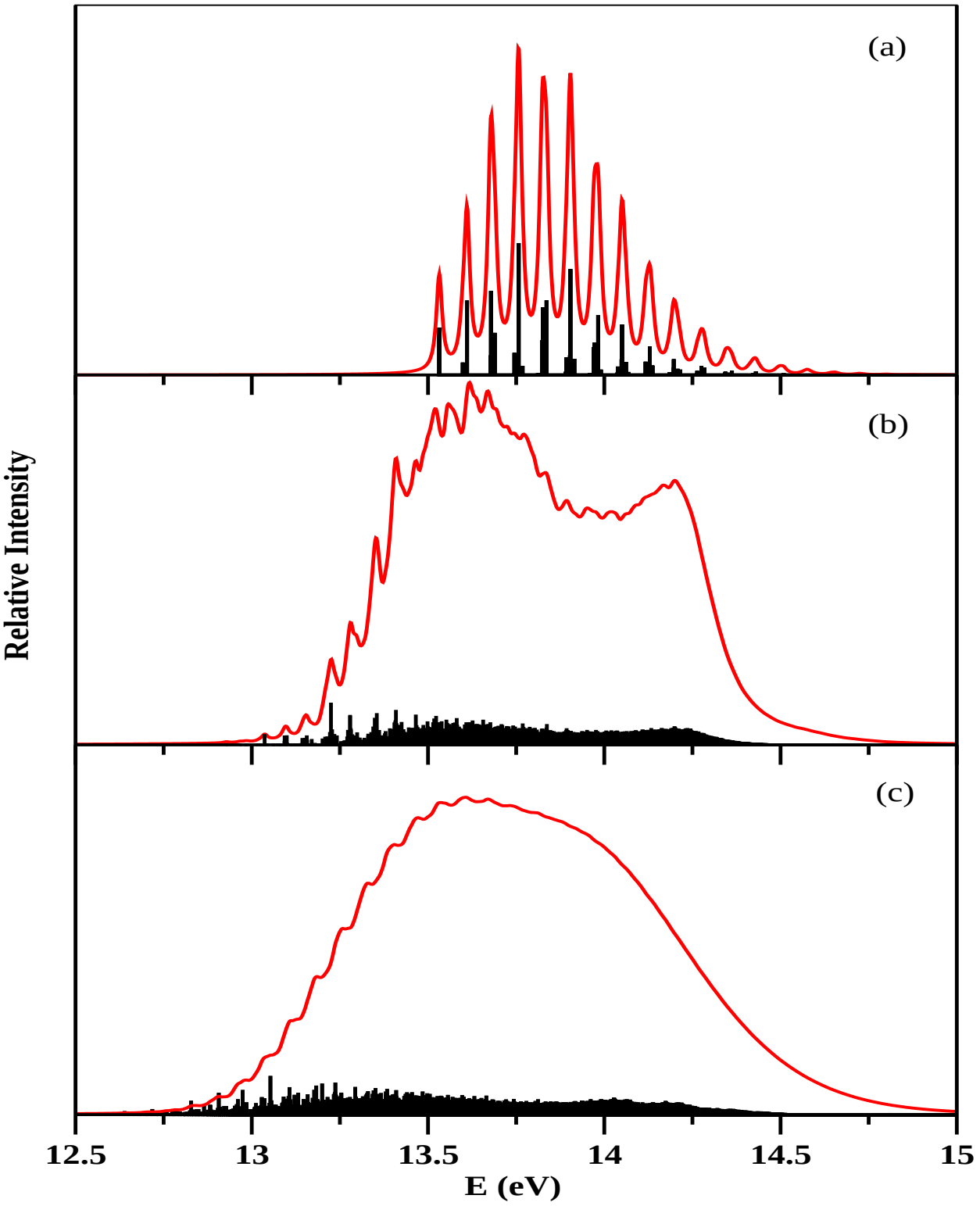

Figure 4.4: Same as Fig. 4.3, for the $\widetilde{B}^2E'$ electronic manifold of $TFBz^+$.

respectively, in the $\widetilde{B}$ state. In contrast to the $\widetilde{X}$ state spectrum of Fig. 4.3(a), the spectrum in Fig 4.4(a) exhibits an extended progression owing to the larger coupling strength of ν_2 and ν_3 (cf., Table 4.3) in the $\widetilde{B}$ state. The spectrum for the JT active e' vibrational modes for the $\widetilde{B}$ state, shown in Fig. 4.4 (b), exhibits much complex structure compared to that for the $\widetilde{X}$ state (cf., Fig. 4.3(b)). Note that the potential energy curves of the lower adiabatic sheet of the JT split $\widetilde{B}$ state are extremely flat along ν_9 and ν_{10} vibrational modes (cf., Fig. 4.2). This leads to a convergence problem of the e$'$ mode spectrum of Fig. 4.4(b). We carried out several test calculations and the best results obtained with 9, 5, 5 and 12 basis functions along ν_9, ν_{10}, ν_{12} and ν_{13} modes are shown in this figure. We mention with caution that while the above results reproduces the low resolution photoelectron spectrum further refinements of the potential energy curves along these two modes are necessary for high resolution spectroscopic application. The complex energy level structure of Fig. 4.4(b) clearly reveals stronger JT coupling effects in the $\widetilde{B}$ state and as a result the composite band of this state (panel c) becomes highly diffuse and structureless.

The vibronic energy level spectrum of the uncoupled (without the PJT coupling) nondegenerate $\widetilde{A}$ and $\widetilde{C}$ electronic states are shown in panel a and b of Fig. 4.5, respectively. The vibronic structure of the uncoupled $\widetilde{A}$ electronic state reveals dominant excitation of the ν_2 and ν_3 vibrational mode and the corresponding peak spacings are ∼0.167 eV and ∼0.130 eV, respectively. In the $\widetilde{C}$ state spectrum (panel b) all three symmetric vibrational modes form progressions and the peak spacings of ∼0.144 eV, ∼0.118 eV and ∼0.066 eV due to ν_2, ν_3 and ν_4 vibrational modes, respectively, can be estimated from the spectrum. To this end, it is worthwhile to mention that, the dominant progressions observed above for different states are in good agreement with the experimental results [79]. For example, progression of ν_2, ν_3 and ν_4 vibrational modes are estimated from the experimental band of the $\widetilde{X}$ electronic state. Line spacing of ∼0.180 eV, ∼ 0.120 eV and ∼0.070 eV are found [79] in that order, in good accord with the theoretical

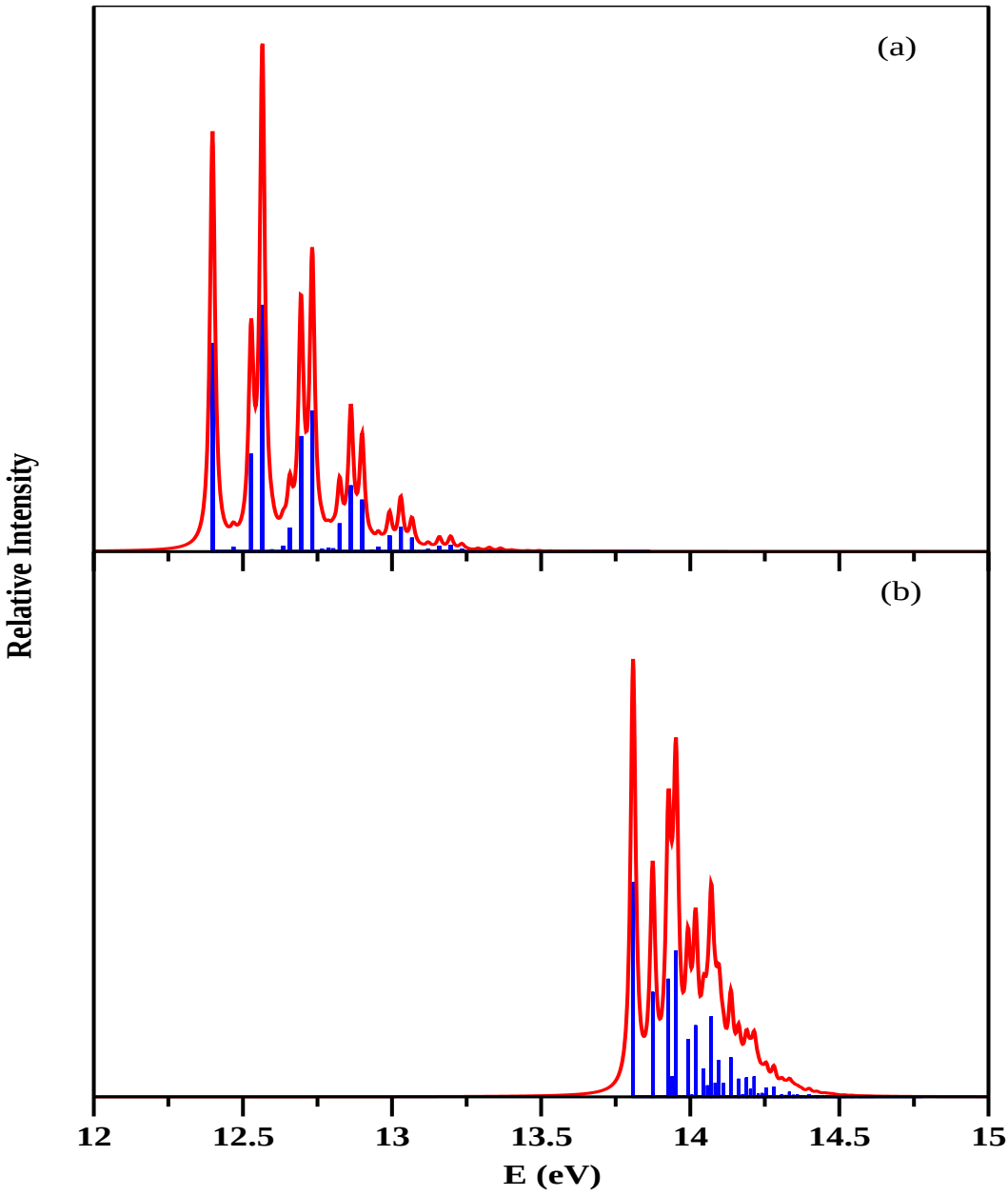

Figure 4.5: Same as in Fig. 4.3, for the nondegenerate $\widetilde{A}^2A_2''$ (panel a) and $\widetilde{C}^2A_2'$ (panel b) electronic states of $TFBz^+$ and calculated with the symmetric vibrational modes ν_2-ν_4 only.

results of ∼0.169 eV, ∼0.126 eV and ∼0.078 eV, respectively.

It is discussed above that the $\widetilde{X}$ state is energetically well separated from the $\widetilde{A}$, $\widetilde{B}$ and $\widetilde{C}$ states and the $\widetilde{X}$ -$\widetilde{A}$ conical intersections occur much beyond the energy range of the recorded vibronic bands. The $\widetilde{A}$, $\widetilde{B}$ and $\widetilde{C}$ electronic states on the other hand, are energetically close and conical intersections among them are shown to occur within this energy range. It is therefore necessary to include the relevant PJT interactions in the full simulation of the nuclear dynamics in the $\widetilde{X}$ -$\widetilde{A}$ -$\widetilde{B}$ -$\widetilde{C}$ electronic manifold in order to make a detailed comparison with the experimental band structures.

The nuclear motion is simulated below including twenty three relevant vibrational modes employing the vibronic Hamiltonian of Eq. 4.2. This leads to a huge increase of the dimension of the Hamiltonian matrix which can not be diagonalized to calculate its eigenvalues and eigenvectors. We therefore use the MCTDH algorithm [118–123], and propagate WPs to calculate the eigenvalue spectrum. The required normal mode combinations, sizes of the primitive and single particle bases in the WP propagation using the MCTDH algorithm [118–123] in the coupled $\widetilde{X}$ -$\widetilde{A}$ -$\widetilde{B}$ -$\widetilde{C}$ electronic states are given in Table 4.5.

Table 4.5: Normal mode combinations, sizes of the primitive and the single particle basis used in the WP propagation within the MCTDH framework in the ($\widetilde{X}$ -$\widetilde{A}$ -$\widetilde{B}$ -$\widetilde{C}$) coupled electronic manifold using the complete vibronic Hamiltonian of Eqs. (4.2-4.5e). The CPU time and the required memory of each WP calculation are also given.

Normal modes[a]	Primitive basis[b]	SPF basis[c]	CPU time	Required RAM [Mbyte]	Figure
		[$E''_{X,x}$, $E''_{X,y}$, A''_2 $E'_{B,x}$, $E'_{B,y}$, C'_2]			
(ν_2, ν_{11x}, ν_{11y}, ν_{19x}, ν_{19y})	(24, 4, 4, 4, 4)	[8, 8, 8, 8, 8, 4]	$E''_{X,x}$: 24h 33min 37.83s	1094.06	
(ν_{9x}, ν_4, ν_{14y}, ν_{20x}, ν_5)	(18, 5, 5, 4, 4)	[6, 6, 4, 10, 10, 10]	$E''_{X,y}$: 26h 31min 51.55s	1094.06	
(ν_{9y}, ν_{12x}, ν_{14x}, ν_{20y}, ν_{16})	(18, 8, 5, 4, 4)	[6, 6, 4, 8, 8, 4]	A''_2: 16h 43min 59.38s	1094.06	Fig. 4.6
(ν_{13x}, ν_{12y}, ν_{18x}, ν_3)	(36, 8, 4, 7)	[6, 6, 5, 7, 7, 4]	$E'_{B,x}$: 19h 37min 01.37s	1094.06	
(ν_{13y}, ν_{10x}, ν_{18y}, ν_{10y})	(36, 5, 4, 5)	[7, 7, 4, 6, 6, 5]	$E'_{B,y}$: 22h 09min 42.13s	1094.06	
			C'_2: 22h 08min 00.79s	1094.06	

The calculations were converged with respect to the spectrum. [a]Vibrational modes bracketed together were treated as a single particle, e.g., particle 1 is a 5-dimensional particle that combines ν_2, ν_{11x}, ν_{11y}, ν_{19x}, and ν_{19y} vibrational modes. [b] The primitive basis is the number of harmonic oscillator DVR functions, in the dimensionless coordinate system required to represent the system dynamics along the relevant mode. The full primitive basis consists of a total of 1.479 $\times 10^{19}$ functions. [c] The SPF basis is the number of single-particle functions used, one set for the each component of the seven electronic states. Here they are same in numbers in order to give equal weight for the x and y components of the degenerate $\widetilde{X}$ and $\widetilde{B}$ electronic state. Total number of configurations is 83712. The calculations are carried out employing the MCTDH program package of Ref. [[118]].

Six calculations are carried out by initially preparing the WP separately on each component of the $\widetilde{X}$ -$\widetilde{A}$ -$\widetilde{B}$ -$\widetilde{C}$ electronic manifold. The WP in each calculation is propagated for 200 *fs*. The time autocorrelation functions from these six calculations are combined, damped with an exponential function, e^{-t/τ_r} (with τ_r=14 fs.), and finally Fourier transformed to calculate the composite vibronic bands. The damping of the autocorrelation function corresponds to a convolution of the vibronic line spectrum with a Lorentzian function of 94.3 meV FWHM. The final theoretical results are presented in panel b of Fig. 6 along with the experimental results of Ref. [151] in panel a. It can be seen that the theoretical results are in good accord with the low resolution experimental spectrum. We note that, it was necessary to adjust the vertical ionization energies of the $\widetilde{A}$, $\widetilde{B}$ and $\widetilde{C}$ electronic states within the error limit of the OVGF data ($\sim \pm 0.3$ eV) to reproduce the adiabatic ionization positions of the bands at their experimental value. The adjusted ionization energies are also given in Table 4.3. Apart from these, no other parameters are adjusted in the theoretical simulations.

The nonadiabatic coupling among the $\widetilde{X}$ -$\widetilde{A}$ -$\widetilde{B}$ -$\widetilde{C}$ electronic manifold leads to the complex structures of the vibronic bands in Fig. 4.6. While the first two bands exhibit poor vibrational structure at the experimental resolution, the third one is highly diffuse and overlapping in nature. We note that precise quantitative informations on the vibronic energy levels could not be extracted from these experimental bands [151]. Somewhat better resolved experimental $\widetilde{X}$ and $\widetilde{A}$ bands are shown in Fig. 4.7 along with the theoretical results. Three distinct vibrational intervals of 565, 968 and 1452 cm^{-1} were found in the experimental data of both the bands [79]. These frequencies compare well with our theoretical data of 631, 1019 and 1365 cm^{-1} for the $\widetilde{X}$ band and 566, 1045, 1349 cm^{-1} for the $\widetilde{A}$ band, respectively. The 1452 cm^{-1} vibration is strongly excited in both the bands. This is followed by a moderate and weak excitation of the 968 and 565 cm^{-1} vibrations, respectively. The excitation of the 968 cm^{-1} vibration is relatively stronger and that of 565 cm^{-1} one is relatively weaker in the $\widetilde{A}$ state compared to the $\widetilde{X}$ state.

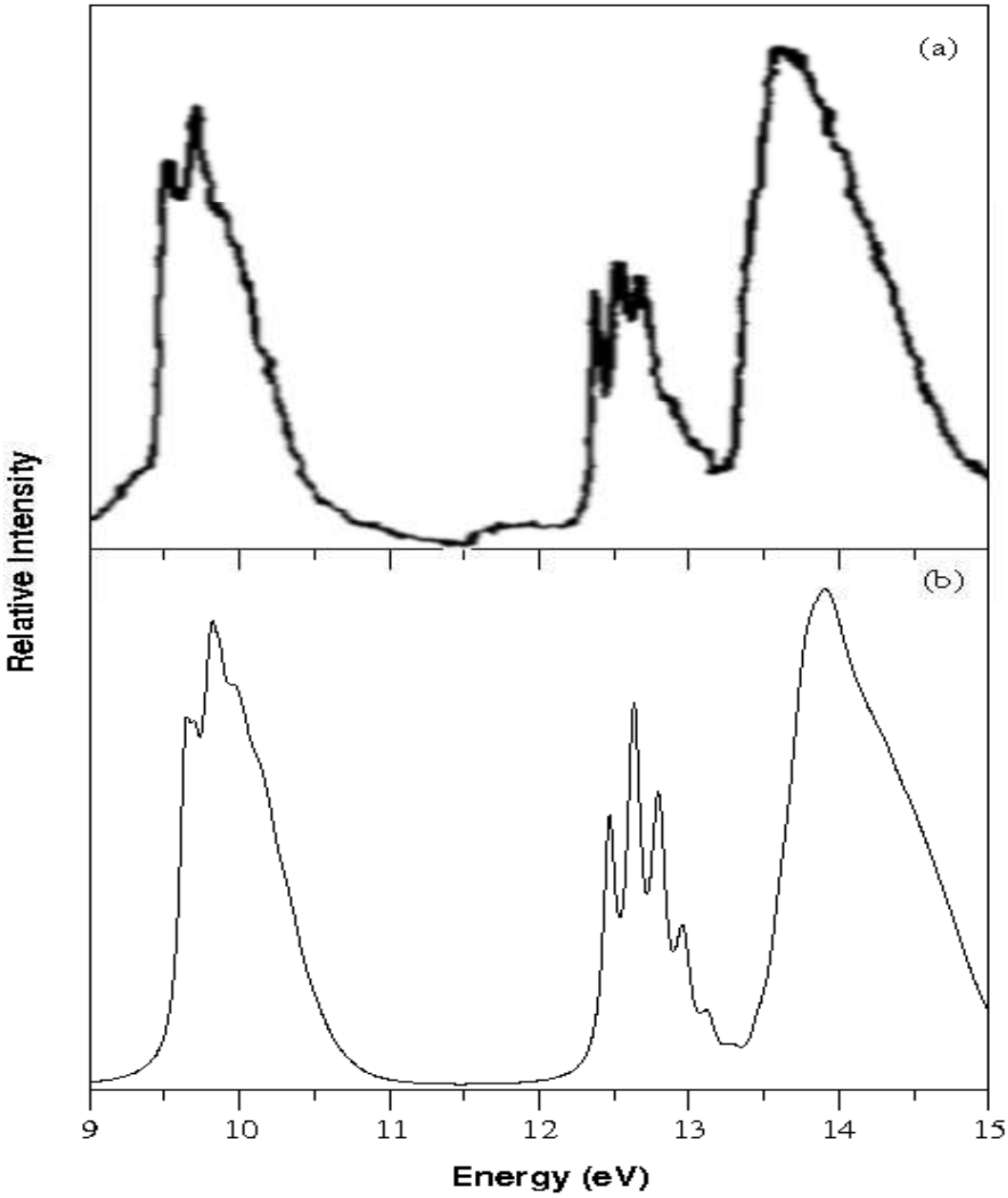

Figure 4.6: Vibronic bands of the coupled $\widetilde{X}$ -$\widetilde{A}$ -$\widetilde{B}$ -$\widetilde{C}$ states of $TFBz^+$. The experimental [151] and theoretical results are shown in panel a and b, respectively. The intensity (in arbitrary unit) is plotted along the energy (relative to minimum of the $^1A_1'$ state of TFBz) of the final vibronic states.

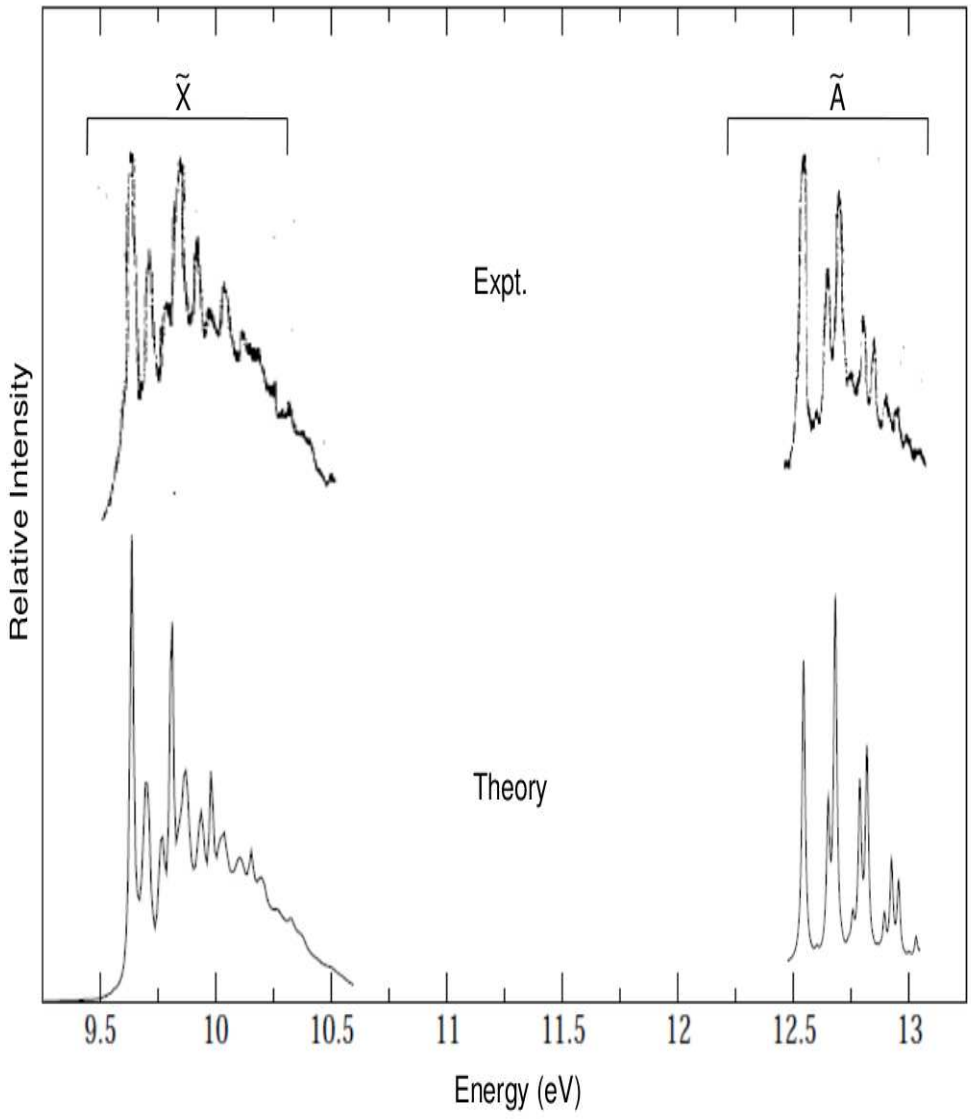

Figure 4.7: Vibronic band structure of the $\widetilde{X}$ and $\widetilde{A}$ electronic states of $TFBz^+$. The experimental results are reproduced from Ref. [79]. The theoretical stick spectrum is convoluted with a Lorentzian function of 20 meV FWHM to generate the spectral envelope.

These observations are in good accord with our theoretical findings. The three vibrations discussed above correspond to the ν_2, ν_3 and ν_4 vibrational modes (cf., 4.2) of $TFBz^+$.

The effect of the $\widetilde{X}$ -$\widetilde{A}$ PJT coupling on the dynamics of the $\widetilde{X}$ state is negligible. The energetic minimum of $\widetilde{X}$ -$\widetilde{A}$ CIs is estimated to occur at ∼21.23 eV within the present theoretical model. Understandably, this is too high in energy to be relevant for the nuclear dynamics on the present time scale. As a result, the vibrational structure of the $\widetilde{X}$ state is not affected by these CIs. However, the $\widetilde{B}$ state is moderately coupled with the $\widetilde{A}$ state through degenerate e'' vibrational modes and strongly coupled with the $\widetilde{C}$ state through degenerate e' vibrational modes (cf., Table 4.4). The energetic minimum of the $\widetilde{B}$ -$\widetilde{C}$ CIs occurs very close to the equilibrium minimum of these states (see the discussion in Sec. 4.4). The vibrational structures of both the $\widetilde{B}$ and $\widetilde{C}$ states are therefore, strongly and that of the $\widetilde{A}$ state weakly perturbed by the associated nonadiabatic coupling. This finally leads to a highly overlapping and diffuse vibrational structure (as can be seen from Fig. 4.6) of the $\widetilde{B}$ and $\widetilde{C}$ electronic states.

4.5.2 The MATI spectrum of the $\widetilde{X}^2E''$ electronic state

The low resolution photoelectron spectroscopy data discussed above do not allow to identify all the major vibrational progressions in the band. The better resolved MATI spectrum recorded by Kwon *et al.* [152] revealed a rich vibrational structure of the $\widetilde{X}^2E''$ electronic manifold of $TFBz^+$. The MATI measurements involve an excitation to a Rydberg state whereas, we directly excite the molecule from its neutral ground state to the relevant cationic states in our theoretical model. We therefore, do not expect to reproduce the intensities so as to compare with the experiment and only the line positions can be compared directly. The theoretical spectra reported below are calculated by a matrix diagonalization method employing the Lanczos algorithm [116]. Since the coupling of the $\widetilde{X}$ state with the

$\widetilde{A}$ state is very weak (cf., Table 4.4) and the corresponding conical intersections occur at high energies (as discussed in Sec. 4.4), we do not expect any effect of this coupling in the low-lying vibronic structure of this state. We therefore exclude it from the calculations discussed below. The vibronic eigenvalue spectrum of the $\widetilde{X}$ state obtained with six JT active e' modes (ν_9-ν_{14}) and three totally symmetric a_1' modes (ν_2-ν_4) is shown in the lower panel along with the experimental MATI spectrum reproduced from Ref. [152] in the upper panel of Fig. 4.8. The converged stick spectrum of the lower panel is obtained by diagonalizing a secular matrix of dimension 1.87 $\times 10^7$ using 5000 Lanczos iterations. The stick data is convoluted with a Lorentzian function of 2 meV FWHM to generate the spectral envelope. The high frequency C-H stretching modes ν_1 (a_1') and ν_8 (e') have very low coupling strength and are excluded from the calculations. A close look at the spectra of Fig. 4.8 reveals that despite a good agreement between the theory and experiment, the theoretical spectrum possesses rich vibronic structure also at high energies. This is presumably arising from the fact that the theoretical calculations consider a direct ionization whereas, the experimental MATI measurement involves an intermediate Rydberg state. The energetic location of some of the intense peaks obtained from the above calculations are reported in Table 4.6 along with the experimental MATI [152], LIF [146] and (2+1) resonance enhanced multiphoton ionization (REMPI) [158] spectroscopy data.

The nonadiabatic effects due to the JT interactions within the $\widetilde{X}$ state solely contributes to its dense vibrational structure. Understandably, a complete identification and assignment of all the vibrational levels of Fig. 4.8 is an impossible task. Therefore, some of the prominent lines appearing in Fig. 4.8 are reported only in Table 4.6 and compared with the experiment to reveal the accuracy of the theoretical model developed here. It can be seen from the collected data in Table 4.6 that the fundamentals of all the vibrational modes are excited closer to an experimental line at that frequency. The intense peak at $\sim$569 cm^{-1} is assigned to the fundamental of ν_{13}. This is consistent with the assignment of Sears

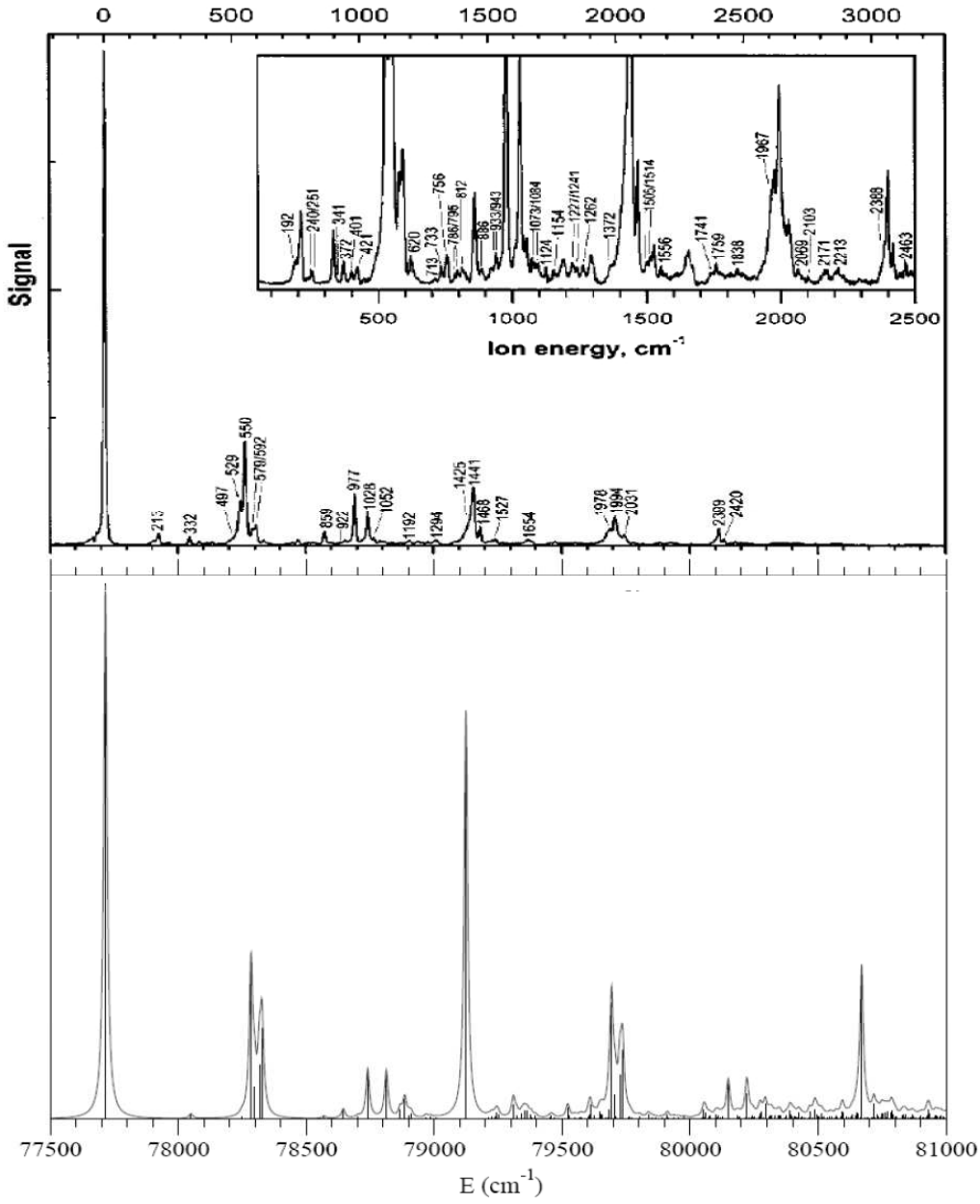

Figure 4.8: The vibronic structure of the $\widetilde{X}^2E''$ electronic manifold of $TFBz^+$. The better resolved experimental MATI spectrum (upper panel) is plotted along with the present theoretical results (lower panel). The theoretical stick spectrum is convoluted with a 2 meV Lorentzian to generate the spectral envelope. The magnified view of a subset of the experimental spectrum [152] is given in the inset of the upper panel.

Table 4.6: Vibrational energy levels of the $\widetilde{X}^2E''$ electronic manifold of $TFBz^+$ (in cm^{-1}). The present theoretical results are given along with the experimental MATI [152], LIF [146] and REMPI [158] spectroscopy data.

Present	MATI	LIF	REMPI	Most probable assignment
235	240	249	-	-
334	332	334	347	ν_{14}
569	550	557	557	ν_{13}
583	592	596	-	ν_4
854	859	-	860	$\nu_{13}+\nu_{14}$
930	943	945	982	ν_{12}
1025	1028	1043	1070	ν_3
1152	1154	-	-	ν_{13}^2
1170	1192	-	-	ν_{11}
1271	1262	-		$\nu_{12}+\nu_{14}$
1409	1441	-	1435	ν_2
1529	1527	-	-	ν_{10}
1637	1654	-	1660	ν_9
1743	1741	-	1694	ν_{13}^3
1978	1978	-	2000	$\nu_2+\nu_{13}$
2049	2031	-	-	ν_3^2
2196	2171	-	-	$\nu_9+\nu_{13}$
2263	2213	-	-	ν_{13}^4
2385	2399	-	-	$\nu_2+\nu_{12}$
2434	2420	-	2430	$\nu_2+\nu_3$

and coworkers, who found this peak at ∼557 cm^{-1} in their LIF emission spectrum [146]. This assignment was not unambiguously settled for the corresponding MATI peak at ∼550 cm^{-1} [152]. Corresponding peak found by Philis *et al.* at ∼557 cm^{-1} in their (2+1) REMPI spectrum [158]. ν_{13} is the strongest JT active mode in the $\widetilde{X}$ state therefore, many of its overtones and combination levels are excited in the spectrum and a few of them are also listed in Table 4.6. The fundamental of much weaker JT active mode ν_{14} appears at ∼334 cm^{-1} in good accord with the MATI [152], LIF [146] and REMPI [158] data. The fundamental of ν_{12} appears at ∼930 cm^{-1}, also in good accord with the MATI [152], LIF [146] and REMPI [158] data. The fundamentals of ν_{10} and ν_9 appears at ∼1529 cm^{-1} and ∼1637 cm^{-1}, respectively. These are absent in the LIF data [146] but lines closer

to these frequencies are present (as noted in Table 4.6) in both the MATI [152] and REMPI [158] data. However, a different assignment is proposed in the MATI data.

Among the totally symmetric a_1' vibrational modes the C-H stretching vibration ν_1 revealed no excitation in the experiment and as mentioned before that it is dropped from the present calculations. The fundamental of the strongest Condon active mode ν_2 appears at ∼1409 cm^{-1} in good accord with both the MATI data of ∼1441 cm^{-1} and REMPI data of ∼1435 cm^{-1}. The ν_2 fundamental is very intense and its overtones are also found at high energies. The Condon activity of ν_3 is much weaker than ν_2 (cf., Table 4.3). The fundamental of ν_3 appears at ∼1025 cm^{-1} and its intensity is about ten times smaller than that of ν_2. The fundamental of ν_3 appears at ∼1028 cm^{-1}, ∼1043 cm^{-1} and ∼1070 cm^{-1} in the MATI [152], LIF [146] and REMPI [158] data, respectively, in good accord with our theoretical results. As can be seen from Table 4.3 that the excitation strength of ν_4 is extremely small in the $\widetilde{X}$ state. A weak line at ∼583 cm^{-1} is attributed to the fundamental of this mode and is in good accord with its location found at ∼596 cm^{-1} in the LIF emission spectrum [146]. A corresponding weak peak (in accordance with our results) observed in the MATI spectrum at ∼592 cm^{-1} [152] and not unambiguously assigned, can be assigned to this fundamental. Apart from these fundamentals, a large number of overtones and combination levels are excited in the theoretical data. A one-to-one comparison of these levels with the experiment is understandably impossible and therefore, we list a few most intense ones in Table 4.6 along with the line closer to it found from the MATI [152] and REMPI [158] spectrum.

4.6 Electronic population dynamics

In order to understand the impact of complex nonadiabatic coupling on the dynamics of the excited electronic states, the time dependence of the diabatic elec-

tronic populations in the $\widetilde{X}$ -$\widetilde{A}$ -$\widetilde{B}$ -$\widetilde{C}$ coupled electronic manifold of $TFBz^+$ is recorded and discussed in this section. These electronic populations are obtained by initially locating the WP on one component of the JT split $\widetilde{X}$ state, the $\widetilde{A}$ state, one component of the JT split $\widetilde{B}$ state and the $\widetilde{C}$ state are shown in Figs. 4.9(a-d), respectively. It can be seen from panel a that an extremely small population transfer occurs to the $\widetilde{A}$ state when the WP is initially prepared on one component of the JT split $\widetilde{X}$ state. All other states remain unpopulated in this situation. The electronic population in panel a moves back and forth between the two components of the $\widetilde{X}$ state driven solely by the JT intersections. The initial decay of the population relates to a nonradiative internal conversion rate of ~ 80 *fs* of the $\widetilde{X}$ state.

The electronic population dynamics for an initial transition of the WP to the $\widetilde{A}$ state is depicted in panel b of Fig. 4.9. It can be seen that hardly any internal conversion takes place in this case. A reconsideration of the topographical features of the $\widetilde{A}$ state discussed in section 4.4 shows that the energetic minimum of the $\widetilde{X}$ -$\widetilde{A}$ conical intersections occurs ~ 11.66 eV above the minimum of the $\widetilde{A}$ state. The minimum of the $\widetilde{A}$ -$\widetilde{B}$ conical intersections occurs at $\sim$13.56 eV, which is $\sim$1.43 eV above the $\widetilde{B}$ state minimum. It therefore follows that the WP does not have sufficient energy to access these high energy conical intersections, when initially prepared on the $\widetilde{A}$ state. Also the $\widetilde{A}$ -$\widetilde{B}$ intersections occur for large values of dimensionless normal coordinates of the a_1' and e' vibrational modes (cf., Figs. 4.1 and 4.2). These regions of the surfaces are sufficiently away from the Franck-Condon zone center and remain less explored by the WP during its dynamical evolution. In addition, the $\widetilde{A}$ -$\widetilde{B}$ PJT coupling is generally small (cf., Table 4.4). These considerations imply a long-lived nature of the $\widetilde{A}$ state and forms the mechanistic basis underlying the observed emission of $TFBz^+$. We return to this point again in the next section.

The electron population dynamics becomes more complex and involved when the WP is initially prepared either on the $\widetilde{B}$ (panel c) or $\widetilde{C}$ (panel d) electronic

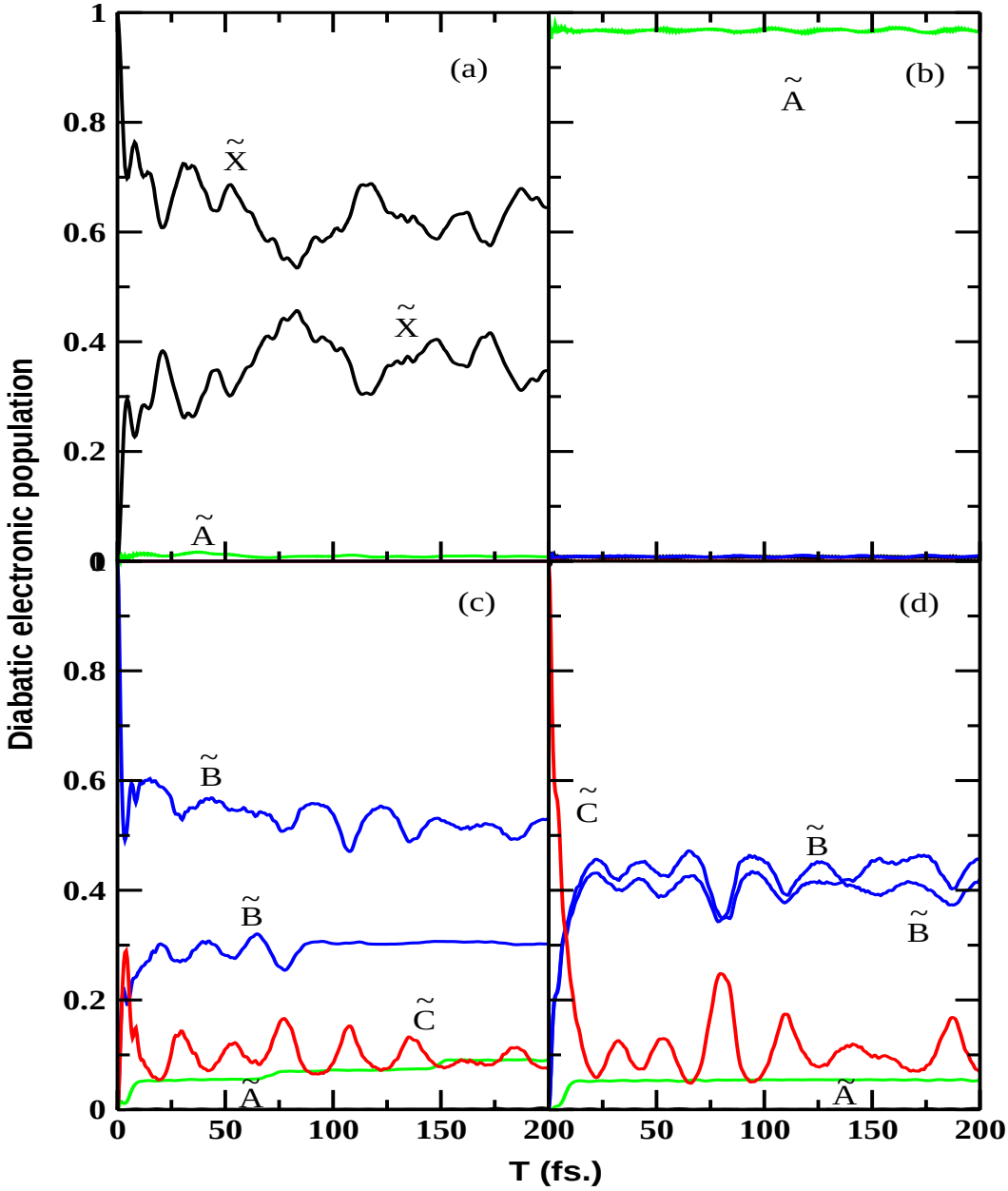

Figure 4.9: Time-dependence of diabatic electronic populations in the $\widetilde{X}$ -$\widetilde{A}$ -$\widetilde{B}$ -$\widetilde{C}$ coupled state nuclear dynamics of $TFBz^+$. The results obtained by initially locating the WP on one component of the JT split $\widetilde{X}$ state, $\widetilde{A}$ state, one component of the JT split $\widetilde{B}$ state and $\widetilde{C}$ state are shown in panel a-d, respectively.

state. In these cases the WP can access the $\widetilde{A}$ -$\widetilde{B}$ -$\widetilde{C}$ conical intersections and internal conversion to all three states becomes feasible. The $\widetilde{A}$ -$\widetilde{B}$ and $\widetilde{B}$ -$\widetilde{C}$ PJT intersections occur ∼1.43 eV and ∼0.076 eV above the minimum of the $\widetilde{B}$ and $\widetilde{C}$ states, respectively. These energetic considerations allow significant population transfer within the $\widetilde{A}$ -$\widetilde{B}$ -$\widetilde{C}$ coupled electronic manifold. The population transfer to the $\widetilde{A}$ state is significantly less due to the reasons discussed above. The initial sharp decay of the population of the $\widetilde{B}$ and $\widetilde{C}$ electronic states in panel c and d relates to the nonradiative decay rate of ∼51 fs and ∼7 fs of these states, respectively. A very fast decay of the $\widetilde{C}$ state population arising from the strong $\widetilde{B}$ -$\widetilde{C}$ PJT coupling particularly, along the degenerate C-C stretching mode ν_{10}. Also the $\widetilde{B}$ -$\widetilde{C}$ conical intersections occurs below the zero point level of the $\widetilde{C}$ electronic state. As a result the WP upon transition to the $\widetilde{C}$ state is immediately perturbed by the strong nonadiabatic effects.

4.7 Fluorescence dynamics

The emissive properties of the parent Bz^+ and its fluoroderivatives have been investigated experimentally [94, 95, 140, 143–146] to understand the dynamics of their excited electronic states. The emission of fluorescence was observed for at least three-fold fluorination of Bz^+ [94,95]. Analogously, the monofluoro benzene radical cation ($MFBz^+$) and difluoro benzene radical cation ($DFBz^+$) (except the meta isomer which emits weakly [145]) do not show any emission [145]. Details of this observations have been investigated in recent theoretical studies by examining the topography of the low-lying electronic states of these systems [139, 159–162]. These studies established conical intersections of potential energy surfaces as the crucial mechanistic element for quenching of fluorescence emission. Fluorination of Bz causes a re-ordering of its MOs and a stabilization of the σ type of MOs. The extent of stabilization increases with increasing fluorination (an effect called the "perfluoro effect"). This stabilization causes a shift of the corresponding ionic

state to higher energy. As a result, the energetic minimum of the seam of various conical intersections and the equilibrium minimum of a state changes varies with fluorine substitution causing a difference in its emissive properties.

To portray this situation more clearly a few valence canonical MOs of Bz, MFBz, difluoro benzene (DFBz) and TFBz are shown in Fig. 4.10. These MOs are calculated at the MP2/cc-pVTZ level of theory. Their symmetry assignments are in general agreement with the literature except for the *p*-DFBz for which a different choice of the C_2 axis leads to somewhat different assignment of symmetry, without affecting the energetic ordering. The highest occupied MO (HOMO) of all these molecules is of π-type. The degenerate E_{1g} HOMO of Bz transforms into two nondegenerate MOs in MFBz and DFBz due to a reduction of symmetry from D_{6h} to C_{2v}. The electronic degeneracy is restored again in the symmetric TFBz because of its D_{3h} equilibrium symmetry. The next σ-type degenerate E_{2g} MO (HOMO-1) of Bz undergoes considerable energy shift upon fluorination. The states derived from this MO corresponds to $\widetilde{B}^2B_2$-$\widetilde{D}^2A_1$, $\widetilde{C}^2A_1$-$\widetilde{D}^2B_2$, $\widetilde{C}^2A_1$-$\widetilde{D}^2B_2$, $\widetilde{B}^2B_{3g}$-$\widetilde{D}^2B_{2u}$ and $\widetilde{B}^2E'$ symmetry species in $MFBz^+$, *o*-$DFBz^+$, *m*-$DFBz^+$, *p*-$DFBz^+$ and $TFBz^+$, respectively. The vertical ionization energies of the electronic states of Bz^+ , $MFBz^+$, $DFBz^+$ and symmetric $TFBz^+$ are plotted in Fig. 4.11. It can be seen that owing to a stabilization of the underlying MOs upon fluorination (cf., Fig. 4.10), all $^2E_{2g}$ derived states shifts to the higher energies in the fluoroderivatives. The energies of the next π-type state ($\widetilde{C}$ state in Bz^+ , $MFBz^+$ and *p*-$DFBz^+$; $\widetilde{B}$ state in *o*- and *m*-$DFBz^+$ and $\widetilde{A}$ state in $TFBz^+$) derived from π-type A_{2u} MO (HOMO-2) of Bz remain almost unchanged (cf., the horizontal line in Fig. 4.11).

The lack of fluorescence emission in Bz^+ has been explained to be due to the multimode dynamical JT effect, which leads to low energy conical intersections between the upper and lower JT sheets of the $\widetilde{X}$ and $\widetilde{B}$ states, respectively [138]. In $MFBz^+$ and $DFBz^+$ the low-lying electronic states split into two sets *viz.*, $\widetilde{X}$ -$\widetilde{A}$ and $\widetilde{B}$ -$\widetilde{C}$ -$\widetilde{D}$ [159–162]. The minimum energy of intersections of these

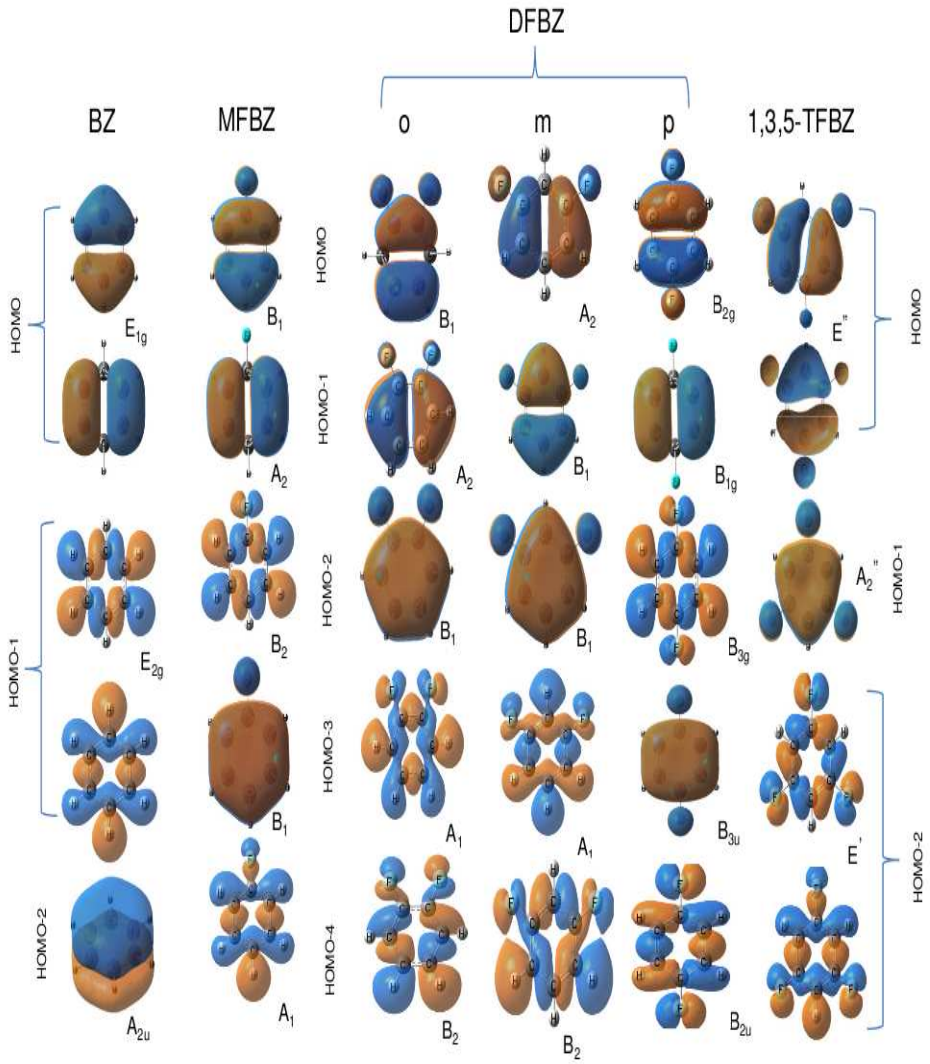

Figure 4.10: Schematic plot of the canonical MOs of benzene and its fluoroderivatives.

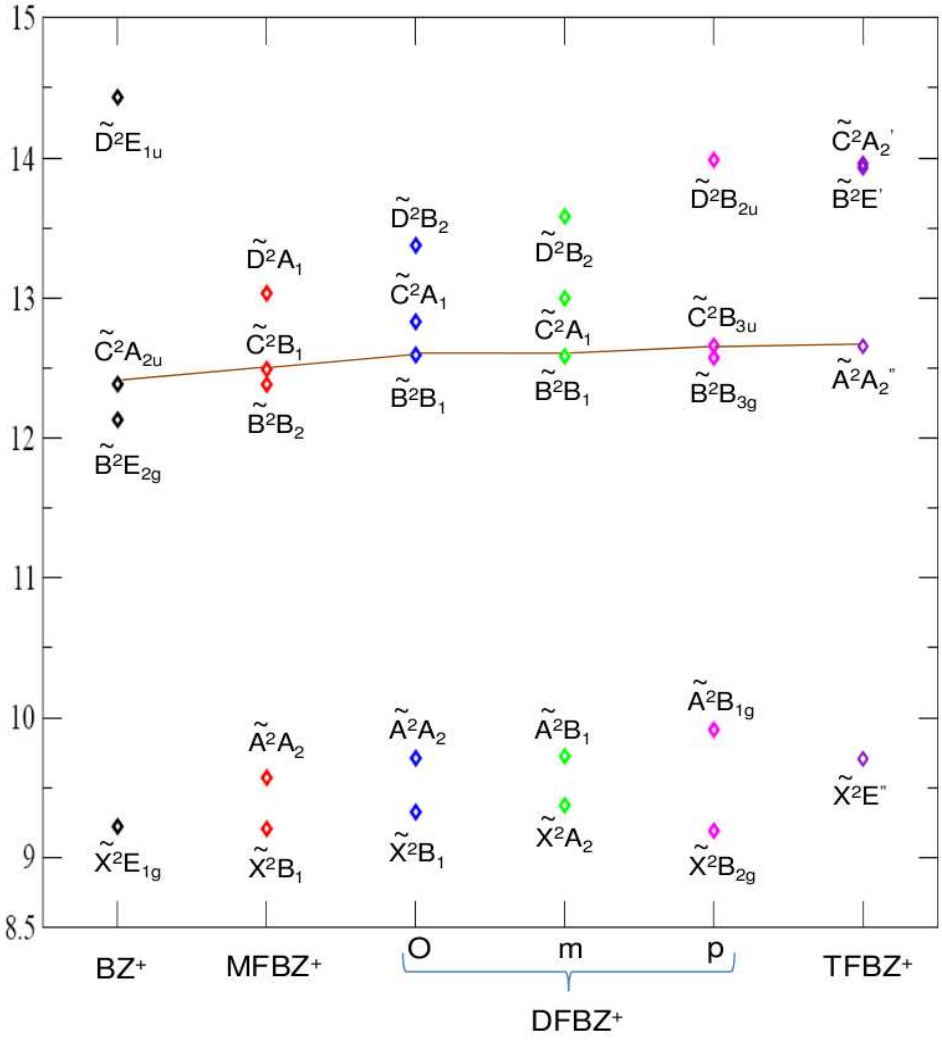

Figure 4.11: The energy of the ionic states of Bz^+ and its fluoroderivatives by ionizing an electron from the MOs (vertically) shown in Fig. 4.10.

two sets of states governs nonradiative decay of excited states and a quenching of fluorescence emission. These two sets of states are connected through both $\widetilde{X}$ -$\widetilde{B}$ and $\widetilde{A}$ -$\widetilde{B}$ crossings in $MFBz^+$ [160]. In $DFBz^+$ these sets are connected through $\widetilde{A}$ -$\widetilde{C}$ curve crossings in the ortho and meta isomers and through $\widetilde{A}$ -$\widetilde{B}$ crossings in the para isomer [161]. The minimum energy of crossings between these sets is ∼12.29 eV in $MFBz^+$ and ∼13.11 eV, ∼13.65 eV and ∼13.08 eV in the ortho, meta and para $DFBz^+$, respectively [160, 161]. In the parent Bz^+ this energy is ∼11.58 eV [138] between the $\widetilde{X}$ and $\widetilde{B}$ states. Therefore, it can be seen that the minimum energy of crossings between the relevant states progressively increases upon fluorine substitution. This energy is being highest for the meta $DFBz^+$ which does not allow much of the WP to access this intersection and therefore, gives rise to weak fluorescence emission [145].

The above scenario dramatically changes in case of 1,3,5-$TFBz^+$. The degenerate E_{2g} MO of Bz transforms to E′ in TFBz . The vertical ionization potential of the $\widetilde{B}^2E'$ state of $TFBz^+$ is ∼2.2 eV higher than the corresponding state in Bz^+ [145]. In this case the ground $\widetilde{X}^2E''$ state remains essentially decoupled from the excited states. The present theoretical model yields the minimum energy of the $\widetilde{X}$ -$\widetilde{A}$ and $\widetilde{A}$ -$\widetilde{B}$ intersections at ∼21.23 eV and ∼13.56 eV, respectively. These intersections occur at much higher energies and also the PJT coupling between these states is also weak (cf., Table 4.4). Therefore, these intersections remain essentially inaccessible for the WP to nonradiatively relax to the $\widetilde{X}$ state. Such dynamical features already emerged from the time dependence of electronic populations shown in Fig. 4.9. It can be seen from the latter that on the present time scale hardly any WP returns to the $\widetilde{X}$ state when initially prepared on one of the excited electronic state. This is quite notable for the dynamics of the $\widetilde{A}$ state (cf., Fig. 4.9(b)). In this case only ∼0.3% WP moves to the other states in 200 fs and since the population curve is nearly parallel to time axis, no significant transfer of WP is expected at longer times. Therefore, unlike Bz^+ and its mono- and di-fluoroderivatives, occurrence of high energy conical intersections

prevents a nonradiative internal conversion and leads to the fluorescence emission in $TFBz^+$.

4.8 Summary and outlook

Static and dynamic aspects of multimode JT and PJT interactions in the four lowest electronic states of $TFBz^+$ have been theoretically investigated. A vibronic coupling model is developed through extensive *ab initio* electronic structure calculations and first principles simulations are carried out to examine the electronic nonadiabatic effects on the nuclear dynamics. The theoretical results are found to be in good accord with the available experimental results.

The vibronic Hamiltonian is constructed in a diabatic electronic basis, including the JT coupling within the degenerate $\widetilde{X}$ and $\widetilde{B}$ electronic states and the possible PJT coupling of these JT split states with the other nondegenerate electronic states of $TFBz^+$. The coupling parameters of the vibronic Hamiltonian are determined by calculating the adiabatic potential energy surfaces of the $\widetilde{X}^2E''$, $\widetilde{A}^2A_2''$, $\widetilde{B}^2E'$ and $\widetilde{C}^2A_2'$ electronic states along the relevant vibrational modes of $TFBz^+$.

The nuclear dynamical simulations are carried out both by the time-independent and time-dependent quantum mechanical methods. A careful examination of various theoretical results reveals that the symmetric vibrational modes ν_2 and ν_3 are strongly excited in the vibronic bands of the $\widetilde{X}$ -$\widetilde{A}$ -$\widetilde{B}$ -$\widetilde{C}$ electronic manifold. While ν_3 causes low-energy crossings of the $\widetilde{A}$ -$\widetilde{B}$ electronic states, all three symmetric vibrational modes (ν_2-ν_4) are important for the low-energy crossings of $\widetilde{B}$ -$\widetilde{C}$ electronic states. The JT effect in the $\widetilde{X}$ electronic state is far weaker compared to that in the $\widetilde{B}$ state. The JT stabilization energies of ~ 0.142 eV and ~ 0.346 eV are estimated, respectively, for these electronic states. The vibronic structure of the $\widetilde{X}$ state is mostly dominated by progressions due to the symmetric ν_2 and degenerate ν_9 and ν_{13} vibrational modes. This state is ener-

getically well separated from others and impact of PJT coupling on its vibronic structure is not significant. Among the $\widetilde{A}$, $\widetilde{B}$ and $\widetilde{C}$ states, The $\widetilde{B}$ and $\widetilde{C}$ states undergo fast internal conversions in 51 fs and 7 fs, respectively. The coupling of the $\widetilde{A}$ state with either $\widetilde{X}$ or the $\widetilde{B}$ state is weak and occurs at higher energies. Therefore, the low-amplitude nuclear motion in the $\widetilde{A}$ state remains unaffected by these couplings. This leads to a long-lived nature of the $\widetilde{A}$ state and triggers fluorescence emission in $TFBz^+$.

Chapter 5

Photophysics of fluorinated benzene and perfluoro effect

5.1 Introduction

So far we have investigated the JT and PJT effects on the low-lying doublet electronic states of fluorinated radical cations of organic hydrocarbons. The effect of fluorine atom substitution, addressed long back in the literature, on the electronic structure and dynamics of benzenoid system is investigated here with renewed vigor [73–78,81–91]. In this chapter we discuss the role of vibronic interactions on the photophysics of the low-lying excited singlet electronic states of neutral fluorinated benzene to understand the recent measurements [73–78, 81–91]. Apart from a systematic study portraying individual examples in this chapter, we have considered a set of fluorinated benzene (monofluorobenzene (MFBz), ortho-difluorobenzene (*o*-DFBz), meta-difluorobenzene (*m*-DFBz) and pentafluorobenzene (PFBZ)) molecules.

Benzene (Bz) and its halogenated derivatives are prototype organic molecules of fundamental importance. The electronic structure and spectroscopy of these molecules studied with renewed vigor in recent years [73–78, 81–91]. Historically,

the absorption band arising from lowest singlet state of Bz represents the first example of an electronic transitions in a polyatomic molecule [36]. Although forbidden by symmetry, such a transition was interpretated using vibronic selection rules [36]. The forbidden electronic transitions in Bz however, become symmetry allowed in the substituted Bz.

Among the halogenated derivatives of Bz, the fluorobenzene molecules have received special attentions to study the chemical impact of fluorine atoms on the electronic structure and properties of Bz. Increasing fluorine substitution is known to stabilize the σ orbitals of the system and the phenomenon is known as perfluoro effect in the literature [92,93]. Although several experimental and theoretical studies on neutral fluorobenzene molecules have appeared in the literature over the past decades [73–78,81–91], a detailed understanding of the spectroscopic and dynamical properties of their electronic excited states is still not achieved. We note that, there has been some detailed theoretical work carried out to understand these properties of fluorobenzene cations in recent years [160–163].

Spectroscopic [82,85] and photophysical [76,78] studies have revealed that the features of the electronic absorption and emission bands and lifetimes of fluorescence strongly depends on the number of substituted fluorine atoms. For example, C_6F_n with n $\leq$ 4 exhibit structured $S_1 \leftarrow S_0$ absorption band, large quantum yield and nanosecond lifetime of fluorescence. On the other hand, C_6F_n with n=5 and 6 exhibit structureless $S_1 \leftarrow S_0$ absorption band [82,85], low quantum yield [76,78], picosecond and nanosecond lifetime of fluorescence emission [86]. Furthermore, a biexponential decay of fluorescence is observed for the latter molecules [86]. Experimental measurements of Philis *et al.* [85] have revealed that lowering of D_{6h} symmetry of Bz by fluorine substitution leads to the appearance of additional bands within 8.0 eV not resolved in the parent Bz molecule. For example, apart from three singlet-singlet transitions analogous to the $B_{2u} \leftarrow A_{1g}$, $B_{1u} \leftarrow A_{1g}$ and $E_{1u} \leftarrow A_{1g}$ transitions in Bz, one additional band has been observed in MFBz and in *o*-DFBz in the region of the $^1B_{1u}$ band. This band is characterized as

the 3s member of $^1E_{1g}$ Rydberg state of Bz molecule [85]. Similarly one additional band has been identified in PFBz at ∼5.85 eV and is designated as the C-band [84]. A clear understanding of the origin of these additional bands is still lacking. Furthermore, these additional bands are highly diffuse and exhibit irregular structures and hardly allow any definitive vibrational assignments. Even though the excited states of fluorobenzene molecules contributing to the absorption bands within 8.0 eV are known, their excitation energies are not accurate enough for a satisfactory theoretical interpretation of the observed vibrational structures [85]. On the theoretical front, a study of nuclear dynamics following the electronic excitation, the possible energy redistribution and relaxation mechanism of neutral fluorobenzene molecules has not been attempted so far.

We address some of the unresolved issues observed in the optical spectra of fluorobenzene molecules and attempt to understand them by performing detail *ab initio* electronic structure calculations and first principles simulations of nuclear dynamics. The PESs and the coupling surfaces of the low-lying electronic states of MFBz, *o*-DFBz, *m*-DFBz and PFBz molecules are constructed by calculating the vertical excitation energies (VEEs) by the equation-of-motion coupled-cluster singles and doubles (EOM-CCSD) method [164] implemented in MOLPRO suite of program [165]. For the VEEs, EOM-CCSD is a well studied method [164] and fully equivalent to the symmetry adapted cluster method [166] and coupled-cluster linear response theory [167]. It also provides affordable computational cost and reasonably good accuracy. The VEEs are calculated along the dimensionless normal displacement coordinates of all vibrational modes of the four fluorobenzene molecules. The calculated adiabatic energy points are fitted to the theoretical models devised in this chapter. The coupling between different electronic states is taken into consideration in accordance with the symmetry selection rules.

To this end we mention that all four molecules belong the C_{3v} symmetry point group at the equilibrium configuration of their electronic ground state (S_0).

The symmetry, nature, vertical excitation energy (VEE) and oscillator strength of their low-lying excited electronic states at the reference geometry of the respective S_0 state are given in Table 5.1 along with the data available from the literature. It can be seen from Table 5.1 that the present VEEs are generally closer to the experimental data compared to those available in the literature [83].

5.2 Details of electronic structure calculations

The geometry optimization and calculation of harmonic vibrational frequencies of the electronic ground state [S_0 ($^1A_1$)] of MFBz, *o*-DFBz, *m*-DFBz and PFBz are carried out at the second-order Møller-Plesset perturbation (MP2) level of theory employing the augmented correlation-consistent polarized valence double-ζ (aug-cc-pVDZ) basis set of Dunning [155]. The Gaussian-03 suite of program [128] is used for this purpose. The optimized equilibrium geometry data for the ground state thus obtained agree very well with the available literature data [156] for MFBz, *o*-DFBz and PFBz molecules. These theoretical results along with the literature data are given in Table 5.2-5.5, respectively. The harmonic vibrational frequencies (ω_i) are calculated by diagonalizing the *ab initio* force constant matrix. These vibrational frequencies are recorded in Table 5.6. The mass-weighted normal coordinates of the vibrational modes are calculated from the eigenvectors of the force constant matrix. These are then multiplied with $\sqrt{\omega}_i$ (in a_0) to obtain the dimensionless normal coordinates (Q_i) of the vibrational modes.

Table 5.1: Vertical excitation energy (VEE) and symmetry of the low-lying excited singlet states of MFBz, *o*-DFBz, *m*-DFBz and PFBz within 8.0 electron Volt (eV). Oscillator strengths are given in parentheses along with the VEEs (in eV). Note that states with zero oscillator strength (as given in Fig. 5.7) are not listed in this table.

Molecule	State symmetry	Transition	VEE calculated in this work	Experimental VEE estimated by Frueholz *et al.* [84]	VEE calculated by Duke *et al.* [83]
MFBz	$S_1(^1B_2)$	$(\pi\pi^*)$	5.055 (0.0072)	4.780	4.627
	$S_2(^1A_1)$	$(\pi\pi^*)$	6.469 (0.0003)	6.230	5.760
	$S_3(^1B_1)$	$(\pi\sigma^*)$	6.724 (0.0058)		
	$S_4(^1B_2)$	$(\pi\pi^*)$	7.288 (0.6520)	6.990	6.629
	$S_5(^1A_1)$	$(\pi\pi^*)$	7.317 (0.6756)	6.990	6.639
o-DFBz	$S_1(^1A_1)$	$(\pi\pi^*)$	5.075 (0.0083)	4.760	4.504
	$S_2(^1B_2)$	$(\pi\pi^*)$	6.503 (0.0002)	6.220	5.577
	$S_3(^1B_1)$	$(\pi\sigma^*)$	6.796 (0.0191)		
	$S_4(^1B_2)$	$(\pi\pi^*)$	7.323 (0.6605)	7.020	6.460
	$S_5(^1A_1)$	$(\pi\pi^*)$	7.378 (0.6522)	7.020	6.477
m-DFBz	$S_1(^1B_2)$	$(\pi\pi^*)$	5.084 (0.0074)	4.790	4.531
	$S_2(^1A_1)$	$(\pi\pi^*)$	6.492 (0.0002)	6.170	5.632
	$S_3(^1A_1)$	$(\pi\pi^*)$	7.272 (0.6295)	6.960	6.472
	$S_4(^1B_2)$	$(\pi\pi^*)$	7.382 (0.6574)	6.960	6.489
PFBz	$S_1(^1B_2)$	$(\pi\pi^*)$	5.111 (0.0086)	4.790	4.184
	$S_2(^1B_1)$	$(\pi\sigma^*)$	6.314 (0.0013)	5.850	
	$S_3(^1A_1)$	$(\pi\pi^*)$	6.597 (0.0041)	6.360	5.180
	$S_4(^1A_1)$	$(\pi\pi^*)$	7.475 (0.6697)	7.120	6.040
	$S_5(^1B_2)$	$(\pi\pi^*)$	7.509 (0.6537)	7.120	6.041

Table 5.2: The equilibrium geometry of the electronic ground state of MFBz along with the available experimental [156] data. The theoretical calculations are carried out at the MP2 level of theory employing the aug-cc-pVDZ basis set.

Bond distance (Å)			Bond angle (deg)		
Bond	Theory	Experiment [156]	Angle	Theory	Experiment [156]
C_4-C_5	1.399	1.377	C_3-C_4-C_5	122.85	123.40
C_4-F_{12}	1.369	1.364	F_{12}-C_4-C_5	118.58	118.30
C_5-C_6	1.408	1.389	C_4-C_5-C_6	118.15	117.88
C_6-C_1	1.408	1.388	C_5-C_6-C_1	120.49	120.37
–	–	–	C_6-C_1-C_2	119.85	120.10

Table 5.3: Same as in Table 5.2, for o-DFBZ.

Bond distance (Å)			Bond angle (deg)		
Bond	Theory	Experiment [156]	Angle	Theory	Experiment [156]
C_4-F_{11}	1.358	1.346	F_{11}-C_4-C_5	120.29	120.73
C_4-C_5	1.397	1.376	F_{11}-C_4-C_3	119.06	118.31
C_4-C_3	1.401	1.378	C_3-C_4-C_5	120.64	120.95
C_1-C_2	1.407	1.389	C_2-C_3-C_4	120.64	120.82
C_1-C_6	1.407	1.384	C_1-C_2-C_3	119.07	118.67
–	–	–	C_6-C_1-C_2	120.29	120.56

Table 5.4: Same as in Table 5.2, for m-DFBZ.

Bond distance (Å)		Bond angle (deg)	
Bond	Theory	Angle	Theory
C_4-F_{10}	1.366	H_{12}-C_3-C_4	121.67
C_4-C_5	1.399	C_3-C_4-C_5	123.08
C_4-C_3	1.399	C_4-C_5-C_6	118.01
C_3-H_{12}	1.091	C_5-C_6-C_1	121.14
C_5-C_6	1.401	C_3-C_4-F_{10}	118.03
C_5-H_8	1.092	F_{10}-C_4-C_5	118.89
—	–	C_4-C_5-H_8	120.03

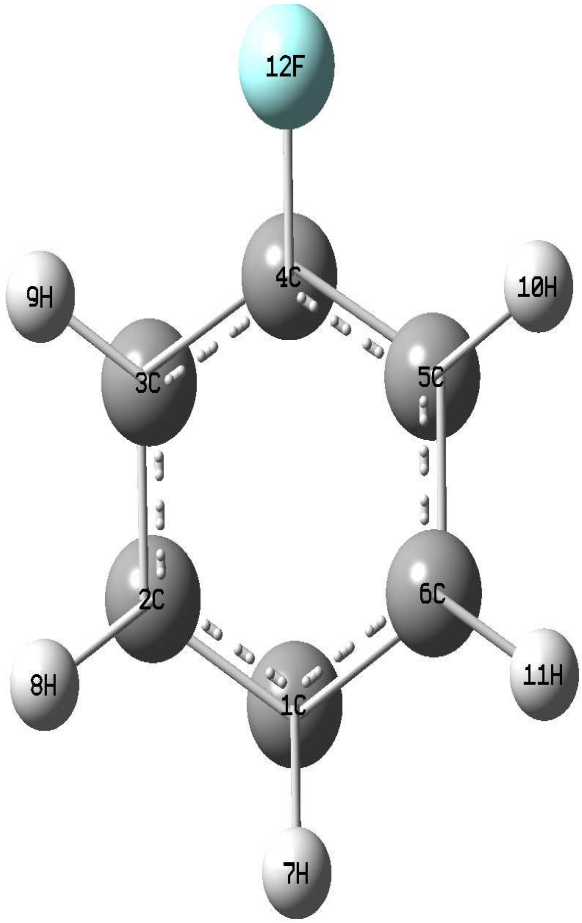

Figure 5.1: *Ab initio* calculated chemical structure of the electronic ground state of MFBz at the MP2/aug-cc-pVDZ level of theory.

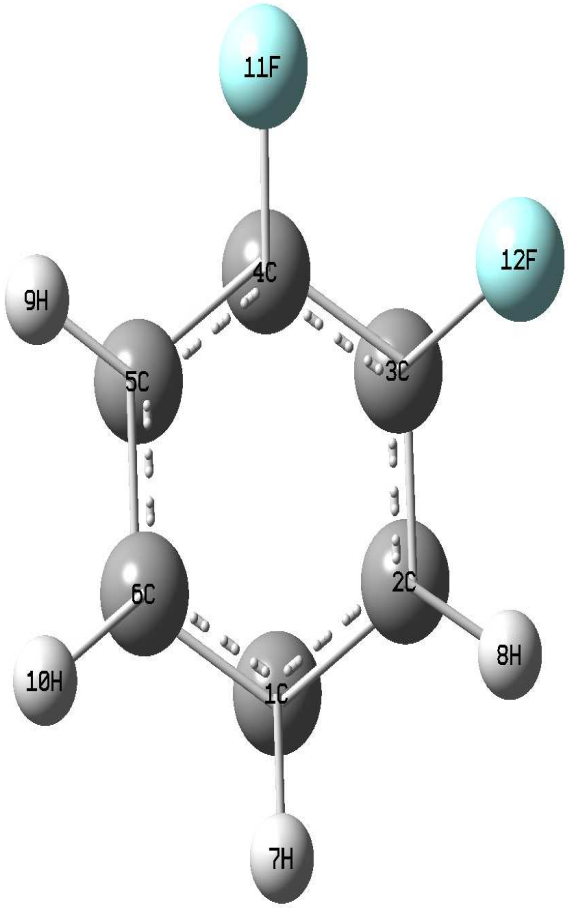

Figure 5.2: Same as in Fig. 5.1, for o-DFBZ.

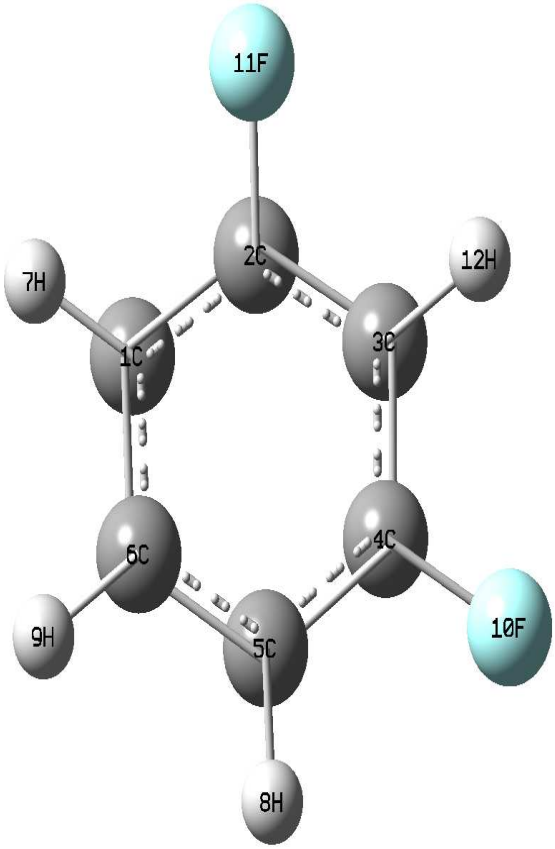

Figure 5.3: Same as in Fig. 5.1, for m-DFBZ.

Table 5.5: Same as in Table 5.2, for PFBZ.

Bond distance (Å)			Bond angle (deg)		
Bond	Theory	Experiment [156]	Angle	Theory	Experiment [156]
C_6-F_{10}	1.354	1.340	F_{10}-C_6-C_1	118.57	118.30
C_6-C_1	1.400	1.367	F_{10}-C_6-C_5	119.95	120.00
C_6-C_5	1.398	1.373	C_1-C_6-C_5	121.48	121.70
C_1-F_{11}	1.348	1.341	F_{11}-C_1-C_6	120.97	121.00
C_1-C_2	1.401	1.371	F_{11}-C_1-C_2	119.88	119.50
C_2-F_{12}	1.347	1.337	C_6-C_1-C_2	119.14	119.50
C_5-H_7	1.111	–	F_{12}-C_2-C_1	119.80	120.20
–	–	–	F_{12}-C_2-C_3	119.80	120.00
–	–	–	C_1-C_2-C_3	120.40	119.80

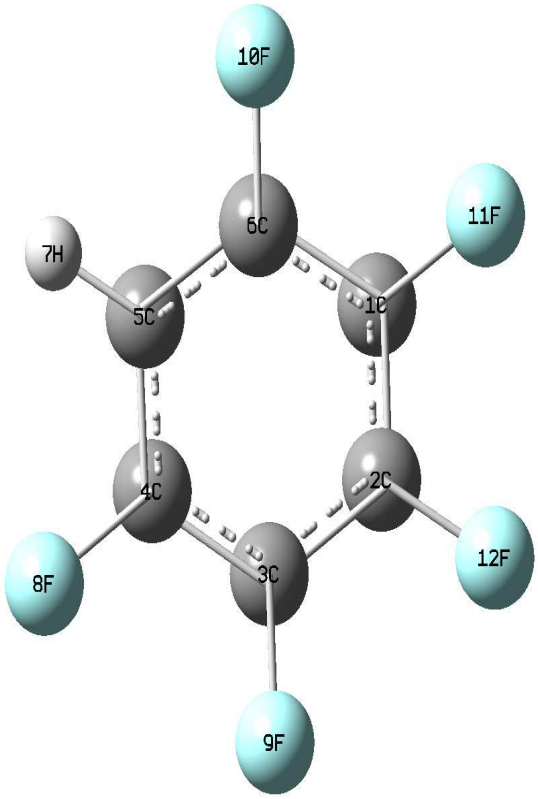

Figure 5.4: Same as in Fig. 5.1, for PFBZ.

Table 5.6: *Ab initio* calculated harmonic frequencies of the vibrational modes of MFBz, *o*-DFBz, *m*-DFBz and PFBz at the MP2/aug-cc-pVDZ level of theory. All values are in eV.

Mode	MFBz	Symmetry	*o*-DFBz	Symmetry	*m*-DFBz	Symmetry	PFBz	Symmetry
ν_1	0.4021		0.4025		0.4038		0.4038	
ν_2	0.4008		0.4007		0.4032		0.2087	
ν_3	0.3981		0.2049		0.3998		0.1901	
ν_4	0.2018		0.1885		0.2051		0.1762	
ν_5	0.1851		0.1836		0.1815		0.1572	
ν_6	0.1525	a_1	0.1588	a_1	0.1586	a_1	0.1318	a_1
ν_7	0.1439		0.1437		0.1339		0.0888	
ν_8	0.1277		0.1286		0.1256		0.0711	
ν_9	0.1245		0.0941		0.0907		0.0579	
ν_{10}	0.0997		0.0700		0.0640		0.0402	
ν_{11}	0.0632		0.0350		0.0401		0.0331	
ν_{12}	0.1139		0.1126		0.1147		0.1043	
ν_{13}	0.1093		0.0936	b_1	0.1067		0.0734	
ν_{14}	0.0932	b_1	0.0555		0.0960	b_1	0.0673	b_1
ν_{15}	0.0772		0.0357		0.0791		0.0394	
ν_{16}	0.0609		0.4017		0.0562		0.0254	
ν_{17}	0.0288		0.3992		0.0280		0.0196	
ν_{18}	0.4018		0.2031		0.4026		0.2082	
ν_{19}	0.3993		0.1807		0.2037		0.1924	
ν_{20}	0.2036		0.1558		0.1852		0.1834	
ν_{21}	0.1831		0.1473	b_2	0.1836		0.1469	
ν_{22}	0.1800	b_2	0.1362		0.1571	b_2	0.1399	b_2
ν_{23}	0.1605		0.1038		0.1442		0.1174	
ν_{24}	0.1442		0.0671		0.1390		0.0848	
ν_{25}	0.1338		0.0535		0.1182		0.0532	
ν_{26}	0.0752		0.1130		0.0624		0.0372	
ν_{27}	0.0494		0.1028		0.0584		0.0337	
ν_{28}	0.1153		0.0761	a_2	0.1084		0.0783	
ν_{29}	0.1017	a_2	0.0664		0.0733	a_2	0.0477	a_2
ν_{30}	0.0510		0.0229		0.0300		0.0164	

Ab initio calculations of electronic energies of the low-lying singlet states of MFBz, *o*-DFBz, *m*-DFBz and PFBz are carried out along the dimensionless normal coordinates of their 30 vibrational degrees of freedom. Hereafter, these electronic states are designated as S_0, S_1, S_2, S_3, $\cdots$ etc. in the order of increasing energy at the reference equilibrium geometry of the S_0 state. The VEEs of these electronic states are calculated for $Q_i = \pm 0.25$ (0.25) ± 1.00 and ± 1.00 (0.50) ± 3.00, along i^{th} vibrational mode (keeping others at their equilibrium value) using the EOM-CCSD method as implemented in MOLPRO program package [165]. While the aug-cc-pVDZ basis set [155] used for carbon and fluorine atoms, the hydrogen atoms are described by the standard cc-pVDZ basis set [155] for MFBz, *o*-DFBz and *m*-DFBz. For PFBz (having 41 occupied MOs) use of a basis set as described above turned out to be computationally very expensive. Therefore, for PFBz we used energy-consistent pseudopotentials of Stuttgart/Cologne group [168] for the fluorine atoms in addition to the basis set as described above for the carbon and hydrogen atoms. These pseudopotentials include one component (non-relativistic and scalar-relativistic) effective-core potentials (ECP). Two 1s electrons of the fluorine atoms are treated as core electron and are described by the pseudopotential. The advantage of this pseudopotential method is that it restricts the explicit quantum chemical treatment to the valence shell, while the effects of the core shells are simulated by the pseudopotentials. This causes a drastic reduction of the computational cost without compromising the accuracy to a significant extent as compared to the all-electron calculations.

While the computational overheads restrict the use of larger basis sets for these molecular systems, we however, examined the basis set dependencies of the results whenever possible. For example, the MFBz and PFBz molecules have been studied with somewhat larger basis sets in order to add to the reliability of the results presented in this chapter. To this effort, the aug-cc-pVDZ basis set used for MFBz is replaced by the aug-cc-pVTZ basis. The computational time thereby increases six fold. The results obtained on the VEEs at the reference

geometry of the S_0 state are summarized in the first half of Table 5.7. It can be seen from the data presented in this table that the deviations are within the acceptable limit of accuracy. Next, in order to establish a reliable basis for using ECPs for fluorine atoms, we have done test calculations of the VEEs of the low-lying electronic states of PFBz with and without ECPs. The results are tabulated in the second half of Table 5.7. It can be seen from Table 5.7 that the change in VEEs for all five states are very minor (the average deviation is ∼0.034 eV), indicating the reliability of ECPs to describe the excited state PESs of PFBz.

Table 5.7: Basis set dependencies of the vertical excitation energies (VEEs) of the low-lying excited singlet states of MFBz and PFBz. VEEs are in eV.

Molecule	State symmetry	aug-cc-pVDZ	aug-cc-pVTZ	ECP
MFBz	$^1B_2$ (S_1)	5.055	5.049	
	$^1A_1$ (S_2)	6.469	6.412	
	$^1B_1$ (S_3)	6.724	6.724	
	$^1B_2$ (S_4)	7.288	7.267	
	$^1A_1$ (S_5)	7.317	7.290	
PFBz	$^1B_2$ (S_1)	5.142		5.111
	$^1B_1$ (S_2)	6.244		6.314
	$^1A_1$ (S_3)	6.618		6.597
	$^1A_1$ (S_4)	7.495		7.475
	$^1B_2$ (S_5)	7.537		7.509

5.3 The vibronic Hamiltonian

In order to perform the quantum dynamical studies we first construct the required vibronic Hamiltonians for the low-lying excited singlet electronic states of the fluorobenzene molecules introduced above. The Hamiltonian is constructed in terms of dimensionless normal coordinates of the vibrational modes and is based on a diabatic ansatz for the electronic basis [100].

The 30 vibrational degrees of freedom of the four fluorobenzene molecules de-

compose into the following irreducible representations (IREPs) of the C_{2v} equilibrium symmetry point group.

$$\begin{aligned} MFBz, m-DFBz, PFBz: &\quad \Gamma_{vib} = 11a_1 \oplus 6b_1 \oplus 10b_2 \oplus 3a_2 \\ o-DFBz: &\quad \Gamma_{vib} = 11a_1 \oplus 4b_1 \oplus 10b_2 \oplus 5a_2 \end{aligned} \tag{5.1}$$

The diabatic vibronic Hamiltonian in the normal coordinates of these vibrational modes can be written as

$$\mathcal{H} = \mathcal{H}_0 \mathbf{1_5} + \mathcal{W}_x, \tag{5.2}$$

where $\mathcal{H}_0$ defines the Hamiltonian of the reference ground (S_0) electronic state which is assumed to be harmonic, $\mathcal{H}_0 = \frac{1}{2}\sum_s \omega_s(-\frac{\partial^2}{\partial Q_s^2} + Q_s^2)$. The quantity $\mathbf{1_5}$ is a 5×5 diagonal unit matrix. The nondiagonal matrix Hamiltonian $\mathcal{W}_x$ describes the PESs of the excited electronic states and their coupling surfaces. The elements of this matrix are expanded in a Taylor series around the reference equilibrium geometry at **Q=0**. Employing the symmetry selection rule, the electronic Hamiltonian matrices for the four fluorobenzene molecules are given by

$$\mathcal{W}_{MFBz} = \begin{pmatrix} E^1 + \mathcal{U}^1 & \sum\limits_{s\in b_2} \lambda_s^{1,2} Q_s & \sum\limits_{s\in a_2} \lambda_s^{1,3} Q_s & 0 & \sum\limits_{s\in b_2} \lambda_s^{1,5} Q_s \\ & E^2 + \mathcal{U}^2 & \sum\limits_{s\in b_1} \lambda_s^{2,3} Q_s & \sum\limits_{s\in b_2} \lambda_s^{2,4} Q_s & 0 \\ & & E^3 + \mathcal{U}^3 & \sum\limits_{s\in a_2} \lambda_s^{3,4} Q_s & \sum\limits_{s\in b_1} \lambda_s^{3,5} Q_s \\ & h.c. & & E^4 + \mathcal{U}^4 & \sum\limits_{s\in b_2} \lambda_s^{4,5} Q_s \\ & & & & E^5 + \mathcal{U}^5 \end{pmatrix} \tag{5.3a}$$

$$\mathcal{W}_{o-DFBz} = \begin{pmatrix} E^1+\mathcal{U}^1 & \sum_{s\in b_2}\lambda_s^{1,2}Q_s & \sum_{s\in b_1}\lambda_s^{1,3}Q_s & \sum_{s\in b_2}\lambda_s^{1,4}Q_s & 0 \\ & E^2+\mathcal{U}^2 & \sum_{s\in a_2}\lambda_s^{2,3}Q_s & 0 & \sum_{s\in b_2}\lambda_s^{2,5}Q_s \\ & & E^3+\mathcal{U}^3 & \sum_{s\in a_2}\lambda_s^{3,4}Q_s & \sum_{s\in b_1}\lambda_s^{3,5}Q_s \\ & h.c. & & E^4+\mathcal{U}^4 & \sum_{s\in b_2}\lambda_s^{4,5}Q_s \\ & & & & E^5+\mathcal{U}^5 \end{pmatrix} \quad (5.3b)$$

$$\mathcal{W}_{m-DFBz} = \begin{pmatrix} E^1+\mathcal{U}^1 & \sum_{s\in b_2}\lambda_s^{1,2}Q_s & \sum_{s\in b_2}\lambda_s^{1,3}Q_s & 0 \\ & E^2+\mathcal{U}^2 & 0 & \sum_{s\in b_2}\lambda_s^{2,4}Q_s \\ h.c. & & E^3+\mathcal{U}^3 & \sum_{s\in b_2}\lambda_s^{3,4}Q_s \\ & & & E^4+\mathcal{U}^4 \end{pmatrix}, \quad (5.3c)$$

$$\mathcal{W}_{PFBz} = \begin{pmatrix} E^1+\mathcal{U}^1 & \sum_{s\in a_2}\lambda_s^{1,2}Q_s & \sum_{s\in b_2}\lambda_s^{1,3}Q_s & \sum_{s\in b_2}\lambda_s^{1,4}Q_s & 0 \\ & E^2+\mathcal{U}^2 & \sum_{s\in b_1}\lambda_s^{2,3}Q_s & \sum_{s\in b_1}\lambda_s^{2,4}Q_s & \sum_{s\in a_2}\lambda_s^{2,5}Q_s \\ & & E^3+\mathcal{U}^3 & 0 & \sum_{s\in b_2}\lambda_s^{3,5}Q_s \\ & h.c. & & E^4+\mathcal{U}^4 & \sum_{s\in b_2}\lambda_s^{4,5}Q_s \\ & & & & E^5+\mathcal{U}^5 \end{pmatrix} \quad (5.3d)$$

In Eqs. 5.3a-5.3d, $\mathcal{U}^i = \sum_{s\in a_1} \kappa_s^i Q_s + \frac{1}{2}\sum_{s\in a_1} \gamma_s^i Q_s^2$. E^i is the vertical excitation energy of the i^{th} excited electronic state; κ_s^i and $\lambda_s^{i,j}$ represents the linear intrastate and interstate coupling parameters [4], respectively; γ_s^i denotes the second-order coupling parameter along totally symmetric vibrations of the i^{th} state. The summations run over the normal modes of vibration of specified symmetry. The vibrational modes entering the various coupling terms i.e., diagonal and off-diagonal matrix elements, are in accordance with the symmetry rule. Note that for *m*-DFBz the S_5 state is located at high energies and therefore, not included in Eq. 5.3c. The VEEs calculated in Sec. 5.2 describe the adiabatic potential energies of the excited singlet states of the four fluorobenzene molecules. These energies are fitted to the adiabatic form of diabatic electronic Hamiltonian of Eqs. (5.3a-5.3d) by a least squares procedure to estimate the coupling parameters. These parameters for various vibrational modes are given in Tables 5.8-5.11. A careful examination of the coupling parameters suggests that not all 30 vibrational degrees of freedom play significant role in the vibronic coupling mechanism. Therefore, the relevant modes having significant coupling strengths are retained only in Tables 5.8-5.11 for clarity. Such considerations result 18 nonseparable vibrational degrees of freedom in case of MFBz, 22 in case of *o*-DFBz, 15 in case of *m*-DFBz and 26 in case of PFBz.

Table 5.8: *Ab initio* calculated coupling parameters of the electronic Hamiltonian [cf., Eq. 5.3a] of MFBz. All quantities are in eV.

Symmetry	Mode	κ_s^1	γ_s^1	κ_s^2	γ_s^2	κ_s^3	γ_s^3	κ_s^4	γ_s^4	κ_s^5	γ_s^5
	ν_6	-0.0980	0.0009	-0.0824	-0.0111	-0.0507	-0.0138	-0.0908	0.0008	-0.0935	0.0079
	ν_7	0.0360	0.0035	0.0376	-0.0212	0.0858	-0.0046	0.0349	-0.0010	0.0294	0.0110
	ν_8	-0.0836	-0.0030	-0.0672	-0.0041	-0.0032	-0.0005	-0.0703	-0.0085	-0.0772	-0.0072
a_1	ν_9	0.1080	0.0000	0.0896	-0.0027	0.0400	-0.0067	0.0961	-0.0058	0.0995	-0.0042
	ν_{10}	-0.0864	-0.0023	-0.0527	-0.0053	-0.0212	-0.0090	-0.0339	-0.0066	-0.0698	-0.0029
	ν_{11}	-0.0136	-0.0129	-0.0210	-0.0060	-0.0826	-0.0077	0.0337	-0.0024	-0.0082	-0.0020
			λ_s^{1-2}	λ_s^{1-3}	λ_s^{1-5}	λ_s^{2-3}	λ_s^{2-4}	λ_s^{3-4}	λ^{3-5}	λ^{4-5}	
	ν_{12}					0.0529			0.4175		
	ν_{13}					0.0635					
b_1	ν_{14}					0.0505			0.0428		
	ν_{16}					0.0674			0.0914		
	ν_{17}					0.0476					
	ν_{20}		0.0000		0.2356		0.2254			0.0518	
	ν_{24}		0.0000		0.0112		0.0663				
b_2	ν_{26}		0.0648		0.1123		0.0347			0.0062	
	ν_{27}		0.0235		0.0147		0.0101				
	ν_{28}			0.1656				0.0362			
a_2	ν_{29}			0.1259				0.0273			
	ν_{30}			0.1278							

Table 5.9: Same as in Table 5.8 of the electronic Hamiltonian [Eq. 5.3b] of *o*-DFBz.

Symmetry	Mode	κ_i^1	γ_i^1	κ_i^2	γ_i^2	κ_i^3	γ_i^3	κ_i^4	γ_i^4	κ_i^5	γ_i^5
	ν_3	0.0160	0.0044	-0.1161	-0.0423	-0.1389	-0.0310	-0.1802	0.0267	0.0109	-0.0022
	ν_4	-0.0498	-0.0031	-0.0437	-0.0081	-0.0492	-0.0210	-0.0424	-0.0021	-0.0352	-0.0139
	ν_6	0.1180	0.0032	0.1066	-0.0054	0.0504	-0.0170	0.1124	0.0076	0.1120	-0.0006
	ν_7	-0.0271	0.0054	-0.0216	-0.0094	-0.0527	-0.0146	-0.0312	0.0129	-0.0235	0.0020
a_1	ν_8	0.0991	-0.0013	0.0865	-0.0029	-0.0071	-0.0030	0.0960	-0.0046	0.0984	-0.0065
	ν_9	-0.1077	-0.0020	-0.0655	-0.0036	-0.0656	-0.0302	-0.0607	-0.0048	-0.0791	-0.0030
	ν_{10}	0.0238	-0.0020	-0.0150	-0.0052	0.0664	-0.0148	-0.0224	-0.0034	-0.0193	-0.0010
	ν_{11}	-0.0055	-0.0004	-0.0014	-0.0005	-0.0152	0.0083	0.0021	0.0008	0.0021	-0.0005

		λ_s^{1-2}	λ_s^{1-3}	λ_s^{1-4}	λ_s^{2-3}	λ_s^{2-5}	λ_s^{3-4}	λ^{3-5}	λ^{4-5}
	ν_{12}		0.1709					0.0000	
	ν_{13}		0.1225					0.0000	
b_1	ν_{14}		0.1341					0.0000	
	ν_{15}		0.1100					0.0000	
	ν_{18}	0.0000		0.0000		0.2648			0.0667
	ν_{21}	0.0000		0.0000		0.1058			0.0211
b_2	ν_{23}	0.0000		0.0000		0.0457			0.0189
	ν_{24}	0.0228		0.0000		0.0529			0.0180
	ν_{25}	0.0000		0.0000		0.0624			0.0188
	ν_{26}				0.0631		0.0000		
	ν_{27}				0.0556		0.0000		
a_2	ν_{28}				0.0829		0.0000		
	ν_{29}				0.0729		0.0399		
	ν_{30}				0.0507		0.0000		

Table 5.10: Same as in Table 5.8 of the electronic Hamiltonian [Eq. 5.3c] of *m*-DFBz.

Symmetry	Mode	κ_s^1	γ_s^1	κ_s^2	γ_s^2	κ_s^3	γ_s^3	κ_s^4	γ_s^4
	ν_4	-0.0128	0.0063	-0.0975	-0.0421	0.1353	0.0536	-0.0121	-0.0047
	ν_5	-0.0285	-0.0068	-0.0410	-0.0199	0.0433	-0.0045	-0.0311	-0.0147
	ν_6	-0.1137	-0.0023	-0.1064	-0.0036	-0.1174	-0.0016	-0.1100	-0.0011
a_1	ν_7	0.0360	-0.0041	0.0271	-0.0112	0.0190	0.0028	0.0301	-0.0056
	ν_8	0.1171	0.0000	0.1024	-0.0025	0.1131	-0.0045	0.1130	-0.0027
	ν_9	-0.0918	-0.0044	-0.0467	-0.0063	-0.0353	-0.0035	-0.0559	-0.0030
	ν_{10}	-0.0124	-0.0059	0.0107	-0.0060	0.0175	-0.0036	0.0222	-0.0003

		λ_s^{1-2}	λ_s^{1-3}	λ_s^{2-4}	λ_s^{3-4}
	ν_{19}	0.0000	0.0000	0.2605	0.0666
	ν_{20}	0.0000	0.0000	0.0490	0.0167
	ν_{22}	0.0000	0.0000	0.0535	0.0167
	ν_{23}	0.0000	0.0000	0.0743	0.0210
b_2	ν_{24}	0.0000	0.0000	0.0370	0.0120
	ν_{25}	0.0000	0.0000	0.0353	0.0150
	ν_{26}	0.0000	0.0525	0.0698	0.0244
	ν_{27}	0.0000	0.0000	0.0501	0.0096

Table 5.11: Same as in Table 5.8 of the electronic Hamiltonian [Eq. 5.3d] of PFBz.

Symmetry	Mode	κ_s^1	γ_s^1	κ_s^2	γ_s^2	κ_s^3	γ_s^3	κ_s^4	γ_s^4	κ_s^5	γ_s^5
	ν_2	-0.0130	0.0080	0.1411	-0.0231	-0.1080	-0.0360	-0.0208	-0.0001	-0.0062	-0.0027
	ν_3	-0.0771	0.0009	0.0850	-0.0380	-0.0804	-0.0098	-0.0810	-0.0126	-0.0897	-0.0140
	ν_4	0.1280	0.0001	-0.0220	-0.0098	0.1163	-0.0085	0.1128	-0.0006	0.1068	-0.0050
	ν_5	0.0344	-0.0017	0.0375	-0.0162	0.0282	-0.0075	0.0163	0.0014	0.0196	-0.0039
	ν_6	-0.0209	-0.0032	0.0395	-0.0199	-0.0240	-0.0081	-0.0243	-0.0002	-0.0409	-0.0070
a_1	ν_7	0.0801	-0.0022	0.0190	-0.0085	0.0560	-0.0060	0.0600	-0.0046	0.0751	-0.0034
	ν_8	-0.0851	0.0007	-0.0371	-0.0144	-0.0550	-0.0012	-0.0626	-0.0028	-0.0650	-0.0017
	ν_9	-0.0116	-0.0088	0.0697	-0.0136	0.0235	-0.0095	0.0245	-0.0017	0.0293	-0.0002
	ν_{10}	0.0089	-0.0002	0.0273	-0.0085	0.0025	-0.0012	0.0028	-0.0013	0.0038	-0.0017
	ν_{11}	-0.0124	-0.0020	-0.0434	-0.0026	0.0031	-0.0024	0.0032	-0.0016	-0.0343	0.0051
			λ_s^{1-2}	λ_s^{1-3}	λ_s^{1-4}	λ_s^{2-3}	λ_s^{2-4}	λ_s^{2-5}	λ^{3-5}		λ^{4-5}
	ν_{12}					0.0994	0.2049				
	ν_{13}					0.0747	0.2010				
	ν_{14}					0.0464	0.2491				
b_1	ν_{15}					0.0144	0.2607				
	ν_{16}					0.0243	0.1810				
	ν_{17}					0.0860	0.2229				
	ν_{18}			0.0000	0.0000				0.2919	0.0703	
	ν_{19}			0.0000	0.0000				0.0854	0.0059	
	ν_{20}			0.0000	0.0000				0.1113	0.0200	
	ν_{21}			0.0000	0.0000				0.0907	0.0146	
b_2	ν_{22}			0.0000	0.0000				0.0830	0.0155	
	ν_{25}			0.0000	0.0000				0.1028	0.0311	
	ν_{26}			0.0000	0.0000				0.0370	0.0080	
	ν_{27}			0.0000	0.0000				0.0390	0.0095	
	ν_{28}		0.1401					0.1640			
a_2	ν_{29}		0.1153					0.2376			
	ν_{30}		0.0388					0.1126			

It can be seen from the data in Tables 5.8-5.11 that the linear coupling parameters are of crucial importance to describe the potential energy surfaces and the coupling surfaces of the diabatic electronic states. We have considered the second-order coupling parameters also for the totally symmetric modes. How the coupling constants obtained numerically and how well the quadratic coupling model reproduces the *ab initio* data points are typically illustrated in Fig. 5.5. It displays the *ab initio* data points in comparison with the corresponding potential energy curves (full lines) obtained from the quadratic model. A representative vibrational mode of a_1 symmetry has been chosen for all four molecules. The deviations of the model curves from the *ab initio* points can be seen to be very minor. The quadratic model seems to have some effects in case of PFBz. Importance of the quadratic terms in the vibronic dynamics has been discussed in the literature [169]. These illustrations also confirm the minor importance of the further higher-order (cubic and quartic) coupling parameters and indicate that the quadratic model as adopted in Eqs. (5.3a-5.3d) provides reliable description of the vibronic interactions in the four molecules considered here.

5.4 Potential energy surfaces of the ground and excited electronic states

It is worthwhile to examine the topography of the electronic states of the four fluorobenzene molecules considered here in order to understand the nuclear dynamics on them. This will allow to unravel the complex spectral features recorded in the experiment and the relaxation mechanism of these electronic states. The adiabatic potential energy surfaces can be obtained by diagonalizing the electronic Hamiltonian of the diabatic model developed above in section 5.3. How well these model adiabatic potential energy functions reproduce the computed *ab initio* data is typically illustrated in Fig. 5.6-5.9 for all four molecules. These

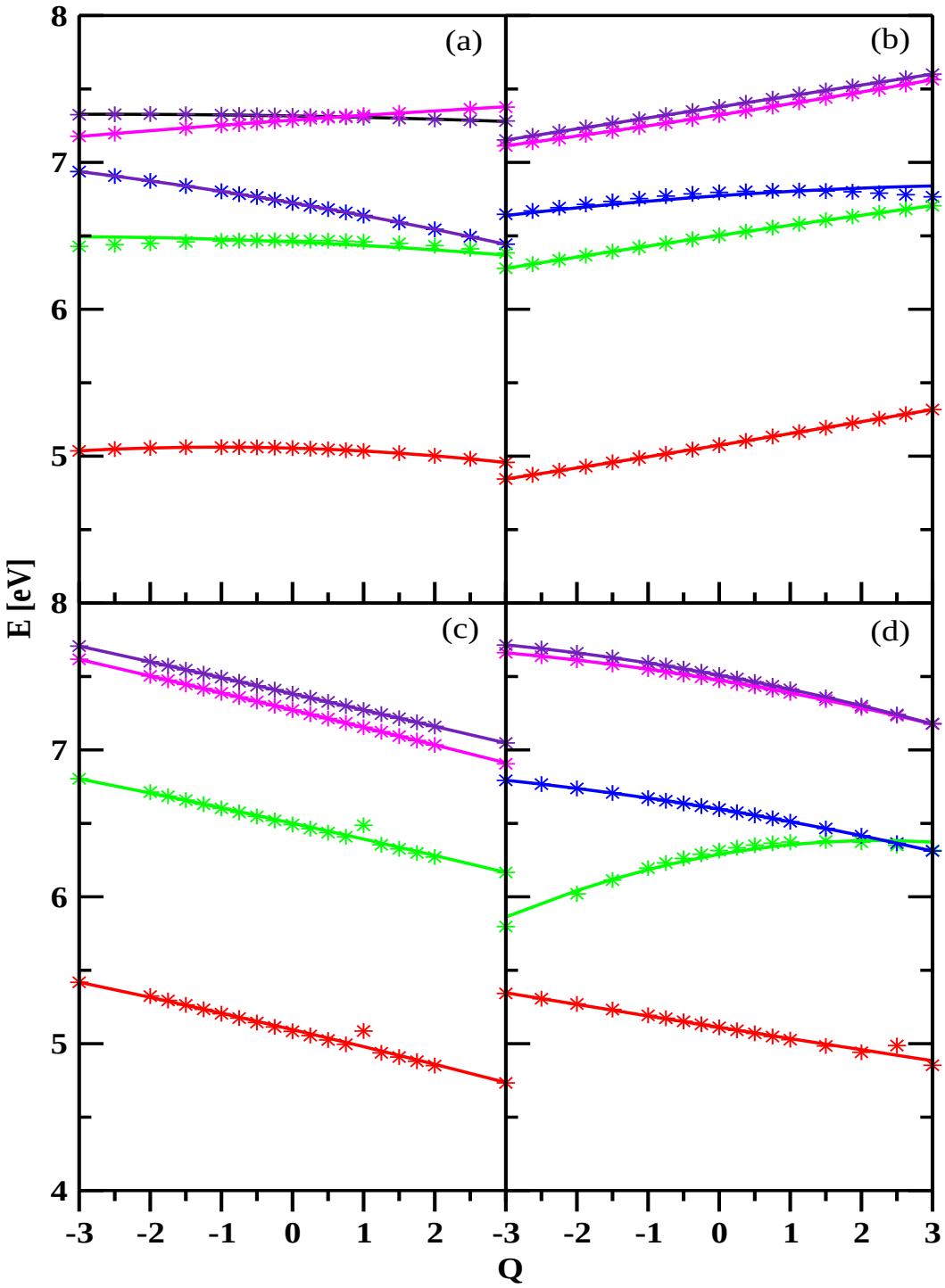

Figure 5.5: Quadratic fit (full lines) to the *ab initio* calculated VEEs (asterisks) for (a) MFBz, (b) *o*-DFBz, (c) *m*-DFBz and (d) PFBz along a representative vibrational mode of a_1 symmetry.

represent one dimensional cuts of the multidimensional potential potential energy hypersurface plotted along the dimensionless normal coordinates of symmetric vibrational mode indicated in each panel. In these figures the solid curves represent the adiabatic potential energies from the model and the points superimposed on them are obtained from *ab initio* quantum chemical calculations as discussed above.

Table 5.12: Energy (eV) of the equilibrium minimum (diagonal entry) and minimum of the seam of the CIs (off-diagonal entry) of various electronic states of MFBz, *o*-DFBz, *m*-DFBz and PFBz molecules.

$MFBz$

	s_1	s_2	s_3	s_4	s_5
s_1		61.36	12.03	45.47	> 100
s_2		6.38	6.74	13.13	47.22
s_3			6.63	7.46	7.69
s_4				7.19	7.20
s_5					7.20

$o-DFBz$

	s_1	s_2	s_3	s_4	s_5
s_1		30.18	8.75	16.21	80.60
s_2		6.41	6.77	19.60	11.57
s_3			6.64	7.40	7.53
s_4				7.14	7.26
s_5					7.26

$m-DFBz$

	s_1	s_2	s_3	s_4
s_1		20.58	18.81	87.43
s_2		6.37	7.69	16.79
s_3			7.12	7.29
s_4				7.27

$PFBz$

	s_1	s_2	s_3	s_4	s_5
s_1		6.92	19.17	86.73	76.83
s_2		6.19	6.47	8.32	8.32
s_3			6.47	17.66	14.00
s_4				7.36	7.39
s_5					7.38

In Fig. 5.6 the potential energy cuts of the ground and five low-lying excited electronic states of MFBz molecule are shown. The S_0 state is vertically well separated from the rest. This also holds for the remaining three molecules [cf., Figs 5.7-5.9]. It can be seen from Fig. 5.6 that for MFBz S_1 state is well separated from the next higher ones. The electronic states S_2, S_3, S_4 and S_5 on the other hand exhibit quasi-degeneracy or even curve crossings. These curve crossings develop into CIs of potential energy surfaces in multidimensions. En-

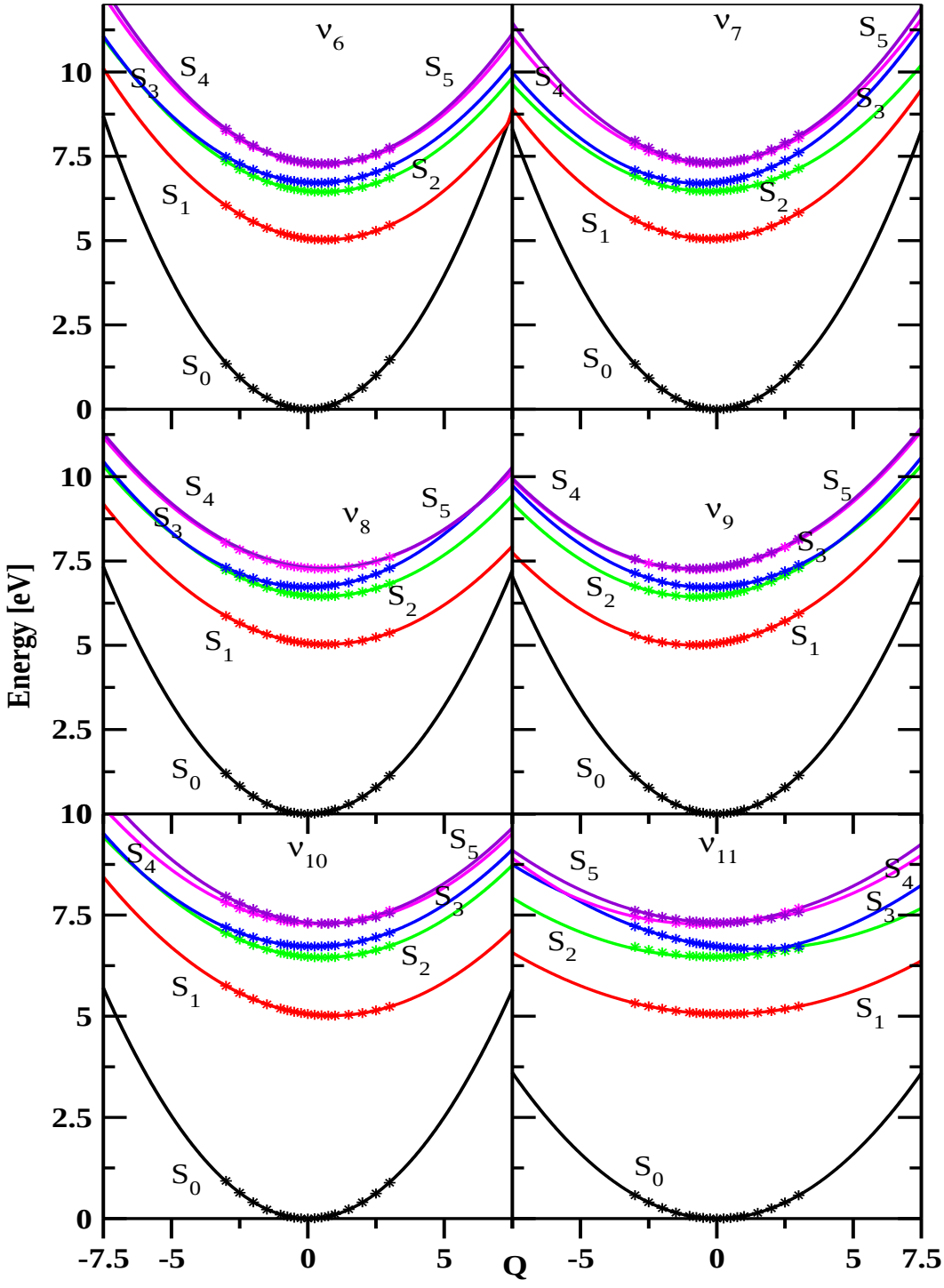

Figure 5.6: Adiabatic potential energies of ground and low-lying excited singlet states of MFBz, along the normal coordinates of totally symmetric vibrational modes. The potential energies obtained from the present vibronic model are shown by the solid lines and the computed *ab initio* data are shown by the asterisks.

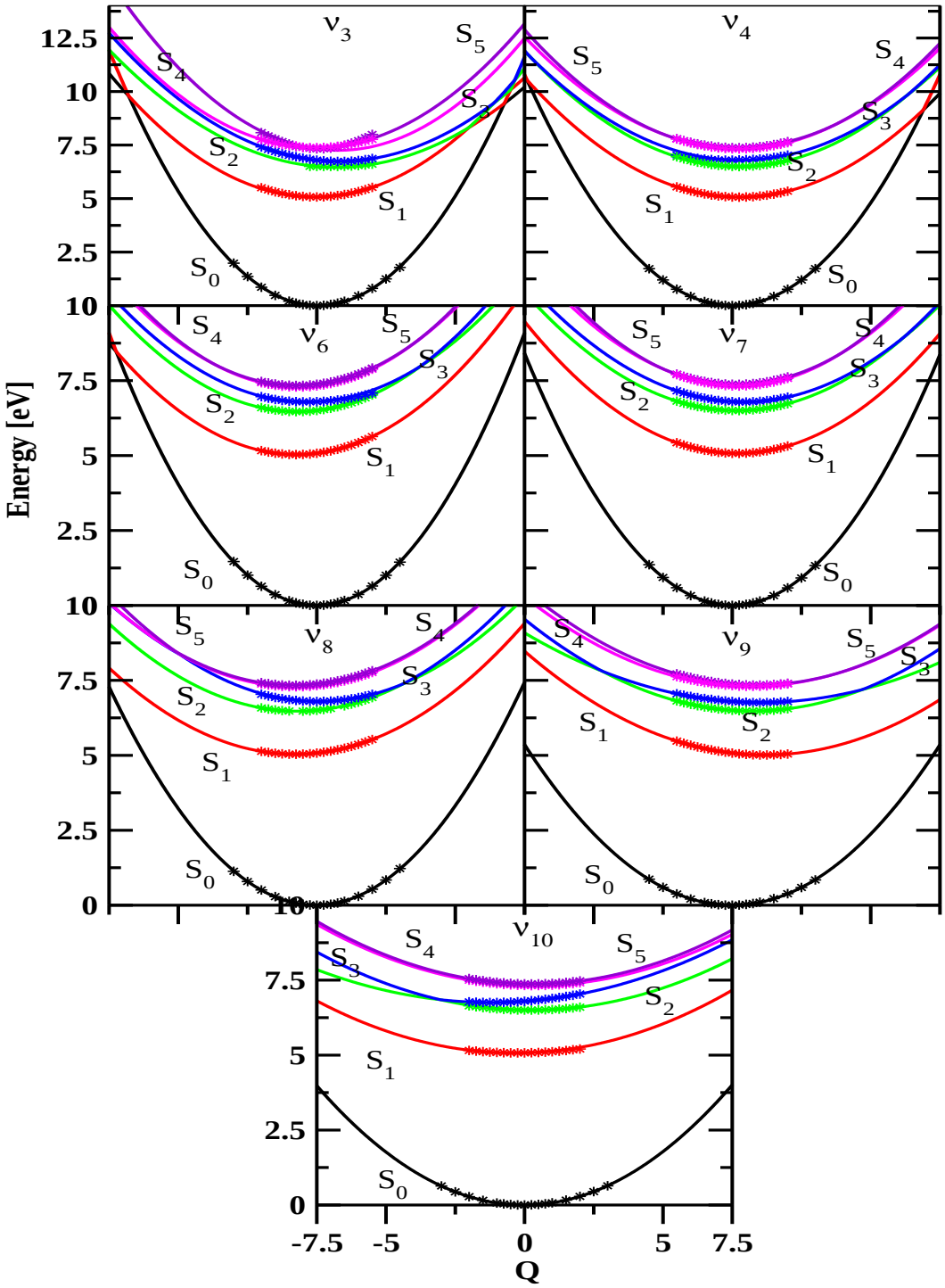

Figure 5.7: Same as in Fig. 5.6 for *o*-DFBz.

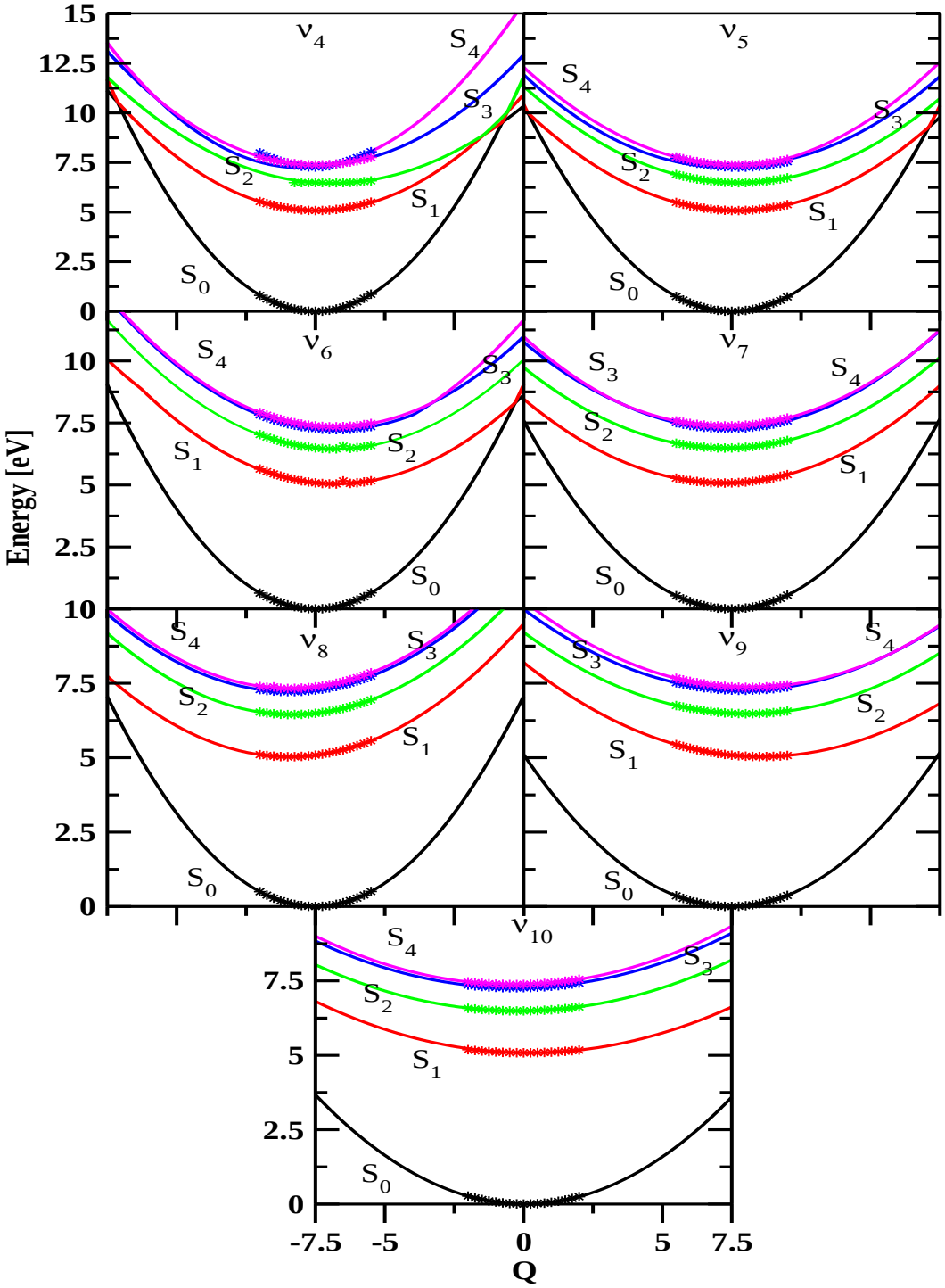

Figure 5.8: Same as in Fig. 5.6 for *m*-DFBz.

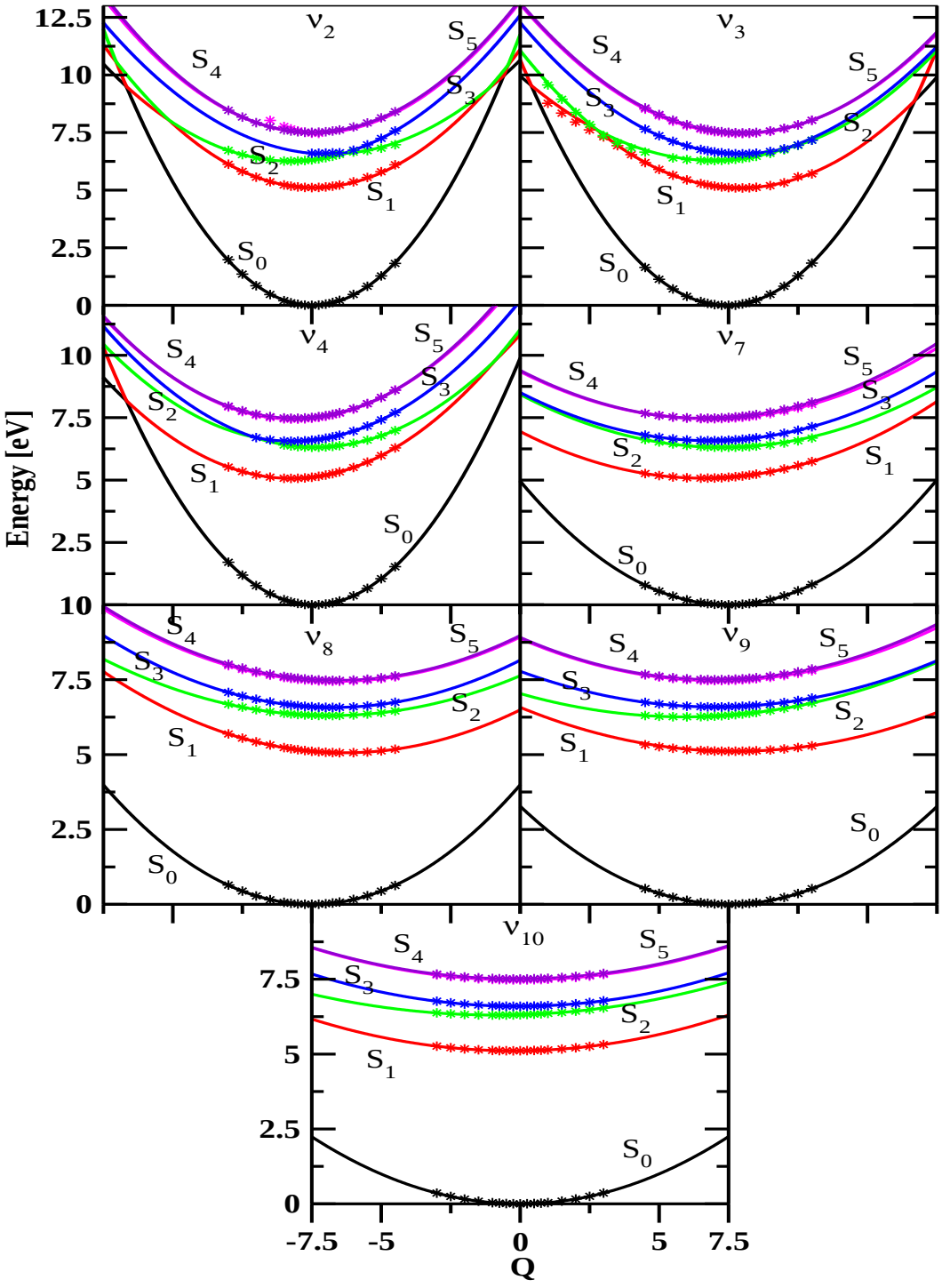

Figure 5.9: Same as in Fig. 5.6 for PFBz.

ergetic minimum of the seam of these CIs plays decisive role in the dynamical evolution of the corresponding state. The energetic location of the minimum of the seam (off-diagonal entries) and equilibrium minimum of the states involved (diagonal entries) for all four molecules are calculated within LVC scheme and given in Table 5.12. When the quadratic terms are included in this calculations, the equations become highly nonlinear (see Ref [160] and appendix of this thesis). Understandably, the solution is ambiguous in this case. But we carried out additional calculations using MATHEMATICA package to check the reproducibility of these numbers by including the quadratic terms and some of the stable solutions are indeed very similar to the numbers given in Table 5.12. These numbers are tabulated in Table 5.13.

Table 5.13: Comparison of the minimum of the seam of the CIs of various electronic states of MFBz, *o*-DFBz, *m*-DFBz and PFBz (in eV) between LVC and QVC scheme.

Molecule	Seam of the CIs of various electronic states	Numbers obtained in LVC scheme	Numbers obtained including quadratic terms
MFBz	S_2-S_3	6.74	7.05
	S_3-S_4	7.46	7.49
	S_3-S_5	7.69	7.66
	S_4-S_5	7.20	7.26
o-DFBz	S_2-S_3	6.77	6.66
	S_3-S_4	7.40	7.65
	S_4-S_5	7.26	7.26
m-DFBz	S_3-S_4	7.29	7.27
PFBz	S_1-S_2	6.92	6.35
	S_2-S_3	6.47	6.46
	S_4-S_5	7.39	7.38

It can be seen from Table 5.12 that for MFBz the minimum of the crossing of the S_1 state with others occurs at very high energies. The minimum of the S_2-S_3 CIs occurs only ∼0.36 eV and ∼0.11 eV above the minimum of the S_2 and S_3 state, respectively. The minimum of the S_3-S_4 CIs occurs ∼0.83 eV and ∼0.27

eV above the minimum of the S_3 and S_4 state, respectively. S_3 also undergoes low-energy curve crossings with S_5. The minimum of the S_3-S_5 CIs occurs ∼1.06 eV and ∼0.49 eV above the minimum of the S_3 and S_5 state, respectively. The S_4 and S_5 states are quasi-degenerate around their equilibrium geometry. The minimum of the S_4-S_5 CIs occurs at or very near to the equilibrium minimum of these states. The importance of these energy data in the mechanistic details of nuclear dynamics is discussed in subsequent section.

The situation is very similar in *o*-DFBz [cf., Fig. 5.7] and *m*-DFBz [cf., Fig. 5.8]. Like in MFBz the S_1 state is well separated from the next higher ones in these molecules also. The CIs of S_1 with others occur at higher energies (cf., Table 5.12). In *o*-DFBz S_2-S_3 CIs, like in MFBz, occur ∼0.36 eV and ∼0.13 eV above the minimum of the S_2 and S_3 state, respectively. The CIs between S_3-S_4, S_3-S_5 and S_4-S_5 occur close to the minimum of the respective interacting states. Analogous situation is also observed for *m*-DFBz [cf., Fig. 5.8 and Table 5.12]. Unlike MFBz and *o*-DFBz, in this case the S_2-S_3 CIs occur at higher energy; ∼1.32 eV and ∼0.57 eV above the minimum of the S_2 and S_3 state, respectively. The energetic locations of the other CIs in *m*-DFBz are nearly identical to those in the MFBz and *o*-DFBz.

The situation is very much different in case of PFBz as illustrated in Fig. 5.9. In this case energies of most of the CIs are lowered compared to the other three discussed above (cf., Table 5.12). It can be seen that the S_1 and S_2 state also cross in PFBz and the energetic minimum of the corresponding CIs occurs at ∼6.92 eV, which is only ∼0.73 eV above the S_2 minimum. The S_2-S_3 CIs occur only ∼0.28 eV above the S_2 minimum and it nearly coincides with the S_3 minimum. The S_4 and S_5 states are quasi-degenerate and their CIs occur very close to their equilibrium minimum. We add that the S_1-S_2 CIs are accessible and significantly contribute to the nuclear dynamics in the S_1-S_2 interacting electronic state of PFBz within the energy range of the present study.

In summary, for all four molecules (discussed above) excited electronic states

are energetically well separated from the S_0 state. The S_1 state undergoes crossing with the S_2 state at very high energies in MFBz, *o*-DFBz and *m*-DFBz. This crossing occurs at much lower energy in PFBz and expected to have noticeable impact on the vibronic structure of these electronic states. For all molecules several low-energy (within 8.0 eV) CIs are established for the S_2 and further higher excited states. These intersections are expected to be the crucial bottleneck controlling the nuclear dynamics in the excited states of these fluorobenzene molecules.

5.5 Optical absorption below 8 eV and perfluoro effect

At this point it is important to discuss a few stringent issues on the optical absorption of the singlet states of all four molecules mentioned above. The electronic structure data presented seem to be accurate enough to interpret and understand the experimental results discussed in the next section. A more pertinent question addressed here is how the increased fluorination modifies the electronic energy and causes a dramatic change in the dynamical outcome of the first two excited states of these benzene derivatives? Fig. 5.10 portrays the nature and energies of the excited electronic states of benzene and its fluoroderivatives within 8.0 eV.

The energies are calculated at the equilibrium geometry of the respective S_0 state. It can be seen that the energy of the two lowest $\pi\pi^*$ states exhibit only mild variation however, the energy of the two lowest $\pi\sigma^*$ states decreases significantly upon increasing fluorination. The first $\pi\sigma^*$ state is formed by the promotion of ring π electron to the σ^* orbital localized on the C-C bond whereas, the second one is due to promotion of similar π electron to the σ^* orbital localized predominantly on the C-F bond. A Mulliken population analysis results (within the present level of theoretical treatment) confirm these designations. The second

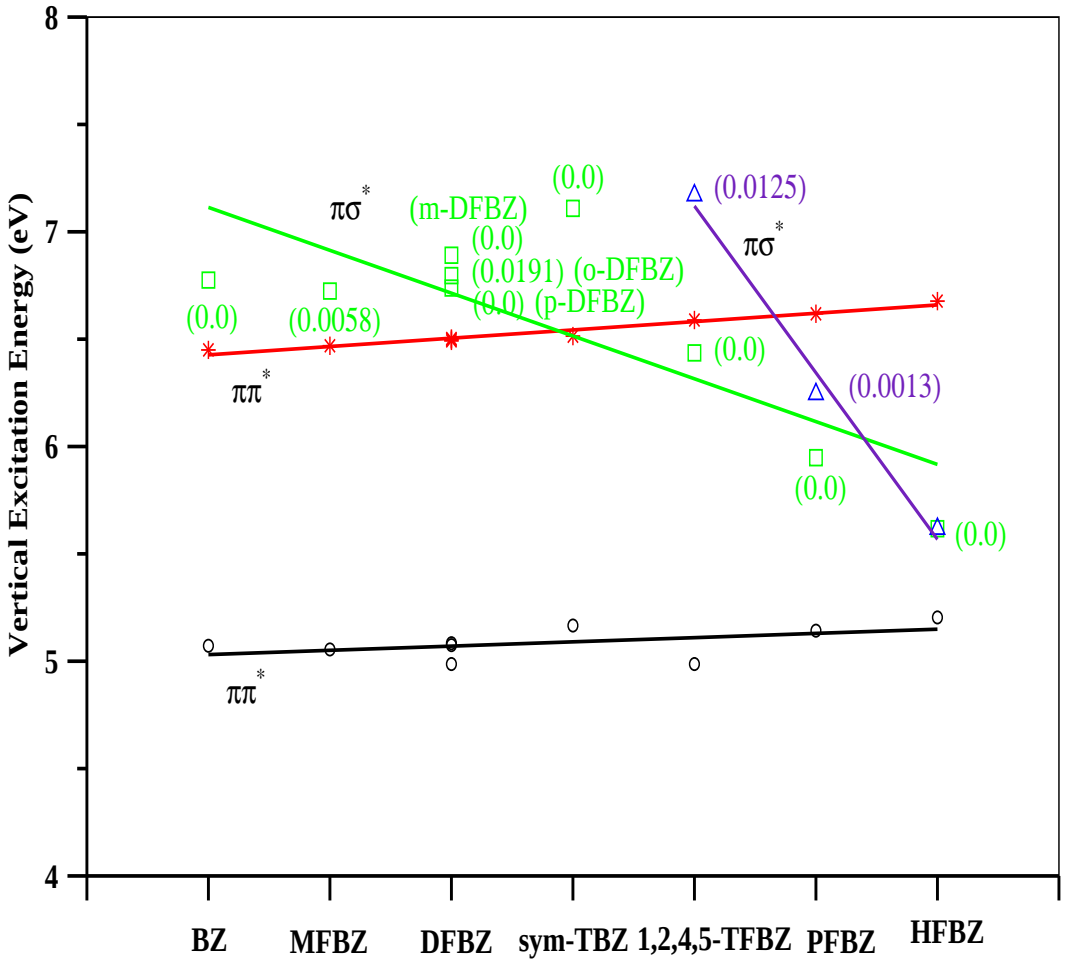

Figure 5.10: The VEEs of the first four low-lying electronic states of fluorobenzene molecules obtained at the reference equilibrium geometry of the respective S_0 state. Some of the oscillator strengths are given in the parenthesis (see text). The abbreviations TBz and TFBz refer to tri-fluorobenzene and tetra-fluorobenzene, respectively.

type of $\pi\sigma^*$ state occurs above 8.0 eV for MFBz and DFBz (not shown in Fig. 5.10 for brevity) and the two $\pi\sigma^*$ states are degenerate in HFBz. The oscillator strengths of the two $\pi\sigma^*$ states are given in the parenthesis in Fig. 5.10. The data provided therein reveal that the second excited state (S_2) in PFBz is of $\pi\sigma^*$ type localized on the C-F bond, since the one localized on the C-C bond has zero oscillator strength. It is seen in Fig. 5.9 that this state undergoes crossing with the S_1 state in PFBz. For molecules with less than five fluorine atom the S_2 state (with nonzero oscillator strength) is however energetically well separated from the S_1 state. Therefore, transition from a structured $S_1 \leftarrow S_0$ absorption band to a blurred and diffused one with increasing fluorination can be attributed to the appearance of the low energy $S_1(\pi\pi^*)$ - $S_2(\pi\sigma^*)$ [σ^* localized on the C-F bond] conical intersections. It is already seen in Table 5.12 that minimum energy of this intersection is substantially lowered in PFBz with respect to the other three molecules considered here.

To this end it is worthwhile to compare the presented data to those available in the literature. Zgierski and co-workers [89] have predicted the lowering of the $\pi\sigma^*$ state [with σ^* localized on the C-F bond] energy with increasing fluorination through time-dependent density functional theory calculations. Their results show that this $\pi\sigma^*$ state becomes nearly degenerate with the lowest $\pi\pi^*$ (C-C) state in PFBz and becomes the LUMO in case of HFBz. A similar observation was also made by Studzinski *et al.* [170]. By comparing the features observed in the fluorescence and absorption spectra of jet cooled PFBz and HFBz with others with less number of fluorine atoms and also supported by their electronic structure data Zgierski and co-workers concluded that the S_1 state of the former molecules deserves a $\pi\sigma^*$ assignment [89]. This assignment differs from that of Holland and co-workers [171] who established with the aid of a combined experimental and computational study that the LUMO of HFBz is of $\pi\pi^*$ (C-C) character. The results of the present study (by a wavefunction based approach) are consistent with the findings of Holland and co-workers [171]. As can be seen

from Fig. 5.10 that the S_1 state of all fluorobenzene molecules is of $\pi\pi^*$ type. The $\pi\sigma^*$ state comes down in energy with increasing fluorination and becomes S_2 in PFBz and HFBz. As already discussed above that the S_1 and S_2 states in PFBz from CIs at lower energies, the energetic minimum of these CIs is expected to be further lowered in HFBz. Because of such vibronic coupling between the $S_1(\pi\pi^*)$-$S_2(\pi\sigma^*)$ states of PFBz and HFBz the adiabatic S_1 state will have a double minimum topography. The biexponential nature of the decay of fluorescence emission of PFBz and HFBz and the differences in their absorption and emission profiles can be ascribed to the effects due to S_1-S_2 vibronic coupling.

5.6 Electronic absorption spectrum

5.6.1 The first absorption band

The first absorption band corresponding to the $S_1 \leftarrow S_0$ transition is calculated by diagonalizing the diabatic Hamiltonian constructed in section 5.3. It is already established that the coupling between the S_1 state with the S_2-S_3- S_4-S_5 electronic manifold occurs much beyond the energy range of the first absorption band of MFBz, *o*-DFBz and *m*-DFBz molecules. The coupling strengths of the relevant vibrational modes are also very weak. Therefore, the nuclear dynamics in the S_1 state of these three molecules remains insensitive to this coupling, and treated to proceed adiabatically on this electronic state. The scenario however changes in case of PFBz as described in section 5.4 above. In this case low-energy CIs between the S_1 and S_2 states are found, which become accessible to the nuclear motion on the S_1 electronic state. The S_1-S_2 coupling in PFBz is also much stronger compared to the other three molecules. Therefore, for PFBz we first calculate the first absorption band without considering any vibronic coupling followed by a dynamical simulation considering such coupling with the excited S_2 state in order to reveal the nonadiabatic coupling effects on the spectral enve-

lope. The theoretical results are finally compared with the available experimental absorption spectra.

According to the symmetry selection rule only totally symmetric vibrational modes can have non-zero first-order (intrastate) coupling in the S_1 state. A careful analysis of all eleven totally symmetric vibrational modes of MFBz reveal that only six ($\nu_6 - \nu_{11}$) of them exhibit large first-order coupling (cf., Table 5.8). We therefore considered linear and quadratic coupling due to these modes in the dynamical simulations. The final theoretical results are presented in panel b of Fig. 5.11 along with the experimental results of Ref. [85], in panel a. The theoretical stick spectrum of Fig. 5.11 is obtained by considering a vibrational basis consisting of 6, 2, 6, 11, 11 and 2 harmonic oscillator functions along $\nu_6 - \nu_{11}$ modes, respectively. This leads to a secular matrix of dimension 17424, which is diagonalized using 5000 Lanczos iterations. The theoretical stick spectrum is convoluted with a Lorentzian line shape function of 20 meV full width at the half maximum (FWHM), to generate the spectral envelope. The same convolution procedure is applied to all the later stick data presented in this chapter. It can be seen from Fig. 5.11 that the theoretical results agree well with the experimental spectrum. The dominant progressions in the band are formed by ν_6, ν_8, ν_9 and ν_{10} vibrational modes. The peaks are ∼0.1534, ∼0.1247, ∼0.1245 and ∼0.0974 eV spaced in energy and correspond to the frequencies of these vibrational modes, respectively. Apart from the excitations of the fundamentals, their overtones and several combination levels are also excited in the band.

The $S_1 \leftarrow S_0$ absorption band of *o*-DFBz is shown in Fig 5.12(a-b). Among the eleven totally symmetric vibrational modes, only seven (ν_3, ν_4, ν_6-ν_{10}) are relevant for the nuclear dynamics in the S_1 state in this case (cf., Table 5.9). A secular matrix of dimension 461700 is obtained by using 2, 5, 9, 5, 9, 19 and 6 harmonic oscillator basis functions along the above vibrational modes, respectively, (in the given order) is diagonalized by employing 5000 Lanczos iterations. The fundamentals of symmetric vibrational modes, ν_6, ν_8 and ν_9 and their over-

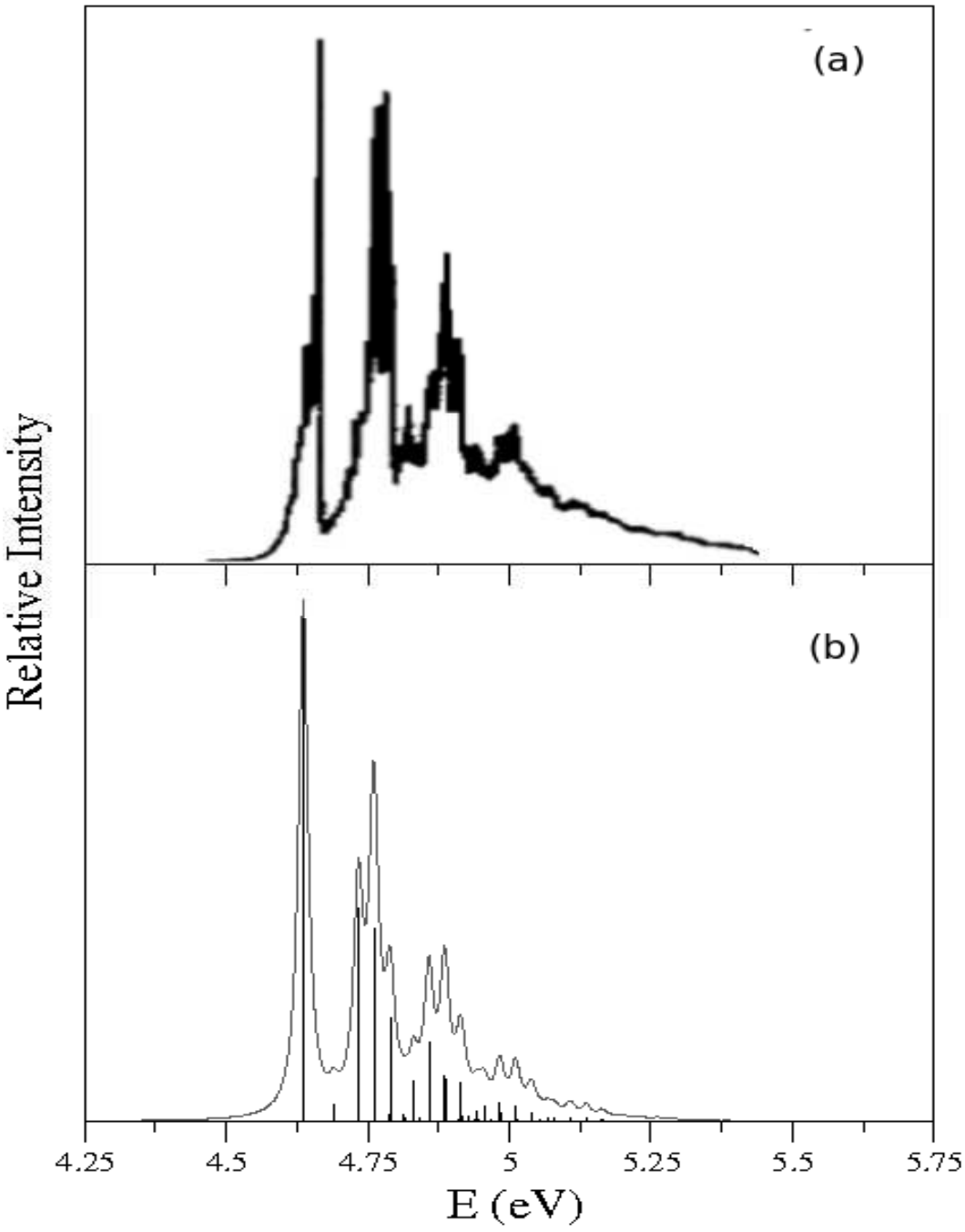

Figure 5.11: Vibronic band structure of the S_1 excited singlet electronic state of MFBz. The experimental [85] and theoretical results are shown in panel a and b, respectively. The relative intensity (in arbitrary units) is plotted as a function of the energy of the final vibronic state. The theoretical stick spectrum of panel b is convoluted with a Lorentzian function of 20 meV FWHM to generate the spectral envelope.

tones and combinations form most of the progressions in the theoretical spectrum shown in the panel b of Fig. 5.12. The intense lines are ∼0.1620, ∼0.1273 and ∼0.0921 eV spaced relative to the band origin and correspond to the frequency of the ν_6, ν_8 and ν_9 vibrational modes, respectively. It can be seen from Fig. 5.12 that the fine structure and the overall envelope of the experimental [85] spectrum is very well reproduced by our theoretical data.

The $S_1 \leftarrow S_0$ optical absorption spectrum of *m*-DFBz is shown in Fig. 5.13. The experimental [85] and present theoretical results are shown in panel a and b, respectively. A careful examination of the coupling parameters (cf., Table 5.10) of all totally symmetric nuclear vibrations indicates seven of them ($\nu_4 - \nu_{10}$) are important in the nuclear dynamics in the S_1 state of *m*-DFBz. The theoretical stick spectrum is therefore calculated including these modes and using 6, 14, 8, 20, 24, 6 and 8 harmonic oscillator basis functions along them (in that order), respectively. The resulting secular matrix of dimension 15482880 is diagonalized using 5000 Lanczos iterations. A very good agreement between theoretical and experimental data can be immediately seen from Fig. 5.13. The calculated spectrum of panel b of Fig. 5.13 reveals that the dominant progressions are formed by the ν_9, ν_8 and ν_6 vibrational modes. Peak spacings of ∼0.0862, ∼0.1256 and ∼0.1563 eV corresponding to the fundamentals of these modes, respectively, are found from the calculated spectrum. Several overtones and combination levels are also excited.

The fluorescence excitation spectrum of the S_1 state of jet cooled *o*-DFBz and *m*-DFBz recorded by Tsuchiya *et al.* [172] revealed numerous weak and strong peaks. These authors have predicted strong vibronic coupling of the S_1 state of these molecules with a nearby state of $\pi\sigma^*$ type. Based on this assumption they assigned the observed weak lines to the excitations of the nontotally symmetric vibrational modes in addition to the expected strong excitations of the totally symmetric vibrational modes. In contrast, the present theoretical analysis reveals that the coupling of the S_1 state with the higher excited states of *o*-DFBz and

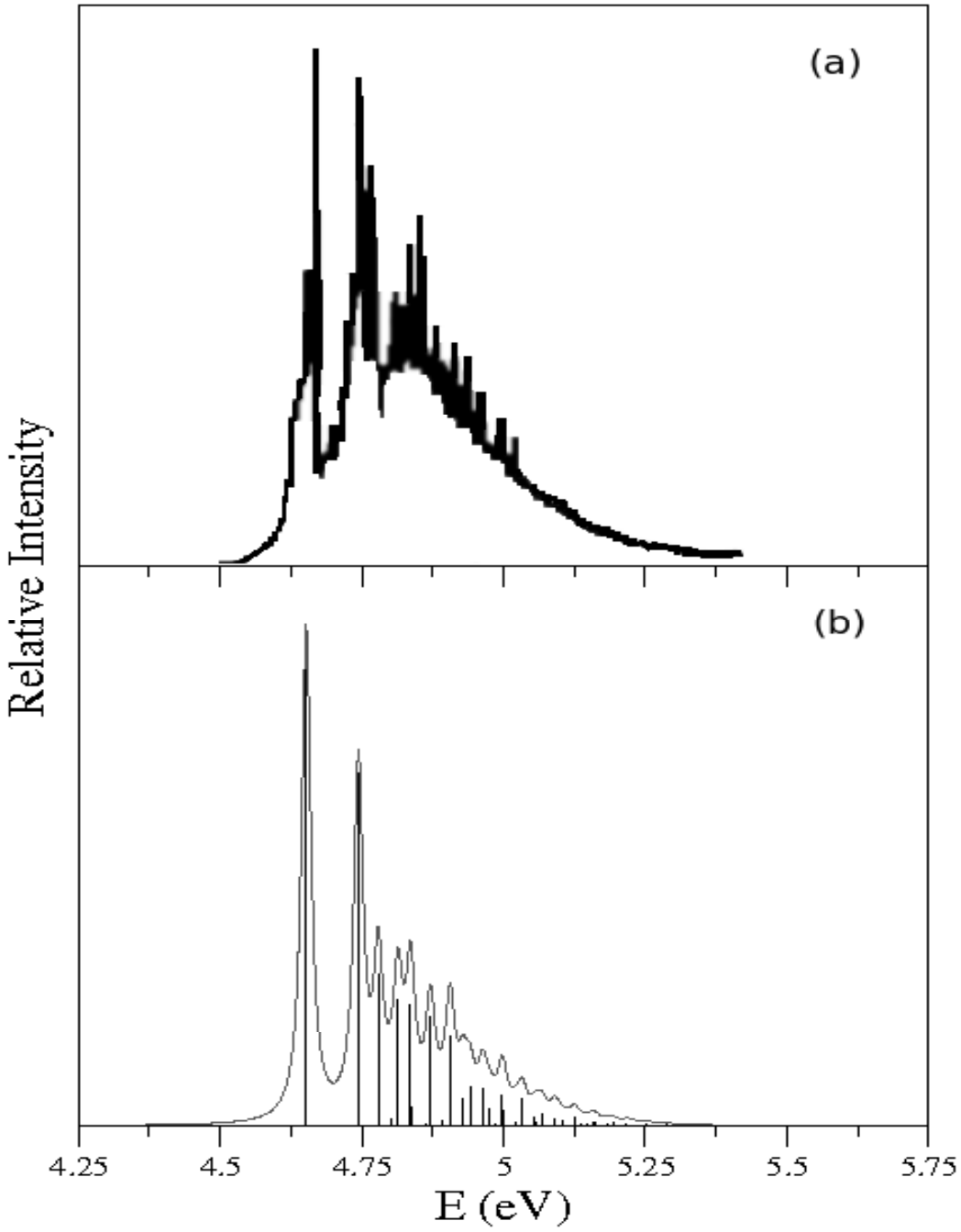

Figure 5.12: Same as in Fig. 5.11, for the *o*-DFBz.

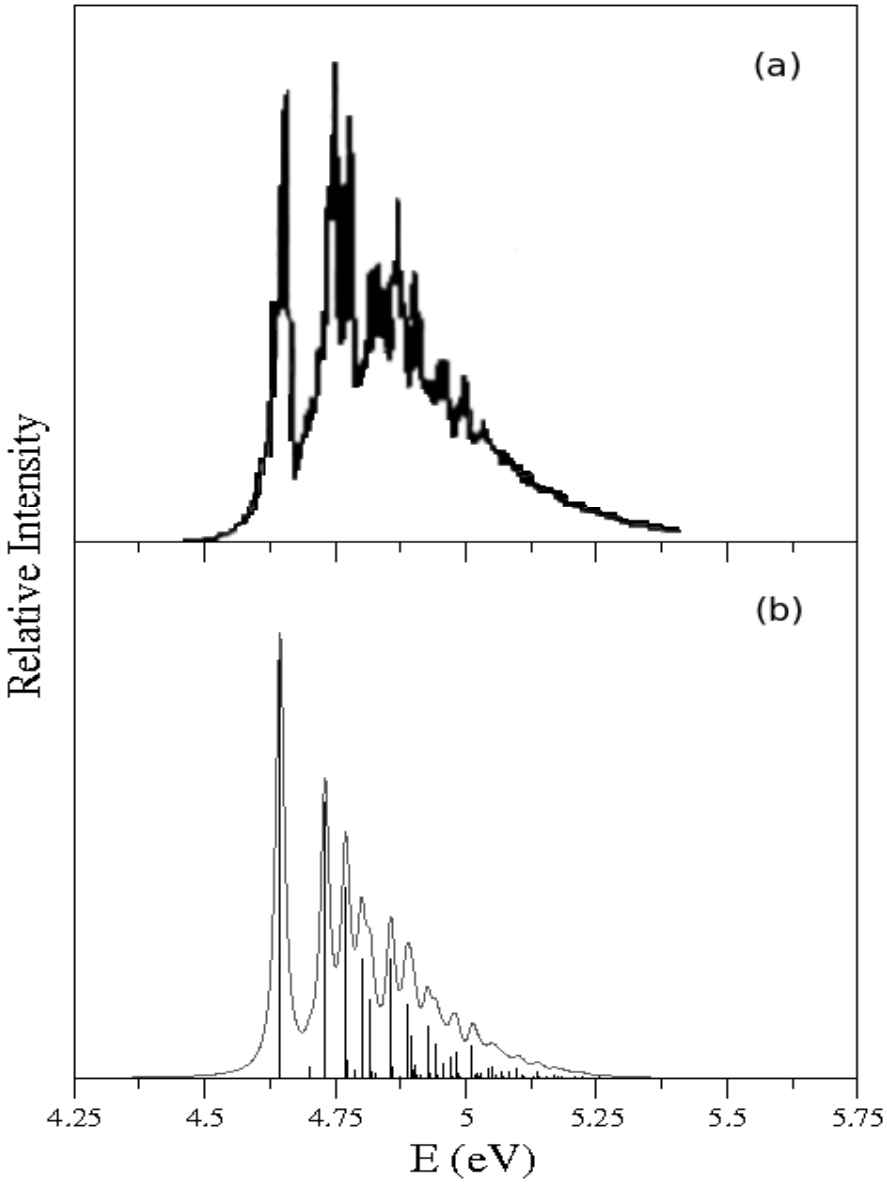

Figure 5.13: Same as in Fig. 5.11, for the *m*-DFBz.

m-DFBz is extremely weak and occurs at much higher energies, much beyond the energy range of the S_1 band. In our theoretical studies we did not observe excitations of any nontotally symmetric vibration in the S_1 band of these molecules. The dominant excitations of symmetric vibrational modes are however in good agreement with those reported by Tsuchiya *et al.* [172]. For comparison, energy eigenvalues of the prominent peaks of the S_1 absorption band of *o*-DFBz and *m*-DFBz are given in Table 5.14 along with the experimental results [172].

Table 5.14: Vibrational energy levels of the S_1 electronic state of *o*-DFBz and *m*-DFBz (in cm^{-1}) The present theoretical results are given along with the experimental fluorescence excitation spectroscopy data of Ref. [172].

Molecule	Present Data	Fluorescence Data	Vibrational assignment
	742	722	ν_9
	1027	925	ν_8
o-DFBz	1306	1265	ν_6
	1485	1445	ν_9^2
	314	317	ν_{11}
	638	682	ν_{11}^2
	695	702	ν_9
m-DFBz	1013	966	ν_8
	1260	1267	ν_6
	1651	1650	$\nu_{11} + \nu_8$
	1708	1712	$\nu_9 + \nu_8$

It can be seen from Table 5.11 that for PFBz seven symmetric vibrational modes, ν_3-ν_5, ν_7-ν_8 and ν_{10}-ν_{11} are relevant for the nuclear dynamics in the S_1 state. As stated above, in this case the S_1 state forms low-energy CIs with the S_2 state. These CIs are accessible for the nuclear motion on the S_1 state. When the S_1-S_2 coupling included, the dynamics becomes more involved. In addition to the above seven, two additional symmetric modes ν_2 and ν_9 become relevant for the dynamics. These two additional modes have relatively larger coupling strength in the S_2 state. The coupling (in first order) between S_1 and S_2 state in PFBz is caused by the three vibrational modes of a_2 symmetry. From Table 5.11 it can be seen that all three modes have large coupling strength ($\lambda^2/2\omega^2$) of $\sim$1.60, $\sim$2.92

and ∼2.79, for ν_{28}, ν_{29} and ν_{30}, respectively.

In order to have a complete overview of the complex structure of the $S_1 \leftarrow S_0$ absorption band of PFBz, we first examined the nuclear dynamics in the isolated (uncoupled) S_1 state. The vibrational basis used for this purpose contains 5, 8, 3, 12, 21, 3 and 3 harmonic oscillator functions along the ν_3-ν_5, ν_7, ν_8, ν_{10} and ν_{11} modes, respectively. This choice leads to a secular matrix of dimension 272160 which is finally diagonalized with 5000 Lanczos iterations. The result emerged from this calculation is presented in panel c of Fig. 5.14. The experimental result reproduced from Ref. [85] is presented in panel a of Fig. 5.14. Understandably, the theoretical results of panel c are not in agreement with the observed diffused $S_1 \leftarrow S_0$ absorption band of PFBz. Major progressions due to ν_4, ν_7 and ν_8 vibrational modes are identified from the theoretical stick spectrum. The lines are ∼0.1763, ∼0.0866 and ∼0.0718 eV spaced corresponding to the excitation of the fundamentals along these vibrational modes, respectively.

In the subsequent attempt we included nine symmetric vibrational modes and three coupling vibrational modes of a_2 symmetry in the dynamical treatment. A diagonalization of matrix Hamiltonian for two coupled electronic states including twelve nuclear degrees of freedom turned out to be very difficult. The spectrum obtained by diagonalizing the two-state vibronic Hamiltonian could not be converged numerically and is not shown here. A huge increase of spectral line density is observed when the coupling between the states included. Finally, the S_1-S_2 coupled state spectrum of PFBz is calculated by the WP propagation approach employing the MCTDH algorithm [118–123]. The numerical details of this calculation are summarized in Table 5.15. The numerically converged spectrum obtained from this calculation is given in panel b of Fig. 5.14. It can be seen that the theoretical results of panel b is in very good accord with the experiment establishing the important role of S_1-S_2 coupling in the detailed shape of the S_1 absorption band of PFBz.

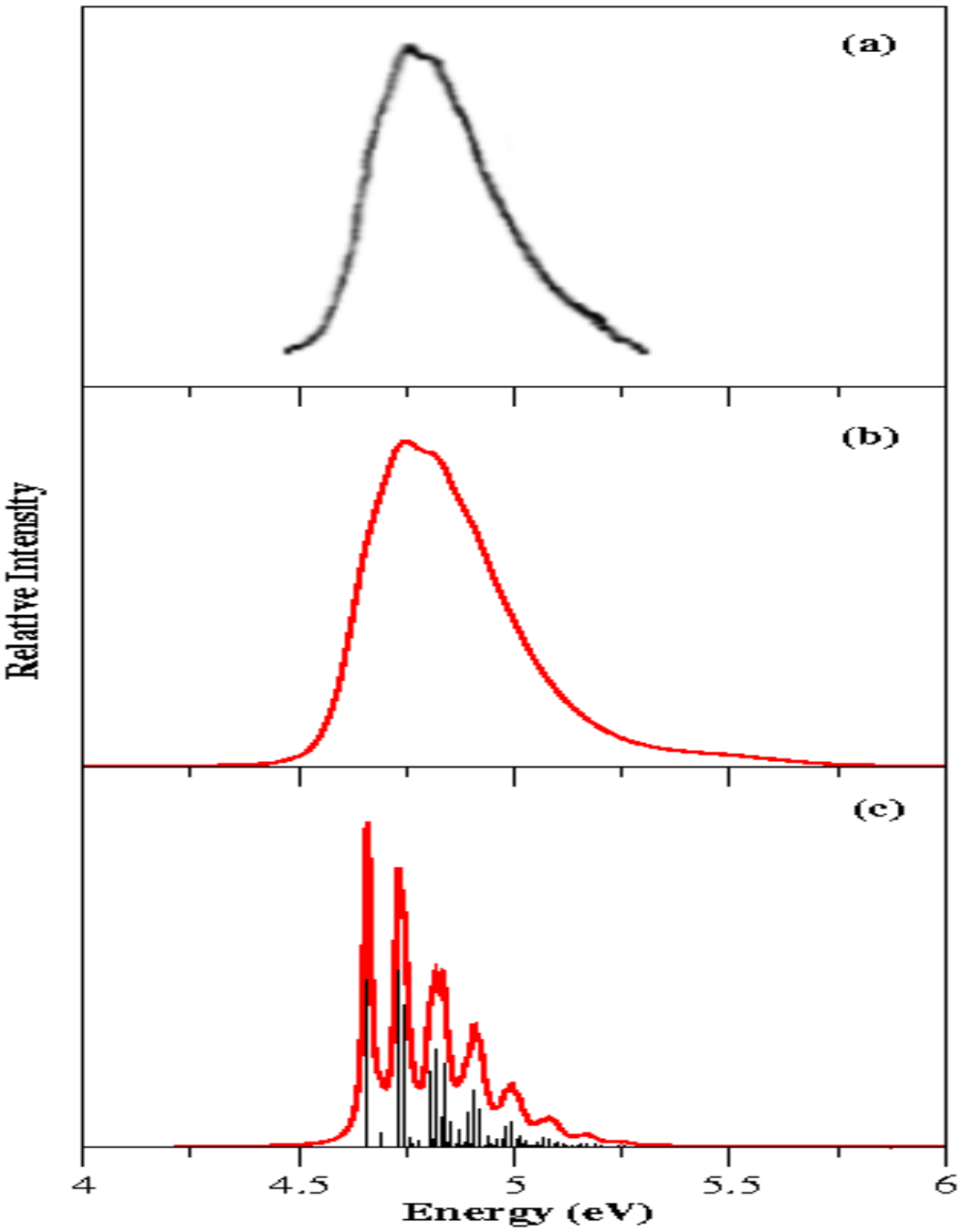

Figure 5.14: Vibronic band structure of S_1 excited singlet electronic state of PFBz: (a) experimental spectrum (reproduced from Ref. [85]); (b) spectrum calculated by diagonalizing the S_1-S_2 coupled state Hamiltonian; (c) uncoupled S_1 state spectrum calculated by the matrix diagonalization approach.

Table 5.15: Normal mode combinations, sizes of the primitive and the single particle basis used in the WP propagation within the MCTDH framework in the coupled electronic manifold using the complete vibronic Hamiltonian of Eqs. (5.2-5.3d). Second column denotes the vibrational degrees of freedom (DOF) which are combined to particles. Third column gives the number of primitive basis functions for each DOF. Fourth column gives the number of single particle functions (SPFs) for each electronic state.

Molecule	Normal modes	Primitive basis	SPF basis	Figure
MFBz	(ν_9, ν_{30}, ν_{14}, ν_{20})	(15, 11, 8, 9)	[7, 6, 4, 6, 7]	5.19 (b)
	(ν_{10}, ν_{13}, ν_{27}, ν_{29})	(10, 8, 9, 10)	[7, 6, 4, 4, 6]	
	(ν_6, ν_{12}, ν_{17}, ν_{28})	(12, 8, 8, 10)	[6, 6, 4, 6, 6]	
	(ν_8, ν_{26}, ν_{16})	(12, 9, 8)	[6, 5, 4, 5, 6]	
	(ν_7, ν_{11}, ν_{24})	(8, 7, 9)	[4, 4, 7, 6, 4]	
o-DFBz	(ν_6, ν_{10}, ν_{12}, ν_{23}, ν_{25})	(12, 10, 8, 6, 10)	[7, 7, 8, 7, 7]	5.20 (b)
	(ν_3, ν_{14}, ν_{24}, ν_{26})	(15, 10, 8, 8)	[5, 5, 8, 8, 5]	
	(ν_4, ν_{11}, ν_{18}, ν_{27}, ν_{30})	(7, 8, 10, 8, 11)	[5, 5, 5, 5, 5]	
	(ν_7, ν_{13}, ν_{15}, ν_{28})	(10, 7, 12, 10)	[5, 5, 7, 5, 5]	
	(ν_8, ν_9, ν_{21}, ν_{29})	(10, 12, 7, 10)	[7, 7, 6, 7, 7]	
m-DFBz	(ν_6, ν_5, ν_{19}, ν_{27})	(14, 7, 10, 8)	[7, 7, 7, 7]	5.21 (b)
	(ν_8, ν_4, ν_{26}, ν_{23})	(14, 14, 8, 9)	[7, 7, 7, 7]	
	(ν_9, ν_7, ν_{22}, ν_{25})	(14, 8, 8, 6)	[7, 5, 4, 6]	
	(ν_{10}, ν_{20}, ν_{24})	(10, 6, 6)	[5, 5, 6, 6]	
PFBz	(ν_2, ν_{11}, ν_4, ν_{28})	(10, 12, 4, 15)	[8, 10]	5.14 (b)
	(ν_3, ν_8, ν_9, ν_{29})	(7, 9, 12, 15)	[9, 10]	
	(ν_6, ν_7, ν_{10}, ν_{30})	(6, 5, 12, 157)	[8, 7]	
PFBz	(ν_4, ν_{13}, ν_{16}, ν_{25})	(4, 11, 10, 12)	[7, 8, 8, 8, 8]	5.22 (b)
	(ν_3, ν_{12}, ν_{20}, ν_{26})	(7, 14, 11, 6)	[4, 9, 9, 4, 4]	
	(ν_9, ν_{15}, ν_{17}, ν_{27})	(12, 7, 15, 6)	[4, 8, 5, 5, 5]	
	(ν_6, ν_{11}, ν_{18}, ν_{22}, ν_{28})	(6, 12, 10, 7, 15)	[4, 6, 4, 4, 7]	
	(ν_8, ν_{10}, ν_{19}, ν_{21}, ν_{29})	(9, 12, 10, 7, 15)	[7, 4, 5, 6, 6]	
	(ν_7, ν_2, ν_{14}, ν_{30})	(5, 10, 9, 15)	[4, 7, 4, 4, 5]	

5.6.2 The overlapping second and third absorption bands

The second and third absorption bands of all four molecules are highly overlapping and extremely diffuse. These bands correspond to the $^1B_{1u} \leftarrow {}^1A_{1g}$ and $^1E_{1u} \leftarrow {}^1A_{1g}$ transitions in the parent benzene molecule. Because of symmetry lowering the electronic states of the four fluorobenzene molecules considered here are all nondegenerate. The low-lying excited states S_2, S_3, S_4 and S_5 are energetically close and undergo crossing with each other and form several low-energy CIs as discussed in detail in section 5.4. Except for the *m*-DFBz (in which the states up to S_4 occur within 8.0 eV), the vibronic structures of electronic states up to S_5 are relevant for the observed features of the second and third absorption bands.

In addition to the above, in PFBz the S_1 state also contributes to the observed experimental data. As already shown, the coupling between the S_1 and S_2 states significantly contributes to the broadening of the $S_1 \leftarrow S_0$ absorption spectrum in this case. Therefore, it is obvious that this coupling will have significant effect on the low-energy wing of the S_2 band. In order to examine the vibronic structure of the second and third absorption bands of the four fluorobenzene molecules systematically, we first consider each electronic state without considering the coupling with its neighbors and simulate the nuclear dynamics on it. In the next step all possible couplings between the states are included in the dynamical treatment and the results are compared with the available experimental data [85]. While the matrix diagonalization method is employed for the uncoupled electronic states, the final results in the coupled states situation are obtained by propagating WPs employing the MCTDH algorithm [118–123].

The vibrational energy level spectrum of the uncoupled S_2, S_3, S_4 and S_5 electronic states of MFBz are shown in panel a, b, c and d, respectively, of Fig. 5.15. The energy eigenvalues are obtained by the matrix diagonalization method using the most important symmetric vibrational modes; ν_6-ν_{11} for S_2; ν_4, ν_6, ν_7 ν_9-ν_{11} for S_3; ν_6-ν_{11} for S_4 and ν_4, ν_6-ν_{10} for S_5. The theoretical spectra presented in Fig.

5.15 and also the latter ones in Figs. 5.16, 5.17 and 5.18 converged with respect to the numerical parameters used in the calculations. The vibronic structure of the uncoupled S_2 electronic state of MFBz reveals dominant excitation of the ν_6, ν_8, ν_9 and ν_{10} vibrational modes and the corresponding peak spacings of ∼0.1410, ∼0.1235, ∼0.1218 and ∼0.0943 eV, respectively, are found from the spectrum of Fig. 5.15(a). In the $S_3 \leftarrow S_0$ spectrum presented in Fig. 5.15(b), ν_4, ν_7, and ν_{11} vibrational modes form the dominant progressions. The peak spacings found at ∼0.1967, ∼0.1392 and ∼0.0550 eV, respectively, correspond to the fundamental excitations along these vibrations. Similarly, the theoretical results indicate excitation of ν_6, ν_8, ν_9, ν_{10} and ν_{11} fundamentals in the $S_4 \leftarrow S_0$ absorption spectrum presented in Fig 5.15(c). Peak spacings of ∼0.1533, ∼0.1188, ∼0.1185, ∼0.0928 and ∼0.0607 eV along these vibrational modes, respectively, are found from the theoretical data. The $S_5 \leftarrow S_0$ spectrum presented in Fig. 5.15(d) is dominated by the progressions along the ν_4, ν_6, ν_8, ν_9 and ν_{10} vibrational modes and peak spacings of ∼0.2208, ∼0.1602, ∼0.1202, ∼0.1202 and ∼0.0967 eV, respectively, corresponding to these modes are estimated from the theoretical data. In addition to the excitation of the fundamentals, various overtones and combination peaks are also excited. Similar observations are made for all other fluorobenzene molecules discussed in this chapter.

Electronic absorption spectra of the uncoupled S_2, S_3, S_4 and S_5 electronic states of *o*-DFBz are shown in panel a, b, c and d of Fig. 5.16, respectively. In this case the theoretical data reveal dominant excitation of the ν_6, ν_8 and ν_9 vibrational modes in the S_2 band; ν_3, ν_9 and ν_{10} vibrational modes in the S_3 band; ν_3, ν_6, ν_8 and ν_9 vibrational modes in the S_4 band and ν_6, ν_8 and ν_9 vibrational modes in the S_5 band. Apart from the fundamentals several overtone and combination levels are also excited.

Similar electronic absorption spectra of the uncoupled S_2, S_3 and S_4 excited electronic states of *m*-DFBz are shown in panel a, b and c of Fig. 5.17, respectively. The theoretical data indicate that ν_6, ν_8 and ν_9 vibrational modes form

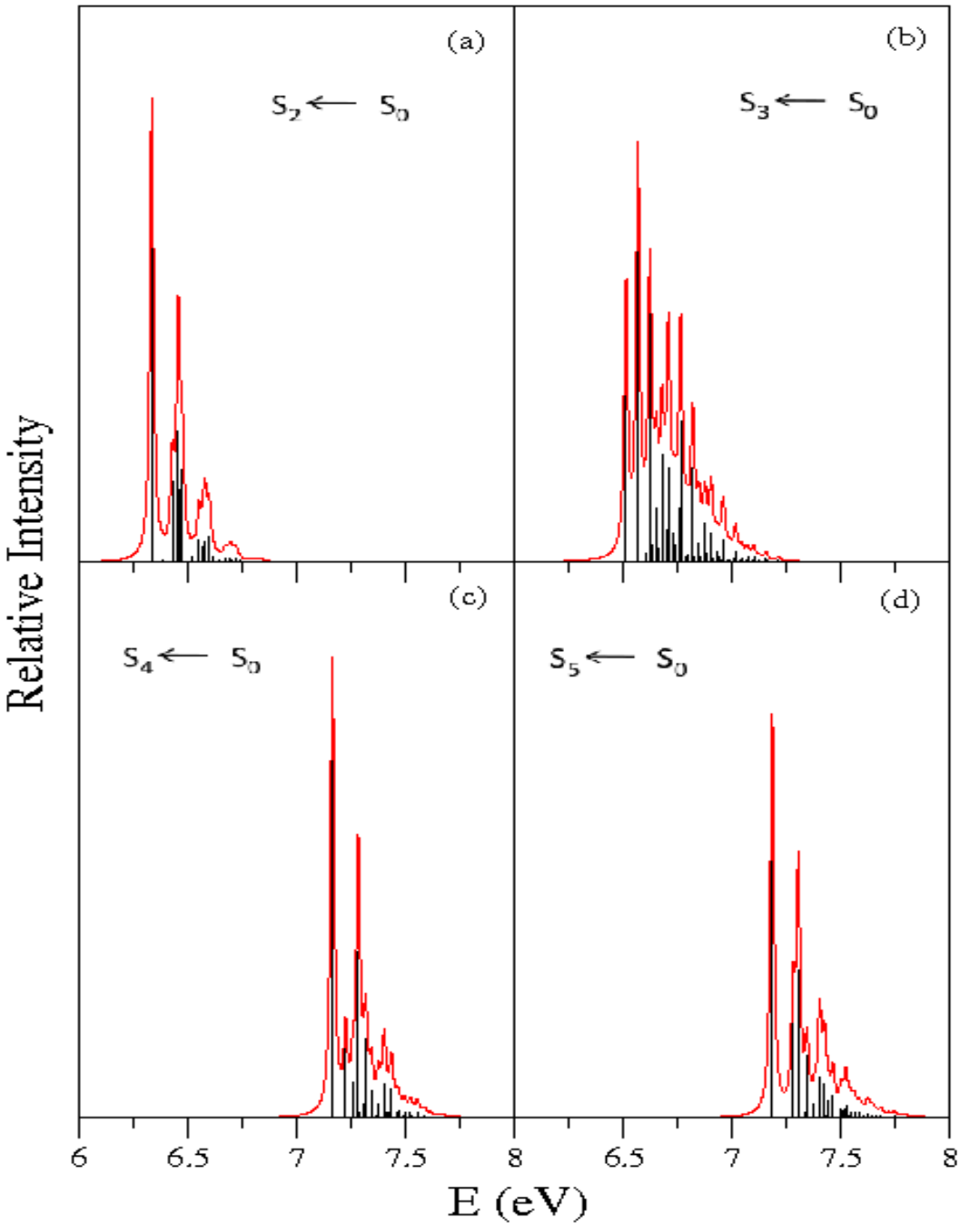

Figure 5.15: Electronic absorption bands of the uncoupled excited singlet electronic states (indicated in the panel) of MFBz. Relative intensity (in arbitrary units) is plotted as a function of the energy of the vibrational levels of the final electronic state. The zero of energy corresponds to the equilibrium minimum of the S_0 state.

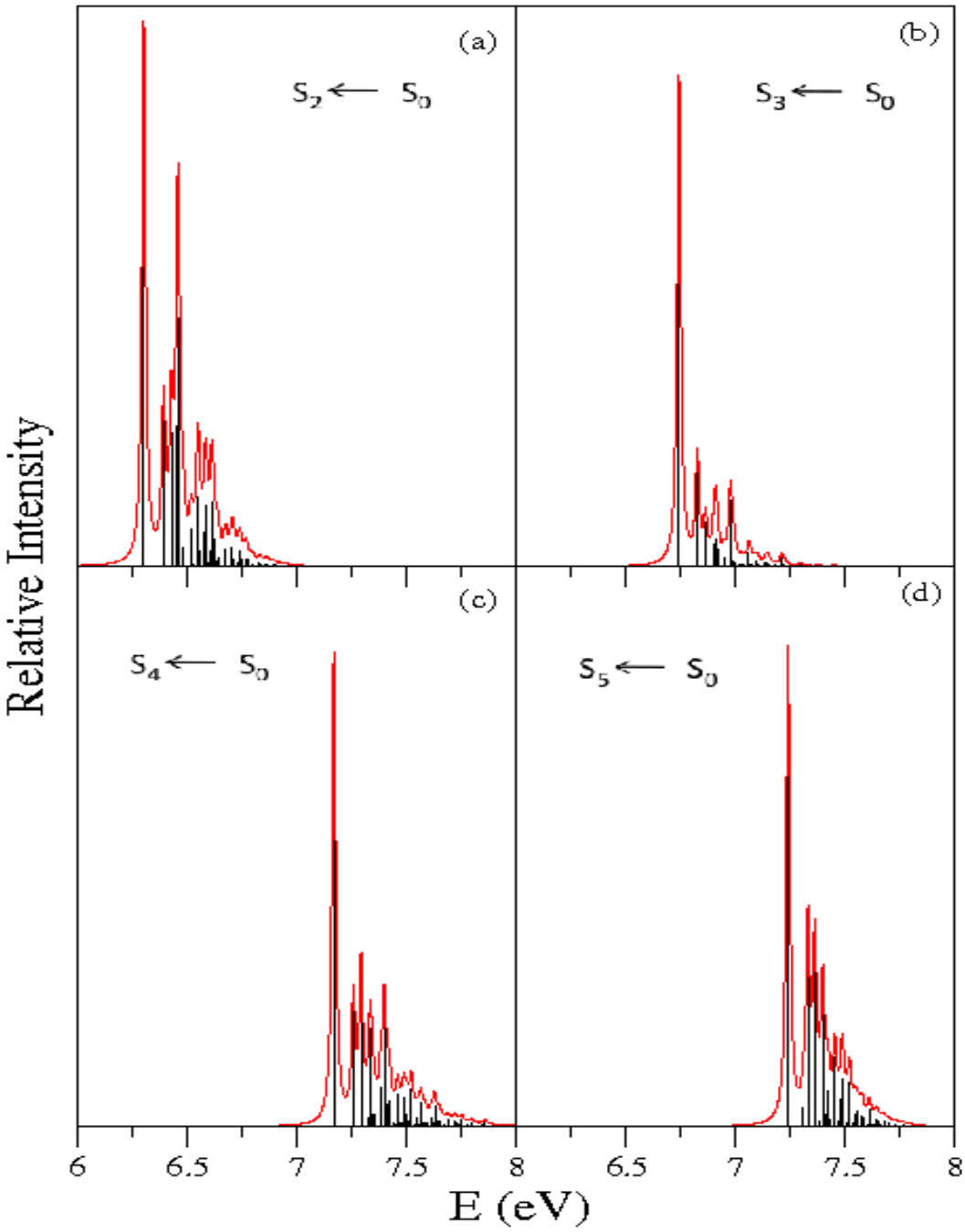

Figure 5.16: Same as in Fig. 5.15, for *o*-DFBz.

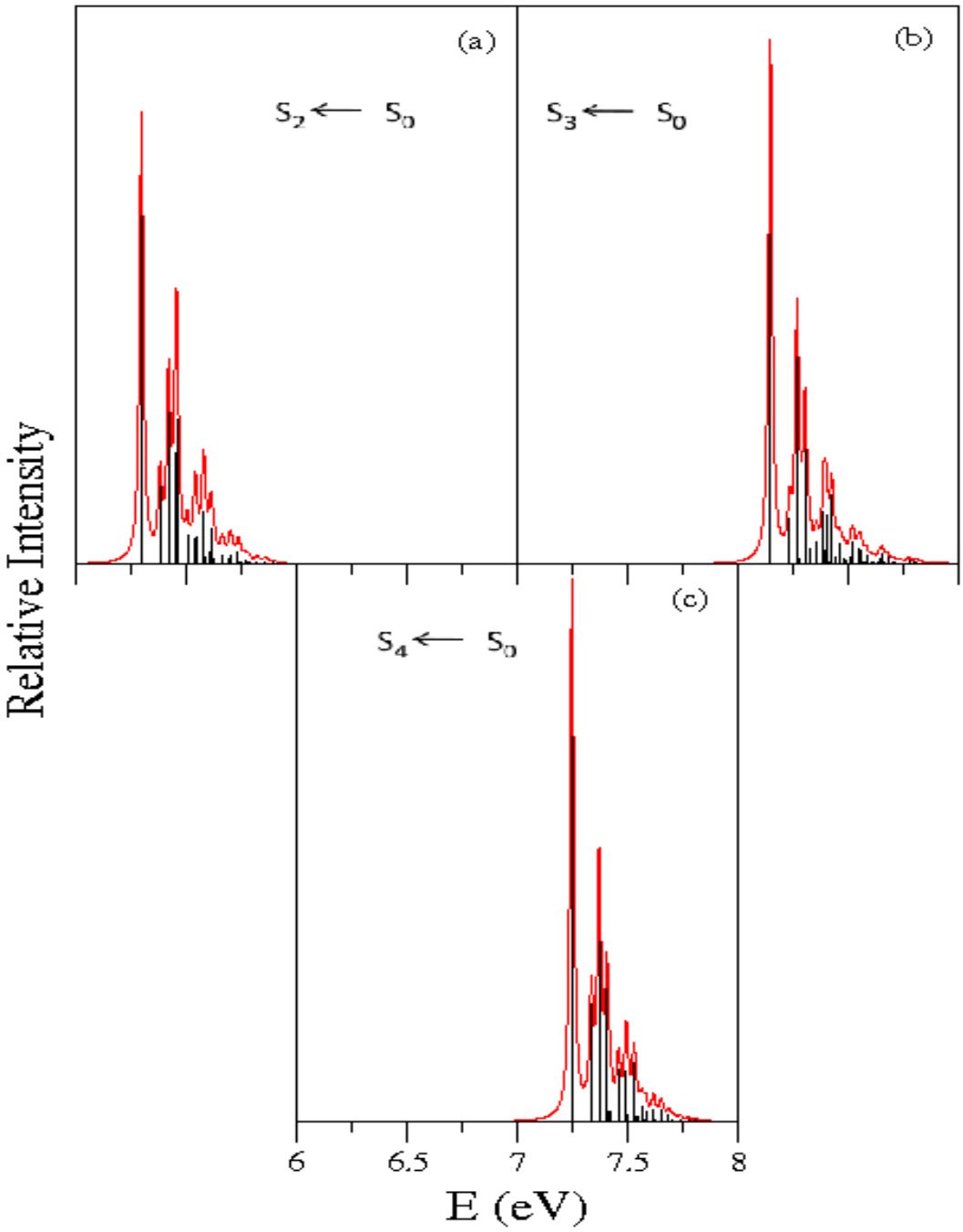

Figure 5.17: Same as in Fig. 5.17, for *m*-DFBz.

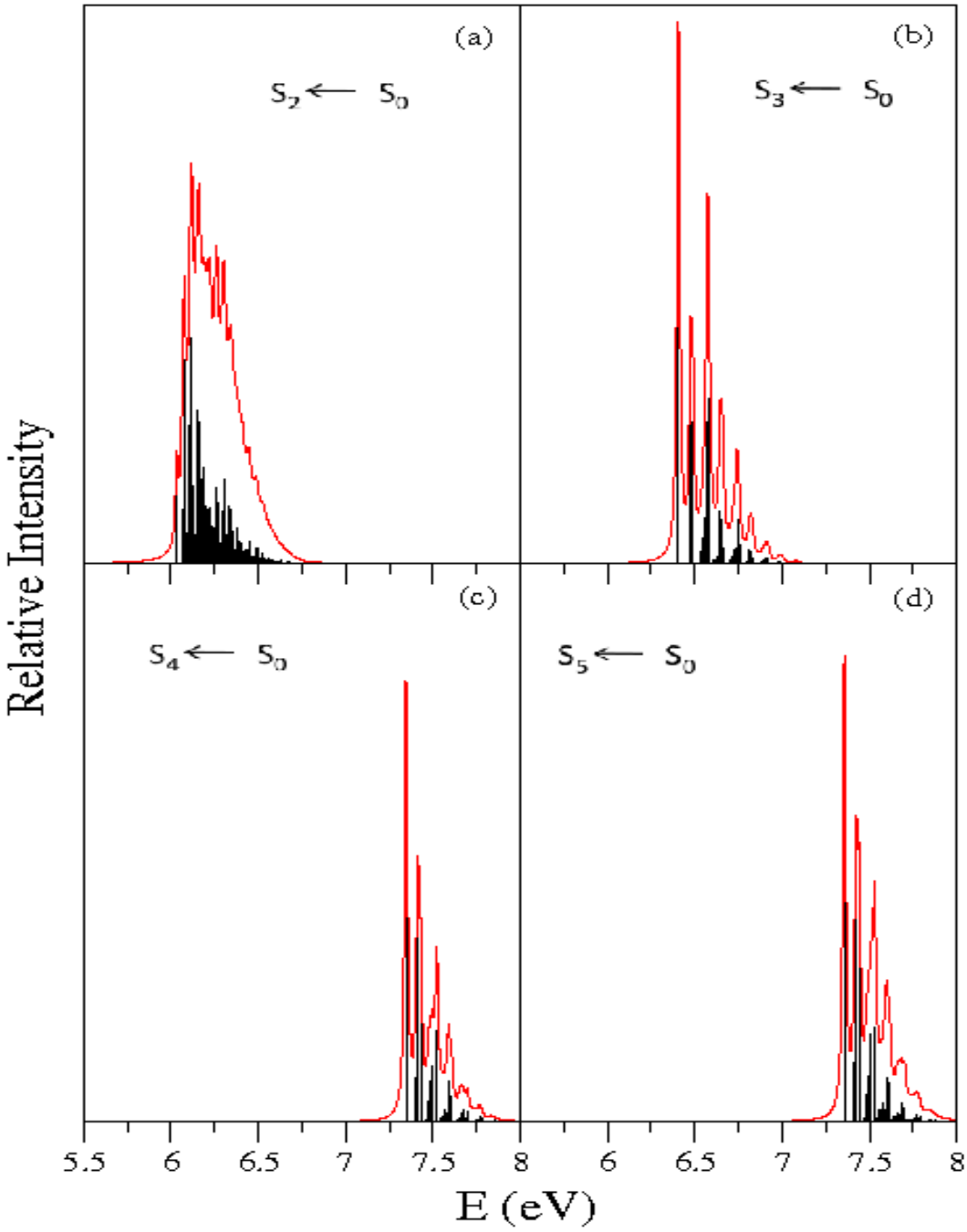

Figure 5.18: Same as in Fig. 5.18, for PFBz.

the major progressions in the S_2 and S_4 bands and ν_4, ν_6, ν_8 and ν_9 vibrational modes form the major progressions in the S_3 band of *m*-DFBz.

The electronic absorption spectra of the uncoupled S_2, S_3, S_4 and S_5 electronic states of PFBz are shown in Figs. 5.18(a-d), respectively. Unlike other molecules the S_2 band in PFBz is somewhat broad and diffuse. This is because two low-frequency symmetric vibrational modes ν_9 (0.0579 eV) and ν_{11} (0.0331 eV) are strongly excited in this case (see Table 5.11). Strong excitations of these modes cause a huge increase in the density of the vibrational levels. Note that frequencies of these modes in PFBz are also lower compared to those in other molecules. Energy eigenvalues of dominant peaks observed above in the absorption spectra of four fluorobenzene molecules are given in Tables 5.16-5.19. The most probable assignment of the peaks are also included in these tables.

It is now obvious that the structured electronic absorption bands presented above in Figs. (5.15-5.18) are quite different from the spectral envelopes recorded in the experiment [85]. The experimental spectral envelopes are broad and usually structureless. As described above that a meaningful interpretation of the experimental data requires the nonadiabatic coupling among various states to be considered in the dynamical calculations. Such attempts are made in the rest of this section. It is important to mention that the uncoupled state spectrum presented above contains rich informations on the excitation of vibrational modes, which otherwise can not be deciphered from the results presented below. Understandably, because of the dimensionality problem the matrix diagonalization approach could not be used any further to carry out the first principles simulation of nuclear dynamics on the coupled manifold of multiple electronic states. We therefore resort to the most credible WP propagation approach within the MCTDH framework [118–123] to accomplish the task.

The calculated second and third absorption bands of MFBz, *o*-DFBz, *m*-DFBz and PFBz are shown in panel b of Figs. 5.19, 5.20, 5.21 and 5.22, respectively. The corresponding experimental results are reproduced from Ref. [85] and given

Table 5.16: Line spacings (in eV) of the dominant excitations relative to the band origin extracted from the electronic absorption bands of Fig. 5.15 of MFBz.

Electronic state	Dominant excitation	Line spacing
S_2	ν_6	0.1410
	ν_8	0.1235
	ν_9	0.1218
	ν_{10}	0.0943
	$\nu_9 + \nu_{10}$	0.2160
	$\nu_8 + \nu_{10}$	0.2178
	$\nu_6 + \nu_{10}$	0.2352
	$2\nu_9$	0.2436
	$\nu_8 + \nu_9$	0.2453
	$\nu_6 + \nu_9$	0.2627
	$\nu_6 + \nu_8$	0.2645
S_3	ν_4	0.1967
	ν_7	0.1392
	ν_{11}	0.0550
	$2\nu_{11}$	0.1099
	$3\nu_{11}$	0.1649
	$\nu_7 + 2\nu_{11}$	0.2492
	$\nu_4 + \nu_{11}$	0.2517
S_4	ν_6	0.1533
	ν_8	0.1188
	ν_9	0.1185
	ν_{10}	0.0928
	ν_{11}	0.0607
	$\nu_9 + 2\nu_{11}$	0.1793
	$2\nu_9$	0.2371
	$\nu_8 + \nu_9$	0.2374
	$\nu_6 + \nu_9$	0.2718
S_5	ν_4	0.2208
	ν_6	0.1602
	ν_8	0.1202
	ν_9	0.1202
	ν_{10}	0.0967
	$2\nu_9$	0.2404
	$2\nu_8$	0.2405
	$\nu_6 + \nu_{10}$	0.2569
	$\nu_6 + 2\nu_9$	0.2804

Table 5.17: Same as in Table 5.16, extracted from Fig. 5.16 for *o*-DFBz.

Electronic state	Dominant excitation	Line spacing
S_2	ν_6	0.1575
	ν_8	0.1257
	ν_9	0.0905
	$\nu_8 + \nu_9$	0.2161
	$\nu_6 + \nu_9$	0.2479
	$\nu_6 + \nu_8$	0.2832
	$2\nu_6$	0.3108
S_3	ν_3	0.2338
	ν_9	0.1205
	ν_{10}	0.0834
	$2\nu_{10}$	0.1669
	$\nu_9 + 2\nu_{10}$	0.2040
	$2\nu_9$	0.2411
	$\nu_3 + \nu_{10}$	0.3173
S_4	ν_3	0.2301
	ν_6	0.1662
	ν_8	0.1239
	ν_9	0.0892
	$\nu_8 + \nu_9$	0.2131
	$2\nu_8$	0.2478
	$\nu_6 + \nu_9$	0.2554
	$\nu_6 + \nu_8$	0.2901
	$\nu_3 + \nu_9$	0.3192
S_5	ν_6	0.1582
	ν_8	0.1219
	ν_9	0.0911
	$2\nu_9$	0.1821
	$\nu_8 + \nu_9$	0.2130
	$2\nu_8$	0.2439
	$\nu_6 + \nu_9$	0.2493
	$\nu_6 + \nu_8$	0.2801
	$2\nu_6$	0.3164

Table 5.18: Same as in Table 5.16, extracted from Fig. 5.17 for *m*-DFBz.

Electronic state	Dominant excitation	Line spacing
	ν_4	0.1644
	ν_6	0.1549
	ν_8	0.1230
	ν_9	0.0842
S_2	$\nu_8 + \nu_9$	0.2072
	$\nu_6 + \nu_9$	0.2391
	$2\nu_8$	0.2461
	$\nu_6 + \nu_8$	0.2780
	$2\nu_6$	0.3144
	ν_4	0.2531
	ν_6	0.1570
	ν_8	0.1211
	ν_9	0.0872
S_3	$\nu_8 + \nu_9$	0.2082
	$2\nu_8$	0.2421
	$\nu_8 + \nu_6$	0.2780
	$2\nu_6$	0.3140
	$\nu_4 + \nu_8$	0.3741
	ν_6	0.1575
	ν_8	0.1229
	ν_9	0.0877
S_4	$\nu_8 + \nu_9$	0.2106
	$\nu_6 + \nu_9$	0.2451
	$2\nu_8$	0.2457
	$\nu_6 + \nu_8$	0.2804
	$2\nu_6$	0.3150

Table 5.19: Same as in Table 5.16, extracted from Fig 5.18 for PFBz.

Electronic state	Dominant excitation	Line spacing
	ν_8	0.0548
	ν_9	0.0421
	ν_{11}	0.0305
S_2	$\nu_9 + \nu_{11}$	0.0727
	$2\nu_9$	0.0843
	$\nu_8 + \nu_9$	0.0970
	$\nu_9 + 2\nu_{11}$	0.1032
	$2\nu_9 + \nu_{11}$	0.1148
	ν_2	0.1690
	ν_4	0.1675
	ν_7	0.0826
S_3	ν_8	0.0699
	$2\nu_8$	0.1398
	$\nu_7 + \nu_8$	0.1525
	ν_3	0.1772
	ν_4	0.1756
	ν_7	0.0841
	ν_8	0.0682
	ν_9	0.0562
S_4	$\nu_8 + \nu_9$	0.1244
	$2\nu_8$	0.1365
	$2\nu_7$	0.1681
	$\nu_4 + \nu_8$	0.2438
	$\nu_3 + \nu_8$	0.2455
	ν_4	0.1711
	ν_7	0.0853
	ν_8	0.0693
S_5	ν_9	0.0577
	$\nu_8 + \nu_9$	0.1270
	$2\nu_8$	0.1387
	$\nu_7 + \nu_8$	0.1547

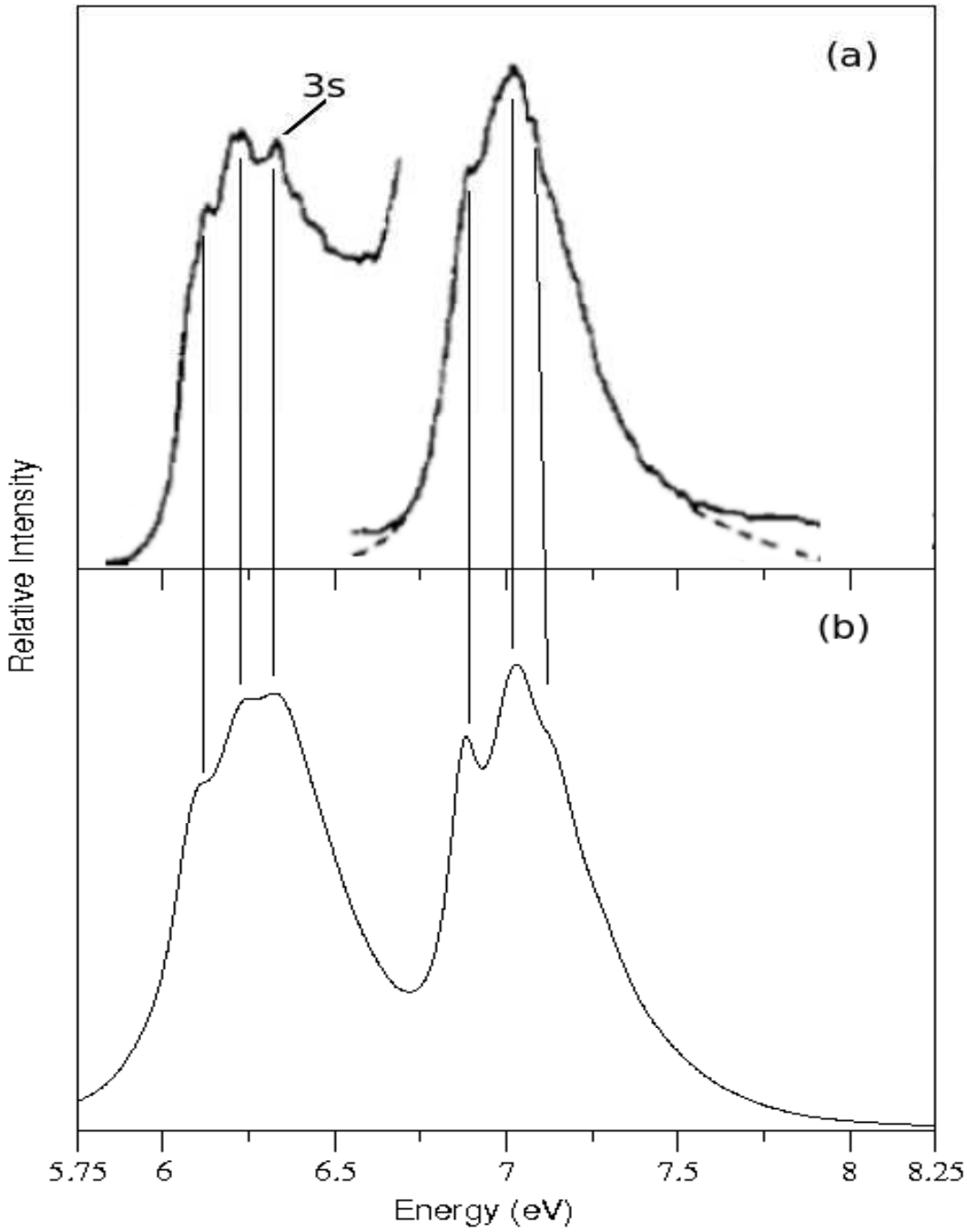

Figure 5.19: The second and third electronic absorption bands of MFBz obtained from the coupled state dynamical studies (see text for details). The experimental [85] and theoretical results are shown in panel a and b, respectively. The intensity (in arbitrary unit) is plotted as a function of the energy of the final vibronic states. The vertical lines are drawn to better reveal the correspondence of the structures in the theoretical spectrum to those in the experimental results.

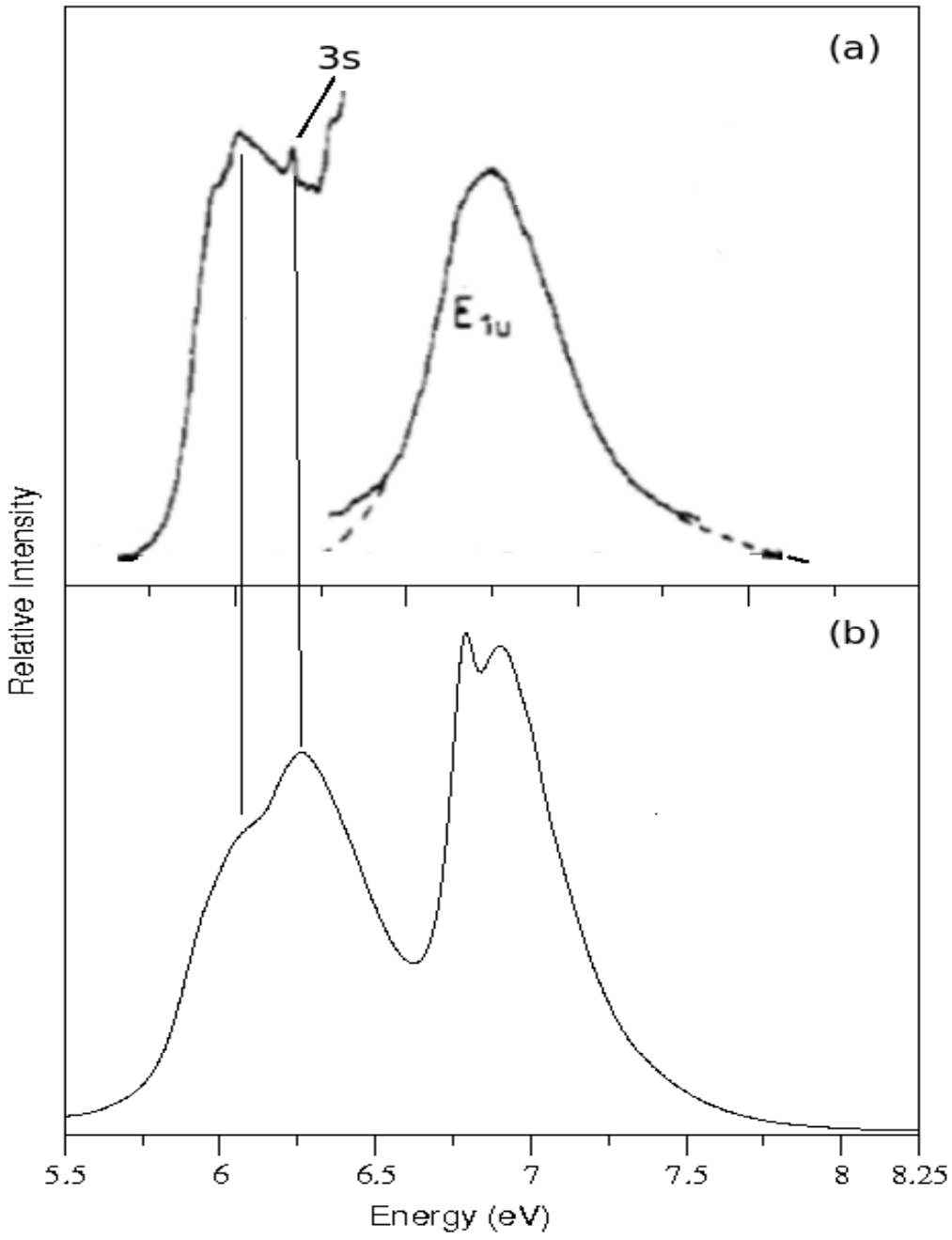

Figure 5.20: Same as in Fig. 5.19, for *o*-DFBz.

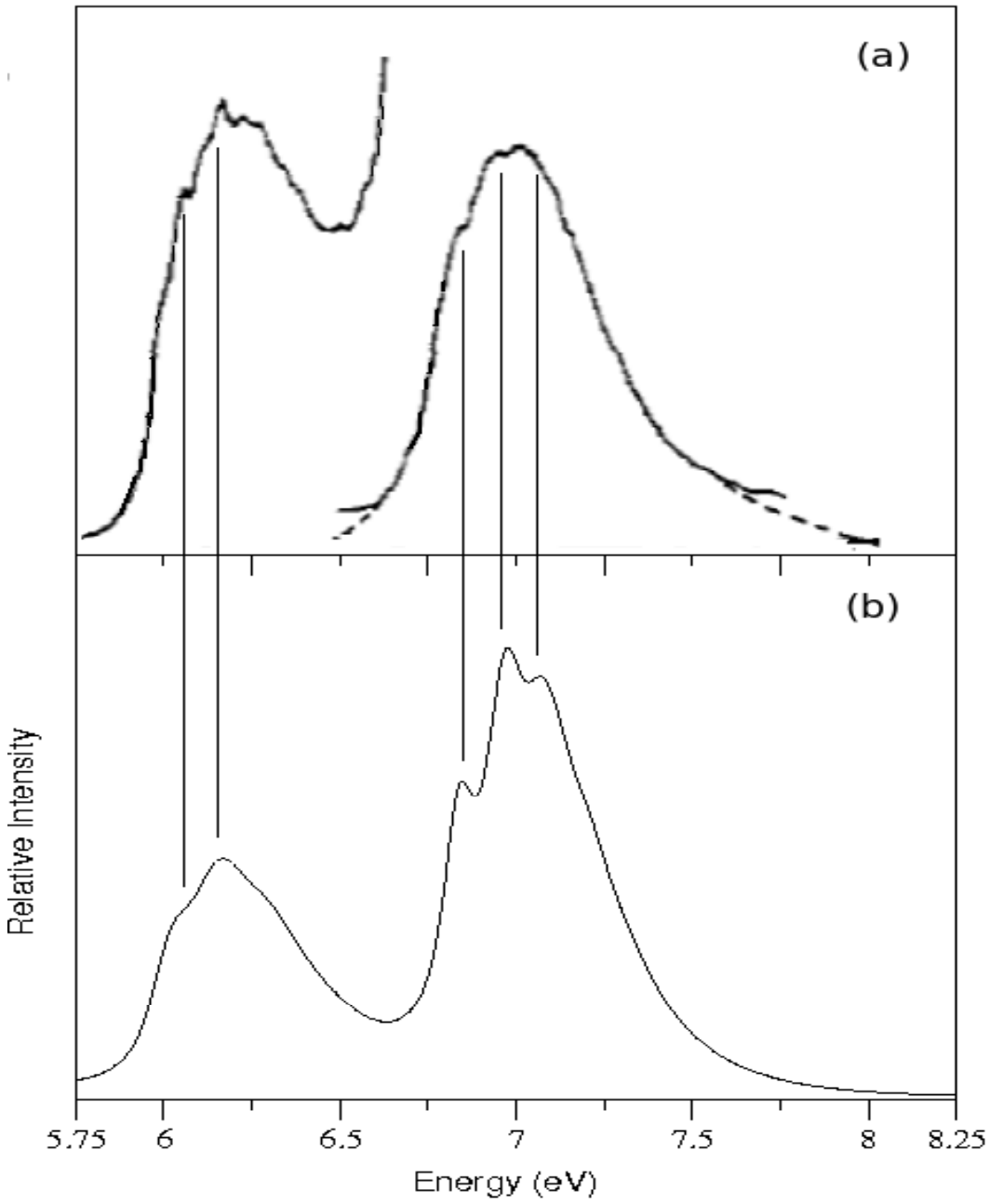

Figure 5.21: Same as in Fig. 5.19, for *m*-DFBz.

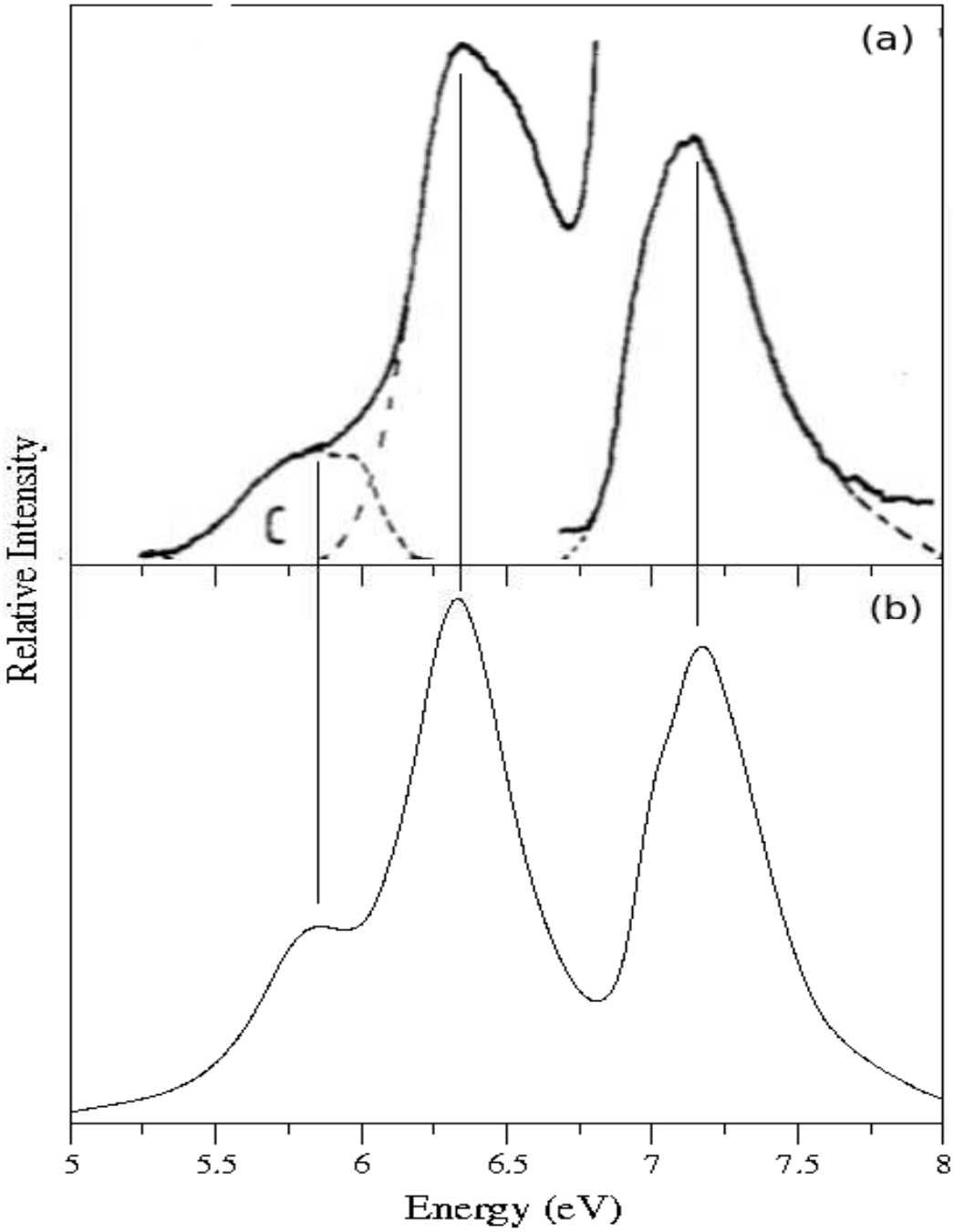

Figure 5.22: Same as in Fig. 5.19, for PFBz.

in panel a of each figure. The two curves in panel a of each figure emerge from a decomposition of the experimental spectrum. This was done to eliminate the overlapping components and to correctly estimate the oscillator strengths of the two curves of $^1B_{1u}$ and $^1E_{1u}$ origin of benzene parentage. Further details on this decomposition of bands are given in Ref. [85]. The technical details of WP calculations by the MCTDH method are given in Table 5.14. The WP calculations are carried out starting from each electronic state of a given molecule. The WP in each calculation is propagated for 200 fs which effectively yields results for 400 fs propagation [134]. The time autocorrelation functions obtained from these calculations are combined, damped with an exponential function, e^{-t/τ_r} (with τ_r=12 fs.), and finally Fourier transformed to calculate the composite vibronic bands for each molecule. The exponential damping corresponds to a spectral broadening equivalent to Lorentzian line shape function of 110 meV FWHM. It can be seen from Figs. 5.19-5.22 that the theoretical results are in satisfactory agreement with the low-resolution experimental data. While all the coupling parameters of the Hamiltonian presented in Tables 5.8-5.11 are used without any adjustments in the present study, it was necessary to adjust some of the VEE values within the error limit of the EOM-CCSD method of average accuracy ∼0.2 eV and maximum deviation of ∼0.4 eV [164] to reproduce the adiabatic excitation positions at their experimental values. Apart from this, no other parameters are adjusted in our theoretical calculations. The VEE values are adjusted in the ∼0.1-0.34 eV range. The adjusted VEE values (in eV) of the concerned electronic states of four fluorobenzene molecules are given below (in the parentheses) along with their *ab initio* calculated values.

State	MFBz	*o*-DFBz	*m*-DFBz	PFBz
S_1	$^1B_2$ 5.055 (5.055)	$^1A_1$ 5.075 (5.075)	$^1B_2$ 5.084 (5.084)	$^1B_2$ 5.111 (5.211)
S_2	$^1A_1$ 6.469 (6.469)	$^1B_2$ 6.503 (6.503)	$^1A_1$ 6.492 (6.492)	$^1B_1$ 6.314 (6.010)
S_3	$^1B_1$ 6.724 (6.553)	$^1B_1$ 6.796 (6.579)	$^1A_1$ 7.272 (7.102)	$^1A_1$ 6.579 (6.420)
S_4	$^1B_2$ 7.288 (7.088)	$^1B_2$ 7.323 (7.163)	$^1B_2$ 7.382 (7.212)	$^1A_1$ 7.475 (7.135)
S_5	$^1A_1$ 7.317 (7.117)	$^1A_1$ 7.378 (7.080)	—	$^1B_2$ 7.509 (7.561)

It is now clear that various CIs between the excited electronic states of the fluorinated benzene molecules play crucial role in the detailed shape of the second and third absorption bands. The associated nonadiabatic coupling causes a demolition of discrete line structure by increasing the vibronic line density. The energetic proximity of CIs to the equilibrium minimum of a state (see Table 5.12 causes the individual bands (as presented in Figs. (5.15-5.18) to overlap strongly. For MFBz, *o*-DFBz and *m*-DFBz weak vibronic structures embedded in a continuum background have been observed in the experiment. In case of PFBz these weak structures are no longer seen and an additional broad band appears at ∼5.85 eV near the onset of the second band. This additional band is absent in the parent benzene and also in the lower fluoroderivatives. Supported by the electronic structure data given above it is certain that this new band originates from the $\pi\sigma^*$ state with σ^* orbital localized on the C-F bond. Because of the perfluoro effect this state comes down in energy and becomes S_2 in PFBz, whereas, it is located beyond 8 eV in the lower fluoroderivatives and is absent in benzene. The adjusted VEE of this state is ∼6.01 eV which is very close to the estimated experimental location of this state. These findings are also in accord with the suggestions made by Philis *et al.* [85] on the origin of this band in PFBz. The electronic structure data reveal strong coupling between S_1 and S_2 state via the a_2 vibrational modes in PFBz (cf., Table 5.11). The minimum of the seam of

S_1-S_2 CIs located only ∼0.73 eV above the S_2 equilibrium minimum. In addition, the minimum of S_2-S_3 CIs also located ∼0.28 eV above the S_2 minimum. The S_2 and S_3 states are also strongly coupled through the vibrational modes of b_1 symmetry. These considerations explain the observed diffuse band structure of the S_2 state of $\pi\sigma^*$ origin in PFBz.

Nonadiabatic transition to the neighboring electronic states also contributes to the low quantum yield of fluorescence emission of this state. Another novel observation made in the experimental second photoabsorption band of MFBz and *o*-DFBz is the following. A new peak (not observed for the remaining fluorobenzene molecules) appeared in their absorption band. This peak disappears when the spectrum of MFBz recorded in the nitrogen matrix and in the pure solid state [85]. This observation favored an assignment of this peak to the 3s member (marked 3s in the panel a of Fig. 5.19 and 5.20) of the $^1E_{1g}$ Rydberg series of the parent benzene molecule. Based on the electronic structure data presented in the Fig. 5.10, we propose that this "extra" peak in these two molecules originates from a transition to their $\pi\sigma^*$ state (with σ^* localized on the C-C bond). The corresponding oscillator strength is nonzero only for MFBz and *o*-DFBz. Also in case of *o*-DFBz the experimental peak located at ∼6.37 eV, quite close to our adjusted theoretical VEE value of ∼6.58 eV. Further analysis reveal large values of the second moment of electronic charge, ∼125.74 (vs. the ground state value of ∼90.31) for MFBz and ∼135.2 (vs. ground state value of ∼100.58) for *o*-DFBz (cf., Table 5.20) supporting a 3s Rydberg character of this $\pi\sigma^*$ state.

Table 5.20: One electron properties (a.u) for gorund and lowest $\pi\sigma^*$ excited singlet state of MFBz and *o*-DFBz at their equilibrium geometries.

Molecule	Electronic state	$\langle z\rangle$	$\langle x\rangle$	$\langle y\rangle$	$\langle x^2\rangle$	$\langle y^2\rangle$	$\langle z^2\rangle$	$\langle r^2\rangle$
MFBz	Ground state	-0.65			4.41	5.56	1.45	90.31
	$\pi\sigma^*$	1.58			3.93	1.86	5.79	125.74
o-DFBz	Ground state	1.08			-3.10	3.87	-0.77	-100.58
	$\pi\sigma^*$	-0.98			8.55	7.36	-15.91	-135.19

5.7 Internal conversion dynamics

Nonradiative transfer of electronic populations in the coupled states dynamics of fluorobenzene molecules discussed in the previous section is examined here. Dynamics of excited electronic states in terms of variation of diabatic electronic populations in time is portrayed in Figs. 5.23-5.26, for MFBz, *o*-DFBz, *m*-DFBz and PFBz molecules, respectively. The panels in a given figure differ in terms of the initial location of the WP. The initial location can be immediately identified from the population value 1.0 of the prepared state at t=0. The population curves in all figures are marked with the appropriate state label. Interesting observations on the dynamical mechanism can be obtained from these population curves in conjunction with the coupling parameters and the stationary points on the potential energy surfaces detailed section 5.4.

Excited state electronic populations displayed in Fig. 5.23 for MFBz reveal minor population flow to the other states when the WP is located initially on the S_1 state (cf., panel a). This state is essentially decoupled from the rest and the minimum of all CIs with others is located at very high energies. The minimum of the S_1-S_3 CIs occurring at ∼12.03 eV, is the lowest among them. Also, the S_1-S_3 coupling via the a_2 vibrational modes is moderately strong (see Tables 5.8 and 5.12). This enables the high energy tail of the WP to move to the S_3 state which can be seen from the small growth of population of this state in time. Significant population flows to the S_3 and S_5 states when the S_2 state is initially populated (cf., Fig. 5.23(b)). The minimum of S_2-S_3 CIs located ∼0.36 eV and ∼0.11 eV above the minimum of S_2 and S_3 state, respectively. The S_2-S_5 CIs occur at much higher energies and are not accessible to the WP during its evolution in the present time scale. The minimum of the S_3-S_5 CIs occurs at ∼ 1.06 eV and ∼0.49 eV above the minimum of S_3 and S_5 state, respectively. These electronic states are strongly coupled by the vibrational modes of b_1 symmetry. Therefore, the WP initially prepared on the S_2 state flows into the S_3 state in time and

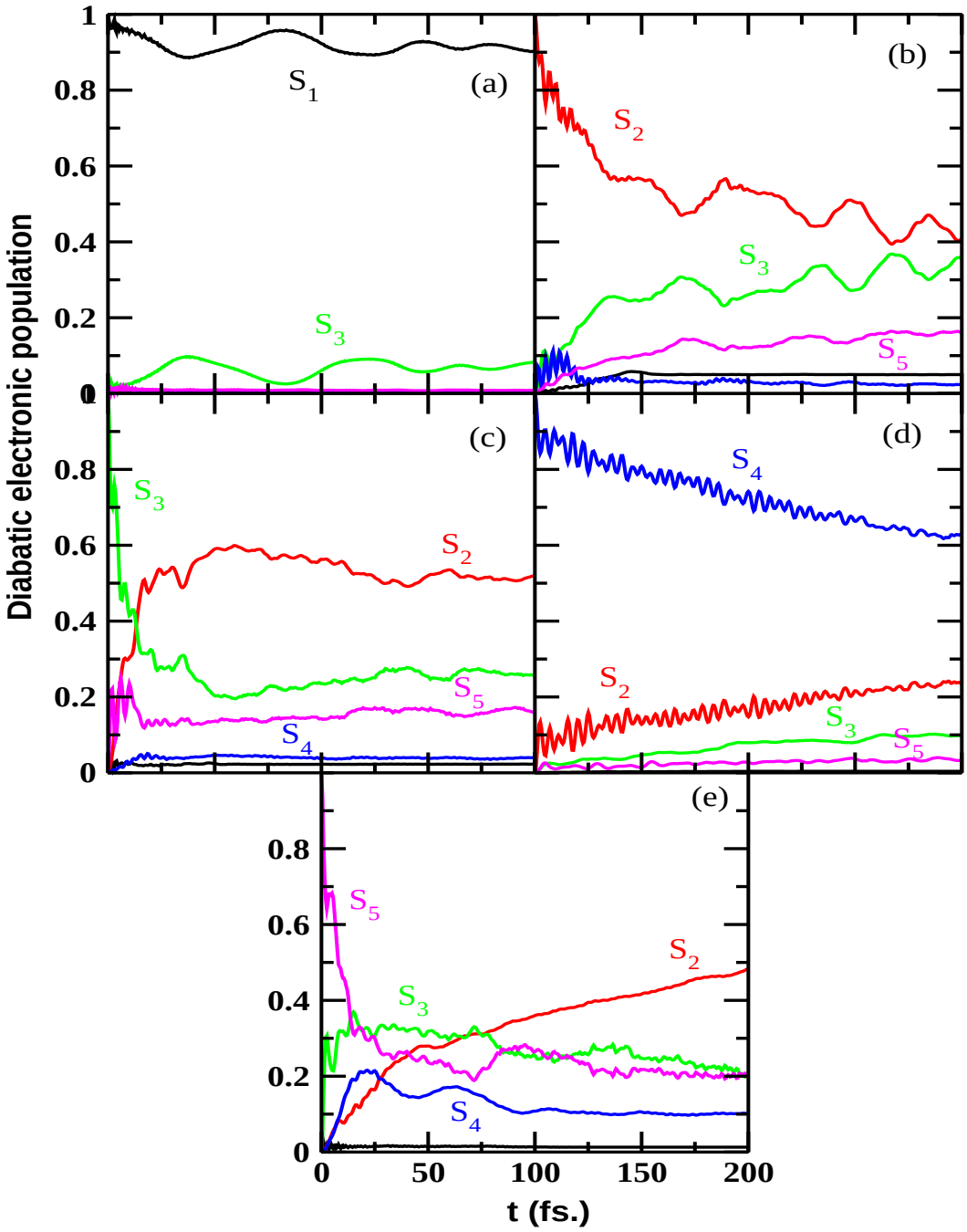

Figure 5.23: Time-dependence of diabatic electronic populations in the S_1-S_2-S_3-S_4-S_5 coupled state nuclear dynamics of MFBz. The results obtained for five different initial locations of the WP are given in panels a-e, respectively.

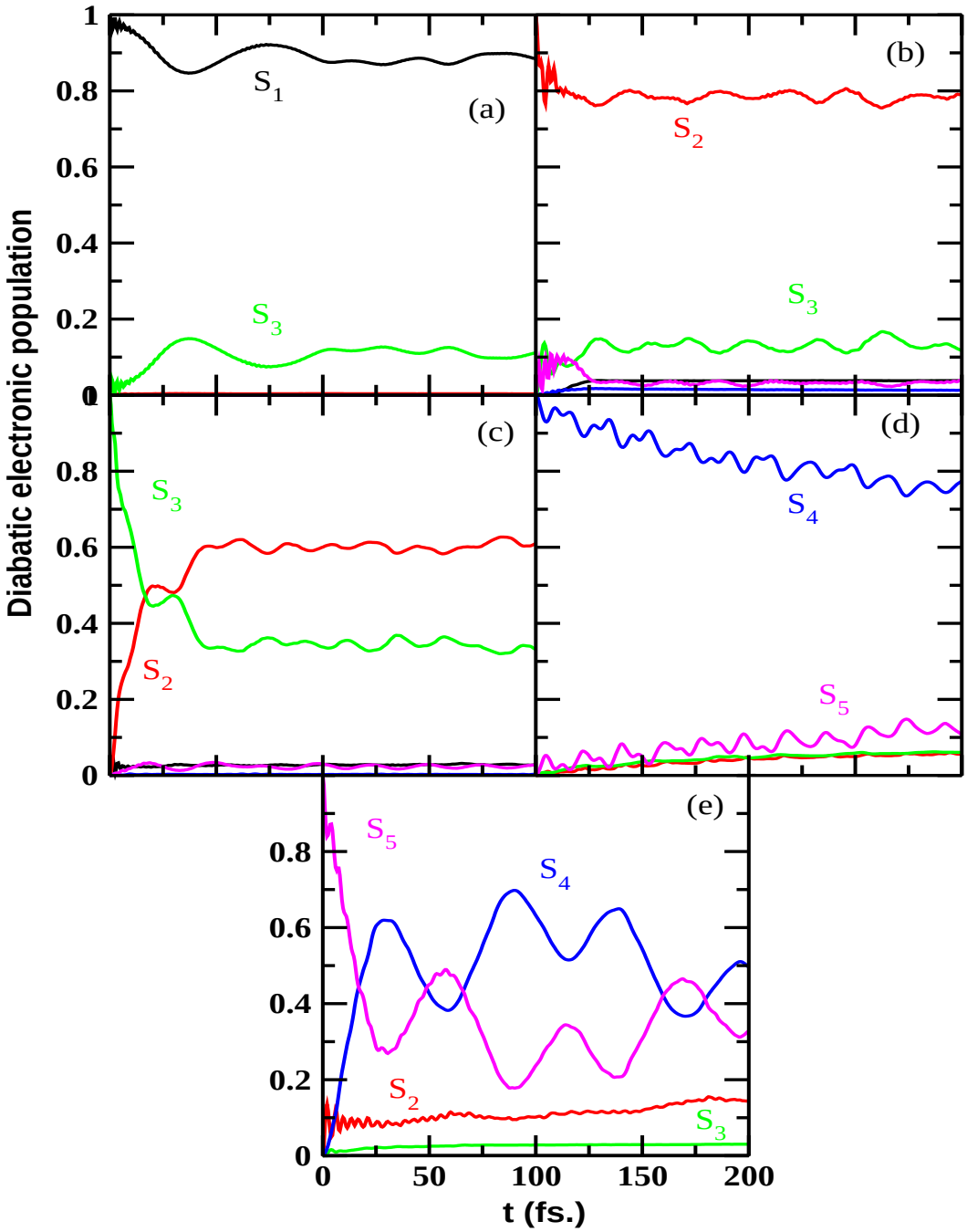

Figure 5.24: Same as in Fig 5.23, for *o*-DFBz.

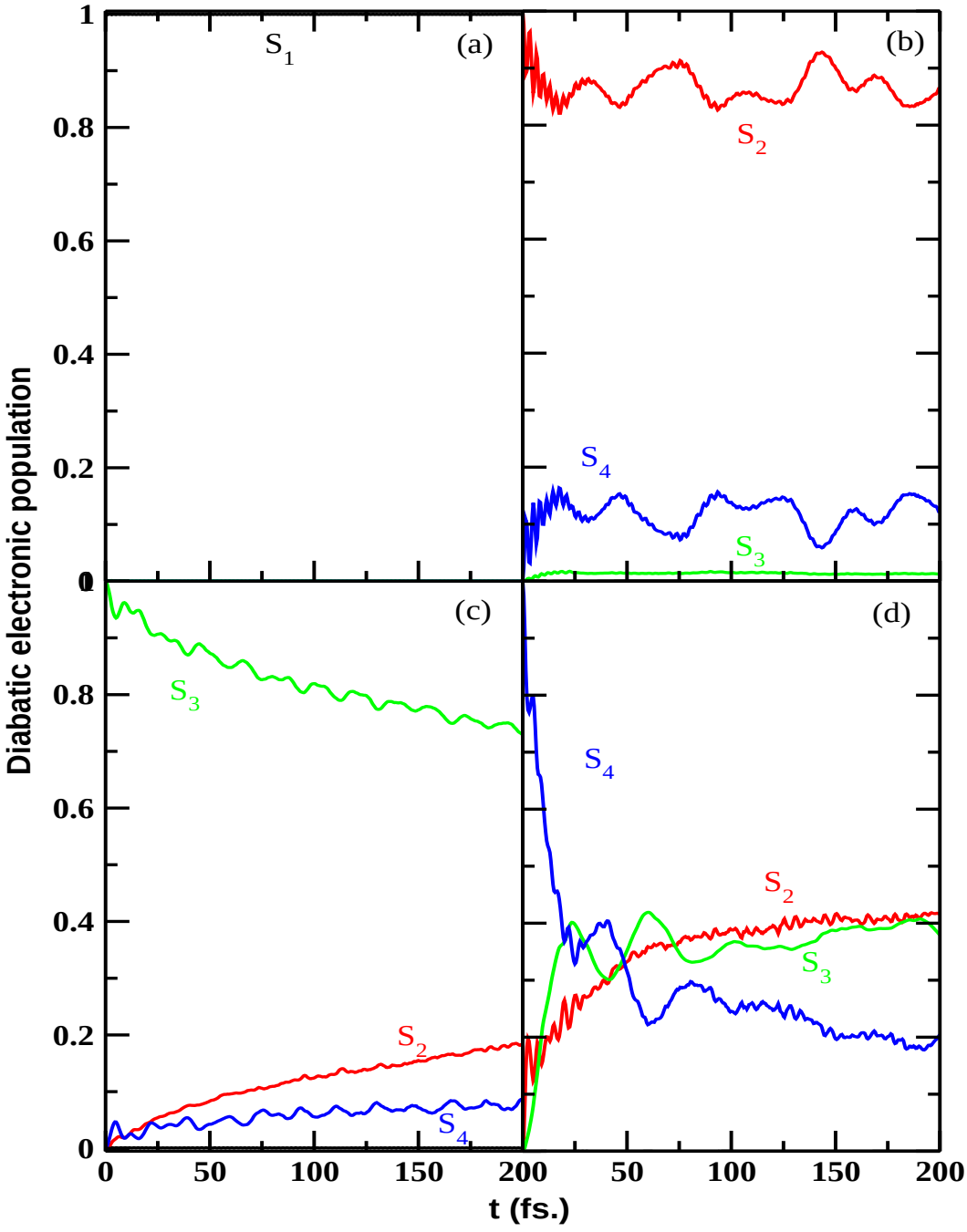

Figure 5.25: Same as in Fig 5.23, for S_1-S_2-S_3-S_4 coupled state dynamics of *m*-DFBz.

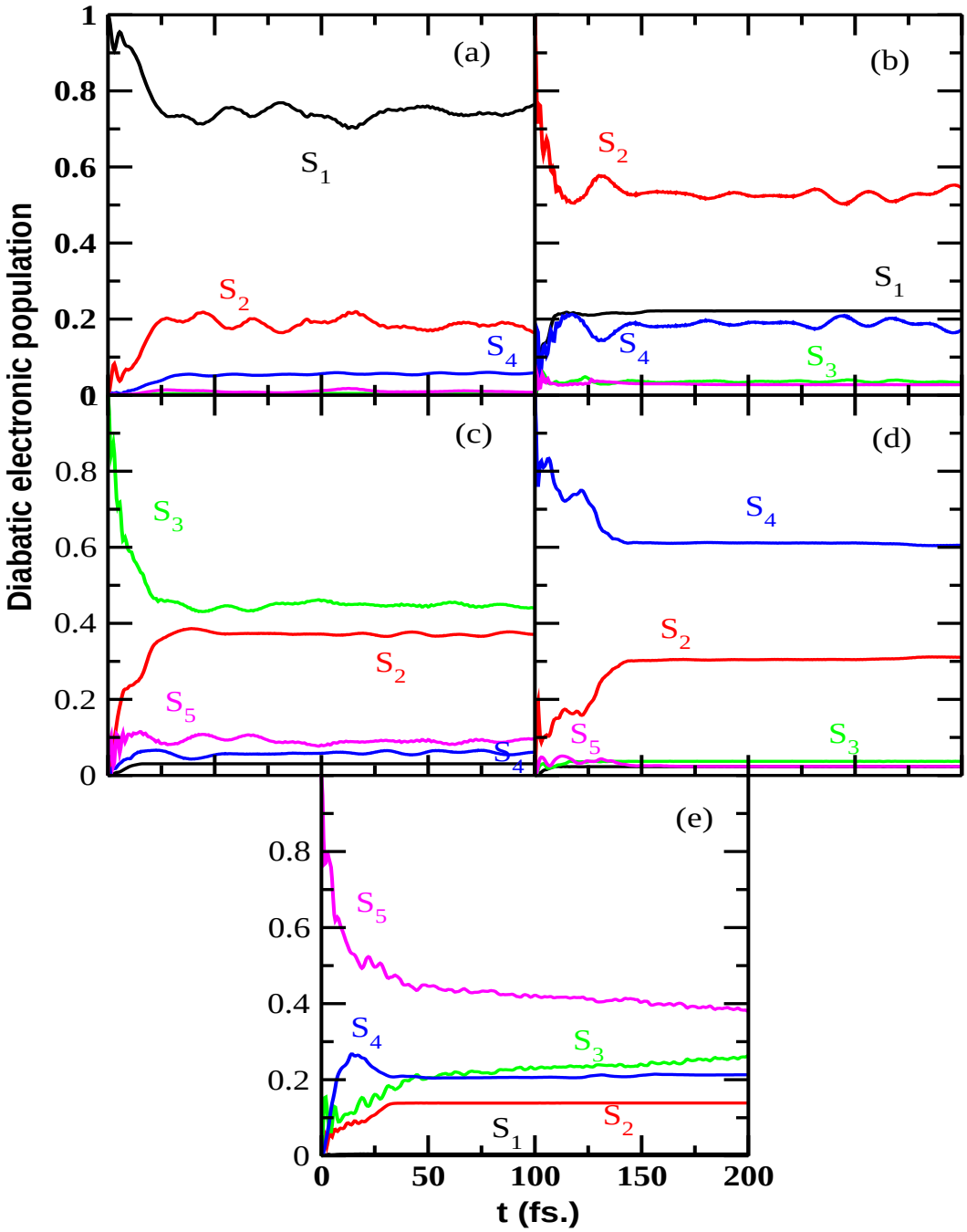

Figure 5.26: Same as in Fig 5.23, for PFBz.

subsequently moves to the S_5 state via S_3-S_5 CIs. The initial fast decay of the population relates to a decay rate of ∼79 fs for the S_2 state. Similar situation arises when the WP is initially located on the S_3 (panel c) and S_5 (panel e) state. In these cases the S_4 state is also populated via the low-lying S_3-S_4 and S_4-S_5 CIs. The minimum of the latter CIs located nearly at the minimum of the S_5 state. Nonradiative decay rate of ∼23 fs can be estimated for both the S_3 and S_5 states from the population curves. S_4 state is weakly coupled with the other states. Therefore, no significant population transfer takes place to the other states when the WP is initially located on the S_4 state as can be seen from panel d of Fig. 5.23.

Electron population dynamics of *o*-DFBz shown in Fig. 5.24 reveals analogous characteristics as that of MFBz when the WP is initially located on the S_1 state (panel a). In this case owing to a lowering of the minimum of the S_1-S_3 CIs somewhat more population (when compared to MFBz) flows to the S_3 state. Although the minimum of the S_2-S_3 CIs in *o*-DFBz located only ∼0.36 eV above the minimum of the S_2 state, because of weak coupling (cf., Table 5.9), no significant population transfer takes place to the S_3 state when the WP is initially prepared on the S_2 state (panel b). Similarly, because of weak coupling of S_4 state with the others, small population flows to the other states when the WP is initially prepared on it (panel d). The minimum of the S_2-S_3 CIs occurs nearly at the minimum of the S_3 state, owing to this quasi-degeneracy, significant population flows to the S_2 state when the WP is initially prepared on the S_3 state (panel c). The initial decrease of S_3 population relates to a decay rate of ∼42 fs of this state. Similar quasi-degeneracy exists between the minimum of S_4-S_5 CIs and the equilibrium minimum of S_5 state. As a result, significant population flows to the S_4 state during the evolution of the WP on the S_5 state (panel e). A nonradiative decay rate of ∼43 fs can be estimated from the initial decrease of the population of the S_5 state.

The CIs of S_1 state of *m*-DFBz with other states occur at very high energies.

Therefore, as can be seen from panel a of Fig. 5.25, that these CIs are not accessible to the WP prepared on the S_1 state. Small population transfer takes place to the S_4 and also to the S_2 state during the evolution of the WP on the S_2 and S_3 state (panel b and c). The WP initially prepared on the S_3 state moves to the S_4 state via S_3-S_4 CIs, which subsequently flows to the S_2 state via S_2-S_4 CIs. The minimum of the S_3-S_4 CIs is quasi-degenerate with the equilibrium minimum of the S_3 and S_4 state. WP initially launched on the S_4 state (panel d) therefore moves to the S_3 state in time. The WP from the latter state subsequently flows to the S_2 state as the minimum of the S_2-S_3 CIs located only ∼0.57 eV above the equilibrium minimum of the S_3 state. The initial sharp decay of the population in Fig. 5.25(d) relates to a nonradiative decay rate of ∼34 fs of the S_4 state of *m*-DFBz.

Finally, the electron population dynamics of PFBz molecule is displayed in Fig. 5.26. As found in section 5.4 that the minimum of S_1-S_2 CIs comes down in energy and therefore it becomes accessible for the WP moving on the S_1 state in the energy range of the present investigations. As can be seen from Fig. 5.26(a) that both the S_2 and S_4 states are populated in this case, in contrast to the situation in MFBz and *o*-DFBz in which the S_3 state is populated [cf., Fig 5.23(a) and 5.24(a)]. Like in *m*-DFBz the S_1-S_3 CIs occur at high energies in PFBz. The minimum of the S_1-S_4 CIs also occurs at a very high energy in this case. However, some population flows to the S_4 state via relatively low-lying S_2-S_4 CIs. It is discussed above that the S_1-S_2 CIs are the bottleneck underlying the broadening of the $S_1 \leftarrow S_0$ absorption band in PFBz. We repeat that the S_2 state in PFBz is of $\pi\sigma^*$ origin, with σ^* MO localized on the C-F bond. The corresponding state in the other fluorobenzene molecules discussed here occurs beyond 8.0 eV. The unique feature of the S_2 state in PFBz is that it forms energetically low-lying CIs (cf., Table 5.12) with all other states. Therefore, the S_2 state is populated for all five different initial locations of the WP shown in Fig. 5.26. A nonradiative decay rate of ∼69 fs can be estimated from the population curve of S_2 state

given in panel b. Similarly, decay rate of ∼52 fs can be estimated for the S_3 and S_5 state. Like other fluorobenzene molecules, the S_4-S_5 intersection minimum is quasi-degenerate with the equilibrium minimum of S_4 and S_5 state. Overall, it appears that the nonadiabatic coupling effect in the electronically excited PFBz molecule is relatively greater compared to others. This leads to the appearance of much broader and diffuse electronic absorption bands in PFBz.

5.8 summary and outlook

The structure of the electronic ground and low-lying excited singlet states of MFBz, *o*-DFBz, *m*-DFBz and PFBz is theoretically studied by EOM-CCSD method. Detail topography of these electronic states is examined and diabatic electronic states are derived from the calculated adiabatic energies. The diabatic coupling surfaces among various electronic states are also derived along the relevant vibrational modes in accordance with the symmetry selection rules. The electronic structure data establish multiple CIs in the excited electronic states of all four molecules. The energetic minimum of these CIs and also the equilibrium minimum of electronic states are estimated and are related to the observed spectral features of these molecules. Vibronic eigenvalue spectra and time-dependent dynamics of the excited electronic states are calculated from first principles. The theoretical results are found to be in very good accord with the available experimental results [85].

The important outcomes of this study are the following. The S_0 ground electronic state of all four molecules is energetically well separated from the excited states. The nature of their S_1 state (LUMO) is $\pi\pi^*$ localized on the C-C bond. While the nature of the S_2 state is $\pi\pi^*$ (localized on the C-C bond) type up to tetrafluorobenzene, this state is of $\pi\sigma^*$ type (with σ^* localized on the C-F bond) in PFBz and HFBz. The latter state occurs at high energy for fluoroderivatives with four or less fluorine atoms. Owing to the perfluoro effect this state comes

down in energy and becomes S_2 in PFBz and HFBz. Low-energy CIs between the S_1 and S_2 states of PFBz have been found. These intersections will have crucial roles in the observed absorption and fluorescence spectra of PFBz, which are different from other three molecules treated here. The further higher excited states S_3 , S_4 and S_5 are energetically close (often quasi-degenerate) in all four molecules (except the S_5 state of m-DFBz which occurs beyond 8 eV) and they form numerous CIs. The vibronic energy level structure of these electronic states of all four molecules is systematically investigated through reduced dimensional matrix diagonalization calculations. The final theoretical simulations using the full Hamiltonian of Eqs. (5.2-5.3d) are carried out by propagating the WPs using the MCTDH algorithm [118–123]. The structured $S_1 \leftarrow S_0$ electronic absorption bands of MFBz, *o*-DFBz and *m*-DFBz are in good agreement with the experimental results. This band in PFBz is blurred due to the occurrence of low-energy $S_1(\pi\pi^*) - S_2(\pi\sigma^*)$ CIs. The coupling between these states is also very strong and the resulting nonadiabatic effects cause a huge increase of the spectral line density. A biexponential decay of fluorescence emission originates from this coupling. The second and third absorption bands are formed by energetically close-lying S_2, S_3, S_4 and S_5 electronic states of these molecules (except for *m*-DFBz for which states up to S_4 are relevant). Because of energetic proximity these bands strongly overlap and occurrence of numerous CIs between these electronic states contributes significantly to the complex structureless pattern of these bands. While weak vibronic structures embedded in a continuum background have been found in MFBz, *o*-DFBz and *m*-DFBz, such structures are absent in PFBz because of relatively stronger surface coupling effects. In contrast to the other fluoroderivatives (considered here) and the parent benzene, an additional band observed near the onset of the second absorption band is attributed to originate from the S_2 $(\pi\sigma^*)$ state of PFBz. It bears an evidence of the effect due to increasing fluorine substitution and is discussed in detail in the text. The strong coupling between the $S_1 - S_2$ and $S_2 - S_3$ states contributes to the observed diffused and broad

structure of this additional band in PFBz. Another novel finding of this paper is related to the experimental findings of a new peak in the band structures of MFBz and *o*-DFBz. This peak is not observed in the remaining fluoroderivatives. This is assigned to be due to the 3s member of the $^1E_{1g}$ Rydberg series of the parent benzene molecule. We find that this peak originates from the $\pi\sigma^*$ (with σ^* MO localized on the C-C bond) state of these two molecules. The oscillator strength for this transition is nonzero for this two molecules only and supports this assignment. In addition, the Rydberg character of this $\pi\sigma^*$ state in these two molecules is confirmed by examining the second moment of the electronic charge.

Chapter 6

Conclusions and future directions

A detailed description of the photoinduced quantum nonadiabatic dynamics of the low lying electronic states of organic fluorinated hydrocarbons and radical cations is presented in this thesis. The investigations are carried out with the aid of *ab initio* electronic structure calculations and quantum dynamical simulations of underlying nuclear motion. Clearly, the study of multimode molecular dynamics on the coupled electronic surfaces reveals a challenging theoretical and computational problem. The success of the present theoretical approach lies on the adoption of simple VC model Hamiltonian. The essential simplifications are the assumptions of harmonic diabatic potentials and truncation of Taylor series (around the equilibrium geometry of the neutral molecule and along the dimensionless nuclear coordinates) in low-order. We, in the present thesis, have concentrated on the systems where the interplay of the nontotally symmetric coupling mode(s) with the totally symmetric tunning mode(s) leads to a CI of the adiabatic PESs. The advantages of this approach are its conceptual and technical simplicity. It also allow the exact numerical solution of the Scrödinger equation via diagonalization of large sparse matrices. This technique therefore enabled us to carry out intensive and thorough investigation into a new regime of non-BO phenomena *i.e.* strong VC involving several nonseparable vibrational modes. The results reveal a wealth of the interesting physical phenomena. The

typical spectroscopic effects of CIs have been identified and more or less quantitatively reproduced in the photoelectron spectra of CF_3CN and $C_6H_3F_3$, and the absorption spectra of MFBz, *o*-DFBz, *m*-DFBz and PFBz.

The basic concept of the VC leading to the crossings of the electronic PESs is discussed. The theoretical treatment of VC employing state-of-the art quantum chemistry and first principles quantum dynamical methods is presented at length. The complexity in the assignment of these vibronic spectra of polyatomic molecules is addressed by showing the recent results of the representative examples mentioned above. The calculated high density vibronic levels have been interpreted for a typical CI situation and with associated intersecting adiabatic PESs. The mechanistic details of the ultrafast nonradiative dynamics of the excited states is studied. These dynamical observables are compared with the available experimental data to validate the established theoretical model. The discussions in this thesis reveal the need of understanding the complex VC mechanisms while dealing with the electronically excited molecules in particular, and the recent advent in the experimental and theoretical techniques to observe and treat them.

The main findings of the present work are given below.

1. (a) The symmetric vibrational modes C-N stretching (ν_1) and C-C stretching (ν_2) are crucial and strongly excited in the $\widetilde{X}$ -$\widetilde{A}$ -$\widetilde{B}$ -$\widetilde{C}$ -$\widetilde{D}$ electronic manifold of CF_3CN. Whereas the former leads to low-energy crossings of the $\widetilde{X}$ -$\widetilde{A}$ electronic states, the latter and umbrella bending (ν_4) are both important for the low-energy $\widetilde{B}$ -$\widetilde{C}$ -$\widetilde{D}$ electronic states.

(b) The JT effects in the $\widetilde{X}$ electronic states is far weaker compared to that in the $\widetilde{D}$ state. The JT stabilization energy of $\sim$4.6 $\times$ 10^{-3} and $\sim$0.48 eV are estimated, respectively, for these electronic states.

(c) The JT and PJT interactions of the $\widetilde{X}$ -$\widetilde{A}$ electronic states mostly contribute to the overall vibronic structure of the first photoelectron band. The PJT coupling due to ν_8 vibrational mode is found to be the strongest, and the

vibrational modes ν_2, ν_7 and ν_8 are found to make progressions in this band.

(d) Energetically close lying $\widetilde{B}$ -$\widetilde{C}$ -$\widetilde{D}$ electronic states are found to be responsible for the highly overlapping structure of the second photoelectron band. The relatively stronger JT coupling within the $\widetilde{D}$ electronic state and appreciable PJT coupling due to ν_5 and ν_6 vibrational modes among these electronic states contributes to the diffuse vibronic structure of this band. The vibrational modes ν_2, ν_4, ν_5 and ν_7 form the major progressions in this band.

(e) An ultrafast nonradiative decay rate of $\sim$ 21 fs for the $\widetilde{D}$ state is estimated from the decay of electronic population in the coupled electronic manifold.

2. (a) The vibronic spectrum of coupled $\widetilde{X}$ -$\widetilde{A}$ -$\widetilde{B}$ -$\widetilde{C}$ electronic manifold of $TFBz^+$ is calculated including 23 relevant vibrational modes by employing the MCTDH WP propagation method. The resulting spectrum is found to be in excellent accord with broad band photoelectron spectroscopy results certifying the reliability of the present theoretical model.

(b) The vibrational energy level spectrum of the $\widetilde{X}$ state of $TFBz^+$ is simulated by performing reduced dimensional calculations employing the matrix diagonalization scheme. The precise locations and assignments of the vibrational levels are compared with the highly resolved MATI, LIF and (2+1) REMPI spectroscopy results. Results are found to be in very good agreement with the experimental data.

(c) Symmetric vibrational modes ν_2 and ν_3 are strongly excited in the vibronic bands of the $\widetilde{X}$ -$\widetilde{A}$ -$\widetilde{B}$ -$\widetilde{C}$ electronic manifold. While ν_3 causes low-energy crossings of the $\widetilde{A}$ -$\widetilde{B}$ electronic states, all three symmetric vibrational modes (ν_2-ν_4) are important for the low-energy crossings of $\widetilde{B}$ -$\widetilde{C}$ electronic states.

(d) The JT effect in the $\widetilde{X}$ electronic state is far weaker compared to that in the $\widetilde{B}$ state. The JT stabilization energies of $\sim$ 0.142 eV and $\sim$ 0.346 eV are estimated, respectively, for these electronic states.

(e) The vibronic structure of the $\widetilde{X}$ state is mostly dominated by progressions due to the symmetric ν_2 and degenerate ν_9 and ν_{13} vibrational modes. This state

is energetically well separated from others and impact of PJT coupling on its vibronic structure is not significant.

(f) Among the $\widetilde{A}$, $\widetilde{B}$ and $\widetilde{C}$ states, the $\widetilde{B}$ and $\widetilde{C}$ states undergo fast internal conversions in 51 fs and 7 fs, respectively. The coupling of the $\widetilde{A}$ state with either $\widetilde{X}$ or the $\widetilde{B}$ state is weak and occurs at higher energies. Therefore, the low-amplitude nuclear motion in the $\widetilde{A}$ state remains unaffected by these couplings. This leads to a long-lived nature of the $\widetilde{A}$ state and triggers fluorescence emission in $TFBz^+$.

3. (a) The optical absorption spectrum of the electronic ground and low-lying excited singlet states of MFBz, *o*-DFBz, *m*-DFBz and PFBz is theoretically calculated by employing WP propagation approach. The theoretical results are in excellent agreement with the available experimental data.

(b) The S_0 ground electronic state of all four molecules is energetically well separated from the excited states. The nature of their S_1 state (LUMO) is $\pi\pi^*$ localized on the C-C bond.

(c) While the nature of the S_2 state is $\pi\pi^*$ (localized on the C-C bond) type up to tetrafluorobenzene, this state is of $\pi\sigma^*$ type (with σ^* localized on the C-F bond) in PFBz and HFBz.

(d) This $\pi - \sigma^*$ state occurs at high energy for fluoroderivatives with four or less fluorine atoms. Owing to the perfluoro effect this state comes down in energy and becomes S_2 in PFBz and HFBz. Low-energy CIs between the S_1 and S_2 states of PFBz have been found. These intersections will have crucial roles in the observed absorption and fluorescence spectra of PFBz, which are different from other three molecules treated here.

(e) The structured $S_1 \leftarrow S_0$ electronic absorption bands of MFBz, *o*-DFBz and *m*-DFBz are in good agreement with the experimental results. This band in PFBz is blurred due to the occurrence of low-energy $S_1(\pi\pi^*) - S_2(\pi\sigma^*)$ CIs.

(f) The coupling between S_1 and S_2 states of PFBz is very strong and the resulting nonadiabatic effects cause a huge increase of the spectral line density.

A biexponential decay of fluorescence emission originates from this coupling.

(g) The complex structureless pattern of the second and third absorption bands are formed by the occurrence of numerous CIs between energetically close-lying S_2, S_3, S_4 and S_5 electronic states of these molecules (except for *m*-DFBz for which states up to S_4 are relevant).

(h) In contrast to the other fluoroderivatives (considered here) and the parent benzene, an additional band observed near the onset of the second absorption band is attributed to originate from the S_2 ($\pi\sigma^*$) state of PFBz which bears an evidence of the effect due to increasing fluorine substitution.

(i) The strong coupling between the $S_1 - S_2$ and $S_2 - S_3$ states contributes to the observed diffused and broad structure of this additional band in PFBz.

(j) Another novel finding of this work is related to the experimental findings of a new peak in the band structures of MFBz and *o*-DFBz.

In conclusion, the present study clearly indicates the out most importance of electronic nonadiabatic interactions in the broad and diffuse nature of the observed vibronic bands, ultrafast nonradiative decay and low quantum yield of fluorescence of electronically excited fluorinated hydrocarbons. The chemical impact of increasing fluorine substitution on the electronic structure and nuclear dynamics is established. The study also highlights the difficulty involved in full quantum mechanical solutions of problems in which a large number of electronic and nuclear degrees of freedom are relevant (like in the present case) and opens the doorway for further research in this important area of chemical physics.

To this end we mention that the present work is restricted to the VC of electronic states with same spin multiplicities (e.g., singlet-singlet VC for optical absorption spectra). This study can be further extended to the systematic investigation of VC for electronic states of different spin multiplicities (e.g., singlet-triplet VC). In addition, further refinements of the potential energy curves particularly along low-frequency modes is highly desirable. This is because our previous experience (in case of $TFBz^+$) shows that the potential energy curves

of the lower adiabatic sheet of the JT split $\widetilde{B}$ state are extremely flat along ν_9 and ν_{10} vibrational modes, which leads to a convergence problem in the spectrum calculation. Therefore, although the present potential energy curves reproduces the low resolution photoelectron spectrum very well, further refinements of the potential energy curves are necessary for high resolution spectroscopic application. Another possible extension of this work is the inclusion of rotational degrees of freedom in the present model VC Hamiltonian to obtain information on rovibronic levels of isolated molecules.

Furthermore, a recent recording of vibronic structures of the Rydberg series converging to the first ionization threshold of HFBz and 1,3,5-TFBz through (2+1) REMPI experiment [158] have left the ambiguity over the justification of vibrational assignments given by Kwon *et al.* [173]. It appears from the work done by Kwon *et al.* [173] that for HFBz, the linear JT coupling parameters of ν_{17} (C-C-C bend, ∼488 cm^{-1}) vibration is about three times larger than ν_{18} (C-F bend, ∼286 cm^{-1}) vibration. Both these modes have considerable quadratic coupling strength [173]. Therefore, the overtones and combination levels of these modes are expected to be excited in the spectrum. The peak at ∼326 cm^{-1} in the work done by Philis *et al.* has been observed at ∼321 cm^{-1} in MATI [173] spectrum and at ∼326 cm^{-1} or ∼335 cm^{-1} in the B2A$_{2u}$ → X2E$_{1g}$ emission spectrum of HFBz$^+$ [174]. This is assigned to $17^1_0(3/2)$ by Kwon and Kim [173]. However in the experimental measurement of Philis *et al.* [158], the intensity of this peak is higher than the ∼286 cm^{-1} peak and both are reduced when circularly polarized light is used. The $17^1_0(3/2)$ level has E$_{2g}$ symmetry in the d$_1$e$_{1g}$ Rydberg state (see Fig. 4 of ref [175] for the case of Bz) and therefore it cannot be attenuated under circular polarized excitation. The attenuation of the peak at ∼326 cm^{-1}, under the circular excitation, suggests that it cannot be a j=3/2 level. It has to be a level with an overall A$_{1g}$ symmetry. Therefore, extensive theoretical studies are required to assign this and other observed peaks unambiguously.

Appendix A

Adiabatic potential energy surfaces and conical intersections

The concept of adiabatic electronic potential energy surfaces (PESs) is important for the interpretation and understanding of all kinds of phenomena in molecular physics and chemistry. Therefore, we shall consider in some detail of the adiabatic PESs. To start with, let us consider a 2×2 model diabatic Hamiltonian containing N tuning modes (totally symmetric, Q_{gi}) and M coupling (non-totally symmetric, Q_{uj}) vibrational modes and is given as

$$\mathcal{H} = (\mathcal{T}_N + \mathcal{V}_0)\mathbf{1} + \begin{pmatrix} E_1 + \sum_{i=1}^{N} \kappa_i^{(1)} Q_{gi} & \sum_{i=1}^{M} \lambda_j Q_{uj} \\ \sum_{i=1}^{M} \lambda_j Q_{uj} & E_2 + \sum_{i=1}^{N} \kappa_i^{(2)} Q_{gi} \end{pmatrix}, \quad \text{(A.1a)}$$

Where

$$\mathcal{T}_N = -\frac{1}{2}\sum_{i=1}^{N} \omega_i \left(\frac{\partial^2}{\partial Q_{gi}^2}\right) - \frac{1}{2}\sum_{j=1}^{M} \omega_j \left(\frac{\partial^2}{\partial Q_{uj}^2}\right), \quad \text{(A.1b)}$$

$$\mathcal{V}_0 \;=\; \frac{1}{2}\sum_{i=1}^{N}\omega_i Q_{gi}^2 + \frac{1}{2}\sum_{j=1}^{M}\omega_j Q_{uj}^2, \tag{A.1c}$$

The quantities κ and λ represents the intrastate and interstate coupling parameters. Here E_1 and E_2 (assuming $E_1 < E_2$) are the ionization or excitation energies of the coupled electronic states at the reference geometry $\mathbf{Q}$=0, where $\mathbf{Q}$ represents collectively the set of nuclear coordinates (Q_g, Q_u). T_N is the nuclear kinetic energy operator and V_0 is the potential energy operator.

The adiabatic PESs are obtained by diagonalizing the above Hamiltonian in the fixed-nuclei limit, $T_N \rightarrow 0$, as follows [4].

$$\mathbf{S}^{\dagger}(\mathcal{H} - T_N 1)\mathbf{S} \;=\; V \tag{A.1d}$$

$$V \;=\; \begin{pmatrix} V_1(\mathbf{Q}) & 0 \\ 0 & V_2(\mathbf{Q}) \end{pmatrix} \tag{A.1e}$$

Here $\mathbf{S}$ is a 2×2 unitary matrix which describes the diabatic to adiabatic transformation. V_1 ($\mathbf{Q}$) and V_2 ($\mathbf{Q}$) are the adiabatic PESs of Hamiltonian (A. 1a).

For detail discussion of the static aspects of the adiabatic PESs, it is convenient to rewrite $\mathcal{H}$ of Eq. (A.1a) in the following general form:

$$\mathcal{H} \;=\; \mathcal{H}_0\mathbf{1} + \begin{pmatrix} -d & c \\ c & d \end{pmatrix} \tag{A.1f}$$

where

$$\mathcal{H} = \mathcal{T}_N + \mathcal{V}_0 + \Sigma + \sigma Q_g \tag{A.1g}$$

$$\Sigma = (E_1 + E_2)/2 \tag{A.1h}$$

$$\Delta = (E_2 - E_1)/2 \tag{A.1i}$$

$$\sigma_i = (\kappa_i^{(1)} + \kappa_i^{(2)})/2 \tag{A.1j}$$

$$\delta_i = (\kappa_i^{(2)} - \kappa_i^{(1)})/2 \tag{A.1k}$$

$$d = \Delta + \sum_{i=1}^{N} \delta_i Q_{gi} \tag{A.1l}$$

$$c = \sum_{i=} \lambda_j Q_{uj} \tag{A.1m}$$

The expression of adiabatic potentials within the linear vibronic coupling (LVC) model are then read

$$V_{1,2}(\mathbf{Q}) = V_0(\mathbf{Q}) + \Sigma + \sum_{i=1}^{N} \sigma_i Q_{gi} \mp W \tag{A.1n}$$

$$W = \sqrt{d^2 + c^2} \tag{A.1o}$$

Now the conditions for the occurrence of a CI of the adiabatic PESs of the above Hamiltonian are simply $d = 0$ and $c = 0$. These conditions define a hypersurface of dimension $N + M - 2$ in the $N + M$ dimensional coordinate space i.e in case of one coupling mode and two tuning modes, for example, we obtain a line of CIs in three dimensional space.

The minimum of the seam of CIs within LVC scheme is given by

$$V_{min}^{(c)} = \Sigma + \frac{(F-\Delta)^2}{2D} - \frac{1}{2}\sum_{i=1}^{N} \sigma_i^2/w_{gi} \tag{A.2}$$

The position of the minimum in the space of the tuning mode within LVC scheme is

$$(Q_{gi}^{(c)})_{min} = \frac{(\delta_i/\omega_{gi})(F-\Delta)}{D} - \frac{\sigma_i}{w_{gi}}, \quad i = 1, \cdots, N \tag{A.3}$$

The minimum of the seam of the CIs relative to the minimum of the upper adiabatic PES is given by

$$V_{min}^{(c)} - (V_2)_{min} = \frac{1}{2D}(\Delta - D - F)^2 \tag{A.4}$$

where

$$D = \sum_{i=1}^{N} \frac{\delta_i^2}{w_{gi}} \tag{A.5}$$

$$F = \sum_{i=1}^{N} \frac{\delta_i \sigma_i}{w_{gi}} \tag{A.6}$$

Next we shall examine the CI of two diabatic surfaces (j = 1,2) described by diabatic potentials containing both linear ($\kappa_i^{(j)}$) and quadratic ($\gamma_i^{(j)}$) coupling term (*cf.* Eq. A.1f) *i.e.* within QVC scheme

$$V_j(\mathbf{Q}) \;=\; E_j + \sum_{i=1}^{N} \kappa_i^{(j)} Q_i + [\frac{\omega_i}{2} + \gamma_i^{(j)}] Q_i^2. \tag{A.7}$$

Since $\mathrm{V}_1(\mathbf{Q}) = \mathrm{V}_2(\mathbf{Q})$ at CI, one immediately obtains the equation of the conical intersection in the $\mathbf{Q}$-space as

$$\Delta + \sum_{i=1}^{N} (\delta_i Q_i + \gamma_i Q_i^2) \;=\; 0, \tag{A.8}$$

where $\gamma_i = (g_i^{(2)} - g_i^{(1)})/2$. We mention that inclusion of quadratic coupling term in the diabatic potential, as obtained in the l.h.s. of Eq. (A.8), making the hypersurface to differ from a hyperline as encountered in the LVC case.

The energies at the conical intersection seam are given by $\mathrm{V}_2(\mathbf{Q})$ (or $\mathrm{V}_1(\mathbf{Q})$), with $\mathbf{Q}$ subjected to the constraint (A.8). To obtained the minimum of the seam of the CI, one has to consider the functional $F(\mathbf{Q}) \equiv V_2(\mathbf{Q}) + \mu G(\mathbf{Q})$, where μ is a Lagrange multiplier and $G(\mathbf{Q})$ is a shorthand for the l.h.s. of Eq. (A.8). By imposing $\frac{\partial F(\mathbf{Q})}{\partial Q_i} = 0$ one straightforwardly gets [160]

$$Q_i \;=\; -\frac{\kappa_i^{(2)} + \mu\delta_i}{\omega_i + 2g_i^{(2)} + 2\mu\gamma_i}. \tag{A.9}$$

The insertion of the above expressions for Q_i into Eq. (A.8) yields

$$\Delta + \sum_{i=1}^{N} \left[-\delta_i \frac{\kappa_i^{(2)} + \mu\delta_i}{\omega_i + 2g_i^{(2)} + 2\mu\gamma_i} + \gamma_i \left(\frac{\kappa_i^{(2)} + \mu\delta_i}{\omega_i + 2g_i^{(2)} + 2\mu\gamma_i} \right)^2 \right] \;=\; 0. \tag{A.10}$$

To find the seam minimum, we have to solve the above equation for the Lagrange multiplier μ. Within the LVC model ($\gamma_i = 0$), Eq. (A.10) is linear in μ, possessing

therefore exactly one root. Putting this root value in Eq. (A.9), one can get an unique solution of the minimization problem irrespective of the number of the tuning modes. In contrast to this, within QVC model we are lead to the problem of solving an algebraic equation of order 2N+1, where N is the number of tuning modes possessing nonvanishing quadratic couplings ($\gamma_i \neq 0$). In general, out of the total number 2N+1 of its roots, there are several real roots. To determine the energy E_s of the minimum of the seam of the CI, one has to select thereof that root for μ, which, inserted into Eq. (A.9), leads to the smallest value of $V_2(\mathbf{Q})(= E_s)$. To solve the minimization problem along the approach described above, we used the MATHEMATICA package version 5.1. Fortunately, it succeeded to find the roots of the highly nonlinear equation (A.10) for fluorobenzene molecules where upto 7 tuning modes were accounted for.

Bibliography

[1] M. Born and R. Oppenheimer, Ann. Physik (Leipzig) **84**, 457 (1927).

[2] M. Born, Nachr. Akad. Wiss. Göttingen, Math. -Physik. Kl. II, Berlin, 1951.

[3] M. Born and K. Huang, *The Dynamical Theory of Crystal Lattices* (Oxford University Press, London, UK, 1954).

[4] H. Köppel, W. Domcke, and L. S. Cederbaum, Adv. Chem. Phys. **57**, 59 (1984).

[5] E. Teller, J. Phys. Chem. **41**, 109 (1937).

[6] G. Herzberg and H. C. Longuet-Higgins, Discuss. Farad. Soc. **35**, 77 (1963).

[7] T. Carrington, Discuss. Farad. Soc. **53**, 27 (1972); Acc. Chem. Res. **7**, 20 (1974).

[8] D. R. Yarkony, J. Phys. Chem. **100**, 18612 (1996); Acc. Chem. Res. **31**, 511 (1998).

[9] M. A. Robb, F. Bernardi, and M. Olivucci, Pure and Appl. Chem. **67**, 783 (1995).

[10] F. Bernardi, M. Olivucci, and M. A. Robb, Chem. Soc. Rev. **25**, 321 (1996).

[11] *Conical intersections in photochemistry, spectroscopy and chemical dynamics*, Chem. Phys. **259**, 121-337 (2000).

[12] M. A. Robb, *Reviews in Computational Chemistry*, edited by K. Lipkowitz and D. Boyd, (Wiley, New York, **15**, 87 (2000)).

[13] *The Role of Degenerate States in Chemistry*, edited by M. Baer and G. D. Billing, Adv. Chem. Phys. Vol. **124** (Wiley, Hoboken, 2002).

[14] *Conical Intersections: Electronic Structure, Dynamics and Spectroscopy*, edited by W. Domcke, D. R. Yarkony, and H. Köppel (WorldScientific, Singapore, 2004).

[15] H. A. Jahn and E. Teller, Proc. Roy. Soc. London, Ser. A **161**, 220 (1937).

[16] H. A. Jahn, Proc. R. Soc. London, Ser. A **164**, 117 (1938).

[17] R. Englman, *The Jahn-Teller Effect in Molecules and Crystals* (Wiley, New York, 1972).

[18] I. B. Bersuker *The Jahn-Teller Effect and Vibronic Interactions in Modern Chemistry* (Plenum Press, New York, 1984).

[19] G. Fischer, *Vibronic Coupling* (Academic Press, London, 1984).

[20] *The Dynamical Jahn-Teller Effect in Localized Systems*, edited by Y. E. Perlin and M. Wagner (North-Holland, Amsterdam, 1984).

[21] I. B. Bersuker and V. Z. Polinger, *Vibronic Interactions in Molecules and Crystals* (Springer-Verlag, Berlin, 1989).

[22] I. B. Bersuker, Chem. Rev. **101**, 1067 (2001) and the references therein.

[23] I. B. Bersuker, *The Jahn-Teller Effect* (Cambridge University Press, 2006).

[24] H. C. Longuet-Higgins, U. Öpik, M. H. L. Pryce and R. A. Sack, Proc. R. Soc. London, Ser. A **244**, 1 (1958).

[25] H. C. Longuet-Higgins, in *Advances in Spectroscopy*, H. W. Thompson (Ed.), Interscience, New York, 1961, Vol. II, p.420.

[26] H. Köppel, L. S. Cederbaum and W. Domcke, Mol. Phys. **41**, 669 (1980).

[27] J. E. Huheey, E. A. Keiter, and R. L. Keiter, *Inorganic Chemistry: Principles of structure and reactivity, 4th ed.* (Haper Collins, New York, 1993).

[28] M. D. Sturge, Solid State Phys. **20**, 91 (1967).

[29] M. D. Kaplan and B. G. Vekhter, *Cooperative phenomena in Jahn-Teller Crystals* (Plenum Press, New York, 1995).

[30] L. R. Falvello, J. Chem. Soc., Dalton Trans. **23**, 4463 (1997).

[31] *In Molecular Ions: Spectroscopy, Structure, and Chemistry*, edited by T. A. Miller and V. E. Bondybey (North-Holland, Amsterdam, 1983).

[32] H. Köppel, Z. für Physikal. Chemie. **200**, 3 (1997).

[33] T. A. Barckholtz and T. A. Miller, Int. Rev. Phys. Chem. **17**, 435 (1998).

[34] T. A. Barckholtz and T. A. Miller, J. Phys. Chem. A **103**, 2321 (1999).

[35] C. C. Chancey and M. C. M. O'Brien, *The Jahn-Teller Effect in C_{60} and Other Icasahedral Complexes* (Princeton University Press, Princeton, New Jersey, 1997).

[36] G. Herzberg, *Molecular Spectra and Molecular Structure* (Van Nostrand, New York, 1966), Vol. **III**.

[37] S. Mahapatra, G. A. Worth, H. -D. Meyer, L. S. Cederbaum, and H. Köppel, J. Phys. Chem. A **105**, 5567 (2001).

[38] H. Köppel, M. Döscher, I. Bâldea, H. -D. Meyer, and P. G. Szalay, J. Chem. Phys. **117**, 2657 (2002).

[39] C. Woywod, S. Scharfe, R. Krawczyk, W. Domcke, and H. Köppel, J. Chem. Phys. **118**, 5880 (2003).

[40] S. Mahapatra and H. Köppel, J. Chem. Phys. **109**, 1721 (1998); H. Köppel, M. Döscher, and S. Mahapatra, Int. J. Quant. Chem. **80**, 942 (2000).

[41] S. Mahapatra, Acc. Chem. Res. **42**, 1004 (2009).

[42] U. Öpik and M. H. L. Pryce, Proc. R. Soc. London, Ser. A **238**, 425 (1957).

[43] M. H. Perrin and M. Gouterman, J. Chem. Phys. **46**, 1019 (1967); J. H. van der Waals, A. M. D. Berghuis, and M. S. de Groot, Mol. Phys. **13**, 301 (1967); J. H. van der Waals, A. M. D. Berghuis, and M. S. de Groot, Mol. Phys. **21**, 497 (1971); P. J. Stephens, J. Chem. Phys. **51**, 1995 (1969).

[44] M. Z. Zgierski and M. Pawlikowski, J. Chem. Phys. **70**, 3444 (1979).

[45] H. Köppel, L. S. Cederbaum and W. Domcke, J. Chem. Phys. **89**, 2023 (1988).

[46] S. Mahapatra, L. S. Cederbaum and H. Köppel, J. Chem. Phys. **111**, 10452 (1999).

[47] L. S. Cederbaum, W. Domcke and H. Köppel, Chem. Phys. **33**, 319 (1978).

[48] J. G. Bednorz and K. A. Müller, Perovskite type oxides: The new approach to high-Tc superconductivity, in: Nobel Lectures, Physics 1981-1990, (World Scientific, Singapore, 1993).

[49] R. Renner, Z. Phys. **92**, 172 (1934).

[50] A. N. Petelin and A. A. Kieslev, Int. J. Quantum Chem. **6** 701 (1972).

[51] A. J. Merer and D. N. Travis, Can. J. Phys. **43** 1795 (1965).

[52] C. F. Chang and Y. N. Chiu, J. Chem. Phys. **53** 2186 (1970).

[53] J. T. Hougen and J. P. Jesson, J. Chem. Phys. **38** 1524 (1963).

[54] J. T. Hougen, J. Chem. Phys. **36** 519 (1962).

[55] P. Rosmus, G. Chambaud, *The Renner-Teller effect and the role of electronically degenerate states in molecular ions*, in: C. Y. Ng (Ed.), Photoionization and Photodetachment, Vol. 10A, World Scientific, Singapore, 2000, Ch. 5.

[56] J. von Neumann and E. P. Wigner, Physik. Z. **30**, 467 (1929).

[57] C. A. Mead and D. G. Truhlar, J. Chem. Phs. **70**, 2284 (1979).

[58] M. Desouter-Lecomte, C. Galloy, J. C. Lorquet, and M. Vaz Pires, J. Chem. Phys. **71**, 3661 (1979).

[59] W. Domcke and G. Stock, Adv. Chem. Phys. **100**, 1 (1997).

[60] B. Heumann, R. Düren and R. Schinke, Chem. Phys. Lett. **180**, 583 (1991).

[61] B. Heumann, K. Weide, R. Düren and R. Schinke, J. Chem. Phys. **98**, 5508 (1993).

[62] B. Heumann and R. Schinke, J. Chem. Phys. **101**, 7488 (1994).

[63] N. Matsunaga and D. R. Yarkony, J. Chem. Phys. **107**, 7825 (1997).

[64] D. R. Yarkony, J. Chem. Phys. **104**, 7866 (1996).

[65] G. J. Atchity, S. S. Xantheas, K. Ruedenberg, J. Chem. Phys. **95**, 1862 (1991).

[66] A. Migani and M. Olivucci, Chapter 6, In; *Conical Intersections: Electronic Structure, Dynamics and Spectroscopy*, edited by W. Domcke, D. R. Yarkony, and H. Köppel (WorldScientific, Singapore, 2004).

[67] M. J. Paterson, M. A. Robb, L. Blancafort and A. D. DeBellis, J. Phys. Chem. A **109**, 7527 (2006).

[68] D. R. Yarkony, J. Phys. Chem. A **105**, 6277 (2001).

[69] J. Michl and V. Bonacic-Koutecky, *Electronic Aspects of Organic Photochemistry* (Wiley, New York, 1990).

[70] H. C. Longuet-Higgins, Proc. Roy. Soc. London, Ser. A, **344**, 147 (1975).

[71] D. R. Yarkony, Rev. Mod. Phys. **68**, 985 (1996).

[72] H. Köppel and W. Domcke, Encyclopedia of Computational Chemistry, Ed., P. V. R. Schleyer, Wiley: New York, 1998, P. 3166.

[73] H. Sponer, J. Chem. Phys. **22**, 234 (1954).

[74] C. D. Cooper, J. Chem. Phys. **22**, 503 (1954).

[75] K. N. Rao and H. Sponer, Can. J. Phys. **35**, 332 (1957).

[76] D. F. Evans, J. Chem. Soc. (1959) 2753.

[77] P. D. Singh and A. N. Pathak, Indian J. Pure Appl. Phys. 7 (1969) 39.

[78] D. Philips, J. Chem. Phys. **46**, 4679 (1967).

[79] R. Gilbert, P. Sauvageau and C. Sandorfy, Can. J. Chem. **50**, 543 (1972).

[80] G. L. Loper and E. K. C. Lee, Chem. Phys. Lett. **13**, 140 (1972).

[81] J. Metcalfe, M. G. Rockley and D. Philips, J. Chem. Soc. Faraday Trans. **270**, 1660 (1974).

[82] M. B. Robin, *Higher Excited States of Polyatomic Molecules*, Vol. III (Academic, New York, 1975), and references therein.

[83] C. B. Duke, K. L. Yip, G. P. Ceaser, A. W. Potts and D. G. Streets, J. Chem. Phys. **66**, 256 (1976).

[84] R. P. Frueholz, W. M. Flicker, O. A. Mosher and A. Kuppermann, J. Chem. Phys. **70**, 3057 (1979).

[85] J. Philis, A. Bolovinos, G. Andritsopoulos, E. Pantos and P. tsekeris, J. Phys. B: At. Mol. Phys. **14**, 3621 (1981).

[86] D. V. O'connor, M. Sumitani, J. M. Morris and K. Yoshihara, Chem. Phys. Lett. **93**, 350 (1982).

[87] O. Plashkevych, L. Yang, O. Vahtras, H. Ågren and L. G. M. Pettersson, Chem. Phys. **222**, 125 (1997).

[88] C. D. Keefe, J. Barrett and L. L. Jessome, J. Mol. Struc. **734**, 67 (2005).

[89] M. Z. Zgierski, T. Fujiwara and E. C. Lim, J. Chem. Phys. **122**, 144312 (2005).

[90] S. H. Lee, C. Y. Wu, S. K. Yang and Y. P. Lee, J. Chem. Phys. **125**, 144301 (2006).

[91] I. Pugliesi, N. M. Tonge and M. C. R. Cockett, J. Chem. Phys. **129**, 104303 (2008).

[92] C. R. Brundle, M. B. robin and N. A. Kuebler, J. Am. Chem. Soc. **94**, 1451 (1972).

[93] C. R. Brundle, M. B. robin and N. A. Kuebler, J. Am. Chem. Soc. **94**, 1466 (1972).

[94] G. Dujardin, S. Leach, O. Duyuit, T. Govers and P. M. Guyon, J. Chem. Phys. **79**, 644 (1983).

[95] Y. Tsuchiya, M. Fujii and M. Lto, J. Chem. Phys. **90**, 6965 (1989).

[96] M. Born, Nachirichten Akad. Wiss. Göttingen, Math.-Physik Kl. II, Berlin, (1951).

[97] L. S. Cederbaum and W. Domcke, Adv. Chem. Phys. **36**, 205 (1977).

[98] B. H. Lengsfield and D. R. Yarkony, Adv. Chem. Phys. **82**, 1 (1992).

[99] G. A. Worth and L. S. Cederbaum, Ann. Rev. Phys. Chem. **55**, 127 (2004).

[100] W. Lichten, Phys. Rev. **164**, 131 (1967); F. T. Smith, Phys. Rev. **179**, 111 (1969); T. F. O'Malley, Adv. At. Mol. Phys. **7**, 223 (1971); T. Pacher, L. S. Cederbaum, and H. Köppel, Adv. Chem. Phys. **84**, 293 (1993).

[101] M. Baer, Mol. Phys. **40**, 1011 (1980).

[102] C. A. Mead and D. G. Truhlar, J. Chem. Phys. **77**, 6090 (1982).

[103] M. Baer, Chem. Phys. Lett. **35**, 112 (1975).

[104] V. Sidis, Adv. Chem. Phys. **82**, 73 (1992).

[105] M. Baer, Adv. Chem. Phys. **82**, 187 (1992).

[106] R. K. Preston and J. C. Tully, J. Chem. Phys. **54**, 4297 (1971).

[107] G. Hirsch, P. J. Bruna, R. J. Buenker, and S. D. Peyerimhoff, Chem. Phys. **45**, 335 (1980)

[108] H. J. Werner and W. Meyer, J. Chem. Phys. **74**, 5802 (1981).

[109] T. Pacher, L. S. Cederbaum, and H. Köppel, Adv. Chem. Phys. **84**, 293 (1993).

[110] A. Thiel and H. Köppel, J. Chem. Phys. **110**, 9371 (1999).

[111] H. Köppel, J. Gronki, and S. Mahapatra, J. Chem. Phys. **115**, 23771 (2001).

[112] H. Köppel in Ref. [14], p.429

[113] E. B. Wilson Jr., J. C. Decius, and P. C. Cross, *Molecular vibrations* (McGraw-Hill, New York, 1955).

[114] R. Meiswinkel and H. Köppel, Chem. Phys. **144**, 117 (1990).

[115] W. Domcke, H. Köppel, and L. S. Cederbaum, Mol. Phys. **43**, 851 (1981).

[116] J. Cullum and R. Willoughby, *Lanczos Algorithms for Large Symmetric Eigenvalue Problems* (Birkhäuser, Boston, 1985), Vols. I and II.

[117] E. Heller, J. Chem. Phys. **68**, 2066 (1978); Acc. Chem. Res. **84**, 293 (1981).

[118] G. A. Worth, M. H. Beck, A. Jäckle, and H. -D. Meyer, The MCTDH Package, Version 8.2, (2000), University of Heidelberg, Germany. H. -D. Meyer, Version 8.3, (2002). See http://www.pci.uni-heidelberg.de/tc/usr/mctdh/

[119] H. -D. Meyer, U. Manthe, and L. S. Cederbaum, Chem. Phys. Lett. **165**, 73 (1990).

[120] U. Manthe, H. -D. Meyer, and L. S. Cederbaum, J. Chem. Phys. **97**, 3199 (1992).

[121] M. Ehara, H. -D. Meyer, and L. S. Cederbaum, J. Chem. Phys. **105**, 8865 (1996).

[122] M. H. Beck, A. Jäckle, G. A. Worth, and H. -D. Meyer, Phys. Rep. **324**, 1 (2000).

[123] *Multidimensional Quantum Dynamics : MCTDH Theory and Applications* : Edited by H. -D. Meyer, F. Gatti and G. A. Worth, WILEY-VCH, Weinheim, Germany, 2009.

[124] P. A. M. Dirac, Proc. Cambridge Philos. Soc. **26**, 376 (1930).

[125] J. Frenkel, *Wave Mechanics* (Clarendon, Oxford, 1934).

[126] H. Bock, R. Dammel and D. Lentz, Inorg. Chem. **23**, 1535 (1984).

[127] D. M. P. Holland and L. Karlsson, J. Electron Spectrosc. and Related Phenom. **150**, 47 (2006).

[128] M. J. Frisch, et al., *Gaussian* 03, revision B.05; Gaussian, Inc., Pittsburgh, PA, 2003.

[129] Y. Shimizu, K. Ueda, H. Chiba, M. Okunishi, K. Ohmori, Y. Sato, I. H. Suzuki, T. Ibuki and K. Okada, Chem. Phys. **244**, 439 (1999).

[130] L. Åsbrnk, A. Svensson, W. Von Niesson and G. Bieri, J. Electron Spectrosc. Relat. Phenom. **24**, 293 (1981).

[131] T. Shimanouchi, Tables of molecular vibrational frequencies, consolidated volume I NSRDS NBS-39. see http://srdata.nist.gov/cccbdb/

[132] S. Faraji, H. Köppel, W. Eisfeld and S. Mahapatra, Chem. Phys. **347**, 110 (2008).

[133] L. S. Cederbaum, J. Phys. B, **8**, 290 (1975).

[134] V. Engel, Chem. Phys. Lett. **189**, 76 (1992).

[135] S. Ghanta and S. Mahapatra, Chem. Phys. **347**, 97 (2008).

[136] T. Cvitas, H. Güsten, L. Klasinc, I. Novak, and H. Vancik, Z. Naturforsch. **1528**, 32a (1977).

[137] T. Cvitas, I. Novak, and L. Klasinc, Int. J. Quan. Chem. **737**, 21 (1982).

[138] M. Döscher, H. Köppel and P. G. Szalay, J. Chem. Phys. **117**, 2645 (2002).

[139] H. Köppel, M. Döscher, I. Bâldea, H. -D. Meyer and P.G. Szalay, J. Chem. Phys. **117**, 2657 (2002).

[140] B. E. Applegate and T. A. Miller, J. Chem. Phys. **117**, 10654 (2002).

[141] P. M. Johnson, J. Chem. Phys. **117**, 9991 (2002).

[142] A. B. Burrill, Y. K. Chung, H. A. Mann and P. M. Johnson, J. Chem. Phys. **120**, 8587 (2004).

[143] C. Cossart-Magos, D. Cossart and S. Leach, Mol. Phys. **37**, 793 (1979).

[144] D. Klapstein, S. Leutwyler and J. P. Maier, Mol. Phys. **51**, 413 (1984).

[145] M. Allan, J. P. Maier and O. Marthaler, Chem. Phys. **26**, 131 (1977).

[146] T. J. Sears, T. A. Miller and V. E. Bondybey, J. Chem. Phys. **72**, 6070 (1980); V. E. Bondybey, T. A. Miller and J. H. English, J. Chem. Phys. **71**, 1088 (1979).

[147] G. Lembach and B. Brutschy, *J. Phys. Chem. A.* 1998, **102**, 6068.

[148] D. P. Taylor, J. G. Goode, J. E. LeClaire and P. M. Johnson, *J. Chem. Phys.* 1995, **103**, 6293.

[149] K. Müller-Dethlefs and E. W. Schlag, *Annu. Rev. Phys.Chem.* 1991, **42**, 109.

[150] A. W. Potts, W. C. Price, D. G. Streets and T. A. Williams, Faraday Discuss. Chem. Soc. **54**, 168 (1972).

[151] G. Bieri, L. Åsbrink and W. Von Niessen, J. Electron Spectrosc. Relat. Phenom., **23**, 281 (1981).

[152] C. H. Kwon and M. S. Kim, J. Chem. Phys. **121**, 2622 (2004).

[153] J. P. Maier and F. Thommen, Chem. Phys. **57**, 319 (1981).

[154] B. Cage et al., Chem. Phys. Lett. **394**, 188 (2004).

[155] T. H. Dunning, Jr., J. Chem. Phys. **90**, 1007 (1989).

[156] V. R. Thalladi, H. C. Weiss, D. Blässer, R. Boese, A. Nangia and G. R. Desiraju, J. Am. Chem. Soc. **120**, 8702 (1998).

[157] D. A. Braden and B. S. Hudson, J. Phys. Chem. A. **104**, 982 (2000).

[158] J. G. Philis, T. Mondal and S. Mahapatra, Chem. Phys. Lett. **495**, 187 (2010).

[159] I. Bâldea, J. Franz, P. G. Szalay and H. Köppel, Chem. Phys. **329**, 65 (2006).

[160] E. Gindensperger, I. Bâldea, J. Franz and H. Köppel, Chem. Phys. **338**, 207 (2007).

[161] S. Faraji and H. Köppel, J. Chem. Phys. **129**, 74310 (2008).

[162] S. Faraji, H. -D. Meyer and H. Köppel, J. Chem. Phys. **129**, 74311 (2008).

[163] T. Mondal, and S. Mahapatra, Phys. Chem. Chem. Phys. **11**, 10867 (2009).

[164] H. Sekino, and R. J. Bartlett, Int. J. Quantum. Chem., Chem. Symp. **18**, 255 (1984); J. Geertsen, M. Rittby, and R. J. Bartlett, Chem. Phys. Lett. **164**, 57 (1989); J. F. Stanton, and R. J. Bartlett, J. Chem. Phys. **98**, 7029 (1993).

[165] R. D. Amos, A. Bernhardsson, A. Berning, P. Celani, D. L. Cooper, M. J. O. Deegan, A. J. Dobbyn, F. Eckert, C. Hampel, G. Hetzer, et al., MOLPRO, a package of ab initio programs designed by H. -J. Werner, P. J. Knowles, version 2008.1.

[166] H. Nakatsuji, and K. Hirao, Chem. Phys. Lett. **47**, 569 (1977); H. Nakatsuji, ibid. **67**, 329 (1979); **67**, 334 (1979).

[167] E. Dalgaard, and H. J. Monkhorst, Phys. rev. A **28**, 1217 (1983); H. Koch, and P. Jørgensen, J. Chem. Phys. **93**, 3333 (1990); H. Koch, H. J. A. Jensen, P Jørgensen, and T. Helgaker, ibid. **93**, 3345 (1990).

[168] A. Bergner, M. Dolg, W. Kuechle, H. Stoll, and H. Preuss, Mol. Phys. **80**, 1431 (1993).

[169] H. Müller, H. Köppel, and L. S. Cederbaum, New J. Chem. **17**, 7 (1993).

[170] H. Studzinski, S. Zhang, Y. Wang, and F. Temps, J. Chem. Phys. **128**, 164314 (2008).

[171] D. M. P. Holland, D. A. Shaw, M. Stener, and P. Decleva, J. Phys. B: At. Mol. Opt. Phys. **42**, 245201 (2009).

[172] Y. Tsuchiya, K. Takazawa, M. Fujji, and M. Ito, Chem. Phys. Lett. **183**, 107 (1991).

[173] C. H. Kwon and M. S. Kim, J. Chem. Phys. **120**, 11578 (2004).

[174] T. J. Sears, T. A. Miller and V. E. Bondybey, J. Chem. Phys. **74**, 3240 (1981).

[175] R. L. Whetten and E. R. Grant, J. Chem. Phys. **80**, 5999 (1984).

List of Publications

1. **T. Mondal** and S. Mahapatra, *"Photophysics of fluorinated benzene. I. Quantum chemistry"*, J. Chem. Phys. **133**, 084304 (2010).

2. **T. Mondal** and S. Mahapatra, *"Photophysics of fluorinated benzene. II. Quantum dynamics"*, J. Chem. Phys. **133**, 084305 (2010).

3. J. G. Philis, **T. Mondal** and S. Mahapatra, *"Vibronic structure in the low-lying Rydberg states of hexafluorobenzene and 1,3,5-trifluorobenzene detected by two-photon spectroscopy "*, Chem. Phys. Lett. **495**, 187 (2010).

4. **T. Mondal** and S. Mahapatra, *"Jahn-Teller and pseudo-Jahn-teller effects in the low-lying electronic states of 1,3,5-trifluorobenzene radical cation "*, Phys. Chem. Chem. Phys. **11**, 10867 (2009).

5. **T. Mondal** and S. Mahapatra, *"Complex dynamics at conical intersections: Vibronic spectra and ultrafast decay of electronically excited trifluoroacetonitrile radical cation "*, J. Phys. Chem. A **112**, 8215 (2008).

6. **T. Mondal** and S. Mahapatra, *"Jahn-Teller and pseudo-Jahn-teller effects on the photophysics of hexafluorobenzene "*, (Manuscript under preparation).

7. **T. Mondal**, B. Saritha, S. Ghanta, T. K. Roy, S. Mahapatra and M. Durga Prasad, *"On some strategies to design new high energy density molecules "*, J. Mol. Struc. (THEOCHEM) **897**, 42 (2008).

8. T. K. Roy, S. Ghanta, **T. Mondal**, B. Saritha, S. Mahapatra and M. Durga Prasad, *"Conformational preferences of monosubstituted cyclohydronitrogens: A theoretical study "*, J. Mol. Struc. (THEOCHEM) **822**, 145 (2007).

Posters/Paper/Oral Presentations in Symposia

1. Participant in "Theoretical Chemistry Symposium (TCS 2006)",
   December 11-13, 2006, Bharathidasan University, Thiruchirappalli.

2. Poster presented in "Chemfest 2007",
   March 9-10, 2007, School of Chemistry, University of Hyderabad, Hyderabad.

3. Poster presented in "Spectroscopy and Dynamics of Molecules and Clusters (SDMC 2008)",
   February 22-24, 2008, Indian Institute of Technology Madras, Chennai.

4. Poster presented in "Chemfest 2008",
   March 1-2, 2008, School of Chemistry, University of Hyderabad, Hyderabad.

5. Poster presented in "Spectroscopy and Dynamics of Molecules and Clusters (SDMC 2009)",
   February 20-22, 2009, Indian Association for the Cultivation of Science, Kolkata.

6. Oral presentation in "Chemfest 2009",
   March 7-8, 2009, School of Chemistry, University of Hyderabad, Hyderabad.

7. Poster presented in "Chemfest 2009",
   March 7-8, 2009, School of Chemistry, University of Hyderabad, Hyderabad.

8. Poster presented in "Chemfest 2010",
   January 8-9, 2010, School of Chemistry, University of Hyderabad, Hyderabad.

9. Poster presented in "XXth International Symposium on the Jahn-Teller effect ", August 16-20, 2010, University of Fribourg, Fribourg, Switzerland.